

AGENTS FOR HEPATOCELLULAR CARCINOMA:
SYNTHESIS AND MODE OF ACTION

CHEN XIAO
(B.Sc., NANJING UNIVERSITY)

A THESIS SUBMITTED
FOR THE DEGREE OF DOCTOR OF PHILOSOPHY

DEPARTMENT OF PHARMACY
NATIONAL UNIVERSITY OF SINGAPORE


2014

Declaration

I hereby declare that this thesis is my original work and it has been written by me in its entirety. I have duly acknowledged all the sources of information which have been used in the thesis.

This thesis has also not been submitted for any degree in any university previously.

Chen Xiao

Signature: 

Jan 21, 2014

Acknowledgement

I would like to dedicate my acknowledgement to my supervisor, Associate Professor Go Mei Lin for her constant guidance and support. Without her advices and insights, this piece of thesis work would not be possible.

I am grateful to my co-supervisor, Dr Ho Han Kiat for his valuable advices and encouragement. I am grateful to Dr Gautam Sethi from Department of pharmacology, Yong Loo Ling School of Medicine, NUS, for his guidance on most of the pharmacological work. I am grateful to Dr Jin Haixiao from Ningbo University for her guidance of the molecular docking.

Then I would like to thank all my seniors and other labmates for their help on my bench work. Namely, they are Dr Yang Tianming, Dr Zhang Wei, Dr Lee Chong Yew, Dr Sim Hong May, Dr Wee Xi Kai, Dr Yeo Wee Kiang, Dr Pandy Murugappan Ramanujulu Sam, Dr Tan Kheng Lin Meg, Ms Pang Yi Yun, Ms Yap Siew Qi and Mr Ho Si Han Sheman.

I am also appreciated the undergraduate students in our lab, namely Mr Ng Boon Kiang Ivan, Ms Ang Ai Ling Irene, Ms Low Ying Xiu, Ms Loke Mei Xin, Mr Shih Shan Wei Shannon, Mr Lee Kwok Loong Sylvester for their hard work.

I am grateful for the assistance of the lab technicians Mdm Oh Tang Booy, Ms Ng Sek Eng, Mr Li Feng.

I would like to thank the support and encouragement from my family and friends. I would like to thank specially to my fiancé Dr Sun Lingyi for the four-year companionship during the time I pursued the PhD degree.

Finally, I would like to acknowledge the financial support for my graduate studies form the National University of Singapore Research Scholarship.

Table of Content

Declaration	i
Acknowledgement.....	ii
Summary	viii
Abbreviations List.....	xii
List of Figures	xiv
List of Schemes	xx
List of Tables.....	xxi
Chapter 1 Introduction.....	1
1.1. Background of Hepatocellular Carcinoma (HCC): Epidemiology, risk factors and management.....	1
1.2. Molecular targeted therapy for HCC	2
1.3. Sorafenib as targeted therapy for advanced HCC.....	3
1.3.1. Resistance to sorafenib treatment in HCC.....	4
1.4. Other molecular targeted therapies for HCC	8
1.5. Sirtuins as emerging therapeutic targets for HCC	9
1.5.1. Functions of sirtuins	11
1.5.2. Sirtuins and cancer.....	13
1.5.3. Sirtuins in HCC	15
1.5.3.1. SIRT 1 in HCC	15
1.5.3.2. SIRT 2 in HCC	16
1.5.4. Functionalized indolin-2-ones as sirtuin inhibitors	16
1.6. Functionalized indolin-2-ones as inhibitors of kinases.....	17
1.7. Compound 47: A multi-targeting kinase inhibitor with growth inhibitory effects on a panel of HCC cells.	25
1.8. Statement of purpose	26
Chapter 2 Design and Synthesis of Target Compounds: 3-substituted Indolin-2-ones	29
2.1. Introduction	29
2.2. Rationale of design	29
2.3. Chemical considerations.....	35
2.3.1. Syntheses of benzylidene indolinones of Series 1-8.....	35

2.3.2.	Syntheses of 3-formyl-benzenesulfonamide and 3-formyl- <i>N</i> -substituted-benzenesulfonamide	37
2.3.3.	Synthesis of 5,6-difluoro-oxindole	38
2.3.4.	Syntheses of 1-methyl-oxindole and 6-chloro-1-methyl-oxindole	39
2.3.5.	Synthesis of 3-arylimino-2-indolones of Series 8	40
2.4.	Assignment of configuration	40
2.5.	Summary	55
2.6.	Experimental methods	56
2.6.1.	General details	56
2.6.2.	X-ray crystal structure of Compound 6-6	57
2.6.3.	General procedure for the synthesis of 3-benzylidene indolin-2-ones of Series 1-8	58
2.6.4.	Synthesis of sulfamoyl and <i>N</i> -substituted sulfamoyl benzoic acids	58
2.6.5.	Synthesis of formyl benzenesulfonamides	59
2.6.6.	Synthesis of 5,6-difluoro-oxindole	60
2.6.7.	Synthesis of 1-methyl-oxindole and 6-chloro-1-methyl-oxindole	61
2.6.8.	General procedure for the synthesis of 3-phenylimino-2-indolones (8-2, 8-4, 8-6, 8-7)	62
Chapter 3: Investigations into the growth inhibitory activities of Series 1-8 compounds on malignant liver cancer cell lines		63
3.1.	Introduction	63
3.2.	Materials and Methods	63
3.2.1.	Reagents	63
3.2.2.	Cell Lines and cell culture	64
3.2.3.	MTT assay for determination of cell growth inhibition	64
3.2.4.	Detection of Apoptosis by flow cytometry	65
3.2.5.	Preparation of HuH7 cell lysates	66
3.2.6.	Protein quantification	66
3.2.7.	Sodium dodecyl sulfate - polyacrylamide gel electrophoresis (SDS-PAGE)	67
3.2.8.	Western blotting	67
3.3.	Results	68
3.3.1.	Growth inhibitory activities of Series 1-8 on HuH7 cells	68
3.3.1.1.	Growth inhibitory activities of Series 2, 3 and 4 compounds	70

3.3.1.2.	Growth inhibitory activities of Series 6 and 7 compounds.....	72
3.3.1.3.	Growth inhibitory activities of Series 5 compounds	74
3.3.1.4.	Growth inhibitory activities of Series 8 compounds	76
3.3.2.	Growth inhibitory properties of selected compounds on Hep3B and HepG2 ..	78
3.3.3.	Growth inhibitory properties and selectivity ratios of selected compounds on IMR 90 cell	81
3.3.4.	Investigations into the induction of apoptotic cell death of HuH7 cells by selected test compounds	83
3.4.	Discussion.....	87
3.5.	Summary.....	91
Chapter 4 : Investigations into the sirtuin inhibitory activities of selected compounds from Series 1-8.....		93
4.1.	Introduction	93
4.2.	Materials and Methods	93
4.2.1.	Reagents	93
4.2.2.	Principle of sirtuin enzyme assay	94
4.2.3.	Measurement of sirtuin activity.....	95
4.2.4.	Preparation of HuH7 or Hep G2 cell lysates	97
4.2.5.	Protein quantification	97
4.2.6.	Sodium dodecyl sulfate - polyacrylamide gel electrophoresis (SDS-PAGE)...	97
4.2.7.	Western blotting	97
4.2.8.	Molecular Docking.....	97
4.3.	Results	98
4.3.1.	Inhibition of sirtuin activities by selected test compounds.....	98
4.3.2.	Validation of sirtuin inhibition by compounds 5-1 and 8-7 using Western blot analysis	100
4.3.3.	Molecular docking of functionalized benzylidene indolinones in the SIRT2 binding pocket	103
4.3.3.1.	Docking analysis of <i>Z</i> isomers of test compounds on SIRT2.....	106
4.3.3.2.	Docking analysis of <i>E</i> isomers of test compounds on SIRT2.....	113
4.3.4.	Docking analysis of <i>Z</i> isomers and <i>E</i> isomers of test compounds on SIRT1 .	117
4.4.	Discussion.....	117
4.5.	Summary.....	121

Chapter 5: Investigations into the receptor tyrosine kinase (RTK) inhibitory activity of Compound 3-12.....	122
5.1. Introduction	122
5.2. Experimental methods	122
5.2.1. Chemicals and Materials	122
5.2.2. Preparation of HuH7 cell lysates	122
5.2.3. Protein quantification	123
5.2.4. Immunoprecipitation	123
5.2.5. Sodium dodecyl sulfate - polyacrylamide gel electrophoresis (SDS-PAGE).....	123
5.2.6. Western blotting	123
5.2.7. Human receptor tyrosine kinase profiling	124
5.2.7.1. Principle of human phospho-receptor tyrosine kinase array	124
5.2.7.2. Procedure	124
5.2.8. FGFR4 homology model and molecular docking	126
5.3. Results	127
5.3.1. Effects of 47 and 3-12 on the phosphorylated states of RTKs in HuH7 cells	127
5.3.2. Molecular docking of 3-12 in a homology model of human FGFR4	131
5.4. Discussion.....	136
5.5. Summary.....	140
Chapter 6: Investigation of the drug-like properties of selected benzylidene indolinones....	141
6.1. Introduction	141
6.2. Materials and Methods	141
6.2.1. Determination of aqueous solubility.....	141
6.2.2. Determination of <i>in vitro</i> stability of compound 47, 1-23, 3-12, and 7-6 in the presence of rat male liver microsomes	143
6.2.3. Assessment of aggregation tendency by dynamic light scattering (DLS)	144
6.2.4. Determination of PAMPA permeability	145
6.2.5. Determination of cytotoxicities of test compounds	145
6.2.6. Determination of genotoxicities of test compounds	145
6.3. Results	145
6.3.1. Aqueous solubilities of compounds 47, 1-18, 1-23, 3-10, 3-12 and 7-6.....	145
6.3.2. PAMPA permeabilities of compounds 47, 1-18, 1-23, 3-10, 3-12 and 7-6....	146

6.3.3.	<i>In vitro</i> metabolic stability of 47, 1-23, 3-12 and 7-6.....	148
6.3.4.	<i>In vitro</i> cytotoxicities and genotoxicities of 47, 1-23, 3-12 and 7-6.....	149
6.4.	Aggregate formation by test compounds.....	151
6.4.1.	Maximum tolerated dose of 3-12 in mice.....	152
6.5.	Discussion.....	153
6.6.	Summary.....	155
	Chapter 7: Conclusions	156
	Reference.....	161
	Appendix I: Characterization of synthesized analogues.....	174
	Appendix II Compounds that were not done by the candidate: Method and Charaterization	222
	Appendix III:Crystal data and structure refinement for 6-6	233
	Appendix IV : The second attempt of Western blot analysis of sirtuin inhibition by compounds 5-1 and 8-7	234
	Appendix V: Determinations of drug likeness properties of the test compounds that are done by Drug Development Unit of NUS.	235
	Appendix VI: Purity data of the synthesized compounds	238

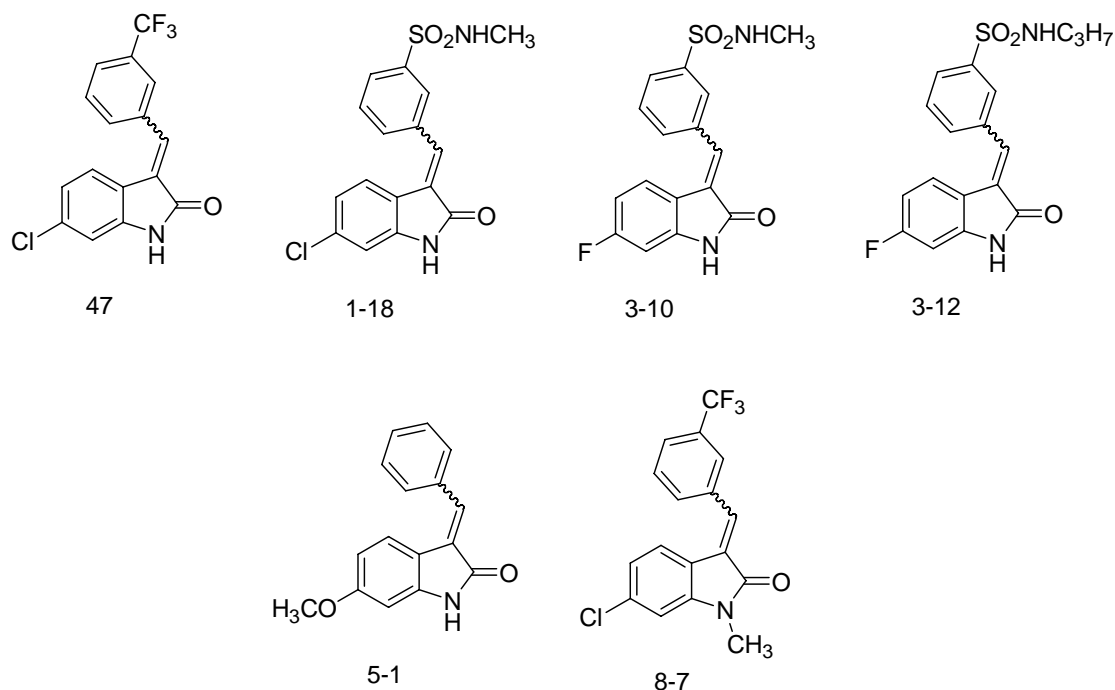
Summary

The benzylideneindolinone scaffold is historically linked to the inhibition of receptor tyrosine kinases (RTKs) and several functionalized analogs have shown promising anticancer activity by inhibiting the aberrant activities of oncogenic RTKs. The compound, E/Z 6-chloro-3-(3-trifluoromethyl-benzyliden)-1,3-dihydroindol-2-one (Compound **47**) identified in the candidate laboratory was of particular interest. It exhibited potent and selective growth inhibitory effects on hepatocellular carcinoma (HCC) cells, inhibited selected RTKs, intercepted prosurvival and proliferation mechanisms and showed *in vivo* efficacy in xenograft models. However **47** was hampered by its poor physicochemical profile. It was a lipophilic molecule (ClogP 5.08) with poor aqueous solubility (0.09 μM or 0.03 $\mu\text{g}/\text{mL}$, pH 7.4) and limited permeability when assessed by the parallel artificial membrane permeation assay (PAMPA). Thus the aim of this thesis was to test the hypothesis that structural elaboration of the underfunctionalized **47** would provide a means of uncovering drug-like compounds with greater potency and selectivity on HCC. It was envisaged that the enhanced potency would arise from kinase or sirtuin inhibition, or possibly, through inhibition of both targets. To this end, 115 compounds across 8 series of functionalized benzylideneindolinones were designed, synthesized and evaluated for their effects on the viability of liver cancer cell lines (HuH7, Hep3B, HepG2). The focus of the design strategy was to enhance the drug-like character of the lead compound **47**, notably its poor solubility and excessive lipophilicity. The approach was to introduce polar substituents at two sites of the scaffold, namely the indolinone ring A and the benzylidene ring B.

Based on the growth inhibitory activities on HuH7 cells, a comprehensive structure activity relationship was deduced for the benzylidene indolinone scaffold. The main points were (i) The E/Z configuration of the exocyclic methine (=C-) bond did not appear to play a major role in influencing activity; (ii) Replacement of the exocyclic methine with azomethine (=C- \rightarrow =N-) abolished activity; (iv) Substitution on the lactam N did not adversely affect activity; (iv) On the indolinone ring A, there was a preference for substitution at position 6 (6-F > 6-Cl) as compared to position 5. Difluoro substitution (at positions 4,5 or 5,6) improved activity but

only when the benzylidene ring was substituted with 3'CF₃. (v) Series 5 compounds which were substituted on ring A with 6-methoxy had exceptionally potent activity but may have a “cytostatic” component in their growth inhibitory effects. (vi) The choice of substituents on the benzylidene ring B had a marked effect on activity, possibly exceeding that of the indolinone ring A. Two substituents were associated with potent activity: 3'CF₃ and 3'N-substituted aminosulfonyl. There was a significant regioisomeric preference for position 3'. Optimal ring A and ring B combinations for potent activity were evident: For 6-F and 6-methoxy on ring A, the *N*-substituted aminosulfonyl was preferred, whereas for 6-Cl on ring A, both CF₃ and *N*-substituted aminosulfonyl sidechains were acceptable. For other halogenated ring A analogs (5-Cl, 4,5-F, 5,6-F), the CF₃ on ring B was preferred. One difference between the two ring B side chains was that analogs with CF₃ were selectively more potent on HuH7 cells compared to non-malignant IMR90 cells; (vii) A robust SAR was observed for compounds bearing the *N*-substituted aminosulfonyl side chain, namely a distinct preference for mono *N*-substitution, an increase in growth inhibitory activity on homologation (H > *N*-methyl > *N*-ethyl > *N*-n-propyl), and the negative impact on potency imparted by branching (propyl → isopropyl) and reversal of the aminosulfonyl side chain (MeNHSO₂- → MeSO₂NH-).

Selected compounds were screened on other hepatoma cells and in general, compounds that were potent on HuH7 (IC₅₀ < 1 μM) were equipotent on Hep3B but less so on HepG2. Interestingly, HuH7 and Hep3B were mutated p53 cell lines whereas HepG2 harboured wild type p53. p53 is the most frequently mutated gene in HCC and the greater susceptibilities of cells bearing mutated p53 may suggest that signaling pathways associated with the loss of function or gain of a new function due to p53 mutations were targeted by these compounds. Several potent compounds induced apoptotic cell death, further underscoring their anticancer potential for HCC.



Compound **3-12** (EZ-[(6-fluoro-2-oxindolin-3-yl)methyl]-*N*-propylbenzenesulfonamide) was one of the more potent and selective compounds affecting the viability of HCC cells. It inhibited the phosphorylation of FGFR4 and HER3 in HuH7 cells at low concentrations (0.5, 2 μ M). Levels of phospho-HER3, phospho-FGFR4 and phospho-Akt were also reduced at comparable concentrations. Molecular docking on a homology model of FGFR4 showed that **3-12** adopted favorable poses at the hinge region of FGFR4. Both the indolinone ring and the *N*-propylaminosulfonyl side chains were involved in productive binding interactions. Inhibition of FGFR4 and HER3 may contribute to the growth inhibitory effects of **3-12** on HuH7 cells.

Several members of the library inhibited SIRT2 activity. Notably **47** and **3-12** were comparable to AGK2 (a selective SIRT2 inhibitor) in their inhibitory potencies. However, the most potent inhibitors were the benzylideneindolinones substituted at position 6 with methoxy (Series 5) and *N*-substituted analogs of **47** (Series 8). Several members in Series 5 were also found to be moderately active SIRT1 inhibitors. Inhibition by representative members (**5-1**, **8-7**) promoted the hyperacetylation of physiological sirtuin substrates (p53 and α -tubulin) and induced the apoptotic cascade in HuH7 cells. Molecular docking on the X ray structure of human SIRT2 provided insight into the interactions of the scaffold with the binding pocket of

the co-factor NAD⁺. sirtuin inhibition may contribute to the growth inhibitory effects of the Series 5 and 8 compounds but may not play a major role for **3-12**, **47** and other potent analogs. Physicochemical characterization of selected potent analogs showed that many of these compounds, in particular those with *N*-substituted aminosulfonyl side chains on ring B (**1-18**, **3-10**, **3-12**) had better solubilities and PAMPA permeabilities than **47**. This was attributed to the presence of the H bonding *N*-alkylaminosulfonyl side chain. Unfortunately, the side chain was a likely metabolic hotspot, thus rendering analogs like **3-12** more susceptible to microsomal metabolism. On the other hand, **3-12** and other benzylidene indolinones were not toxic or mutagenic and did not form aggregates at pharmacologically relevant concentrations. **3-12** was well tolerated in mice up to a dose of 60 mg/kg (IP, twice weekly for 2 weeks). Taken together, the investigations reported in this thesis reinforced the notion that it was possible to improve on the growth inhibitory potencies and drug-like properties of **47** by structural modification. These findings provide a useful platform for future investigations which should focus on more extensive structural elaboration of the scaffold to enhance activity and drug-like profiles.

Abbreviations List

AceCS1	Cytoplasmic acetyl-coa synthetase exist in the cytoplasm
AceCS2	Cytoplasmic acetyl-coa synthetase exist in mitochondria
Akt	Protein kinase B
APE1	Apurinic/aprimidinic endonuclease-1
Bad	Bcl-2-associated death promoter
Bak	Bcl2-antagonist/killer
BAX	Bcl-2-associated X protein
Bcl-2	B-cell lymphoma 2
Bcl-xl	B-cell lymphoma-extra large
c-Met	Cell surface protein-tyrosine kinase receptors for hepatocyte growth factor
CPS1	Carbamoyl phosphate synthetase 1
E2F1	E2F transcription factor 1
EGFR	Epidermal growth factor receptor
Era	Estrogen receptor a
Erk	Extracellular signal-regulated kinases
FOXO	Forkhead box O
FXR	Farnesoid X receptor
GAL	Galanin receptor
GDH	Glutamate dehydrogenase
GRB2	Growth factor receptor-bound protein 2
GSK-3 β	Glycogen synthase kinase 3 beta
HER	Human epidermal growth factor receptor
HIF	Hypoxia-inducible factors
IGFR	Insulin-like growth factor receptor
IL-8	Interleukin 8
JAK	Janus kinase
LXR	Liver X receptor
MAPK	Mitogen-activated protein kinases
Mcl-1	Myeloid cell leukemia 1
Mek	Mitogen activated protein kinase kinase
mTOR	Mammalian target of rapamycin
NBS1	Nijmegen breakage syndrome protein
NF-kB	Nuclear factor kappa-light-chain-enhancer of activated B cells
PCAF	P300/CBP-associated factor
PDGFR	Platelet-derived growth factor receptor
PER2	Period 2
PGC1a	Proliferator-activated receptor c coactivator 1 α
PI3K	Phosphoinositide 3-kinase
PIP3	Phosphatidylinositol 3,4,5-trisphosphate
PPAR γ	Peroxisome proliferator-activated receptor gamma
PTEN	Phosphatase and tensin homolog
Ras	Rat sarcoma
SMAD7 (MADH7)	Mothers against decapentaplegic homolog
STAT	Signal Transducer and Activator of Transcription
SUV39H1	Suppressor of variegation 3-9 homologue

TERT	Telomerase reverse transcriptase
TGF- β	Transforming growth factor beta
TIP 60	Type 1-interacting protein with molecular weight at 60 kda
TNF	Tumor necrosis factor alpha
VEGFR	Receptors for vascular endothelial growth factor
WRN	Werner syndrome, recq helicase-like
XPA/C	Xeroderma pigmentosum group A/C

List of Figures

Figure 1-1 Structure and nomenclature of sorafenib

Figure 1-2: Modes of actions of sorafenib in HCC.

Figure 1-3: PI3K/Akt/mTOR pathway

Figure 1-4. Cartoon illustrating epithelial mesenchymal transition.

Figure 1-5: c-Met signaling pathway in hepatocellular carcinoma.

Figure 1-6: Substrates and products of sirtuin catalyzed deacetylation

Figure 1-7: Mechanism of sirtuin-catalyzed deacetylation of lysine residues.

Figure 1-8: Dual roles of SIRT 1 as tumor promoter and suppressor

Figure 1-9: Structures of benzylidene indolinones as sirtuin inhibitors

Figure 1-10: Interactions of (A) SU 4984 and (B) SU 5402 with the FGFR1 hinge region. (C) Structure of adenosine triphosphate (ATP).

Figure 1-11: (A) 3-(1H-Pyrrol-2-yl)methylene]indolin-2-one and (B) 3-[phenyl(phenylamino)methylene]indolin-2-one scaffolds.

Figure 1-12: Structures of sunitinib, torceranib, semaxinib, hesperadin and BIBF1120

Figure 1-13: Intramolecular H bonding in (A) sunitinib and (B) BIBF1120 locked the exocyclic double bond in its *Z* configuration. (C) *E* and *Z* isomers exist in equilibrium in benzylidene indolinones. (D) The pyrrolylmethylindolinone B5 has an *E* configuration due to the absence of intramolecular H bonding.

Figure 1-14: Structure activity relationships of indolinones with (A) pyrrolylmethylene and (B) benzylidene at position 3 for inhibition of RTKs.

Figure 1-15: Substituted phenyl(phenylamino)methylene indoline-2-ones.

Figure 1-16: Structures of Transforming Growth Factor β receptor 1 inhibitors V, VI and VII

Figure 1-17: E/Z-6-Chloro-3-[3-(trifluoromethyl)benzylidene]indolin-2-one (**47**)

Figure 2-1: Benzylideneindolin-2-one scaffold with modifications made at R₁, R₂ and R₃.

Structure of **47** is given on the right.

Figure 2-2: X-ray structure of Compound **6-6**

Figure 2-3: ¹HNMR spectra (amide proton and aromatic protons only) of compound **47**: (A) Freshly prepared in d₆ DMSO and (B) After 12 hr of standing at room temperature (24°C), protected from light.

Figure 2-4: ¹HNMR spectra (amide proton and aromatic protons only) of compound **6-6**: (A) Freshly prepared in d₆ DMSO and (B) After 12 hr of standing at room temperature (24°C), protected from light.

Figure 2-6: LC-MS spectrum of **47**

Figure 2-7: LC-MS spectrum of **1-18**

Figure 2-8: LC-MS spectrum of **6-6**

Figure 3-1: Dose response curves of determination of (A) IC₅₀ and (B) GI₅₀ of **5-9** on HuH7 cells, 72 h incubation.

Figure 3-2: Dose response curves of determination of (A) IC₅₀ and (B) GI₅₀ of **3-12** on HuH7 cells, 72 h incubation.

Figure 3-3: Comparison of IC₅₀ values of benzylidene indolinones and phenyliminoindolinones.

Figure 3-4: IC₅₀ values of **47** and its *N*-substituted analogs

Figure 3-5: Representative figures showing FACS analysis of HuH7 cells treated with **47**, **3-12** and **5-1**.

Figure 3-6: **3-12** (A), **5-1** (B) and **8-7** (C) induced apoptosis in HuH7 cells as seen from the increased levels of apoptotic markers cleaved caspase 3 and cleaved PARP induced by incubation with these compounds.

Figure 3-7: Graphical summary of the effect of substituents on growth inhibitory potency of benzylidene indolinones on HuH7 cells.

Figure 3-8: Summary of major SAR findings for the growth inhibitory activity of benzylidene indulines on HuH7 cells. EW: Electron withdrawing.

Figure 4-1 (A) Activity versus concentration of SIRT2 at different incubation times (15 min, 30 min, 45 min) (B) Representative dose response curve of **5-1** on SIRT1 activity

Figure 4-2: **5-1** induces hyper-acetylation of p53 and α -tubulin in (A) HepG2 and (B) HuH 7 cells after 12 h incubation.

Figure 4-3: **8-7** induces hyper-acetylation of p53 and α -tubulin in (A) HepG2 and (B) HuH7 cells after 12 hr treatment.

Figure 4-4: **5-1** decreased the expression of the pro-apoptotic protein Bax and increased the expression of anti-apoptotic proteins Bcl-2 and Bcl-xl in HuH7 cells.

Figure 4-5: Cofactor NAD⁺ in SIRT2 pocket (PDB 3ZGV).

Figure 4-6: Bond lengths between lactam moiety (NHCO) of indolinone ring and residues Tyr 104 and Arg 97:

Figure 4-7: The indolinone ring is stacked against the phenyl ring of Phe 96 and well positioned for $\pi\pi$ interactions. Illustrated with compound **2-7**

Figure 4-8: Cation- π interactions between benzylidene ring B and guanidinium side chain of Arg 97 as shown in (A) Compound **3-12** and (B) Compound **5-6**.

Figure 4-9: Orthogonal multipolar interactions are formed between C-F bonds in **47** and guanidinium side chain of Arg 97 and carbonyl O of Ser 263.

Figure 4-10: H bonding between (A) sulfonyl O atoms of **3-12** and Arg 97, Ser 263, Phe 96; (B) Nitro O atoms of III and Ser 263. (C) Overlap of **3-12** and ADP ribose in sirtuin 2 binding pocket (PDB 3ZGV).

Figure 4-11: (A) Overlap of top poses of representative Series 5 compounds (shown in different colors) in SIRT2 pocket. (B) Pose of Compound **5-7** shows H bonding of the lactam NH to amide carbonyl of Gln 167 and lactam CO to NH of imidazole in His 187.

Figure 4-12 Overlap of best poses of compound **47**, **8-7**, **8-8** and **8-9**.

Figure 4-13: (A) 7-Cl of indolinone ring of Compound III is involved in halogen bond formation with carbonyl O of Phe 119. (B) 4-F of Compound 6-6 is oriented towards carbonyl O of Asn 168 (F...O 2.39 Å) and head on orientation is likely to be destabilizing.

Figure 4-14: (A) Docking poses of **47Z** (yellow) and **47E** (green) in SIRT2 binding pocket. (B) Orientations of **47Z** (yellow) and **47E** (green) in SIRT2.

Figure 4-15: Docking poses of (A) Compound **47E** in SIRT2 binding pocket. (B) Compound **5-1E** in SIRT2 binding pocket.

Figure 4-16: Edge to face pp interactions (bracketed) between Ring B of **47 E** and phenyl ring of Phe 235

Figure 4-17: Docking poses of (A) Compound **3-12** and (B) Compound III in SIRT2 pocket.

Figure 4-18: Overlap of best poses of compound **8-7**, **8-8** and **8-9** in SIRT 2 pocket.

Figure 4-19: Summary of SAR for SIRT2 inhibitory activity.

Figure 5-1: Cartoon depicting the principle underlying the detection of phosphorylated RTKs in the Phospho-RTK Array Kit

Figure 5-10: Docking pose of **47Z** in the FGFR4 binding pocket.

Figure 5-11: Docking pose of **47E** in the FGFR4 binding pocket.

Figure 5-12: Orientation of SU 4984 in (A) FGFR1 (PDB 1AGW) and (B) FGFR4 homology model.

Figure 5-2: Coordinates of the antibody array

Figure 5-3: Intensity of blots obtained from (A) untreated HuH7 cells and HuH7 cells treated with (B) **47** at 10 μ M, (C) **3-12** at 0.5 μ M and (D) **3-12** at 2 μ M.

Figure 5-4: (A) **3-12** reduced the phosphorylation of HER3 at Tyr1289 in HuH7 cells after 24 h incubation. Total HER3 protein levels were unchanged under similar treatment conditions. (B) **3-12** reduced the phosphorylation of FGFR4 at all tyrosine sites in the protein.

Figure 5-5: **3-12** reduced the phosphorylation of Akt in HuH7 treated cells (24 h, 37°C, 5% CO₂). Phospho-Akt and total Akt levels were probed by Western blotting. Loading control was total Akt. p-Akt/Akt is the ratio of the signal intensities of respective bands, normalized against the ratio obtained in untreated cells.

Figure 5-6: Structure of SU 4984 (4-[4-(-2-oxo-1,2-dihydroindol-3-ylidene)methyl]-phenyl]-piperazine-1-carbaldehyde)

Figure 5-7: Docking pose of SU 4984 in the FGFR4 binding pocket.

Figure 5-8: Docking pose of **3-12Z** in the FGFR4 binding pocket.

Figure 5-9: Docking pose of **3-12E** in the FGFR4 binding pocket.

Figure 6-1 Percentages of test compounds and positive control midazolam relative to initial amounts (t = 0) in rat liver microsomes on incubation at 37 °C for 5, 15, 30 and 45 min.

Figure 6-2: Changes in (A) body weight, (C) % feed consumption and (C) % water consumption of Balb-c mice treated with **3-12** at 60 mg/kg, 50 mg/kg, and 30 mg /kg.

Figure 7-1: Summary of major SAR findings for the growth inhibitory activity of benzylidene indolinones on HuH7 cells.

List of Schemes

Scheme 2-1: General synthesis pathway for Series 1 to 7, **8-1**, **8-3** and **8-7**.

Scheme 2-2: Knoevenagel reaction between benzaldehyde and malonic acid

Scheme 2-3: Reaction sequences involved in synthesis of 3-formyl-*N*-substituted benzenesulfonamides

Scheme 2-4: Reaction scheme for synthesis of 5,6-difluoro-oxindole

Scheme 2-5 Syntheses of 1-methyl-oxindole and 6-chloro-1-methyl-oxindole

Scheme 2-6: Syntheses of 1-methyl-oxindole and 6-chloro-1-methyl-oxindole

Scheme 4-1: Reaction involved in the sirtuin *in vitro* enzyme assay.

List of Tables

Table 1-1 Major non-histone and non-chromatin substrates

Table 1-2 Examples of biologically active indolinones

Table 2-1: Structures, ClogP and estimated solubilities (pH 7.4) of Series 1 compound

Table 2-2 : Structures, ClogP and estimated solubilities (pH 7.4) of Series 2 to Series 5 compounds

Table 2-3: Structures, ClogP and estimated solubilities (pH 7.4) of Series 6 and Series 7 compounds

Table 2-4: Structures, ClogP and estimated solubilities (pH 7.4) of Series 8 compounds

Table 2-5: Configuration of Series 1-8 compounds based on chemical shifts and peak areas of ortho protons in fresh and aged samples analyzed by ¹H NMR.

Table 2-6 Optimized source-dependent and compound-dependent MS parameters.

Table 3-1: IC₅₀ of Series 1 compounds on HuH7 cells.

Table 3-2: σ_m values and IC₅₀ values of 3'-substituents on phenyl ring B of Series 1

Table 3-3: IC₅₀ of Series 2, 3 and 4 compounds on HuH7 cells.

Table 3-4: IC₅₀ values of ring B 3'-substituents (R₁) in Series 1-4

Table 3-5: IC₅₀ of Series 6 and 7 compounds on HuH7 cells.

Table 3-6: IC₅₀ values of ring B 3'-substituents (R₁) in Series 1-4

Table 3-7: IC₅₀ values of Series 5 compounds. Mean \pm SD for n= 3 determinations.

Table 3-8: IC₅₀ of Series 8 compounds on HuH7 cells.

Table 3-9: IC₅₀ of selected compounds on HepG2 and Hep3B cells.

Table 3-10: 3'Substituents in potent HuH7 and Hep3B compounds ($IC_{50} \leq 1 \mu M$)

Table 3-11: IC_{50} of selected compounds on non-malignant human fibroblast cells IMR90

Table 3-12: Selectivity ratios (SR) of potent compounds (IC_{50} values $\leq 1 \mu M$) against HuH7 and Hep3B.

Table 3-13: Distribution of HuH7 into normal, apoptotic and necrotic categories on compound treatment, as assessed by FACS analysis.

Table 4-1: Inhibition of SIRT2 and SIRT1 activities by potent HuH7 compounds ($IC_{50} < 1 \mu M$)

Table 4-2: Peak ratios of acetylated protein/total protein induced by test compound (**5-1**, **8-7**) in HepG2 and HuH7 cells.

Table 5-1: RTKs corresponding to the coordinates in the antibody array

Table 5-2: Effects of **47** and **3-12** on the intensities of blots (determined by densitometry) corresponding to phosphorylated RTKs that were upregulated in untreated HuH7 cells.

Table 6-1: Aqueous solubilities and effective permeabilities (P_e) of selected benzylidene indolinones

Table 6-2: Estimated half-lives ($T_{1/2}$) and clearance values of test compounds deduced from a plot of \ln (% compound) versus time.

Table 6-3 IC_{50} values of test compounds on mouse hepatocyte (TAMH) and mouse cardiomyocyte (HL-1) cells after 24 h incubation.

Table 6-4: Number of TA98 and TA 100 colonies observed in the presence of test compounds (1 mM, 10 μM) after 48 h of incubation.

Table 6-5: Dynamic light scattering (DLS) count rates of test compounds in phosphate buffer (pH 7.4) containing 1% DMSO

Chapter 1 Introduction

1.1. Background of Hepatocellular Carcinoma (HCC): Epidemiology, risk factors and management

Liver cancer is one of the leading causes of cancer deaths worldwide.¹ The most common type of primary liver cancer is hepatocellular carcinoma (HCC) which accounts for 70%-85% of reported cases.² HCC is particularly widespread in Asia and it was estimated that there would be at least a year 600 000 new cases by the year 2015.³ An analysis of a population-based cancer registry in the United States of America from 1992 to 2004 showed that HCC incidence was highest among Asians, exceeding that of white Hispanics and Caucasians.⁴ While host genetics may have played a role, there are other factors that are associated with the susceptibility of Asians to HCC. Foremost is the high incidence of chronic hepatitis B and hepatitis C infections in Asia. Both viral hepatic infections are recognized as significant risk factors of HCC.⁴ Aflatoxin-B1 is another contributory factor. Consumption of aflatoxin B1-contaminated grain is common in Asia due to climatic factors and poor food processing practices.

HCC is an aggressive cancer characterized by high rates of recurrence and a poor 5-year survival record. Detection of HCC is based on serological markers (alpha-fetoprotein, des-gamma-carboxy prothrombin)⁵ and screening by ultrasound⁶ but these methods are known to detect only about 69% of patients with early stage HCC (defined as 1 tumor or up to 3 nodules < 3cm³ based on the Barcelona Clinic Liver Cancer Staging Classification).⁷ Those not detected thus miss out on urgently needed early treatment. When diagnosed at its latter stages, surgical resection,⁸ liver transplantation⁹ and percutaneous ablation¹⁰ are first line treatment options. However, less than 30% to 40% of these patients are eligible due to the advanced stage of the disease.¹¹ Standard chemotherapeutic agents (doxorubicin, cisplatin, 5-fluorouracil) would then be deployed but outcomes were generally poor, largely due to the

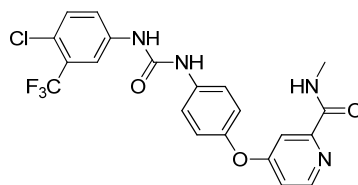
increased expression of drug resistance genes and the nullifying effects of transporter/efflux proteins.^{12, 13}

1.2. Molecular targeted therapy for HCC

A better understanding of the processes and signaling pathways that regulate proliferation, differentiation, angiogenesis, invasion and metastasis of tumors have led to the identification of target proteins that are key drivers of oncogenesis and which if intercepted, would suppress tumor growth or induce regression. The term “molecular targeted therapy” is used to describe this approach and it offers the promise of higher efficiency and less adverse effects compared to conventional chemotherapy. The “ideal” target should have the following characteristics: (i) Overexpressed in cancer cells but present at low or negligible levels in normal cells; (ii) Overexpression should be associated with disease initiation and progression. The corollary would be that inhibition of the target should halt or slow down the process; (iii) The target should be druggable, that is it can be easily screened for small molecule inhibitors or targeted by antibodies. Enzymes and membrane bound receptors are druggable targets.

Viewed in this context, HCC is well placed for molecular targeted therapy. Hepatocarcinogenesis is a multistep process initiated by external stimuli that lead to genetic changes in hepatocytes or stem cells, proliferation and abnormal growth. As mentioned, HCC is strongly associated with chronic viral infections. The mechanisms by which the hepatitis B virus (HBV) and hepatitis C virus (HCV) induce malignant transformation of hepatocytes are illustrative. The viral protein HBx upregulates various oncogenes such as c-myc¹⁴, c-jun¹⁵ and transcription factors NF-kB.¹⁶ It stimulates pro-survival pathways like MAPK¹⁷ and JAK/STAT¹⁸ and activates promoters of genes such as TGF- β ¹⁹, EGFR²⁰, and IL-8.²¹ In the case of HCV, the core protein upregulates Wnt-1 expression.²² Subcellular localization of the core protein had a moderating effect on p21, hence determining the fate of cells.²³

1.3. Sorafenib as targeted therapy for advanced HCC



Sorafenib
4-{4-[3-(4-Chloro-3-trifluoromethyl-phenyl)-ureido]-phenoxy}-pyridine-2-carboxylic acid methylamide

Figure 1-1 Structure and nomenclature of sorafenib

At present, only one drug – sorafenib- is available as a targeted therapy for advanced HCC. Sorafenib is a bi-aryl urea developed by the pharmaceutical companies Bayer and Onyx in 1995. Its discovery was the outcome of high throughput screening of nearly 200 000 compounds against a serine threonine kinase Raf1, made possible by the timely availability of a scintillation proximity assay. Raf1 is the first member of the prosurvival MAPK pathway which is upregulated in HCC.²⁴ This pathway transduces extracellular signals from membrane bound tyrosine kinase receptors (EGFR, IGFR, PDGFR, c-MET) to the nucleus. Growth factor binding to these receptors initiates a sequence of events starting with receptor phosphorylation, activation of an adapter molecule complex (GRB2/SHC/SOS) and activation of the G protein Ras. Downstream from Ras is the family of Raf kinases (ARaf, BRaf, Raf1) which trigger a phosphorylation cascade that eventually leads to the transcription of genes that promote cell proliferation. In retrospect, the decision to target Raf was a timely choice because dysregulated Raf signaling was later found in approximately 30% of cancers²⁵ and in HCC, Raf is activated even in the absence of oncogenic mutations.²⁶

Figure 1-2 summarizes the molecular mechanisms involved in the anticancer activity of sorafenib. Sorafenib inhibits tumor cell proliferation mainly through the inhibition of Raf kinases (BRaf, Raf1). Once inhibited, signaling down the MAPK pathway (Raf→Mek→Erk→Myc) is curtailed. Myc is involved in the transcription of cyclin D1 gene. As cyclin D1 levels fall due to diminished Myc, cell proliferation slows down. Sorafenib also inhibits the tyrosine receptor kinases PDGFR and VEGFR which have important roles in promoting

angiogenesis. Due to the highly vascularized nature of HCC, the formation of new blood vessels delivering nutrients and oxygen is critical for continued tumor growth. Inhibition of PDGFR and VEGFR prevents Ras activation and consequently signaling down the MAPK pathway which is required for the transcription of angiogenesis-promoting genes.

Besides intercepting cell proliferation and angiogenesis, sorafenib induces apoptotic cell death by inhibiting the translation of the prosurvival factor Mcl-1, a member of Bcl-2. Mcl-1 inhibits Bak, a protein that promotes apoptosis, but with less Mcl-1 protein, this inhibition is lifted and apoptotic cell death ensues.

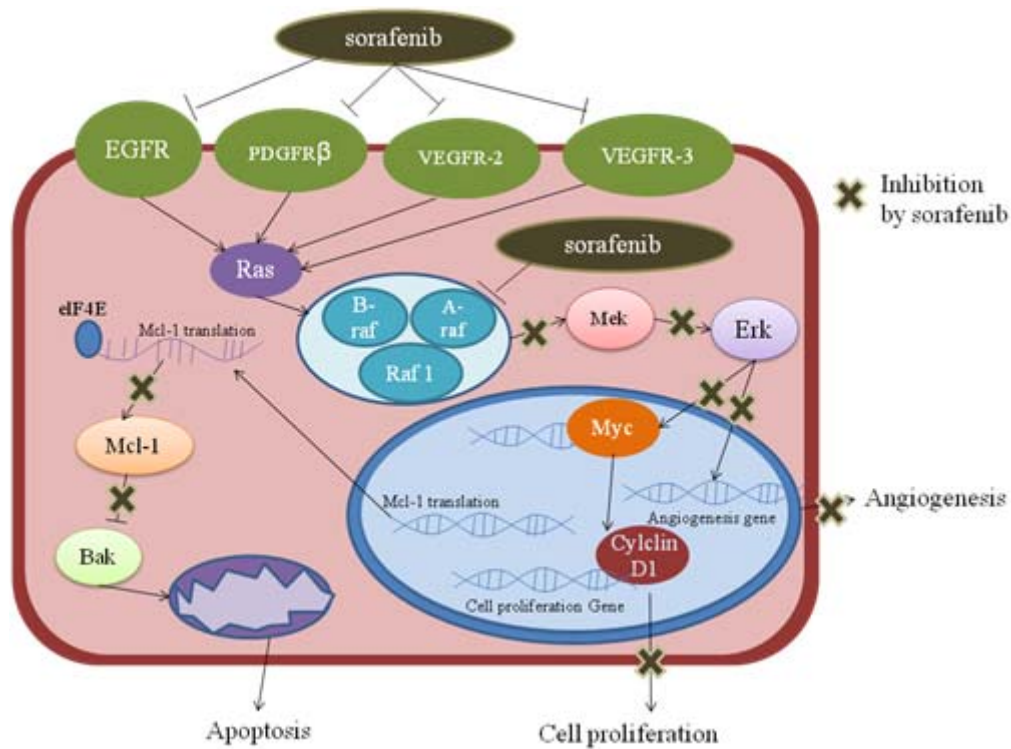


Figure 1-2 Modes of actions of sorafenib in HCC.

1.3.1. Resistance to sorafenib treatment in HCC

Clinical experience with sorafenib has shown that it increases mean survival time by approximately 3 months and it usually fails to induce remission of the disease. This is chiefly due to resistance brought about by the upregulation of certain prosurvival signaling pathways in the tumor, possibly to compensate for those inhibited by sorafenib. These are described briefly in the following paragraphs:

The PI3K/Akt/mTOR pathway is involved in cell growth, survival regulation, metabolism and anti-apoptosis.²⁷ PI3K is activated when growth factors like IGF and EGF bind to their cell surface receptors.²⁸ PI3K subsequently produces the 2nd messenger PIP3 which then activates the serine threonine kinase Akt. Activated Akt phosphorylates several cytosolic proteins, notably m-TOR and Bad.²⁹ Activated mTOR increases cell proliferation. Bad is normally present as a heterodimer with Bcl-2 and Bcl-xl (anti-apoptotic proteins) and when sequestered in the heterodimer, Bcl-2 and Bcl-xl are unable to prevent cytochrome c release through the mitochondrial pore which is required for apoptosis. When Bad is phosphorylated by Akt, it forms the Bad protein homodimer, thus freeing Bcl-2 which is now able to inhibit cytochrome c release, hence curtailing apoptosis. Therefore, activation of the PI3K/AKT/mTOR enhances cell proliferation (via m-TOR) and inhibits apoptosis (via Bad). In non-malignant tissue, the PI3K/Akt/mTOR pathway is suppressed by PTEN which directs PIP3 for dephosphorylation. In HCC, PTEN expression is diminished, resulting in the constitutive activation of the PI3K/Akt/mTOR pathway.³⁰ The pathway is also activated by the higher expression of IGF and IGFR in HCC. Upregulation of Akt has been observed in sorafenib resistant HCC cell lines.³¹

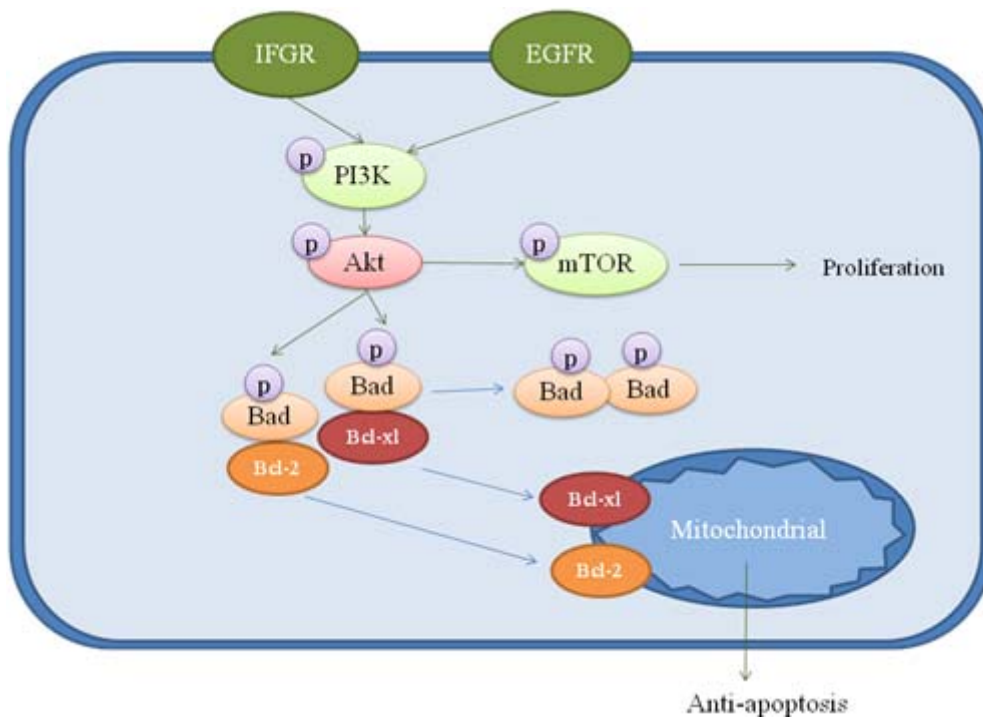


Figure 1-3: PI3K/Akt/mTOR pathway

An increase in EGFR (a member of the human epidermal growth factor receptor HER) may also contribute to sorafenib resistance.³² EGFR contains an intracellular tyrosine kinase domain that can trigger transduction through the MAPK and PI3K/Akt/mTOR pathways. A combination of sorafenib and gefitinib, a drug that inhibits EGFR and HER2 was found to be more effective in inhibiting tumor growth in xenografts than either drug used singly.³²

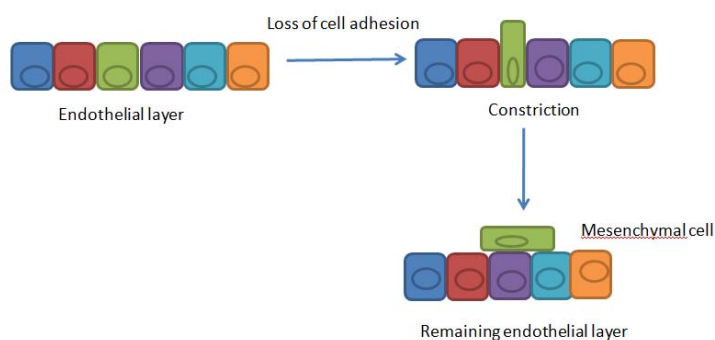


Figure 1-4. Cartoon illustrating epithelial mesenchymal transition.

Epithelial mesenchymal transition (EMT) is another factor contributing to sorafenib resistance. Briefly, EMT occurs when cells lose their polarity and adhesion properties. Constriction of the epithelial layer occurs and mesenchymal cells which have enhanced migratory and invasive properties are released (Figure 1-4). Sorafenib is known to restrain EMT but not in resistant cells.³³

Sorafenib resistance has also been linked to autophagy which involves degradation of redundant or dysfunctional cellular components.³⁴ Tumors that were treated with a combination of sorafenib and chloroquine (an inhibitor of autophagy) were suppressed to a greater extent than when treated with sorafenib alone.³⁴ On the other hand, when sorafenib was combined with an antifolate pemetrexel that stimulates autophagy, suppressed tumor growth was observed.³⁵ Autophagy may promote cancer growth by providing cells with needed nutrients in the face of cellular stress and increased metabolic demands.³⁶ It also suppresses tumor growth by removing damaged organelles and proteins, hence limiting cell

growth and genomic instability.³⁷ Hence, the role of autophagy in cancer remains controversial.³⁸

Besides the aforementioned signaling pathways, c-Met and the canonical WNT/ β catenin pathways are also upregulated in HCC and may elicit resistance.

Overexpression of c-Met is prevalent in HCC where it is linked to diminished survivability.²⁸ C-Met is the tyrosine kinase receptor for the HGF ligand. When activated, it ultimately triggers downstream effectors in the prosurvival pathways MAPK, PI3K/AKT/mTOR and JAK1/STAT (Figure 1-5).

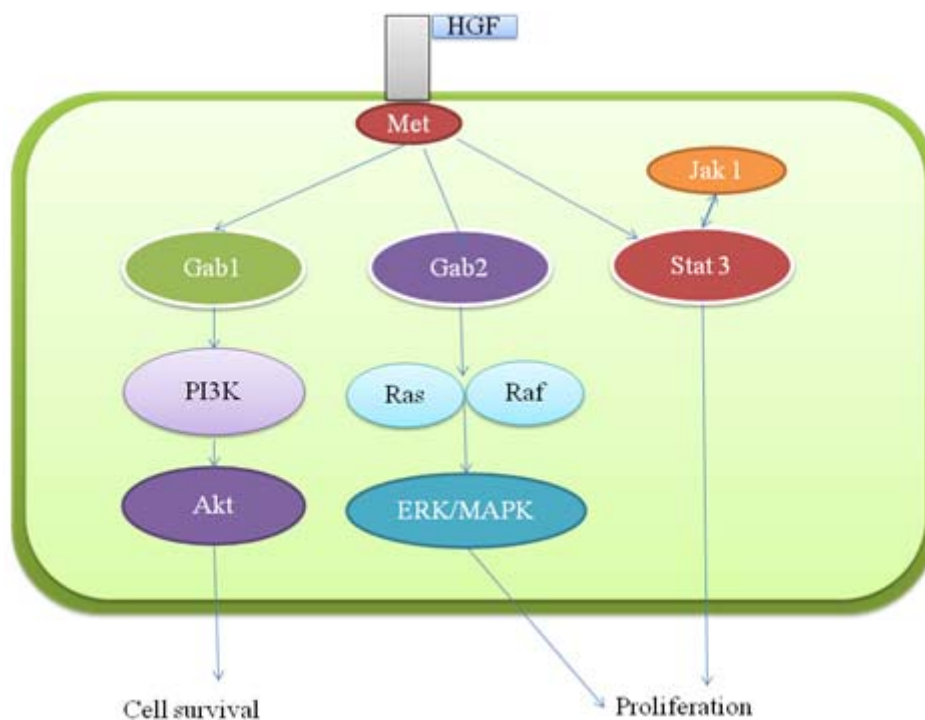


Figure 1-5: c-Met signaling pathway in hepatocellular carcinoma.

Abnormal regulation of the transcription factor β -catenin which is a key component of Wnt signaling is associated with HCC linked to viral hepatitis (HBV, HCV).^{39, 40} Viral infection induce mutations of β catenin, possibly via the core proteins of the virus.^{39, 41} It is proposed that β catenin mutation triggers Wnt/ β catenin signaling by stabilizing β catenin, leading to its translocation to the nucleus where it activates genes involved in cell proliferation.⁴¹

1.4. Other molecular targeted therapies for HCC

Several targeted therapies for HCC have followed in the wake of sorafenib. Sunitinib⁴² and linifanib⁴³ are inhibitors of VEGFR and PDGFR but failed to prolong overall survivability in phase III clinical trials. Brivanib⁴⁴ inhibited VEGFR, PDGFR, and FGFR and had an improved objective response rate and time-to-progression (time to progression refers to the period starting from the point of diagnosis to the point when the cancer deteriorates or undergoes metastasis) compared to sorafenib. The EGFR inhibitor erlotinib when used in combination with sorafenib in a Phase III clinical trial of advanced HCC improved overall survivability to a limited degree.⁴⁵ c-Met is overexpressed in about 20-48% of HCC patients. These patients typically displayed an aggressive phenotype, had poor prognosis and low 5-year survival rates.^{28, 46} Tivantinib, a c-Met inhibitor, was particularly effective in this group of patients. It lengthened the time to progression and improved overall survival compared to placebo in a Phase II trial.⁴⁷ Not surprisingly, it was only modestly effective in HCC patients that do not exhibit c-Met overexpression.⁴⁷ Other c-Met inhibitors failed to exhibit superior efficacies compared to sorafenib.⁴⁸

mTOR inhibitors have also been investigated for their therapeutic efficacy in HCC.⁴⁹ The most widely investigated mTOR inhibitor is everolimus, However it failed to extend overall survival compared to placebo when given to patients who had advanced or metastatic HCC or who were not suited for sorafenib treatment.⁵⁰ Another mTOR inhibitor sirolimus was found to be toxic and prematurely terminated at phase II.⁵¹

Taken together, the somewhat disappointing clinical outcomes with kinase inhibitors designed to be targeted therapeutic agents draw attention to the limitations of the target-based strategy.⁵² Most cancer cells are reliant on a relatively small number of “driver genes” that initiate tumorigenesis, sustain aberrant proliferation and bring about metastasis. Targeting these driver genes and their protein products would enhance the likelihood of success but the task of identifying and validating these genes remain daunting. Thus, the success of targeted

therapy is highly reliant on the selection of the appropriate target protein. However, it is highly unlikely that a compound acts exclusively on one target. A reasonable expectation would be selective activity on the desired target that would translate to minimal adverse effects when the agent is employed in the clinics. Unfortunately, most hit compounds are screened on a limited number of *in vitro* assays which cannot provide the comprehensive information needed to understand their activities on a disease model. Thus, many off-target effects remain undetected at the stage of screening/lead optimization, only to surface with devastating consequences at the later stages of clinical trials. Furthermore, compounds that have potent *in vitro* activity do not necessarily retain potent activity *in vivo*, usually due to pharmacokinetic liabilities. This is a common problem encountered in drug development. Therefore potent compounds against HCC are still required, in spite of the many potent target based kinase inhibitors that are currently available.

1.5. Sirtuins as emerging therapeutic targets for HCC

sirtuins are an ancient family of proteins with a highly conserved structure and function that is maintained in all forms of life. The first member of this family to be identified was Sir2 (silent mating-type information regulator 2) in yeast. It is a histone deacetylase and causes chromatin silencing.⁵³ Interest in Sir2 grew when it was shown that in lower organisms, delivering more Sir2 gene resulted in an extension of lifespan.⁵⁴

Seven mammalian homologs of Sir2 (sirtuins) have been identified. They are found in different subcellular compartments: nucleus (SIRT 1, 6, 7), cytosol (SIRT 2) and mitochondria (SIRT 3, 4, 5). This is a reflection of the varied roles carried out by the different members in spite of their highly conserved structure and their common role as histone deacetylases involved in the deacetylation of lysine residues in histone and non-histone proteins. Unlike other HDACs that catalyze deacetylation through zinc mediated hydrolysis,⁵⁵ sirtuins are dependent on NAD for deacetylation. sirtuins cleave the glycosidic bond between the ADP-ribose and nicotinamide in NAD, and in the process, nicotinamide is released and

the acetyl group is transferred from lysine to ADP ribose to give O-acetyl ADP ribose (Figure 1-6).⁵⁶ The cleavage of NAD is reversible and the nicotinamide that is released is capable of binding to the enzyme again to regenerate NAD in a process called nicotinamide exchange. The latter may prevail over acetyl transfer, resulting in inhibition of the enzyme by nicotinamide.⁵⁶⁻⁵⁸

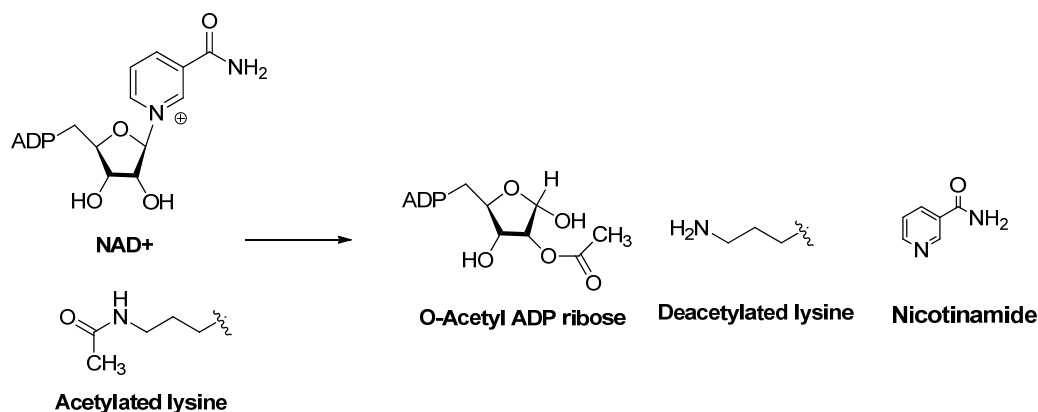


Figure 1-6: Substrates and products of sirtuin catalyzed deacetylation

A more detailed look at the mechanism of the deacetylation reaction is given in Figure 1-7. The initial step involves nucleophilic attack of the acetyl oxygen at C1' of the nicotinamide ribose to give a C1'-O alkylamidate intermediate with concurrent displacement of nicotinamide in an S_N2-like reaction. The 3'OH group of the NAD⁺ ribose is activated by a conserved histidine residue at the active site. Consequently, the 2'OH is primed for an intramolecular attack on the azomethine linkage of the alkylimidate to give a 1',2'-bicyclic intermediate which is then attacked by a base-activated water molecule to give deacetylated lysine and O-acetyl-ADP ribose (OAADPr).^{56, 59, 60}

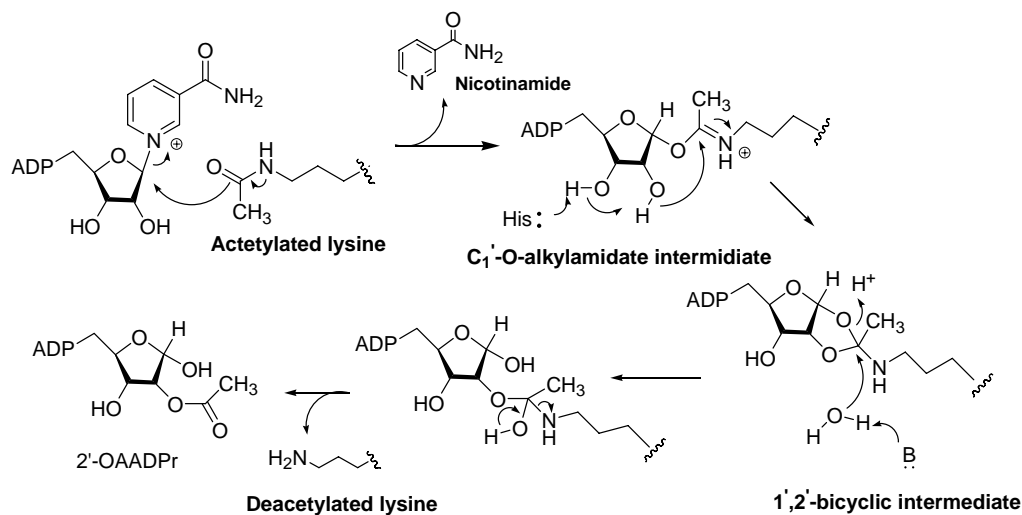


Figure 1-7 Mechanism of sirtuin-catalyzed deacetylation of lysine residues.

Besides deacetylation, some sirtuins function as mono-ADP-ribosyltransferases, either exclusively (SIRT4) or in conjunction with deacetylase activity (SIRT 1-3,6).^{61,62}

1.5.1. Functions of sirtuins

The substrates of sirtuin family fall into two categories: histones and non histones. The histone substrates are H4 acetylated on lysine 16 (H4K16),⁶³⁻⁶⁵ H3 acetylated on lysine 9 (H3K9Ac),⁶⁶ lysine 18 (H3K18)⁶⁷ and lysine 56 (H3K56)⁶⁸ and H1 acetylated on lysine 26 (H1K26).⁶³ The most studied histone substrate is H4K16 which is deacetylated by SIRT 1, 2 and 3.⁶³⁻⁶⁵ It is involved in maintaining DNA integrity,⁶⁹ and cell cycle progression.⁷⁰ Hyperacetylation of H4K16 is recognized as a hall mark of cancer.⁷¹ H4K16 is deacetylated by SIRT1 during formation of constitutive and facultative heterochromatin,⁶³ by SIRT 2 when SIRT 2 translocates to the nucleus during G2/M transition,⁶⁴ and by a small population of nuclear SIRT 3.⁶⁵

The non-histone substrates are broadly classified into 6 groups based on their functional roles as transcription factors, DNA repair machinery elements, nuclear receptors, histone modifying enzymes, cell signaling molecules or metabolic enzymes in the mitochondrial matrix. Table 1-1 lists these substrates and their biological roles.

Table 1-1 Major non-histone and non-chromatin substrates

Group of protein substrate	Name of the protein substrate	sirtuin regulation	Biological roles
Transcription factors	p53	SIRT 1, ^{72, 73} SIRT 2, ⁷⁴ SIRT3 ⁷⁵	Promoting cell survival; Inhibition of senescence and apoptosis
	FOXO	SIRT 1 ^{76, 77} , SIRT 2 ^{78, 79} , SIRT 3 ⁸⁰	Facilitating cell cycle progression; Reducing oxidative stress Promotion of cancer.
	NF-κB	SIRT 1, ⁸¹ SIRT 2, ⁸² SIRT 6 ⁸³	Reducing NF-κB transcriptional activity and NF-κB-dependent gene expression ; Enhancing apoptosis in response to TNFα
	c-MYC	SIRT 1, ^{84, 85} SIRT 2 ⁸⁶	Suppressing cell senescence, Inhibiting c-MYC induced apoptosis, and promoting cell proliferation
	HIF-1α,HIF-2α	SIRT 1, ⁸⁷ SIRT 6 ⁸⁸	Impairing the hypoxic response of HCC; Promoting cell survival in hypoxic environment and nutrient deprivation
	E2F1	SIRT 1 ⁸⁹	Forming mutual loop of regulation of cell proliferation and cell cycle
	DNA repair machinery elements	Ku 70	SIRT 1 ⁹⁰ , SIRT 3 ⁹¹
NBS1, APE1, XPA/C, & WRN		SIRT 1 ⁹²⁻⁹⁵	Maintaining genomic stability
Nuclear receptors, circadian clock & related factors	PGC1a, PPARγ, LXR, FXR, ERα, AceCS1& PER2	SIRT 1 ⁹⁶⁻¹⁰²	Regulation of fatty acid oxidation cholesterol and lipid homeostasis, glucose profiles during nutrient deprivation; Prolonging the life span
Histone-modifying enzymes	SUV39H1	SIRT 1 ¹⁰³	Protecting the cell and genome in the oxidative stress
	p300	SIRT 1 ¹⁰⁴ , SIRT 2 ¹⁰⁵	Maintenance of heterochromatin structure
	TIP 60 & PCAF	SIRT 1 ^{106, 107}	Inhibiting the acetylation of p53 and apoptosis by inhibiting TIP 60
Cell-signaling molecules	STAT3	SIRT 1 ¹⁰⁸	Stimulation of gluconeogenesis by inhibiting Stat 3
	β-catenin	SIRT1 ¹⁰⁹ , SIRT 2 ¹¹⁰	Promoting cell proliferation by inhibition of β-catenin
	SMAD7	SIRT 1 ¹¹¹	Mitigating the TGF-β induced apoptosis by deacetylating SMAD7
	TNF	SIRT 6 ¹¹²	Promoting cell migration
Metabolic enzymes in mitochondrial matrix	CPS1	SIRT 5 ¹¹³	Regulation urea cycle
	GDH	SIRT 3, ¹¹⁴ SIRT 4 ¹¹⁵	Regulation TCA cycle
	AceCS2	SIRT 3 ¹⁰¹	Promoting AceCS2 activity and metabolism

The diversity of non histone substrates reflect the wide ranging regulatory roles of sirtuins in cellular metabolism, cell proliferation and differentiation, DNA damage and stress responses, genome stability, cell survival and apoptosis.¹¹⁶

1.5.2. Sirtuins and cancer

The role of sirtuins in cancer, particularly SIRT1, have been discussed in comprehensive reviews published in 2012 and 2013^{117, 118}. While there is a tendency to classify genes as either tumor promoters or tumor suppressors, Roth and Chen¹¹⁷ noted that very few genes can be unambiguously categorized in this way. Most genes, including sirtuins, have dual roles and may be tumor promoting or suppressing depending on factors like the stage of the tumor, tissue of origin, microenvironment and experimental conditions. The role of SIRT1 in maintaining genome fidelity in cells illustrates this point (Figure 1-8). The expression of SIRT1 protects non-malignant cells against DNA damage, enhances DNA repair capacity and guards against accumulation of mutations, hence improving genome stability and preventing tumorigenesis. When sirtuins mediate these processes in malignant cells, the same benefits accrue these cells. By repairing damaged DNA of oncogenes, SIRT1 promotes mutation acquisition and perpetuates genome instability which leads to high-grade malignancy and drug resistance to chemotherapy.

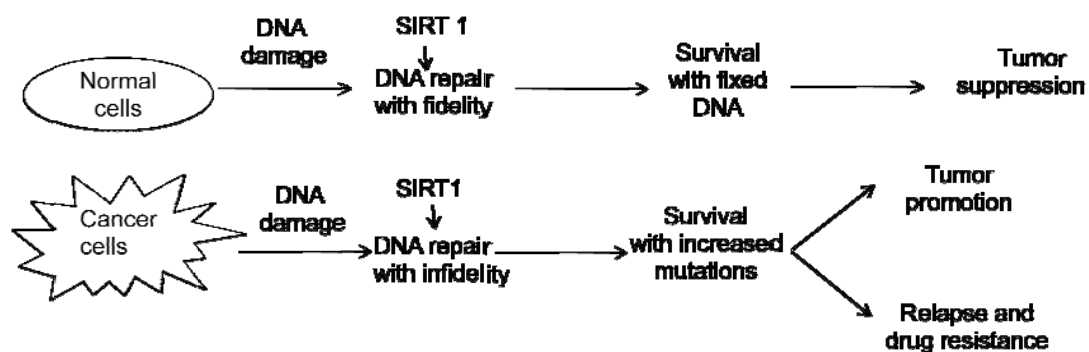


Figure 1-8 Dual roles of SIRT 1 as tumor promoter and suppressor

SIRT1, SIRT2 and SIRT3 appear to have dual roles as tumor promoters and suppressors.¹¹⁷ The present evidence supports a role for SIRT6 in tumor suppression.^{119, 120} The tumor suppressing effects of sirtuins have been linked to the several signaling molecules, some of which are briefly described in the following paragraph.

(i) c-Myc: The c-Myc gene encodes a protooncogenic transcription factor that regulates cell proliferation, growth, apoptosis and stem cell self renewal. c-Myc binds to the SIRT1 promoter and induces SIRT1 expression. However, SIRT1 deacetylates c-Myc and reduces its stability.¹²¹

(ii) HIF: HIF1 and HIF2 are activated in cancer cells because of the chronically low oxygen levels in tumors. HIF1 activates many genes that promote angiogenesis, survival and glucose uptake. HIF-1 α is the regulatory subunit of HIF1 and is subjected to post translational acetylation. SIRT1 deacetylates HIF1 α and represses its tumor promoting properties.¹²² Cancer cells are known to reprogram their glucose metabolism by diverting it from mitochondrial oxidative phosphorylation to glycolysis (Warburg Effect).¹²³ SIRT3 counteracts this switch by destabilizing HIF1 α through downregulation of ROS.^{124, 125}

(iii) β -Catenin: SIRT1 downregulates the pro-growth transcription factor β -catenin by deacetylation. Overexpression of SIRT1 prevented the nuclear accumulation of β catenin.¹⁰⁹

There is a considerable body of evidence to support the tumor promoter activity of SIRT1. SIRT1 promotes the key features characteristic of cancers: resistance to cell death, sustaining proliferative signaling, evasion of growth suppression, induction of angiogenesis, activation of invasion and metastasis and deregulation of cellular energetic and tumor microenvironment.^{117, 126} The tumor suppressor p53 is the most widely known substrate of SIRT1. It is also a substrate of SIRT2 which has many common substrates to SIRT1.^{79, 127-130} SIRT1 deacetylates lysine 382 on p53, thereby reducing its binding affinity for DNA and its ability to initiate transcription of downstream genes. Cells that would normally undergo apoptosis when challenged by DNA damage signals are thus able to bypass p53-mediated apoptosis.^{72, 73} This contributes to the ability of cancer cells to resist cell death and evade growth suppression. SIRT1 promotes sustained proliferative signaling mainly through a positive feedback loop involving *N*-Myc and SIRT1.¹⁰⁰ *N*-Myc induces the expression of SIRT1 which in turn deacetylates and stabilizes *N*-Myc, thereby promoting tumor growth.

1.5.3. Sirtuins in HCC

1.5.3.1. SIRT 1 in HCC

Several reports have surfaced in recent years to support a role for SIRT1 overexpression in HCC tumorigenesis. Significantly higher SIRT1 levels were found in HCC cell lines and patient derived tissues.¹³¹⁻¹³⁴ In one study, SIRT1 overexpression surpassed that of other sirtuins in HCC cells.¹³² The elevated level of SIRT1 was attributed to a post translational event, since SIRT1 mRNA levels were not significantly increased in tumor vis-à-vis normal tissues.^{131, 133, 135} Silencing or inhibiting SIRT1 with small molecule inhibitors in HCC cells impaired proliferation, induced cellular senescence and apoptotic cell death.^{131, 132} These approaches when applied to orthotopic models reduced the tumor progression in animals.¹³² Silencing SIRT1 was shown to sensitize HCC cells to doxorubicin, pointing to a potential therapeutic advantage of a sirtuin inhibitor-doxorubicin combination for SIRT1 overexpressing tumors.¹³¹ Thus, there is proof of concept supporting the therapeutic potential of inhibiting SIRT1 in HCC. Chen *et al*¹³¹ proposed that telomeric dysfunction and genetic instability were the major factors contributing to the suppressed proliferation of HCC cells with silenced SIRT1. They found that SIRT1 silencing induced significant reductions in the expression of telomerase reverse transcriptase (TERT), an enzyme involved in adding back telomere repeats to chromosomes to prevent telomere shortening, and PTPN23, a telomere-binding protein essential for telomere protection. Choi *et al*¹³⁴ noted that there was no correlation between p53 mutation status and expression levels of SIRT1 in HCC cell lines when probed by immunoblotting. Interestingly, they noted that Sirt1 silencing in cells with wildtype p53 caused G1 arrest but this was not observed in cells with mutated p53. The relationship between p53 mutations and SIRT1 remains perplexing with contradictory findings from different investigators.¹³⁶⁻¹³⁸

In contrast to the above mentioned reports that supported a tumor promoter role for SIRT1 in HCC, Srisuttee *et al*¹³⁹ reported that ectopic expression and enhanced activity of SIRT1

(stimulated by an activator, resveratrol) sensitized a HCC cell line that overexpressed the hepatitis B virus X protein (HBX) to oxidative stress-induced apoptosis. Conversely, when SIRT1 activity was suppressed, oxidative stress-induced apoptosis was diminished. Since these findings were made on a specially engineered cell line, it would be necessary to re-confirm them in clinically relevant situations.

1.5.3.2. SIRT 2 in HCC

Dysregulation of SIRT2 has been reported in HCC.^{110, 140} SIRT2 was overexpressed in patient samples^{110, 140} and overexpression in primary HCC tumors was positively correlated to vascular invasion and adverse prognosis.¹¹⁰ Functional studies showed that suppression of SIRT2 reduced cell motility and invasiveness, and hence diminished epithelial-mesenchymal transition (EMT).¹¹⁰ The authors proposed a mechanistic role for SIRT2 in EMT, namely that SIRT2 regulated Akt deacetylation and activity and hence impinged on the GSK-3 β / β -catenin signaling cascade which regulates EMT and cell migration.

In summary, there is support for the view that SIRT1 and SIRT2 are oncogenic proteins that contribute to growth and progression in HCC. They may thus be potentially novel targets for therapeutic intervention. Peck *et al*¹⁴¹ proposed that a clinically useful sirtuin inhibitor should inhibit both SIRT1 and SIRT2 to induce acetylation of p53 and cell death. This is a reasonable requirement since SIRT1 and SIRT2 are found in the same intracellular compartments (SIRT1 in nucleus, SIRT2 in cytosol) as most of the cell cycle and death regulators, besides having prominent roles in controlling cell growth and survival.

1.5.4. Functionalized indolin-2-ones as sirtuin inhibitors

6,7-Dichloro-3-substituted benzylidene indolin-2-ones (I-III) have been reported to be SIRT2 inhibitors (Figure 1-9).¹¹⁸ The authors investigated this scaffold because of an earlier report that identified an oxindole GW5074 as a SIRT2 inhibitor (> 60% inhibition at 12.5 μ M), whose discovery arose from a screening exercise of known compounds that targeted enzymes or receptors that bind adenosine containing co-factors or ligands.¹⁴² Thus the screened library

contained a large number of kinase inhibitors (including indolinones). A follow study was carried out on a small series of compounds which were evaluated for SIRT1-3 inhibitory activity.¹⁴³ Compounds I-III were identified as the most potent SIRT2 inhibitors in this series.

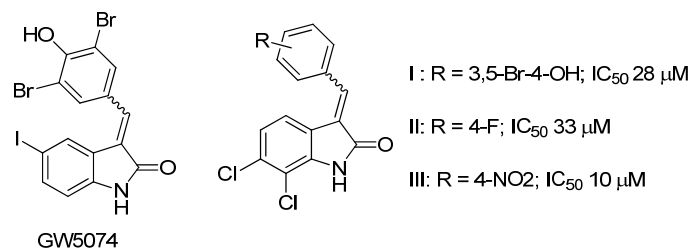


Figure 1-9: Structures of benzylidene indolinones as sirtuin inhibitors

The functional relevance of sirtuin inhibition by I and II was confirmed when they were found to promote the hyperacetylation of α -tubulin,¹⁴⁴ a substrate of SIRT2. A docking study using the human SIRT2 apoenzyme (PDB1J8F) was undertaken to rationalize the SIRT2 inhibitory activity of these compounds. Interestingly, the compounds docked into pocket C in the NAD⁺ binding site which was normally occupied by nicotinamide, and not pocket A which was the binding site of the adenine ring of NAD⁺. Thus functionalized oxindoles were unlikely adenosine mimetics, at least when competing with NAD⁺ for occupancy of its binding pocket. More recently, GW5074 was reported to inhibit the mitochondrial SIRT5 with an impressive IC₅₀ of 19.5 μM.¹⁴⁵ SIRT5 is unusual among sirtuins in that it has NAD⁺ dependent deacetylase as well as deacylase (demalonylase, desuccinylase) activities. The biological significance of SIRT5 is unknown.¹¹⁷ GW 5074 was described as the “first pharmacological scaffold for development into SIRT5 specific inhibitors.”

1.6. Functionalized indolin-2-ones as inhibitors of kinases

The substituted indolin-2-one scaffold is outstanding for its success in yielding a large number of clinical candidates with receptor tyrosine kinase (RTK) inhibitory activity. The privileged status of this scaffold was attributed to the ability of the indolin-2-one core to occupy a site (hinge region which connects the two kinase lobes) which binds the adenine of ATP whereas the substituents attached to the indolin-2-one core contact residues in the

vicinity of the hinge region.¹⁴⁶ This was demonstrated in the co-crystallized structures of FGFR1 with SU4984 and SU 5402 (Fig 1-10).¹⁴⁶ The oxindole NH (N1) and carbonyl oxygen (O2) was H bonded to the backbone carbonyl of Glu562 and amide NH of Ala564 respectively. Glu562 and Ala564 were found in the hinge region (residues 563 to 568) connecting the two lobes of FGFR1. The same back bond groups were H bonded to N1 and N6 of the ATP adenine. Thus, the indolinone ring may be considered to be bioisosteric to adenine.

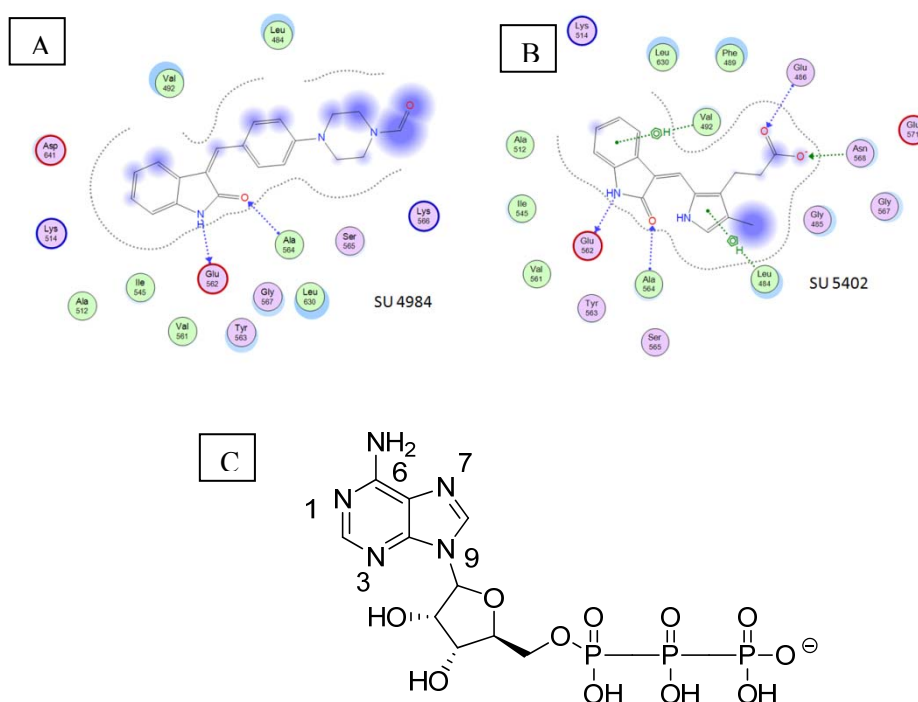


Figure 1-10: Interactions of (A) SU 4984 and (B) SU 5402 with the FGFR1 hinge region. (C) Structure of adenosine triphosphate (ATP). The docking poses of the two compounds were obtained from PDB files 1AGW¹⁴⁶ and IFGI¹⁴⁶ and displayed in a ligand interaction map using MOE (Ver 2011.10, Chemical Computing Group).

SU5402 was found to selectively inhibit FGFR1, compared to SU 4984. This was explained in part by two features in its docking pose in FGFR1.¹⁰⁷ (i) The carboxyethyl group in SU 5402 was H bonded to Asp568. Interestingly, this H bonding interaction was not possible in IGFR and PDGFR because the residue corresponding to Asn568 in these RTKs was the acidic Asp residue. Thus SU5402 was not an outstanding inhibitor of IGFR or PDGFR. (ii) Phe489 on

the nucleotide binding loop which was involved in ATP coordination, extended towards the indolinone ring, capping the hydrophobic pocket in which the indolinone ring was found. The latter caused the nucleotide binding loop to be advantageously well-ordered in the FGFR1-SU5402 complex, but poorly ordered in FGFR1-SU4984 and FGFR1-ATP.

Examination of the docking pose of co-crystallized SU 4984 in FGFR1 showed that the side chain of SU 4984 did not establish as many productive interactions as SU 5402.¹⁰⁷ SU4984 was however a more potent inhibitor of PDGFR than FGFR1. Ala564 (present in FGFR1) was replaced by Cys564 in PDGFR. When cysteine was modeled in place of Ala564 in the FGFR1-SU4894 complex, it was advantageously positioned for a favorable interaction with the phenyl ring in SU4894, and this may explain the greater inhibition of PDGFR by SU4894.

These findings highlighted the critical role played by ring substitution of the indolinone core in imparting selectivity and potency towards RTKs.

Of the large number of indolin-2-ones that been evaluated for kinase inhibitory activity, two of the most successful scaffolds were 3-(1H-pyrrol-2-yl)methylene]indolin-2-one and 3-[phenyl(phenylamino)methylene]indolin-2-one (Figure 1-11).

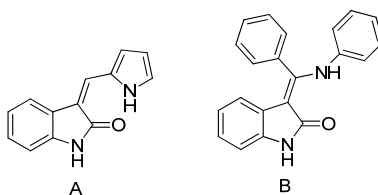


Figure 1-11: (A) 3-(1H-Pyrrol-2-yl)methylene]indolin-2-one and (B) 3-[phenyl(phenylamino)methylene]indolin-2-one scaffolds.

The pyrrolylmethyleneindolinone scaffold was the core structure of kinase inhibitors developed by Pfizer (Sugen), of which sunitinib, torceranib and semaxinib are in clinical use (Figure 1-12). Boehringer Ingelheim focused on the phenyl (phenylamino) methylene indolin-2-one scaffold and their leading compounds were BIBF1120 (Vargate®) and hesperidin (Figure 1-12).

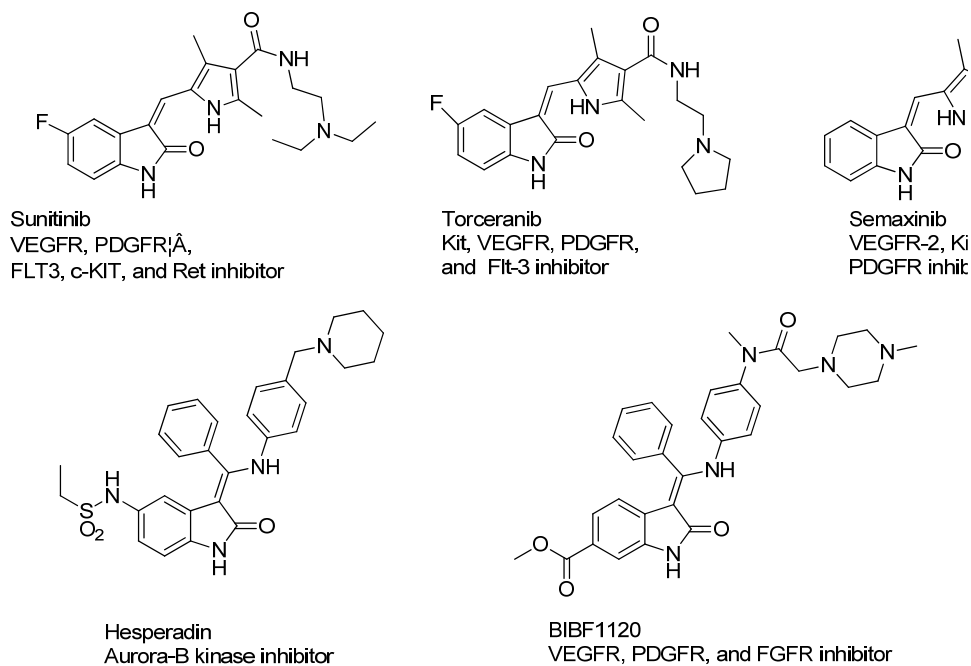


Figure 1-12: Structures of sunitinib, torceranib, semaxinib, hesperadin and BIBF1120

A shared feature of these two scaffolds was the retention of the *Z* isomer as the predominant (or only) isomer. This was due to intramolecular H bonding as shown in Figure 1-13 (A,B) for sunitinib and BIBF1120.

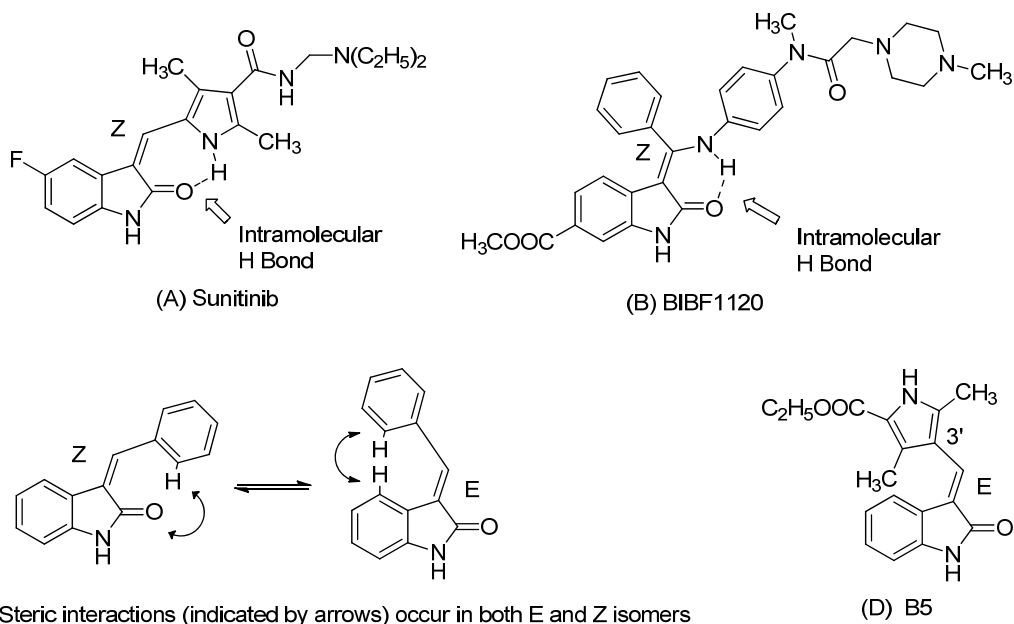


Figure 1-13: Intramolecular H bonding in (A) sunitinib and (B) BIBF1120 locked the exocyclic double bond in its *Z* configuration. (C) *E* and *Z* isomers exist in equilibrium in benzylidene indolinones. (D) The pyrrolylmethylindolinone B5 has an *E* configuration due to the absence of intramolecular H bonding.

The *Z* isomer of indolin-2-ones was proposed to be the active isomer for inhibition of PDGFR and VEGFR.¹⁴⁷ The *Z* isomer was achieved in pyrrolylmethyleneindolin-2-ones by intramolecular H bonding as shown in sunitinib. In the case of benzylideneindolin-2-ones, there was no strict preference for the *E* or *Z* isomer because steric interactions occurred in both isomers (Figure 1-13C).¹⁴⁷ Thus *EZ* isomers were in equilibrium. Sun *et al*¹⁴⁷ cited an example of a benzylideneindoline whose binding configuration to VEGFR was *Z* but existed in the predominant *E* form in solution.¹⁰⁸ They proposed that the *E* isomer would isomerize to the *Z* form before or during binding, and once bound, the *EZ* equilibrium would shift to give more of the *Z* form. Inhibition would understandably be weaker for these compounds.

The importance of the *EZ* configuration was further highlighted in B5, which is a pyrrolylmethyleneindolinone with an *E* configuration (Figure 1-13D). Intramolecular H bonding was not possible in B5 because the pyrrole ring was attached to the indolinone core at position 3'. B5 was a weak inhibitor of PDGFR, FGFR, VEGFR and other RTKs but an exceptionally potent inhibitor of CDK1 and CDK2.¹⁴⁸

Besides the pivotal role played by the *EZ* configuration of the exocyclic double bond, other features of the indolinone scaffold that affected PDGFR/VEGFR inhibition have been proposed.¹⁴⁷ These are summarized separately for pyrrolylmethylene-indolinones and benzylideneindolinones in Figure 1-14.

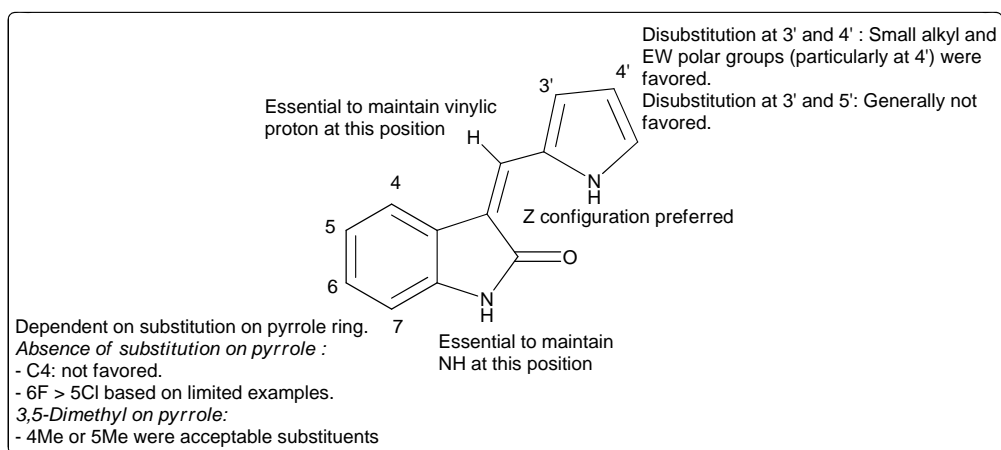
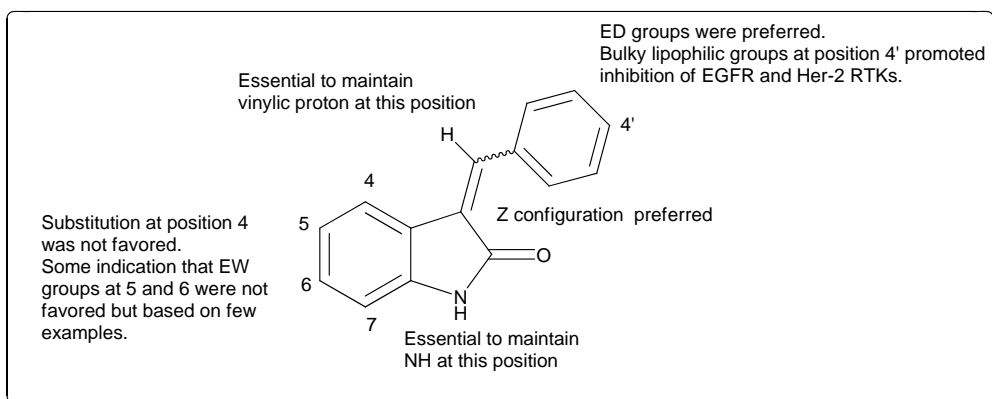


Figure 1-14: Structure activity relationships of indolinones with (A) pyrrolylmethylene and (B) benzylidene at position 3 for inhibition of RTKs.¹⁴⁹ ED = Electron donating; EW = Electronwithdrawing.

BIBF1000 and BIBF 1120 were substituted phenyl (phenylamino) methylene indolin-2-ones which inhibited the pro-angiogenic kinases VEGFR, PDGFR and FGFR (angiokinasas).¹⁵⁰

The fore-runner of both BIBF1000 and BIBF 1120 was the 6-amido substituted indolinone IV (Figure 1-15)

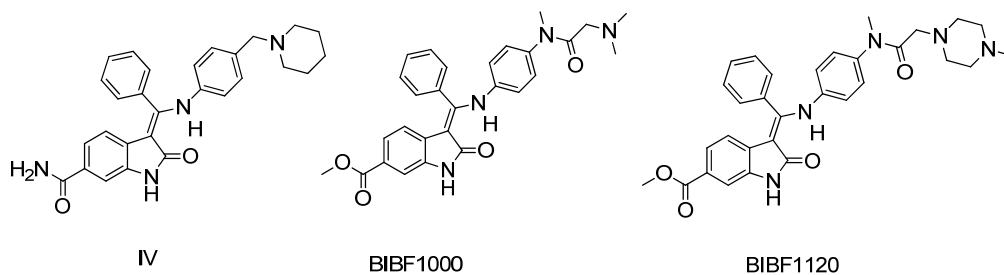


Figure 1-15: Substituted phenyl(phenylamino)methylene indoline-2-ones.

Compound IV was a highly selective and potent (nanomolar) inhibitor of VEGFR2 and initial SAR identified the 6-amido (CONH₂) substituent as a key contributor to inhibitory activity. Molecular docking of IV in the VEGFR2 binding pocket (a homology model) showed that besides the typical canonical H bonds between the lactam moiety and the hinge region, the 6-amido moiety was directed towards the specificity pocket of VEGFR2 which was flanked by the gatekeeper residues Val916 and Lys868. The docking pose showed H bonding between Lys868 and NH of the 6-amido side chain. Since the specificity pocket was lined by hydrophobic residues, analogs of IV were prepared in which the primary 6-amido was *N*-substituted to give secondary amides. Unfortunately, activity was lost with this modification but was paradoxically restored when small polar moieties such as 6-nitro and 6-carboxymethyl were introduced. The 6-carboxymethyl moiety (an ester) proved to be surprisingly resilient to metabolic degradation and thus it was retained in subsequent lead modification approaches which eventually resulted in BIBF1120. BIBF1120 had a good pharmacokinetic profile and encouraging efficacy in xenograft models. Part of its *in vivo* efficacy was attributed to its sustained inhibition (up to 32 h) of VEGFR phosphorylation.

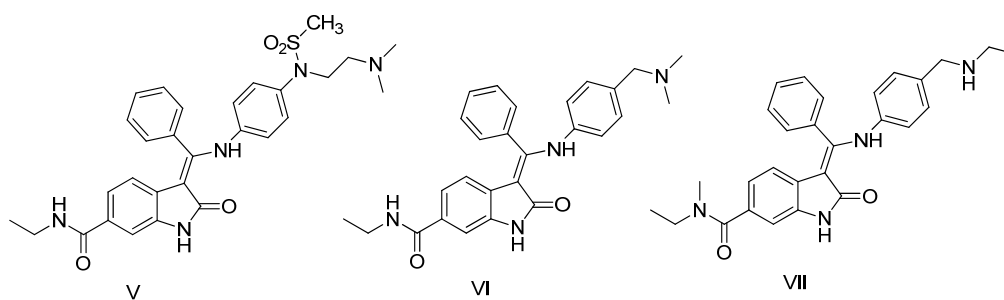


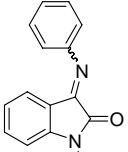
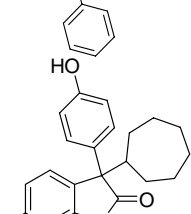
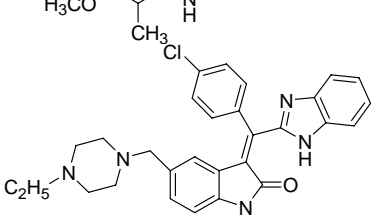
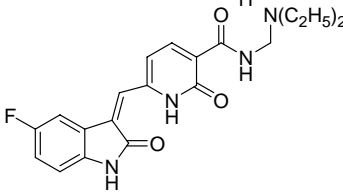
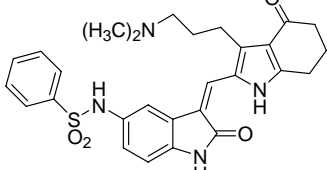
Figure 1-16: Structures of Transforming Growth Factor β receptor 1 inhibitors V, VI and VII

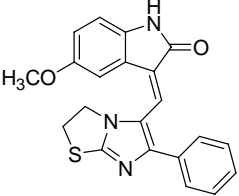
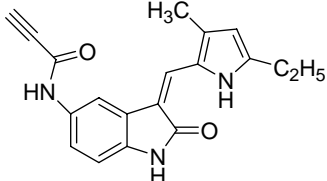
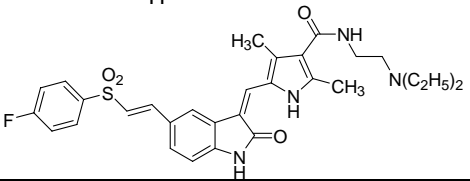
Although the secondary amides of IV proved disappointing as angiokinase inhibitors, they were subsequently found to be good lead structures for inhibition of Transforming Growth Factor β receptor 1 (TGFβR1) which was sought after for the treatment of idiopathic pulmonary fibrosis and cancer.¹⁵¹ The most promising compounds to date were V, VI and VII (Figure 1-16). The structure of a representative member co-crystallized with TGFβR1 showed typical binding to the hinge residues in the ATP binding pocket (via the indolinone lactam)

while the 6-amido side chain was directed towards the specificity pocket flanked by gatekeeper residues Phe262 and Lys232, as observed for IV in the VEGFR2 pocket. The central phenyl moiety was found in the region that is normally occupied by ribose of ATP. The basic side chain on the adjacent phenyl ring projected towards the water phase and is thus a potential site for structural change.

In spite of the extensive patent coverage of the indolinone scaffold, typified by the clinical candidates sorafenib and BIBF 1120, medicinal chemists have continued to undertake novel structural modifications of the scaffold and in some instances, to uncover unexpected targets and good potencies for their compounds. A brief summary is provided in Table 1-2.

Table 1-2 Examples of biologically active indolinones

Compound structure	Major targets	Other remarks
	GAL 3 receptor antagonist ¹⁵²	Feeding, metabolic regulation and noniception
	Unknown ¹⁵³	Inhibited proliferation of MCF 7 and PC 3 cell lines
	Angiokinase inhibitor ¹⁵⁴	Acceptable PK and toxicity profile; effective in several xenograft model;
	VEGFR-2 inhibitor ¹⁵⁵	G1 phase arrest and apoptosis of HCT116 cells.
	Aurora B kinase inhibitor ¹⁵⁶	Inhibited proliferation of HCT116 and HT29 cells

	Inhibitors of tubulin; Inhibition of Akt Phosphorylation ¹⁵⁷	Inhibited proliferation of HT-29; G2/M phase arrest
	Irreversible Nek2 kinase inhibitor ¹⁵⁸	
	FGFR2 inhibitor ¹⁵⁹	Inhibit HUVEC tube formation

1.7. Compound 47: A multi-targeting kinase inhibitor with growth

inhibitory effects on a panel of HCC cells.

c

Figure 1-17: *E*-6-Chloro-3-[3-(trifluoromethyl)benzylidene]indolin-2-one (Compound 47)

E-6-Chloro-3-(3-trifluoromethyl-benzylidene)-1,3-dihydroindol-2-one (Compound 47, Figure 1-17) was first reported as an inducer of NAD(P)H quinone oxidoreductase I (NQO1), an enzyme widely monitored as a biomarker for cancer chemoprevention.¹⁶⁰ It also exhibited low micromolar antiproliferative activity on malignant colon (HCT116) and breast (MCF7) cells. Subsequently, it was found to selectively curtail viability of HCC cell lines (HuH7 IC₅₀ 0.5 μM; HepG2 IC₅₀ 0.6 μM) compared to non-malignant liver cells (THLE2, IC₅₀ > 10 μM). Compound 47 repressed α -fetoprotein (AFP) transcription in HuH7 cells which may imply that it intercepted regulatory pathways controlling AFP gene expression. AFP is a tumor associated antigen that is silenced in normal hepatocytes but reactivated in HCC. Yang et al have reported that silencing AFP expression induced growth arrest and apoptosis in HuH7.¹⁶¹ Compound 47 was screened for inhibition of phosphorylation of RTKs in HuH7 cells using a phosphor-RTK array. It was found to suppress the phosphorylation of IGF1R, Tyro3 and EphA2. IGF1R was reported to control downstream cell cycling and cell death pathways in HCC.¹⁶²⁻¹⁶⁴ There are fewer references to the oncogenic roles of Tyro3 and EphA2 in

HCC.^{165 166} Thus, they may be novel oncogenes in HCC. The functional significance of the diminished phosphorylation of these RTKs was validated by gene silencing which abolished the cytotoxicity of **47** on HuH7. When **47** was administered at 60mg/kg (weekly) intraperitoneally (IP) to mice bearing HCC xenografts, it suppressed the tumor burden to the same extent as sorafenib which was given at greater frequency (30mg/kg, daily, IP). Taken together, **47** has a promising anticancer profile as shown from its potent and selective growth inhibitory effects on HCC cell lines, interception of prosurvival and proliferation mechanisms (angiogenesis, cell migration) and *in vivo* efficacy. Notwithstanding its promising profile, **47** was a lipophilic molecule (ClogP 5.08) with poor aqueous solubility (0.08 μ M or 0.03 μ g /mL) when determined at 25°C, pH 7.4 after 24 h agitation. Such physicochemical features are portents of poor oral bioavailability. The structure of **47** shows that it was exceptionally underfunctionalized compared to other biologically active indolinones (Figure 1-16). Its SAR as a RTK inhibitor (IGFR1, Tyro3, EphA2) and growth inhibitory agent has not been comprehensively explored and in the absence of such information, it would not be possible to undertake rational improvement of its activity profile.

1.8. Statement of purpose

The intent of this thesis is to explore the potential of functionalized benzylidene indolin-2-ones for their anti-cancer activity on HCC. It is motivated by two related factors.

First, the versatility and productiveness of the indolin-2-one scaffold yields analogs with potent growth inhibitory activities on a wide range of malignant cells. Furthermore, the structural diversity of functionalized analogs was matched by their ability to intercept varied kinase targets. The scaffold was clearly a validated privilege motif for kinase inhibition. There was also evidence of non-kinase targets of this scaffold, as shown by the SIRT2 inhibitory activity of some benzylidene indolinones. SIRT 1 and SIRT2 have been shown to promote HCC progression. Functionalization of the scaffold would undoubtedly play a key role in deciding target preference (kinase versus non-kinase). Dual or multiple targeting

members would be desirable given the problems posed by drug resistance in cancer chemotherapy when single agents or single-targeting agents are employed.

Second, the candidate's laboratory had contributed to the discovery of **47**, a multi-kinase inhibitor with good *in vitro* and *in vivo* growth inhibitory activities on HCC. Compound **47** was identified through a process in which compounds were shortlisted on the basis of potency and selectivity on cell based assays and subsequently validated by *in vitro* kinase assays. This approach had the advantage of economy and addressed in part the problem of compounds that had potent *in vitro* kinase inhibitory activity but failed to adequately suppress malignant cell growth. Notwithstanding the promising activity profile of **47** in HCC, its poor aqueous solubility and underfunctionalized structure were of major concern.

Thus, it was hypothesized that structural elaboration of compound **47** would provide a means of uncovering drug-like compounds with greater potency and selectivity on HCC. It was envisaged that the enhanced potency would arise from greater kinase or sirtuin inhibition, or possibly, through inhibition of both targets. While it was reasonable to anticipate analogs of **47** to retain kinase inhibitory activity, the question remained as to whether the same kinases would be affected by the structural changes. The sirtuin inhibitory activity of **47** had not been explored. Concurrent inhibition of kinase and non-kinase targets in the same molecule would be a novel finding with possible therapeutic potential. Even if the investigations did not succeed in identifying such a compound, the SAR established for sirtuin and kinase inhibition would help direct future medicinal chemistry efforts.

To examine this hypothesis, a series of functionalized benzylidene indolinones that were structurally related to **47** and designed to have an improved solubility-lipophilicity balance were synthesized and characterized. The compounds were evaluated on a panel of HCC cell lines to establish structure activity requirements. The more promising analogs were evaluated separately for sirtuin and kinase inhibitory activity to assess their respective impact on the growth inhibition of HCC. The aqueous solubility, permeability, *in vitro* metabolic

susceptibility and *in vivo* toxicity of selected compounds were also examined to determine if the design strategy employed here had met its desired objectives.

Chapter 2 Design and Synthesis of Target Compounds: 3-substituted Indolin-2-ones

2.1. Introduction

The design and synthesis of target compounds are described in this chapter. The compounds are functionalized benzylidene indolin-2-ones with broad structural resemblance to **47** (Figure 2-1). Some of the compounds presented in this chapter were synthesized by Dr Yang Tianming (**8-8**, **8-9**) and undergraduate students (**1-25**, **2-15**, **2-16**, **3-14**, **4-17**, **4-18**, **5-9**, **5-10**, **6-11**, **6-12**, **7-11** and **7-12**) mentored by the candidate for their Honors Year Project.

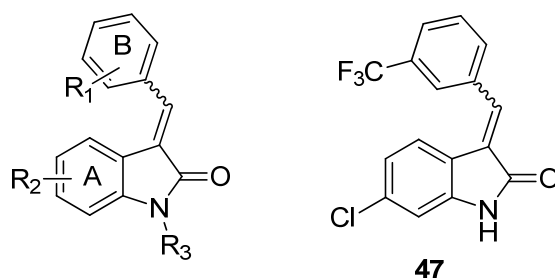


Figure 2-1: Benzylideneindolin-2-one scaffold with modifications made at R₁, R₂ and R₃. Structure of **47** is given on the right.

2.2. Rationale of design

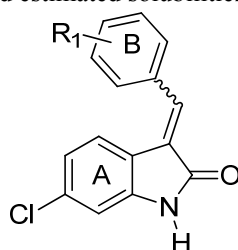
115 compounds were synthesized and characterized by the candidate in the present study. Of these, 91 compounds were not reported when checked on SciFinder Scholar (December 2013). These compounds were organized into eight groups (Series 1-8), depending on the substitution of the indolinone Ring A.

Series 1 compounds closely resembled **47** which is **1-10** in Table 2-1. These compounds retained the 6-Cl substituent of **47** on Ring A but had different substituents on the benzylidene Ring B. The ClogP (5.08) and estimated solubility (3.4 μ M) of **47** indicated that it was a lipophilic molecule with poor solubility. Lipophilic compounds are arguably promiscuous in their choice of targets and associated with a higher incidence of nonspecific toxicity.¹⁶⁷ Poor solubility in a compound would hamper its passage across biological membranes and lead to limited oral absorption. Thus, a key motivation of the design strategy was to improve the drug-like profile of **47**. One approach was to replace the lipophilic trifluoromethyl (CF₃) with

less lipophilic groups. To this end, the electron withdrawing and lipophilic CF₃ of **47** was replaced by polar H bonding groups cyano (CN), methanesulfonyl (MeSO₂-), aminosulfonyl (NH₂SO₂-), *N*-alkylaminosulfonyl (RNH₂SO₂-), methoxy (MeO-) and methanesulfonylamino (MeSO₂NH-) which were electron withdrawing, and which methyl (Me-) was electron donating. Non-H bonding groups that were less lipophilic than CF₃ (π 0.88) were also included and these were methyl Me (π 0.56), chloro Cl (π 0.71) and fluoro F (π 0.14).¹⁶⁸ A more lipophilic substituent trifluoromethoxy CF₃O- (π 1.04) was also included as activity might be dependent on a lipophilic entity. CF₃O is electron withdrawing and likely to be a poor H bond acceptor.

The estimated lipophilicities (clogP) and aqueous solubilities of the Series 1 compounds are given in Table 2-1. As anticipated, except for compounds bearing CF₃O (**1-13** to **1-15**) and the regioisomers of **47** (**1-9**, **1-11**), the other compounds were less lipophilic (lower ClogP values) and more soluble than **47**.

Table 2-1: Structures, ClogP and estimated solubilities (pH 7.4) of Series 1 compound



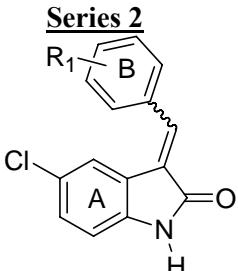
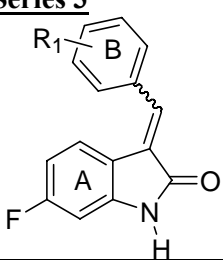
No	R ₁	Clog P ^a	Estimated solubility (μM) ^b	No	R ₁	Clog P ^a	Estimated solubility (μM) ^b
1-1	H	4.2	27	1-14	3'OCF ₃	5.23	2.8
1-2	2'F	4.34	11	1-15	4'OCF ₃	5.23	3.1
1-3	3'F	4.34	8.9	1-16	3'SO ₂ Me	2.56	15
1-4	4'F	4.34	6.3	1-17	3'SO ₂ NH ₂	2.36	25
1-5	3'Me	4.7	12	1-18	3'SO ₂ NHMe	2.98	39
1-6	2'OMe	4.12	14	1-19	3'CN	3.63	7.9
1-7	3'OMe	4.12	17	1-20	3'SO ₂ NMe ₂	3.4	27
1-8	4'OMe	4.12	19	1-21	4'SO ₂ NHMe	2.98	43
1-9	2'CF ₃	5.08	3.3	1-22	3'SO ₂ NHEt	3.3	18
1-10 (47)	3'CF ₃	5.08	3.4	1-23	3'SO ₂ NHPr	3.76	7.9
1-11	4'CF ₃	5.08	3.1	1-24	3'SO ₂ NHiPr	3.76	8.9
1-12	3'4'F	4.41	2.1	1-25^c	3'NHSO ₂ Me	3.01	51
1-13	2'OCF ₃	5.23	2.3				

^a Estimated from ChemDraw Ultra 7.0. Compounds with large ClogP values are more lipophilic. ^b Estimated values from ACD Labs Version 12.00, Toronto, Canada. ^c Not synthesized by candidate.

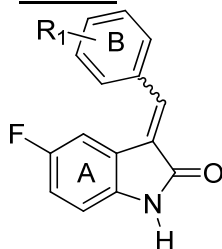
The 6-Cl on the indolinone Ring A of **47** was replaced by 5-Cl in Series 2, 6-F in Series 3, 5-F in Series 4 and 6-MeO in Series 5. As F and MeO have lower π values than Cl, Series 3,4

and 5 compounds were expected to be more polar than their Series 1 counterparts. The estimated ClogP and solubility values in Tables 2-2 supported this notion. The position 5 regioisomers of 6-Cl and 6-F were also explored to determine if there was a positional preference for activity. It should be noted that not all the benzylidene Ring B substituents in Series 1 were investigated in Series 2-5. Notably, the positional isomers of MeO-, CF₃O- and NH₂SO₂- groups were not explored. In addition, only the *N*-methylaminosulfonyl substituent, and not other *N*-alkyl substituents, was investigated.

Table 2-2 : Structures, ClogP and estimated solubilities (pH 7.4) of Series 2 to Series 5 compounds

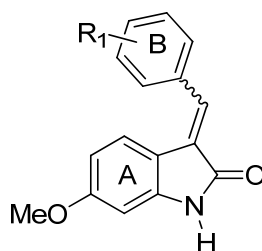
Series 2							
							
No	R ₁	Clog P ^a	Estimated solubility (μM) ^b	No	R ₁	Clog P ^a	Estimated solubility (μM) ^b
2-1	H	4.2	28	2-9	3'4'F	4.41	7.2
2-2	2'F	4.34	11	2-10	3'OCF ₃	5.23	3.0
2-3	3'F	4.34	9.3	2-11	3'SO ₂ Me	2.56	15
2-4	4'F	4.34	6.6	2-12	3'SO ₂ NH ₂	2.36	26
2-5	3'OMe	4.12	18	2-13	3'CN	3.63	8.2
2-6	2'CF ₃	5.08	3.4	2-14	3'SO ₂ NHMe	2.98	41
2-7	3'CF ₃	5.08	3.5	2-15 ^c	3'SO ₂ NHPr	4.03	8.3
2-8	4'CF ₃	5.08	0.6	2-16 ^c	3'NHSO ₂ Me	3.01	54
Series 3							
							
No	R ₁	Clog P ^a	Estimated solubility (μM) ^b	No	R ₁	Clog P ^a	Estimated solubility (μM) ^b
3-1	H	3.63	54	3-8	3'OCF ₃	4.66	5.5
3-2	2'F	3.77	21	3-9	3'SO ₂ Me	1.99	28
3-3	3'F	3.77	18	3-10	3'SO ₂ NHMe	2.41	76
3-4	4'F	3.77	12	3-11	3'SO ₂ NHEt	2.93	34
3-5	2'CF ₃	4.51	6.3	3-12	3'SO ₂ NHPr	3.46	15
3-6	3'CF ₃	4.51	6.6	3-13	3'SO ₂ NHiPr	3.46	17
3-7	4'CF ₃	4.51	6.1	3-14 ^c	3'NHSO ₂ Me	2.44	98

Series 4



No	R ₁	Clog P ^a	Estimated solubility (μM) ^b	No	R ₁	Clog P ^a	Estimated solubility (μM) ^b
4-1	H	3.63	48	4-10	3'CF ₃	4.51	5.8
4-2	2'F	3.77	18	4-11	4'CF ₃	4.51	5.4
4-3	3'F	3.77	16	4-12	3'4'F	3.84	3.6
4-4	4'F	3.77	11	4-13	3'OCF ₃	4.66	4.9
4-5	2'Me	4.13	21	4-14	3'SO ₂ Me	1.99	25
4-6	3'Me	4.13	21	4-15	3'CN	3.06	14
4-7	4'Me	4.13	21	4-16	3'SO ₂ NHMe	2.41	67
4-8	3'OMe	3.54	30	4-17 ^c	3'SO ₂ NHPr	3.46	13
4-9	2'CF ₃	4.51	5.6	4-18 ^c	3'NHSO ₂ Me	2.44	88

Series 5



No	R ₁	Clog P ^a	Estimated solubility (μM) ^b	No	R ₁	Clog P ^a	Estimated solubility (μM) ^b
5-1	H	3.31	81	5-6	3'CF ₃	4.19	10
5-2	2'F	3.45	31	5-7	4'CF ₃	4.19	9.4
5-3	3'F	3.45	26	5-8	3'SO ₂ NHMe	2.08	120
5-4	4'F	3.45	19	5-9 ^c	3'SO ₂ NHPr	3.14	25
5-5	2'CF ₃	4.19	9.8	5-10 ^c	3'NHSO ₂ Me	2.11	150

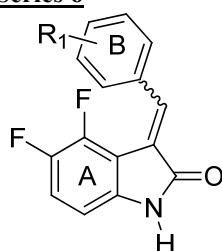
^a Estimated from ChemDraw Ultra 7.0. Compounds with large ClogP values are more lipophilic. ^b Estimated values from ACD Labs Version 12.00, Toronto, Canada. ^c Not synthesized by candidate.

Series 6 and 7 were difluoro benzylidenindolinones (Table 2-3). The indolinone ring A was 4,5-di-fluoro substituted in Series 6 and 5,6-di-fluoro substituted in Series 7. Sun et al reported that the exocyclic double bond in the scaffold existed in an equilibrium of *E* and *Z* forms.¹⁴⁷ They noted that when the indolinone Ring A was substituted at position 4 (as in Series 6), the *Z* isomer predominated because the steric interactions between the substituted C4 position and the ortho H of ring B in the *E* isomer were stronger than the interactions between the indolinone carbonyl (C=O) and the ortho H of Ring B in the *Z* isomer. Thus, it was reasoned that Series 6 compounds should be predominantly *Z*, while Series 7 compounds

would exist as E/Z mixtures. Thus, these two series would provide insight on the role of E/Z isomerism on growth inhibitory activities. Caveats are that a 4-F group may not be sufficiently bulky to completely displace the E/Z equilibrium towards the Z isomer as F is small and widely considered an isostere of hydrogen. On the other hand, while a larger group could have a greater impact on the E/Z equilibrium, it would also cause a greater than desired increase in lipophilicity. Second, substitution at C4 had been noted to adversely affect inhibitory activities against PDGFR and VEGFR.¹⁴⁷ The underlying cause of this negative impact may be stereochemical (displacement of E/Z equilibrium towards Z) or due to other factors such as an effect on electron density. Hence, loss of activity among Series 6 compounds may not necessarily be due to stereochemical factors.

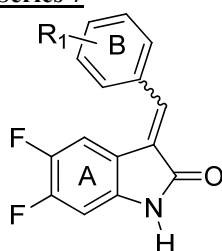
Table 2-3: Structures, ClogP and estimated solubilities (pH 7.4) of Series 6 and Series 7 compounds

Series 6



No	R ₁	Clog P ¹	Estimated solubility (μM) ²	No	R ₁	Clog P ¹	Estimated solubility (μM) ²
6-1	H	3.79	8.7	6-7	4'CF ₃	4.68	0.98
6-2	2'F	3.94	3.3	6-8	3'OCF ₃	4.82	0.90
6-3	3'F	3.94	2.8	6-9	3'SO ₂ Me	2.15	4.6
6-4	4'F	3.94	2.0	6-10	3'SO ₂ NHMe	2.57	12
6-5	2'CF ₃	4.68	1.0	6-11	3'SO ₂ NHPr	3.63	2.5
6-6	3'CF ₃	4.68	1.1	6-12 ^c	3'NHSO ₂ Me	2.60	18

Series 7



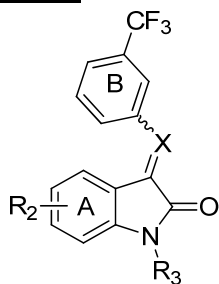
No	R ₁	Clog P ¹	Estimated solubility (μM) ²	No	R ₁	Clog P ¹	Estimated solubility (μM) ²
7-1	H	3.79	22	7-7	4'CF ₃	4.68	2.5
7-2	2'F	3.94	8.6	7-8	3'OCF ₃	4.82	2.3
7-3	3'F	3.94	7.3	7-9	3'SO ₂ Me	2.15	12
7-4	4'F	3.94	5.1	7-10	3'SO ₂ NHMe	2.57	32
7-5	2'CF ₃	4.68	2.6	7-11 ^c	3'SO ₂ NHPr	3.63	6.4
7-6	3'CF ₃	4.68	2.7	7-12 ^c	3'NHSO ₂ Me	2.60	45

^a Estimated from ChemDraw Ultra 7.0. Compounds with large ClogP values are more lipophilic. ^b Estimated values were from ACD Labs Version 12.00, Toronto, Canada. ^c Not synthesized by candidate.

Series 8 was designed to investigate the structure activity relationship (SAR) at the exocyclic methine (C=C) bond and the indolinone nitrogen (N1) (Table 2-4). The exocyclic double bond (C=C) was modified to an azomethine (C=N) to give 3-phenylimino indolin-2-ones. E/Z isomerism was present in this scaffold but as reported by others,¹⁵² the EZ isomers were not readily separated. As seen from the ClogP and solubility values (Table 2-3), phenyliminoindolinones were polar compounds. It should be noted that the azomethine N is a weak base (estimated pKa 1.2) and unlikely to be a strong H bond acceptor. Modifications at the indolinone N involved *N*-substitution with groups of increasing size, namely methyl, ethyl and benzyl.

Table 2-4: Structures, ClogP and estimated solubilities (pH 7.4) of Series 8 compounds

Series 8



No	R ₂	R ₃	X	Clog P ¹	Estimated solubility (μM) ²
8-1	H	H	CH	4.11	14
8-2	H	H	N	3.53	28
8-3	H	Me	CH	4.79	19
8-4	5Cl	H	N	4.25	7.3
8-5	5F	H	N	3.68	30
8-6	6Cl	H	N	4.25	6.8
8-7	6Cl	Me	CH	5.64	4.5
8-8 ^c	6Cl	Et	CH	6.17	2.1
8-9 ^c	6Cl	Bn	CH	6.94	0.08

^a Estimated from ChemDraw Ultra 7.0. Compounds with large ClogP values are more lipophilic. ^b Estimated values were from ACD Labs Version 12.00, Toronto, Canada. ^c Not synthesized by candidate.

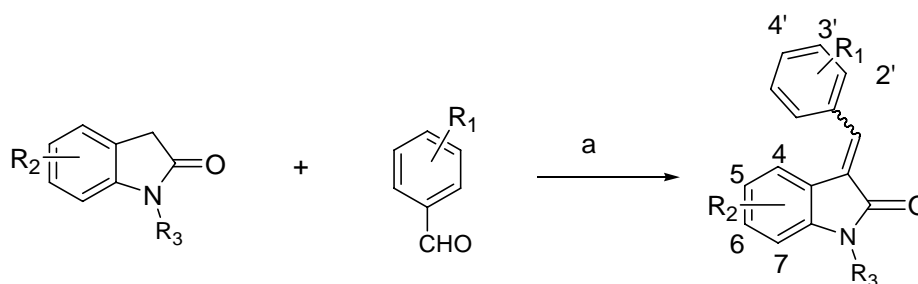
2.3. Chemical considerations

2.3.1. Syntheses of benzylidene indolinones of Series 1-8

This section describes the syntheses of target compounds by the candidate. Compounds that were synthesized by other members of the group (1-25, 2-15, 2-16, 3-14, 4-17, 4-18, 5-9, 5-10, 6-11, 6-12, 7-11, 7-12, 8-8, and 8-9) are described in Appendix II.

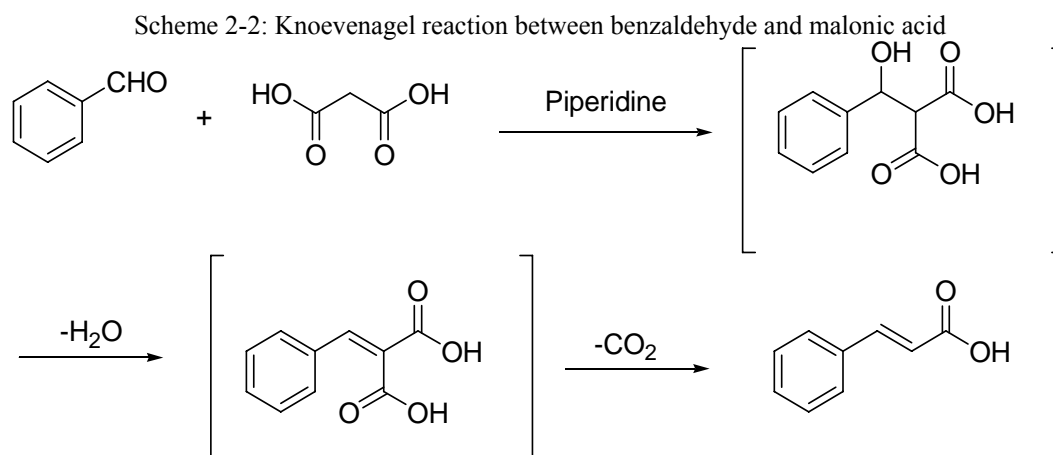
The benzylidene indolinones of Series 1-8 were synthesized by a Knoevenagel reaction between a benzaldehyde and an oxindole (Scheme 2-1).

Scheme 2-1 : General synthesis pathway for Series 1 to 7, 8-1, 8-3 and 8-7.

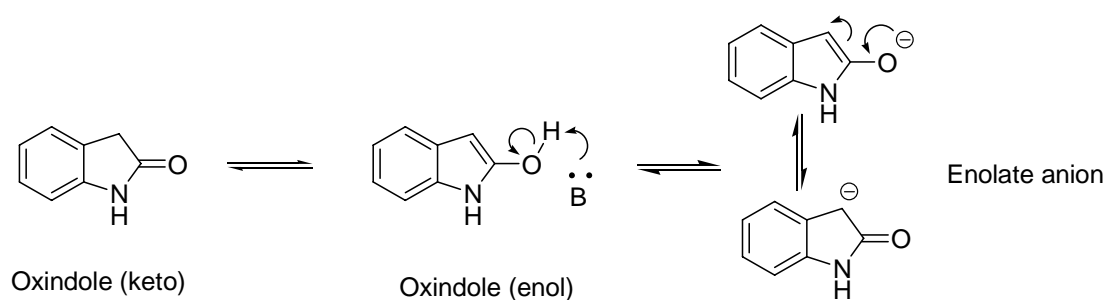


Reagents and conditions: (a) piperidine (cat.), ethanol, microwave, 140 °C, 15 min.

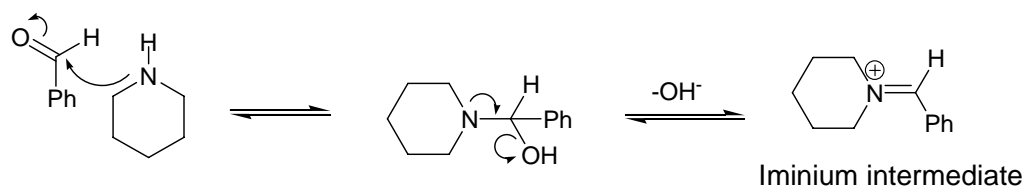
The classical Knoevenagel reaction is a base-catalyzed reaction between an aldehyde or ketone and malonic acid (Scheme 2-2). The characteristic feature of the reaction is the presence of two electron-withdrawing groups flanking the methylene in the carbanion-forming reactant (malonic acid) which allows the condensation to be effected by weaker bases than those used in conventional aldol condensations. Condensation is followed by dehydration to give the $\alpha\beta$ unsaturated dibasic acid which is decarboxylated to give cinnamic acid as product.



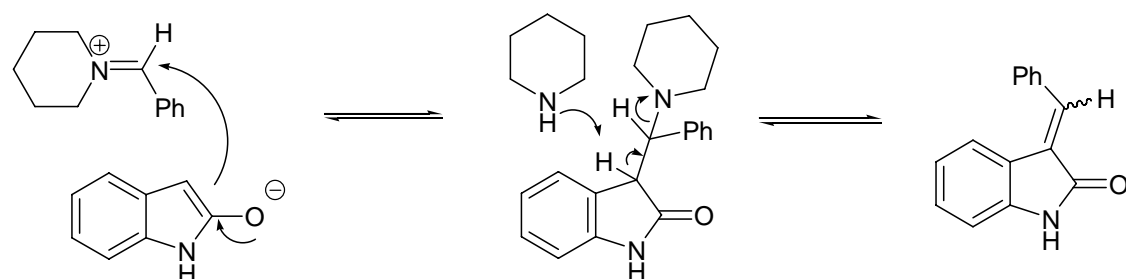
In the present context, the oxindole is the carbanion-forming reactant (Scheme 2-1). The acidic methylene of the oxindole is flanked by the electron-withdrawing amide carbonyl and the sp^2 hybridized carbon of the indolinone Ring A, so it broadly resembles the carbanion-forming malonic acid in the classical Knoevenagel reaction. The condensation was carried out in the presence of piperidine as base catalyst. Piperidine has two important roles in this reaction. First, it promotes the formation of the resonance stabilized C3 carbanion on the oxindole by facilitating deprotonation of the enolic OH.



Second, piperidine enhances the electrophilicity of the carbonyl carbon on the benzaldehyde by forming an iminium intermediate.



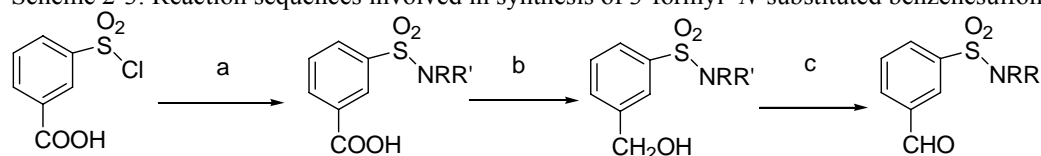
Hence, the benzaldehyde is primed for reaction with the nucleophilic enolate anion. The resulting intermediate undergoes 1,2-elimination to give the 3-substituted indolin-2-one.



2.3.2. Syntheses of 3-formyl-benzenesulfonamide and 3-formyl-*N*-substituted-benzenesulfonamide

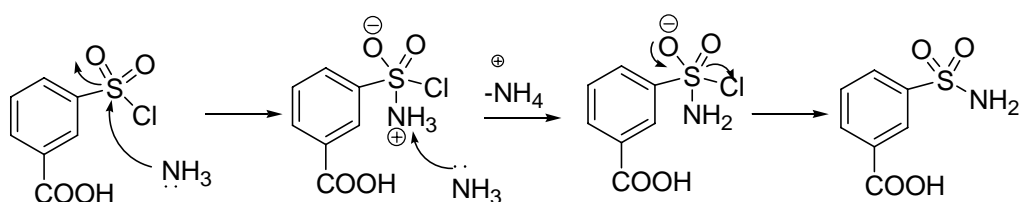
These compounds were required for the synthesis of indolinone compounds with aminosulfonyl and *N*-substituted aminosulfonyl groups. The synthesis of formylbenzenesulfonamide started with the reaction of commercially available 3-chlorosulfonylbenzoic acid and ammonia or other amines to give the sulfamoylbenzoic acid (or *N*-substituted sulfamoylbenzoic acid). The carboxylic acid was then reduced with borane-THF to the corresponding alcohol and then oxidized to the aldehyde with pyridinium dichromate (Scheme 2-3)

Scheme 2-3: Reaction sequences involved in synthesis of 3-formyl- *N*-substituted benzenesulfonamides



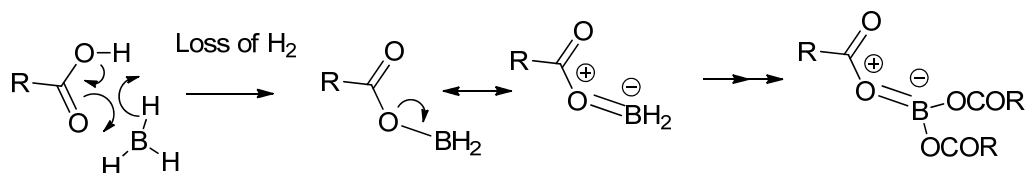
Reagents and conditions: (a) NH_3 , Me-NH_2 , Me_2NH , Et-NH_2 , Pr-NH_2 , iPr-NH_2 (4 eqv, amine,), 0 deg C, 0.5 hr. (b) Borane/THF (1M), 25 deg C, 15 hr (c) Pyridinium dichromate (5 eqv), 25 deg C, 6 hr

The sulfonamides were synthesized by reaction at the electrophilic sulfur by the nucleophilic ammonia or aliphatic amine. The acid HCl released in the course of reaction was neutralized by the excess amine present in the reaction pot.



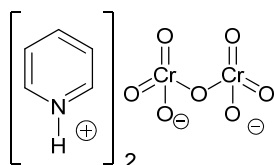
The reduction of the carboxylic acid moiety by borane proceeds by the formation of a triacylborate with evolution of hydrogen gas. The exact mechanism by which the reduction occurs has not been clearly established. A possible reaction sequence is given as follows:¹⁶⁹

The reaction starts with the attack of boron by the π electrons in the p orbital of the carboxylic carbonyl ($\text{C}=\text{O}$), with loss of hydride as hydrogen gas. The reaction proceeds until all the H atoms of borane have been replaced by acyl groups.

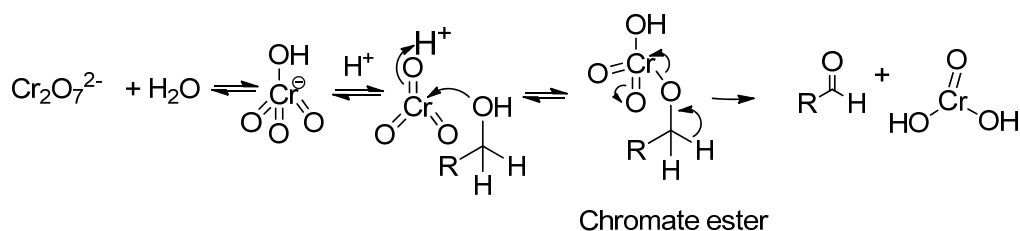


Borane then attacks the carbonyl oxygen on one of the acyl groups in triacylborane. At this stage, the carbonyl carbon gains its first proton. Following subsequent reactions with borane and transfer of protons to the carbonyl carbon, reduction is complete and upon hydrolysis with water, the alcohol is liberated along with the formation of trihydroxyborane.¹⁷⁰

The primary alcohol of the benzenesulfonamide was then oxidized to the aldehyde with pyridinium dichromate (PDC).



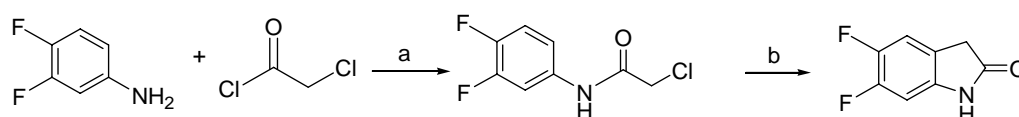
PDC is not as acidic as Cr^{VI} reagents. In PDC, pyridinium (pKa5, a weak acid) is the acidic moiety. The mechanism of reaction is shown as follows:



The dichromate ion from PDC forms HCrO_4^- ions in water and these form chromate esters with the alcohol. The ester decomposes to release the aldehyde and chromous acid H_2CrO_3 (Cr^{IV}) which reacts with other chromium ions of different oxidation states to finally yield Cr^{III} oxides, the final metal containing by-product.

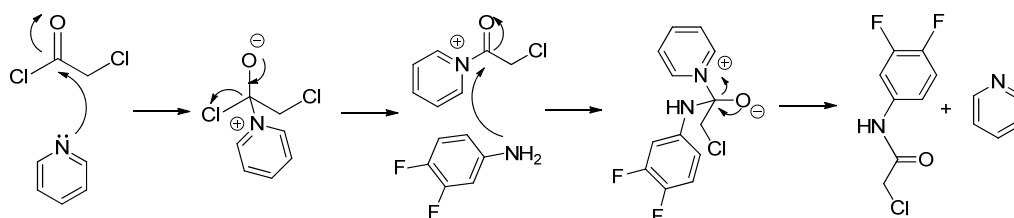
2.3.3. Synthesis of 5,6-difluoro-oxindole

Scheme 2-4: Reaction scheme for synthesis of 5,6-difluoro-oxindole

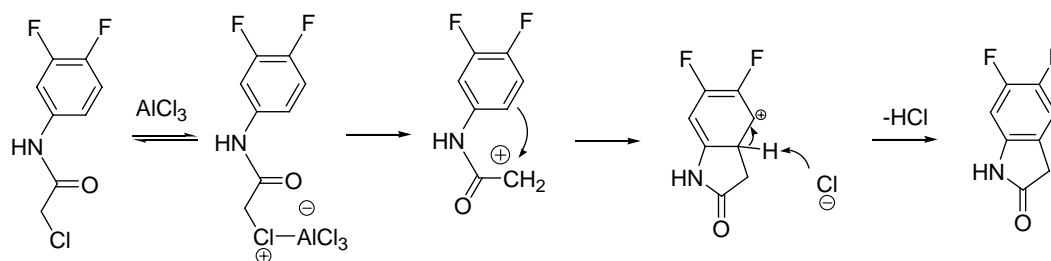


Reagents and conditions: (a) Toluene, pyridine (1 eqv), 5 ° C, overnight; (b) neat reaction, AlCl_3 (4 eqv), 220 ° C, 4h.

5,6-Difluoro-oxindole, required for the synthesis of Series 7, was synthesized in a two-step reaction. The first step involved amide formation and the second step was a Friedel-Crafts alkylation reaction. In the first step, chloroacetylchloride reacted with 3,4-difluoroaniline to form the 2-chloro-*N*-(3,4-difluorophenyl)acetamide. The reaction involved an initial attack by the base catalyst pyridine on the acid chloride to give the reactive intermediate (2-chloro-1-pyridin-1-yl-ethanone). The carbonyl carbon of the latter was then attacked by the weakly nucleophilic aniline N of 3,4-difluoroaniline to give the amide 2-chloro-*N*-(3,4-difluorophenyl)acetamide.



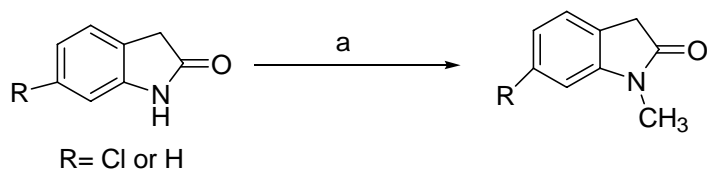
In the subsequent step, the Lewis acid aluminium chloride removed the chlorine atom from the amide to generate a terminal electrophilic carbonium ion. An aromatic electrophilic substitution takes place with intramolecular cyclization to give the indolin-2-one scaffold.



2.3.4. Syntheses of 1-methyl-oxindole and 6-chloro-1-methyl-oxindole

1-Methyloxindole and 6-chloro-1-methyloxindole were required for the syntheses of **8-3** and **8-7** respectively. *N*-Methylation of the oxindole N was achieved by deprotonation of the oxindole NH by sodium hydride followed by an S_N2 reaction between the nucleophilic N and a methyl carbonium from dimethylsulphate. The reaction was facilitated by the good leaving group property of the sulphate anion of dimethylsulphate.

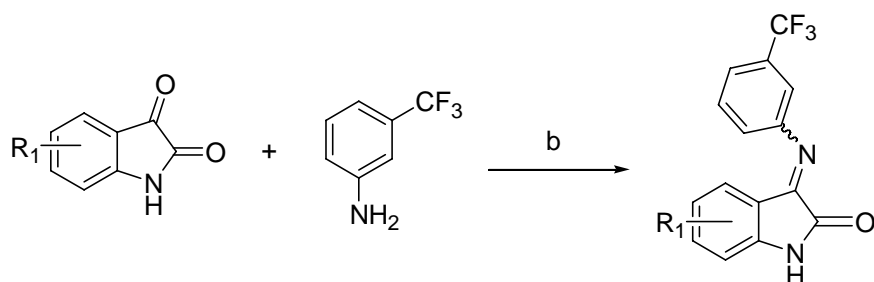
Scheme 2-5 Syntheses of 1-methyl-oxindole and 6-chloro-1-methyl-oxindole



Reagents and conditions: (a) Toluene, NaH (1 eqv), Me₂SO₄ (1 eqv), 100 °C, 2 h.

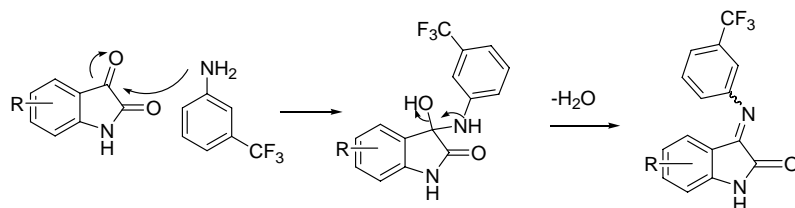
2.3.5. Synthesis of 3-arylimino-2-indolones of Series 8

Scheme 2-6: Syntheses of 1-methyl-oxindole and 6-chloro-1-methyl-oxindole



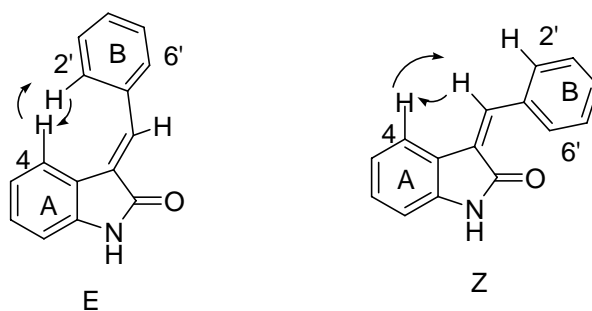
Reagents and conditions: (a) neat reaction, microwave, 140 °C, 15 min.

The 3-arylimino-2-indolones of Series 8 (**8-2**, **8-4**, **8-5**, **8-6**) were synthesized by a condensation reaction between the aniline and isatin to give an iminium salt which was the desired product. The nucleophilic aniline nitrogen attacked the electron deficient non-amide carbonyl carbon of isatin, followed by dehydration to give the arylimino product.



2.4. Assignment of configuration

EZ isomerism is present in the 3-benzylideneindolin-2-ones. The EZ isomers may be distinguished by the Nuclear Overhauser Effect (NOE). In the *E* isomer, irradiation of the proton at C4 of Ring A leads to the NOE enhancement of signals attributed to the aromatic protons at the ortho positions 2' and 6' of Ring B. In the *Z* isomer, irradiation of the C4 proton of Ring A results in the enhancement of the vinyl proton signal.



They are also distinguished by the chemical shifts of the ortho protons.¹⁴⁷ In the *Z* isomer, the ortho protons on Ring B would be deshielded by the carbonyl group of the indolinone ring and hence appear at high ppm (downfield) than the ortho protons in the *E* isomer. In the *E* isomer, the ortho protons are shielded by aromatic protons of the indolinone ring A. Thus, analysis of the chemical shifts of the ortho aromatic protons of ring B is a useful means of distinguishing the *E* and *Z* isomers. Sun *et al.*¹⁴⁷ reported that the chemical shifts of the ortho protons on ring B of the *Z* isomer were found at 8.53 -7.85 ppm and the chemical shifts of the ortho protons on ring B of the *E* isomer were found upfield at 7.84-7.45 ppm .

Zhang *et al*⁶ reported that **47** and **3-6** were present as a mixture of *E* and *Z* isomers.⁶ However, when separated by column chromatography, they were found to comprise a major *E* isomer (ortho protons: 7.90-8.01 ppm) and a minor *Z* isomer (ortho protons: 8.4-8.5 ppm). When **47** and **3-6** were re-synthesized by the candidate, both *E* and *Z* isomers were also obtained but they could not be separated by flash column chromatography, possibly due to the small amounts of the minor isomer. The chemical shifts of the ortho protons in the major isomer were found at 7.90-8.01 ppm which agreed with the findings of Zhang *et al.*⁶ Based on chemical shift values, it was deduced that the major isomer in **47** and **3-6** was *E*.

While this approach worked for **47** and **3-6** because they had been previously reported, it could not be applied to the newly synthesized compounds. This was because in spite of many attempts at separating the major and minor isomers by column chromatography, only the major isomer could be successively separated. To depend on the chemical shifts of only one (major) isomer for assignment of configuration, in the absence of the minor isomer, would not be entirely reliable.

To overcome this problem, another approach was considered. This was based on the tendency of benzylidene indolinones to reach an equilibrium of *E* and *Z* isomers in polar solvents such as methanol or DMSO or when exposed to light.¹⁴⁷ Thus, it was reasoned that monitoring the NMR spectra of a freshly prepared sample in DMSO and the same sample after 12 h (aged sample) would provide clues on the dominant isomer in the freshly prepared sample. This was because the ortho protons of ring B generally had the highest chemical shifts among the aromatic protons. If the aged sample showed additional peaks that were downfield of the original ortho protons, it would imply that the major isomer in the freshly prepared sample was *E*. If the new peaks appeared upfield, then the major isomer in the freshly prepared sample was deduced to be *Z*.

Besides the aforementioned changes in chemical shifts, certain characteristic changes were observed in the peak areas of the ortho protons relative to the lactam NH proton of the indolinone ring. This is elaborated in the following paragraph.

The lactam NH proton of the indolinone ring was observed at 10.00 ppm in the NMR spectra of freshly prepared DMSO solutions of **47** and **6-6**. The predominant forms of **47** and **6-6** were *E* and *Z* respectively. The *Z* configuration of **6-6** was confirmed by X ray crystallography (Figure 2-2), which was anticipated since the C4 of 6-6 position was occupied by 4-F.

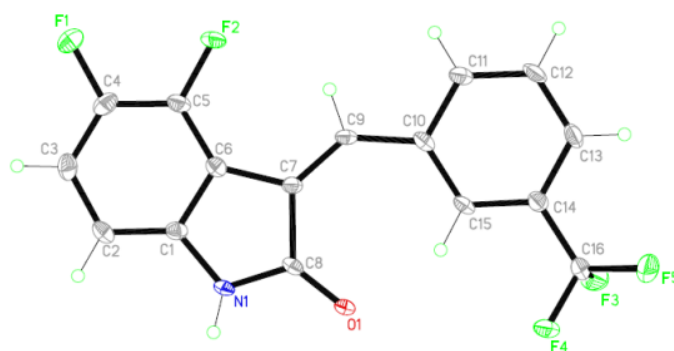


Figure 2-2: X-ray structure of Compound **6-6**

The NH peak was used as a standard for integration and its area was assigned a value of 1.00. The chemical shifts of the ortho protons of **47** (freshly prepared) were found at 8.01 (peaks of the two protons overlapped) and their combined area (integrated against NH) was 2.24

(Figure 2-3 A). When the spectra was collected for the same solution 12 h later, two changes were observed: (i) Two “new” peaks appeared downfield from the original peak at 8.88 and 8.46 ppm and (ii) the area of the original peak was decreased to 1.61 (Figure 2-3 B).

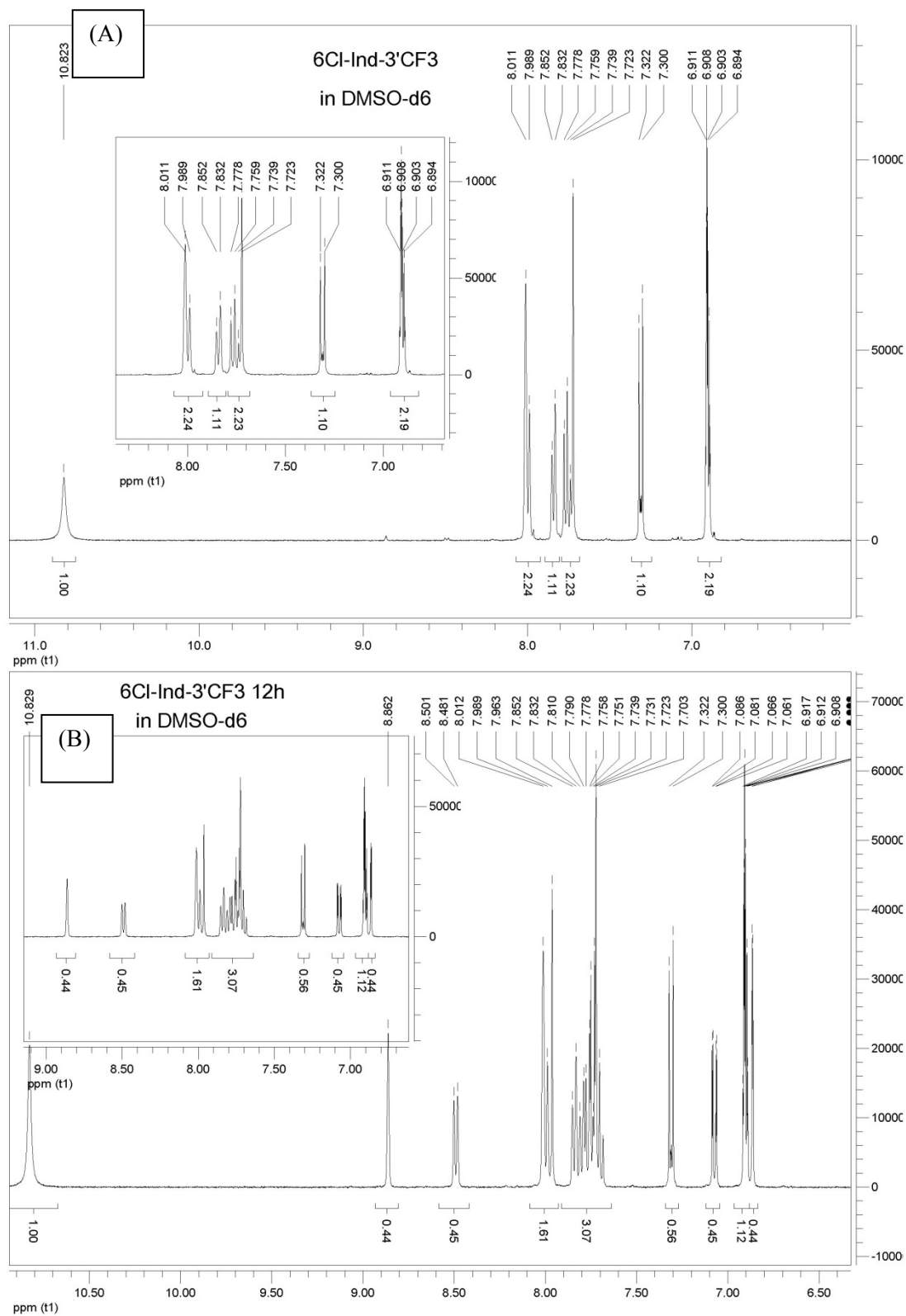


Figure 2-3: ^1H NMR spectra (amide proton and aromatic protons only) of compound **47**: (A) Freshly prepared in d₆ DMSO (B) After 12 hr of standing at room temperature (24°C), protected from light.

In the case of compound **6-6**, the chemical shifts of the ortho protons were 8.76 and 8.33 ppm and their areas were 0.94 and 0.96 respectively (Figure 2-4 A). After 12 hr, new peaks were observed upfield from the original peaks and interestingly the areas of the original peaks diminished only slightly to 0.73 and 0.74 respectively (Figure 2-4 B).

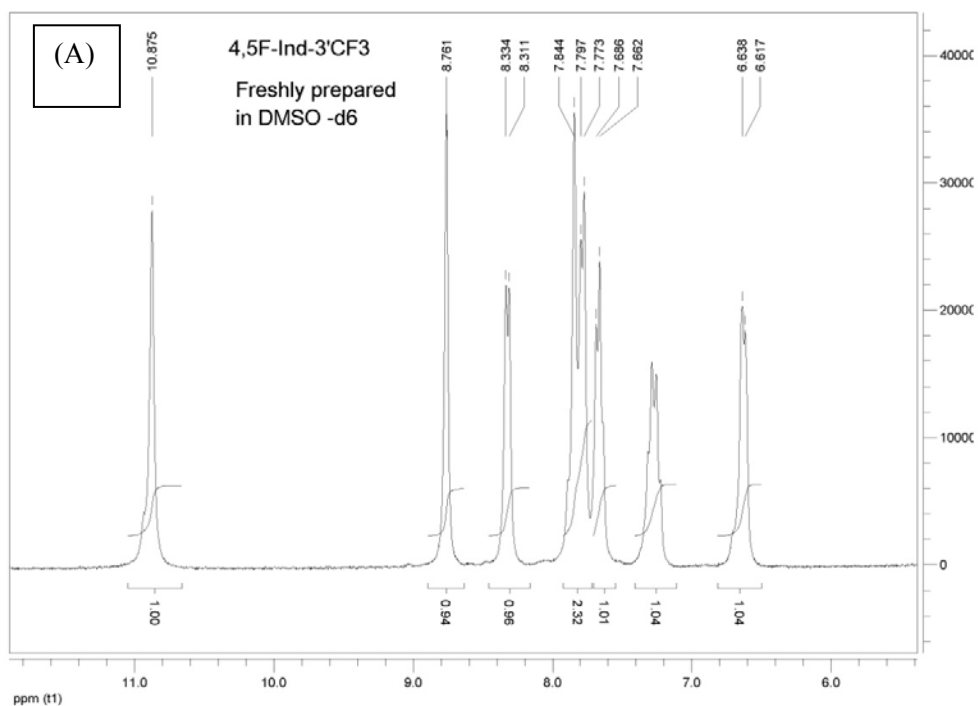


Figure 2-4: ¹H NMR spectra (amide proton and aromatic protons only) of compound **6-6**: (A) Freshly prepared in d₆ DMSO

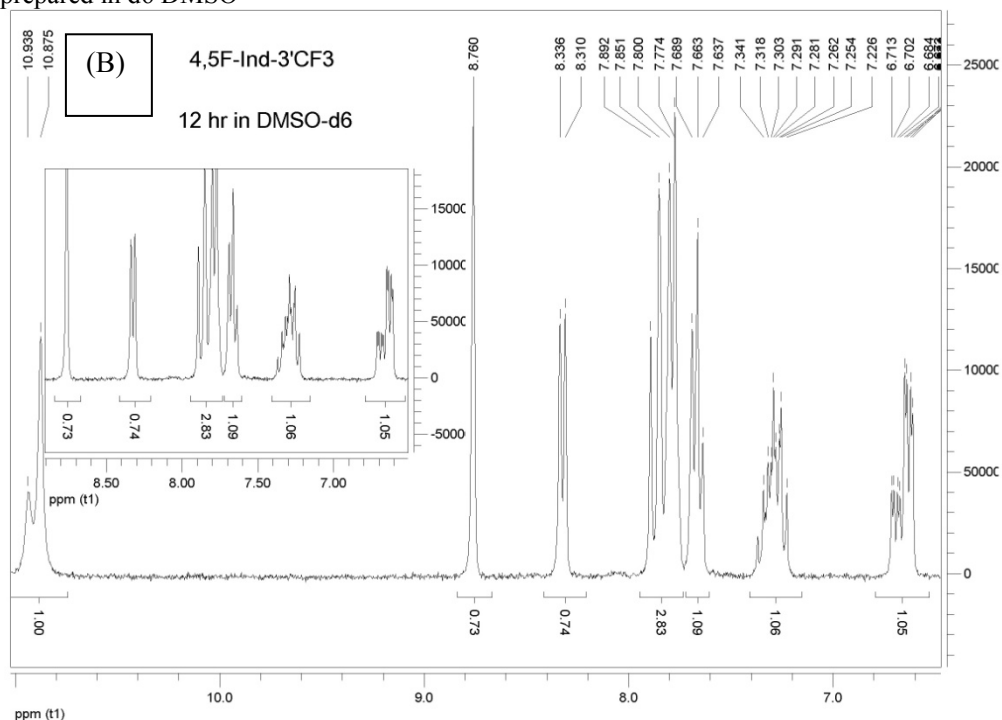


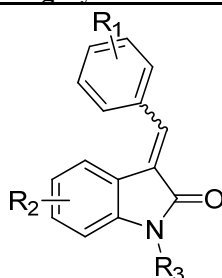
Figure 2-4: ¹H NMR spectra (amide proton and aromatic protons only) of compound **6-6**: (B) After 12 hr of standing at room temperature (24°C), protected from light.

Based on the changes in the spectra of **47** and **6-6** which were taken as representative *E* and *Z* isomers respectively, it was reasoned that the chemical shifts of the “new” peaks and the peak areas of the original ortho protons could be used to deduce if the original compound was predominantly *E* or *Z*. If it was *E*, the new peaks (*Z* isomer) would appear downfield and the peak area of the original ortho protons would decrease. If the original compound was *Z*, then the new peaks (*E* isomer) would appear upfield and the peak areas of the original ortho protons would show a smaller decrease. The changes in the chemical shifts of the ortho protons could be explained by differential shielding/deshielding in the *E* and *Z* isomers. The changes in the peak area of the original ortho protons could be reflect the preference for *E* or *Z* isomer. Thus, when the *E* isomer was the dominant form (as in the fresh sample of **47**), a large proportion of it was converted to the *Z* isomer with time, as seen from the decrease in the original peak area. But when the *Z* isomer was the dominant form (as in the fresh sample of **6-6**), equilibration to the *E* isomer did not occur to the same degree, as reflected by the smaller decrease in peak area of the original ortho protons in the *Z* isomer.

By monitoring changes in chemical shifts and peak areas of ortho protons in fresh and aged samples, the test compounds were classified into 3 categories: Category A (predominantly *E*), Category B (predominantly *Z*) and Category C (no predominant isomer, mixture of *E* and *Z*). Compounds in these categories are listed in Table 2-5.

Table 2-5: Configuration of Series 1-8 compounds based on chemical shifts and peak areas of ortho protons in fresh and aged samples analyzed by ¹H NMR.

Category A: *E* isomers

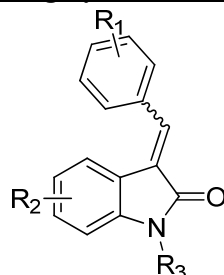


No	R ₁	R ₂	R ₃	No	R ₁	R ₂	R ₃
1-1	H	6Cl	H	3-9	3'OCF ₃	6F	H
1-2	2'F	6Cl	H	3-10	3'SO ₂ Me	6F	H
1-3	3'F	6Cl	H	3-11	3'SO ₂ NHMe	6F	H
1-4	4'F	6Cl	H	3-12	3'SO ₂ NHEt	6F	H

No	R ₁	R ₂	R ₃	No	R ₁	R ₂	R ₃
1-5	3'Me	6Cl	H	3-13	3'SO ₂ NHPr	6F	H
1-6	2'OMe	6Cl	H	3-14	3'NHSO ₂ Me	6F	H
1-7	3'OMe	6Cl	H	4-1	H	5F	H
1-8	4'OMe	6Cl	H	4-2	2'F	5F	H
1-10	3'CF ₃	6Cl	H	4-3	3'F	5F	H
1-11	4'CF ₃	6Cl	H	4-4	4'F	5F	H
1-12	3'4'F	6Cl	H	4-5	2'Me	5F	H
1-13	2'OCF ₃	6Cl	H	4-6	3'Me	5F	H
1-14	3'OCF ₃	6Cl	H	4-7	4'Me	5F	H
1-15	4'OCF ₃	6Cl	H	4-8	3'OMe	5F	H
1-16	3'SO ₂ Me	6Cl	H	4-10	3'CF ₃	5F	H
1-17	3'SO ₂ NH ₂	6Cl	H	4-11	4'CF ₃	5F	H
1-18	3'SO ₂ NHMe	6Cl	H	4-12	3'4'F	5F	H
1-19	3'CN	6Cl	H	4-13	3'OCF ₃	5F	H
1-20	3'SO ₂ NMe ₂	6Cl	H	4-14	3'SO ₂ Me	5F	H
1-21	4'SO ₂ NHMe	6Cl	H	4-15	3'CN	5F	H
1-22	3'SO ₂ NHEt	6Cl	H	4-17	3'NHSO ₂ Me	5F	H
1-23	3'SO ₂ NHPr	6Cl	H	5-1	H	6OMe	H
1-25	3'NHSO ₂ Me	6Cl	H	5-2	2'F	6OMe	H
2-1	H	5Cl	H	5-3	3'F	6OMe	H
2-2	2'F	5Cl	H	5-4	4'F	6OMe	H
2-3	3'F	5Cl	H	5-5	2'CF ₃	6OMe	H
2-4	4'F	5Cl	H	5-6	3'CF ₃	6OMe	H
2-5	3'OMe	5Cl	H	5-7	4'CF ₃	6OMe	H
2-6	2'CF ₃	5Cl	H	5-8	3'SO ₂ NMe ₂	6OMe	H
2-7	3'CF ₃	5Cl	H	5-9	3'SO ₂ NHPr	6OMe	H
2-8	4'CF ₃	5Cl	H	5-10	3'NHSO ₂ Me	6OMe	H
2-9	3'4'F	5Cl	H	7-1	H	5,6F	H
2-10	3'OCF ₃	5Cl	H	7-2	2'F	5,6F	H
2-11	3'SO ₂ Me	5Cl	H	7-3	3'F	5,6F	H
2-13	3'CN	5Cl	H	7-4	4'F	5,6F	H
2-14	3'SO ₂ NHMe	5Cl	H	7-6	3'CF ₃	5,6F	H
2-16	3'SO ₂ NHPr	5Cl	H	7-7	4'CF ₃	5,6F	H
3-1	H	6F	H	7-8	3'OCF ₃	5,6F	H
3-2	2'F	6F	H	7-9	3'SO ₂ Me	5,6F	H
3-3	3'F	6F	H	7-10	3'NHSO ₂ Me	5,6F	H
3-4	4'F	6F	H	8-1	3'CF ₃	H	H
3-5	2'CF ₃	6F	H	8-3	3'CF ₃	6Cl	Me
3-6	3'CF ₃	6F	H	8-6	3'CF ₃	6Cl	Me

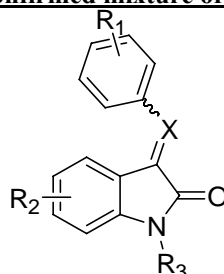
No	R ₁	R ₂	R ₃	No	R ₁	R ₂	R ₃
3-7	4'CF ₃	6F	H	8-8	3'CF ₃	6Cl	Et
3-8	3'OCF ₃	6F	H				

Category B: Z isomers



No	R ₁	R ₂	R ₃	No	R ₁	R ₂	R ₃
6-1	H	4,5F	H	6-6	3'CF ₃	4,5F	H
6-2	2'F	4,5F	H	6-7	4'CF ₃	4,5F	H
6-3	3'F	4,5F	H	6-8	3'OCF ₃	4,5F	H
6-4	4'F	4,5F	H	6-10	3'SO ₂ NHMe	4,5F	H

Category C: Confirmed mixture of E and Z isomers



No	R ₁	R ₂	R ₃	X
1-24	3'SO ₂ NHiPr	6Cl	H	CH
2-12	3'SO ₂ NH ₂	5Cl	H	CH
2-15	3'SO ₂ NHPr	5Cl	H	CH
4-17	3'SO ₂ NHPr	5F	H	CH
6-5	2'CF ₃	4,5F	H	CH
6-9	3'SO ₂ Me	4,5F	H	CH
7-11	3'SO ₂ NHPr	5,6F	H	CH
8-2	3'CF ₃	H	H	N
8-4	3'CF ₃	6Cl	CH ₃	N
8-6	3'CF ₃	5Cl	CH ₃	N
8-7	3'CF ₃	5F	CH ₃	N
8-9	3'CF ₃	6Cl	Bn	CH

The category C compounds comprise the 3-phenylimino indolin-2-ones (8-2, 8-4, 8-5, 8-6) and miscellaneous compounds from different series (1-24, 2-12, 2-15, 4-16, 6-5, 6-9, 7-11, 8-9.) The phenylimino indolin-2-ones are known to exist as inseparable *E* and *Z* isomers due to rapid interconversion at room temperature¹⁵². Thus, their presence in Category C was anticipated. As for the miscellaneous compounds, the isomers could not be separated by column chromatography and thus, no major isomer was isolated from the reaction mixture. Consequently, their NMR spectra could not be analyzed in the same way as the Categories A

and B compounds. However, the *E* and *Z* isomers of some of these compounds (**1-24**, **2-12**, **6-5**, **6-9**, **8-9**) could be separated by HPLC. The chromatogram of the test compound showed two major peaks and LC-MS confirmed that they had the same mass. Since the total area of the two peaks exceeded 95% of total peak area, it was deduced that they were sufficiently pure (> 95%) for biological evaluation.

Next, LCMS was investigated as a means of monitoring the *E* /*Z* isomerization process. In this approach, the test compound was analyzed by LC and the mass of the eluting peaks were assigned by mass spectrometry. If a compound was present as the *E* isomer, it should present only one peak with a specific mass on the chromatogram. If the *E* isomer converted to the *Z* isomer with time, then the chromatogram should show an additional peak (*Z* isomer) with an identical mass to the 1st peak.

This investigation was carried out on selected compounds **47**, **1-18** and **6-6**. Except for **6-6** which was assigned a *Z* configuration based on its X ray structure (Figure 2-2), the other compounds were assigned an *E* configuration based on the NMR criteria described earlier. The investigations involved monitoring the LCMS of samples that were freshly prepared in methanol or DMSO and after 12 hours of storage at 24°C. As DMSO could not be directly injected into the instrument, the sample was diluted with water and extracted with ethyl acetate. The solvent was removed by evaporation under reduced pressure. The residue was reconstituted in methanol and injected into the LCMS. The time taken for this procedure was approximately 10 minutes.

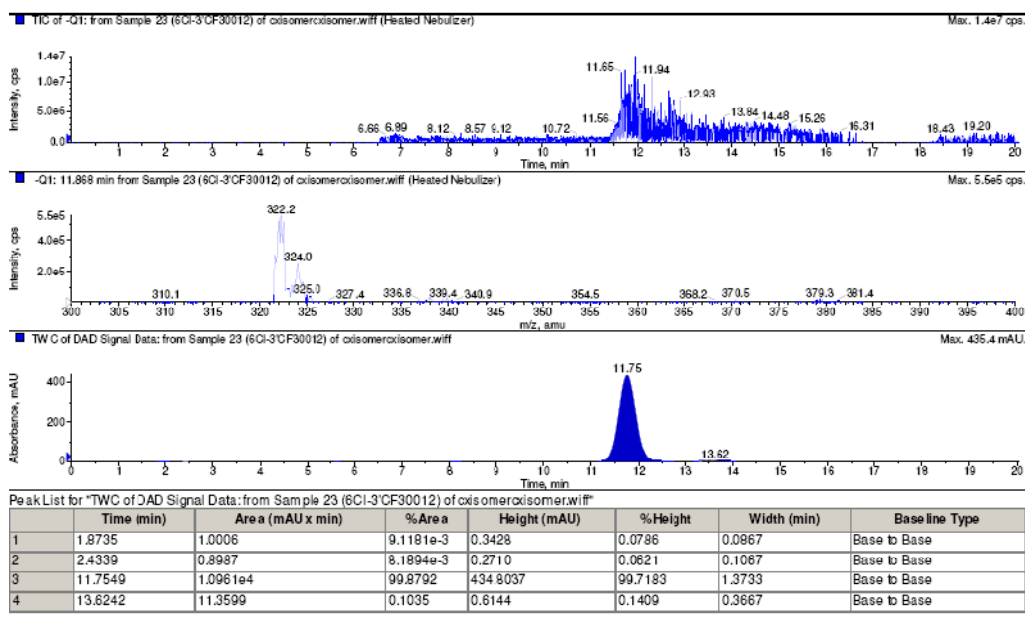


Figure 2-6 A: LC-MS spectrum of **47** (freshly prepared in methanol) MS peak: $[M-H]^- = 322.2$.

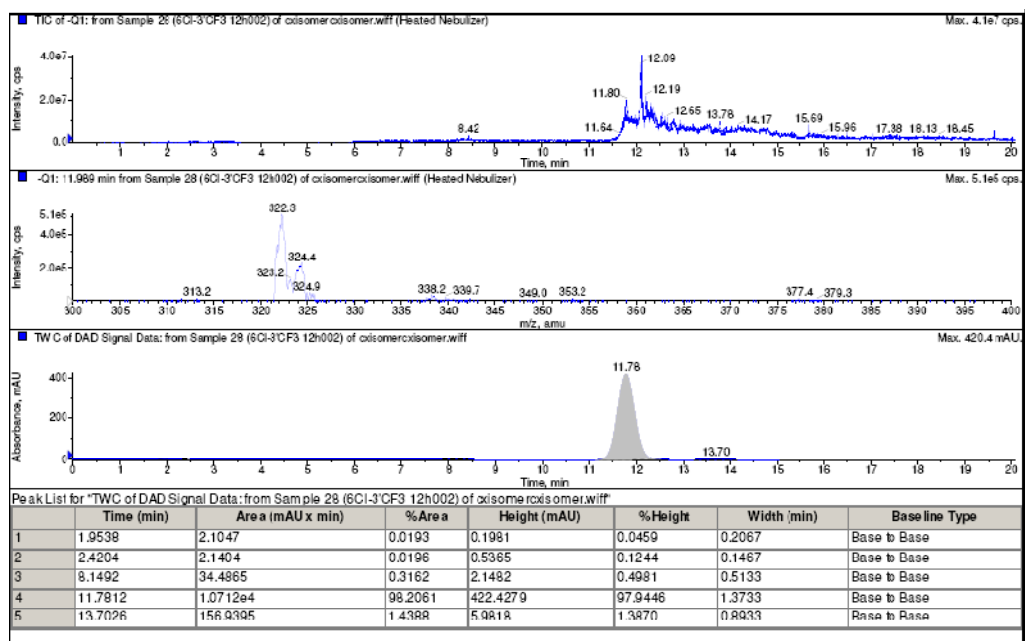


Figure 2-6 B: LC-MS spectrum of **47** (after 12h in methanol) MS peak: $[M-H]^- = 322.2$. No new peak was observed in the LC after this time. Mass of original peak was unchanged.

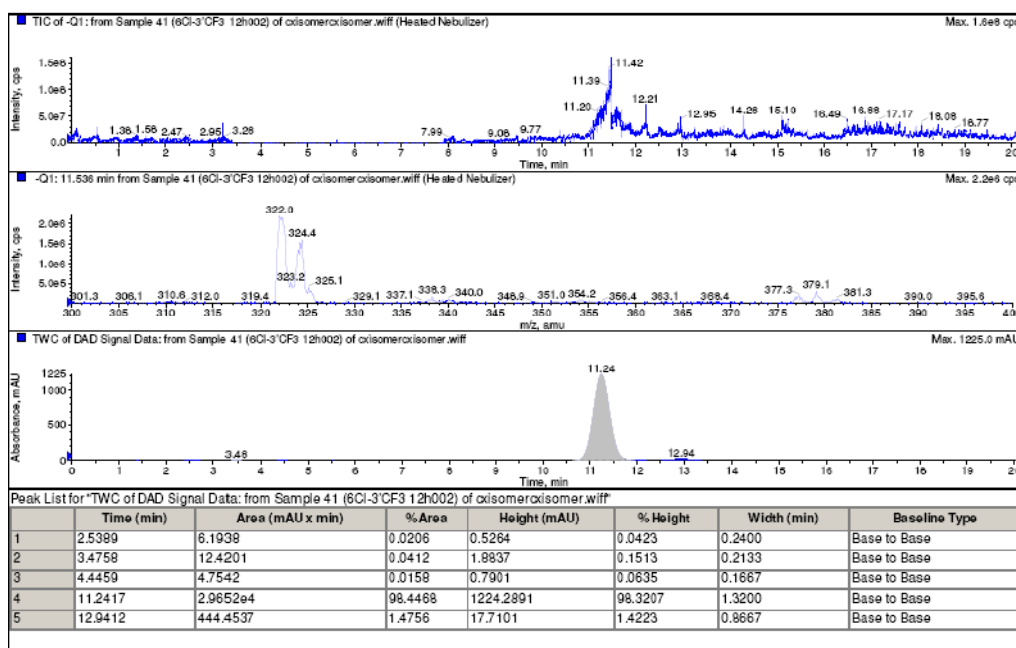


Figure 2-6 C: LC-MS spectrum of **47** (freshly prepared in DMSO) MS peak: $[M-H]^- = 322.2$.

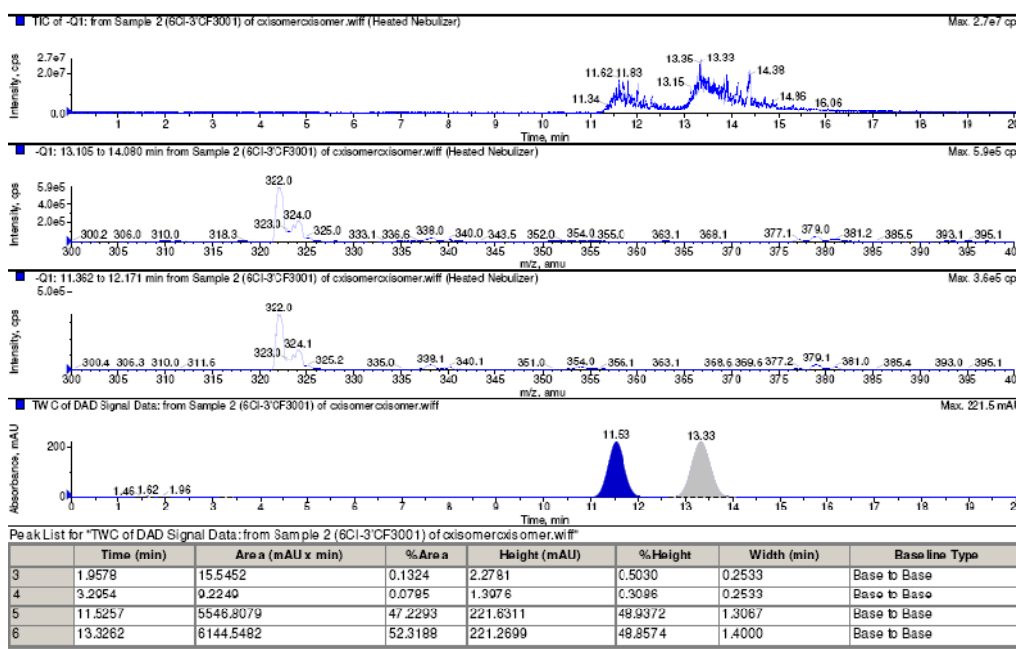


Figure 2-6 D: LC-MS spectrum of **47** (after 12h in DMSO). MS peak: $[M-H]^- = 322.2$. A new peak was observed in the LC (retention time 13.38 min). % Area of new peak (52.3) was close to that of original peak (% Area = 47.2) Mass of the new peak (322.0) was identical to the original peak.

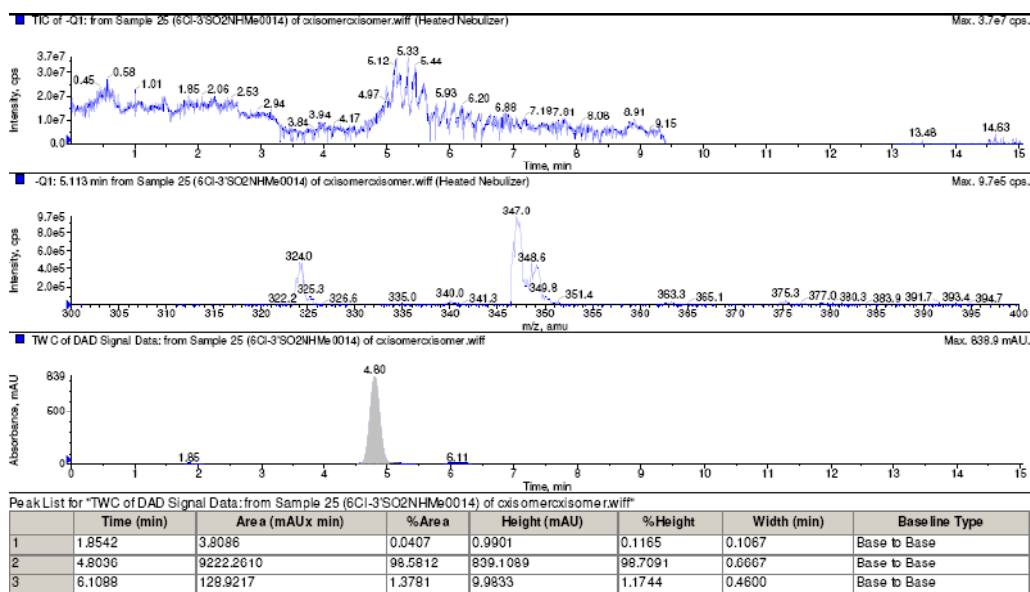


Figure 2-7 A: LC-MS spectrum of **1-18** (freshly prepared in methanol) MS peak: $[M-H]^- = 347.9$.

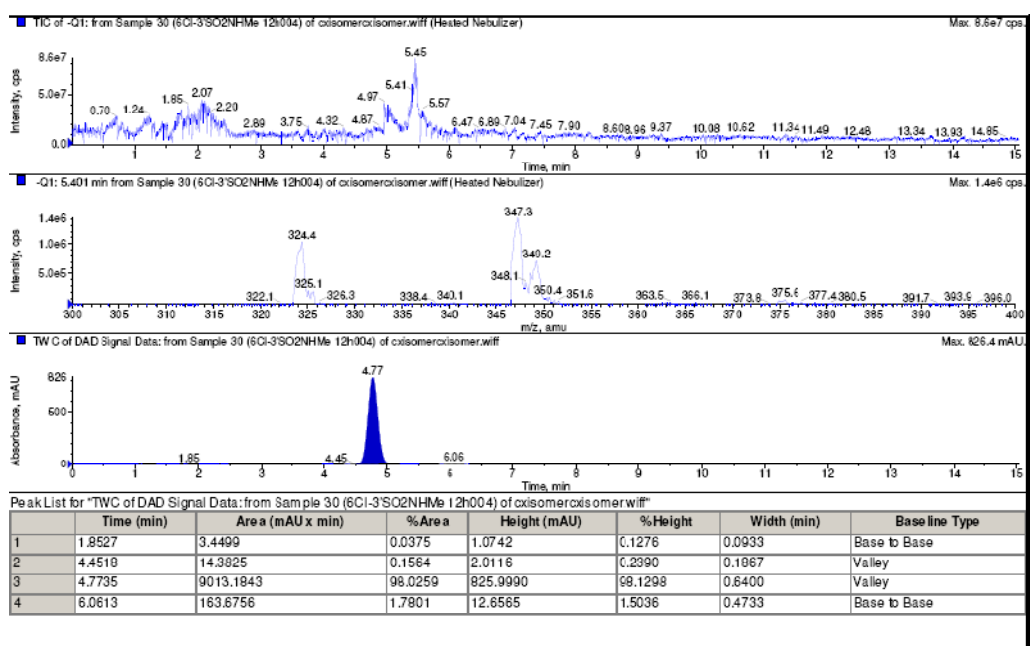


Figure 2-7 B: LC-MS spectrum of **1-18** (12h in methanol), MS peak: $[M-H]^- = 347.9$. No new peak was observed in the LC after this time. Mass of original peak was unchanged.

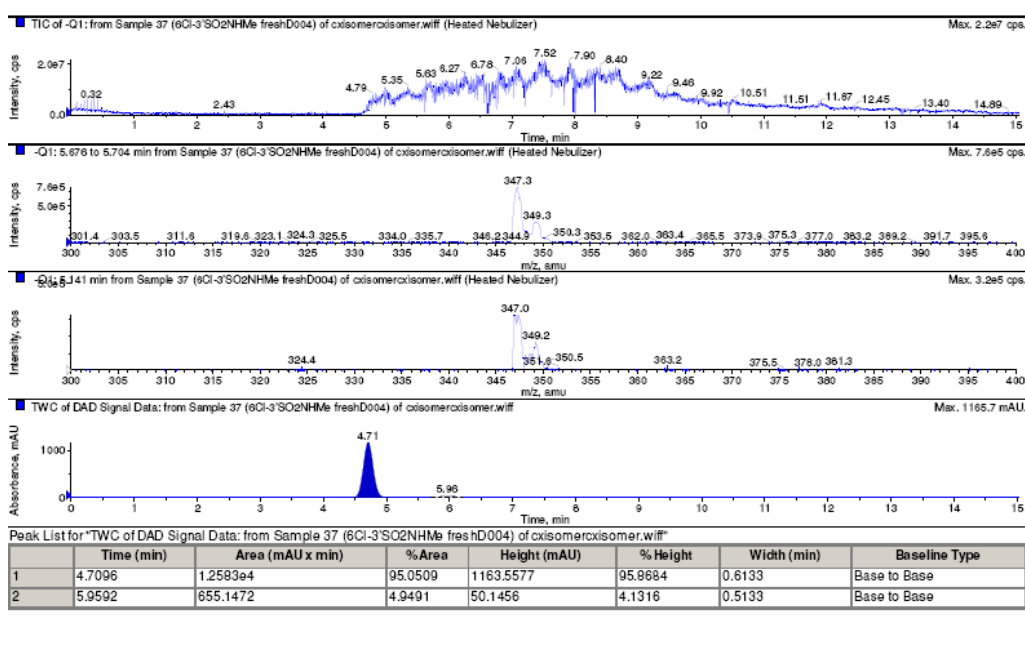


Figure 2-7 C: LC-MS spectrum of **1-18** (freshly prepared in DMSO), MS peak: $[M-H]^- = 347.9$

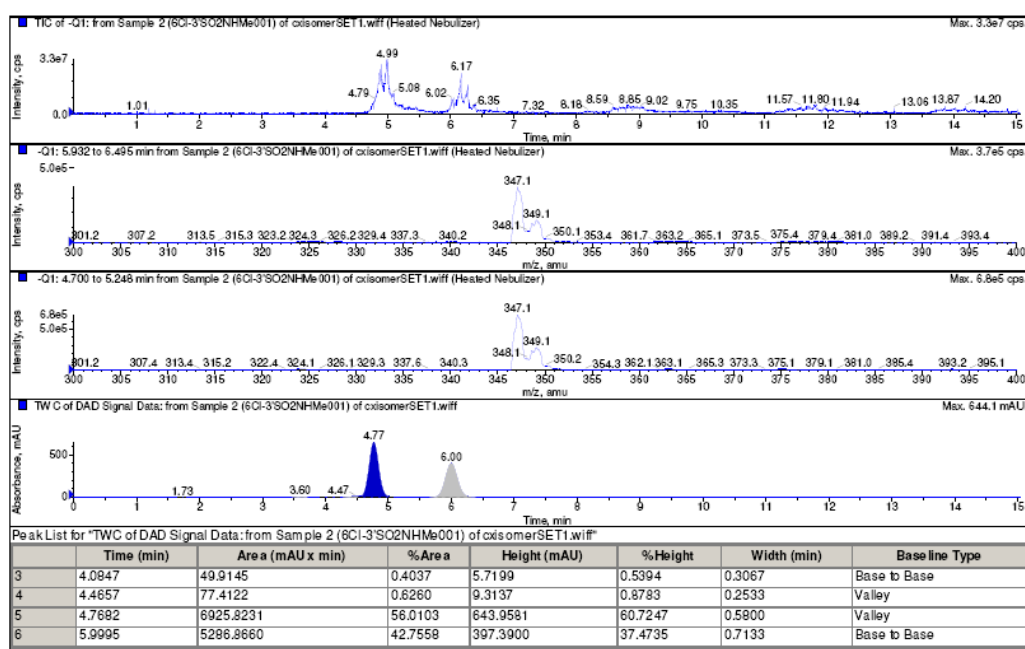


Figure 2-7 D: LC-MS spectrum of **1-18** (12h in DMSO), MS peak: $[M-H]^- = 347.9$. A new peak (347.1) was observed in the LC (retention time 6.0 min). % Area of new peak (42.7) was close to that of original peak. Mass of the new peak (347.1) was identical to the original peak (% Area 56.0).

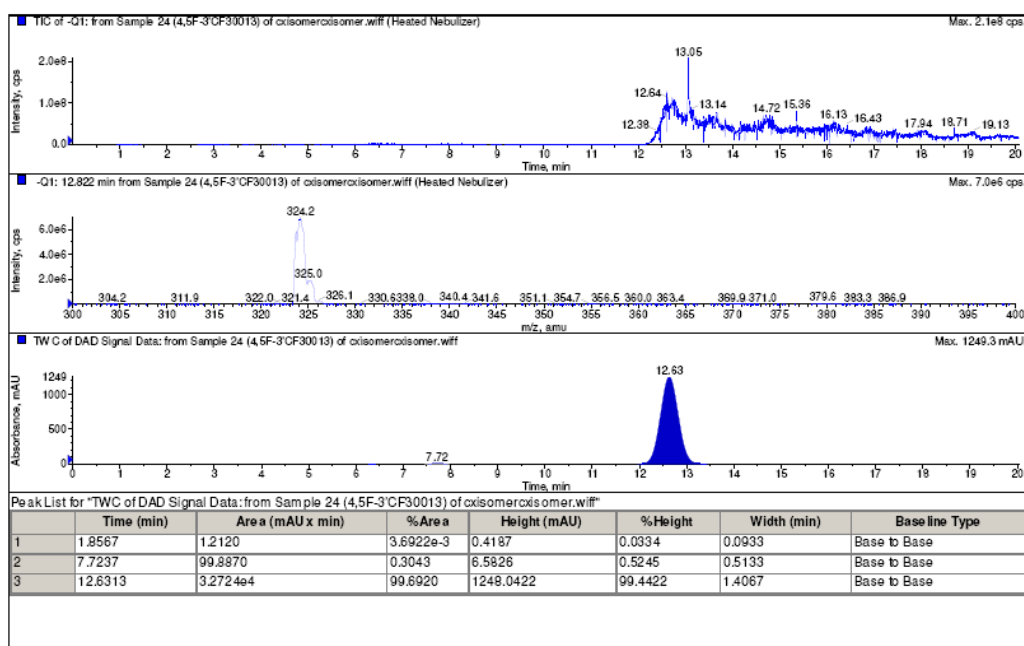


Figure 2-8 A LC-MS spectrum of **6-6** (freshly prepared in methanol) MS peak: $[M-H]^- = 324.2$

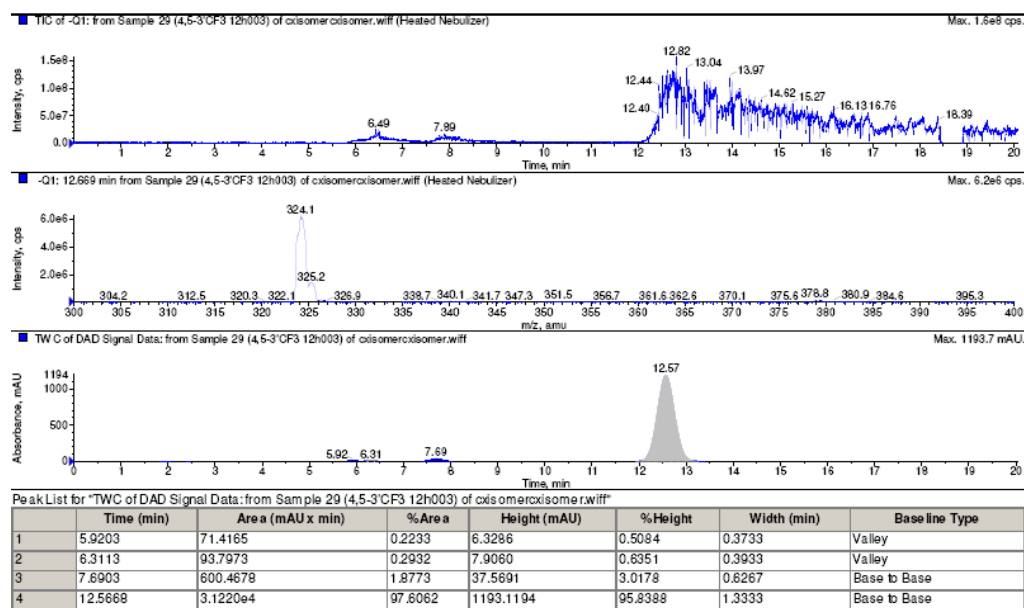


Figure 2-8 B: LC-MS spectrum of **6-6** (12h in methanol), MS peak: $[M-H]^- = 324.2$. No new peak was observed in the LC after this time. Mass of original peak was unchanged.

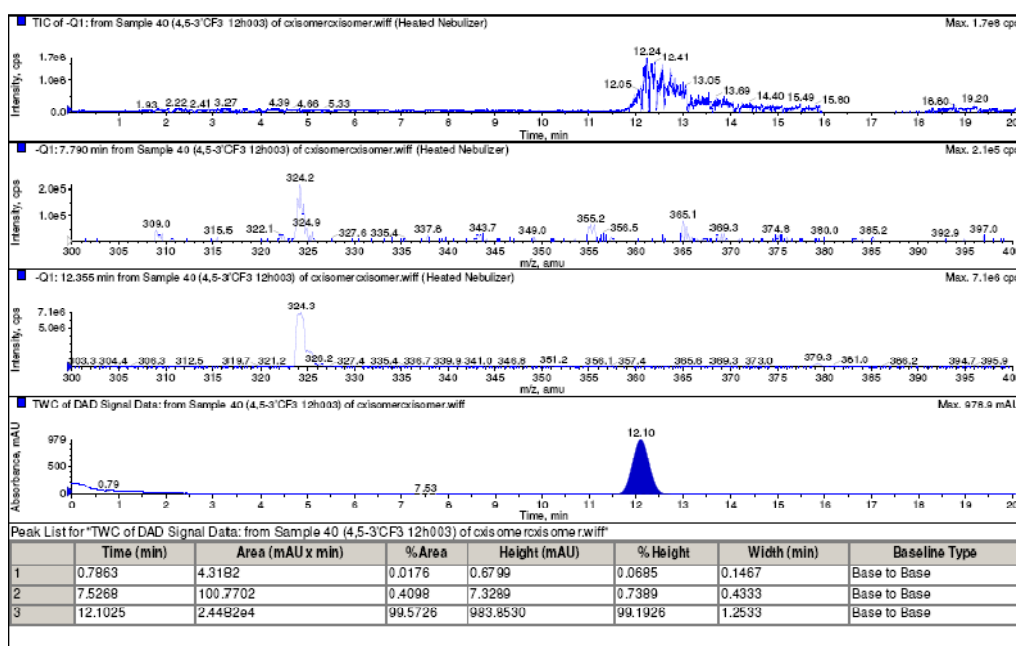


Figure 2-8 C: LC-MS spectrum of **6-6** (freshly prepared in DMSO), MS peak: $[M-H]^- = 324.2$.

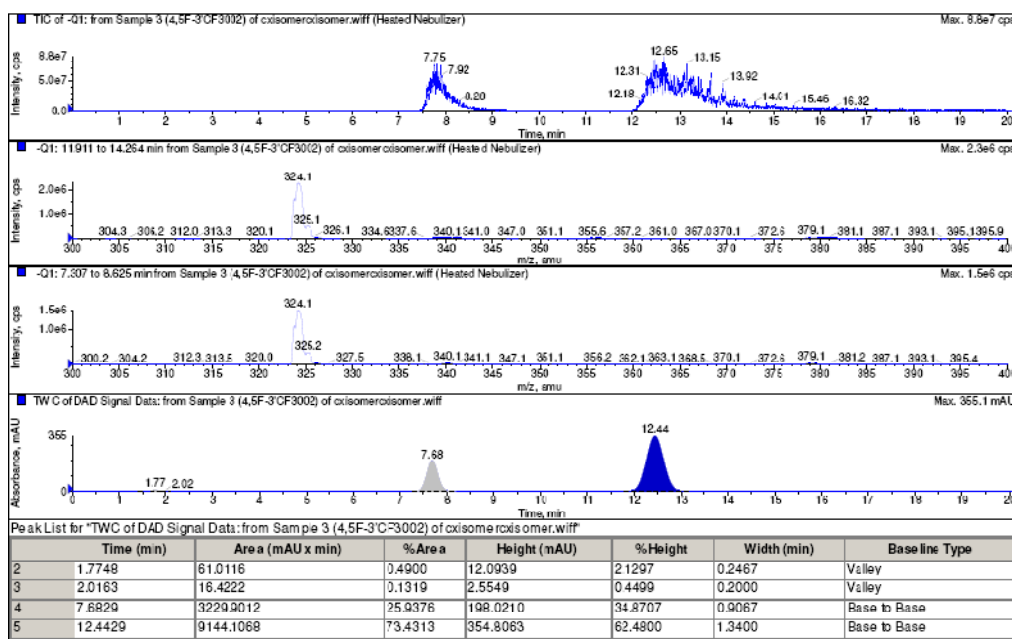


Figure 2-8 D: LC-MS spectrum of **6-6** (12h in DMSO), MS peak: $[M-H]^- = 324.2$. A new peak was observed in the LC (retention time 7.68 min). % Area of new peak (25.9) was approximately one-third that of the original peak (% area = 73.4). Mass of the new peak (324.1) was identical to the original peak.

The results as shown in Figures 2-6 to 2-8 are summarized as follows. The LCMS spectra of the freshly prepared samples in methanol or DMSO showed a single peak with the expected mass. Thus, only one isomer was present in each of the analyzed compounds. After 12 hr, the

LCMS spectra of **47**, **1-18**, and **6-6** in methanol were similar to the spectra of freshly prepared solutions, indicating the absence of isomerization. On the other hand, isomerization was evident in the aged DMSO solutions of **47**, **1-18** and **6-6**, as seen from the appearance of a new peak with the same mass as the original peak in the spectra of these compounds. The ratios of the areas of the two peaks were approximately the same (1:1) for **47** and **1-18**. In contrast, the ratio was significantly different in **6-6**, where the new peak was approximately 1/3rd that of the original peak in terms of % area under the curve. It may signify that only a small proportion of the original isomer was converted to the other isomer after 12 h.

Further investigations should focus on the effect of concentration on the isomerization process. Another area that should be explored was isomerization in the matrix used for biological testing. For example, to determine antiproliferative activity of test compounds, a stock solution in DMSO was prepared and subsequently diluted with growth media to the desired concentration. Therefore, it would be of interest to determine the rate of E/Z isomerization in DMSO-growth media or if this is not feasible, DMSO-aqueous buffer pH7.4 or DMSO-water solutions.

2.5. Summary

115 Functionalized benzylidene indolinones or related analogs were successfully synthesized and characterized. They were purified to at least 95%, with purity evaluated by reverse phase HPLC, using two different mobile phases. The EZ configuration of final compounds was

assigned, where possible, by x-ray crystallography, ¹H NMR or LCMS.

2.6. Experimental methods

2.6.1. General details

The reacting oxindoles (except 4,5-difluoroxindole) and benzaldehydes (except 3-formyl- and 3-formyl-*N*-methyl-benzenesulfonamides), isatins and 3-(trifluoromethyl)aniline were purchased from Sigma-Aldrich (St. Louis, MO, USA). Other reagents were of synthetic grade or better and were used without further purification.

Microwave reactions were carried out on the Biotage Initiator ® Microwave Synthesizer. Merck silica 60 F254 sheets and Merck silica gel (0.040-0.063 mm) were used for thin layer chromatography (TLC) and flash chromatography respectively. ¹H NMR spectra (300 MHz or 400 MHz) were determined on a Bruker DPX 300 spectrometer and Bruker ADVIII 400 spectrometer and peaks were referenced to residual d-chloroform (δ 7.260) or d₆-DMSO (δ 2.500) as internal standards. ¹³C NMR spectra (75 MHz or 100 MHz) were determined on the same instruments and reported in ppm (δ) relative to residual DMSO (δ 39.43). Coupling constants (J) were reported in hertz (Hz). Proton (¹H) NMR spectral information was tabulated in the following format: multiplicity, coupling constant, number of protons. Multiplicities were reported as follows: s=singlet, d=doublet, t=triplet, q=quartet, dd=doublet of doublets, td= doublet of triplet, m= multiplet. Mass spectrum was captured on a Sciex API 3000 Qtrap (Applied Biosystems) equipped with a chemical ionization (APCI) probe and *m/z* values for the molecular ion was reported.

Spectral characteristics of final compounds are given in Appendix I. Purity of final compounds is given in Appendix VI (page 238). Purity was determined by reverse phase HPLC using with two different mobile phase compositions for each compound. Compounds were found to have purity of \geq 95%, unless indicated otherwise.

LC-MS was captured by Agilent 1100 HPLC system couple to Sciex API 3000 Qtrap mass spectrometer with APCI probe. Chromatographic separations were carried out on a Hewlett

Packard HPLC column (200×4.6 mm, 10 μm, C18 reversed phase). The optimized mobile phase was an isocratic solution of 40 % of water and 60% of acetonitrile or methanol. The mobile phase flow rate was 1.0 mL/min. Quadrupole-based single mass spectrometry (Q1 Ms) were performed using negative APCI ionization mode. The optimized source dependent and compound dependent MS parameters for the analytes are shown in Table 2-6.

Table 2-6 Optimized source-dependent and compound-dependent MS parameters.

Curtain gas (psi)	10.0	Ion gas 2 (psi)	10.0
Nebulizer current	-1.0	Declustering potential	-60.0
Temperature (deg C)	200	Entrance potential	10.0
Ion gas 1 (psi)	20.0		

2.6.2. X-ray crystal structure of Compound 6-6

Crystals of **6-6** were grown in t-butanol and mounted on glass fibers. X-ray data were collected with a Bruker AXS SMART APEX diffractometer, using Mo Ka radiation at 223 K, with the SMART suite of Programs (SMART version 5.628 (200), Bruker AXS Inc., Madison, WI). Data was processed and corrected for Lorentz and polarization effects with SAINT (SAINT+ version 6.22a (2001) Bruker AXS Inc., Madison, WI), and for absorption effects with SADABS (SADABS, version 2.10, 2001, University of Göttingen). Structural solution and refinement were carried out with the SHELXTL, suite of programs (SHELXTL, Version 6.14 (2000), Bruker AXS Inc., Madison, WI). The structure was solved by direct methods to locate the heavy atoms, followed by difference maps for the light, non-hydrogen atoms. All non-hydrogen atoms were generally given anisotropic displacement parameters in the final model whereas H-atoms were placed at calculated positions. Crystal data and information on structure refinement of **6-6** are given in the Appendix III.

2.6.3. General procedure for the synthesis of 3-benzylidene indolin-2-ones

of Series 1-8

The method described by Zhang *et al.*¹⁶⁰ was followed. Briefly, oxindole (1 mmol) and benzaldehyde (1 mmol) were dissolved in ethanol (6 mL), a drop of piperidine (20 μ L) was added and the reaction mixture was heated in a sealed 10 mL vial on the microwave synthesizer for 15 min at 140°C. The mixture was then cooled to room temperature on an ice bath. If precipitation was observed, the precipitate was removed by filtration under reduced pressure, washed with cold ethanol and recrystallized with acetonitrile to afford the desired product. If no precipitation was observed, the mixture was then concentrated under reduced pressure and the residue was purified by flash column chromatography with hexane-ethyl acetate.

2.6.4. Synthesis of sulfamoyl and *N*-substituted sulfamoyl benzoic acids

The method of Shen *et al.*¹⁷¹ was followed with some modifications. To a saturated solution of 3-chloro sulfonyl benzoic acid (8 mmol) in ethyl acetate (4 mL) was added cold concentrated alkylamine or an aqueous solution of the ammonia or alkylamine. After stirring for 30 min at 0 °C, the mixture was neutralized with a solution of HCl in dioxane (4M) and extracted with ethyl acetate. The organic phase was concentrated under reduced pressure to give a solid which was recrystallized from acetonitrile to give desired compound.

3-Sulfamoyl-benzoic acid:

White solid, yield 64.6%, ¹HNMR (300 MHz, DMSO-d₆) δ ppm, δ 8.38 (s, 1H, Ar-H), 8.12 (d, J=8.1Hz, 1H, Ar-H), 8.03 (d, J=7.8Hz, 1H, Ar-H), 7.71 (t, J=7.5Hz, J=7.8Hz, 1H, Ar-H), 7.5 (s, 2H, SO₂NH₂)

3-*N*-Methylsulfamoyl-benzoic acid

white solid, yield 54%, ¹HNMR (300 MHz, DMSO-d₆) δ ppm, δ 8.30 (s, 1H, Ar-H), 8.17 (d, J=7.8Hz, 1H, Ar-H), 7.99 (d, J=8.1Hz, 1H, Ar-H), 7.75 (t, J=7.8Hz, 1H, Ar-H), 7.62 (d, J=4.8Hz, 1H, NH), 2.4 (s, 3H, Me).

4-*N*-Methylsulfamoyl-benzoic acid

White solid, yield 59.0%, ¹H NMR (400 MHz, DMSO-d₆) , δ ppm, δ 8.17-8.08 (m, 2H, Ar-H), 7.92-7.84 (m, 2H, Ar-H), 7.64 (dd, *J* = 9.9, 4.9 Hz, 1H, NH), 2.43 (d, *J* = 5.0 Hz, 3H, Me).

3-*N,N*-Dimethylsulfamoyl-benzoic acid

White solid, yield 90.6%, ¹H NMR (400 MHz, DMSO-d₆) δ ppm, δ 8.22 (ddd, *J* = 14.1, 1.4 Hz, 2H, Ar-H), 8.03-7.90 (m, 1H, Ar-H), 7.79 (t, *J* = 7.8 Hz, 1H, Ar-H), 2.63 (s, 6H, Me).

3-*N*-Ethylsulfamoyl-benzoic acid

White solid, yield 68.1%, ¹H NMR (400 MHz, DMSO-d₆), δ ppm δ 8.32 (t, *J* = 1.6 Hz, 1H, NH), 8.20-8.12 (m, 1H, Ar-H), 8.06-7.96 (m, 1H, Ar-H), 7.73 (dd, *J* = 15.1, 6.9 Hz, 2H, Ar-H), 2.78 (dq, *J* = 7.2, 5.8 Hz, 2H, CH₂), 0.96 (t, *J* = 7.2 Hz, 3H, Me).

3-*N-n*-Propylsulfamoyl-benzoic acid

White solid, yield 53.1%, ¹H NMR (400 MHz, DMSO-d₆), δ ppm δ 8.31 (t, *J* = 1.59 Hz, 1H, NH), 8.19-8.13 (m, 1H), 8.00 (ddd, *J* = 7.83, 1.87, 1.16 Hz, 1H, Ar-H), 7.80-7.69 (m, 2H, Ar-H), 2.69 (dd, *J* = 12.95, 6.99 Hz, 2H, N-CH₂), 1.42-1.28 (m, 2H, CH₂), 0.77 (t, *J* = 7.39 Hz, 3H, Me).

3-*N*-Isopropylsulfamoyl-benzoic acid

White solid, yield 38.5 %, ¹H NMR (400 MHz, DMSO-d₆), δ ppm δ 8.19-8.12 (m, 1H, *N*-H), 8.34 (t, *J* = 1.6 Hz, 1H, Ar-H), 8.03 (ddd, *J* = 7.8, 1.8, 1.2 Hz, 1H, Ar-H), 7.79-7.67 (m, 2H, Ar-H), 3.24 (ddd, *J* = 25.0, 12.5, 6.1 Hz, 1H, *N*-CH), 0.94 (d, *J* = 6.5 Hz, 6H, Me).

2.6.5. Synthesis of formyl benzenesulfonamides

To a solution of the sulfamoyl or *N*-substituted sulfamoyl benzoic acid (2 mmol) in anhydrous tetrahydrofuran (6 mL) was added borane-tetrahydrofuran (6 mL) complex (1M). After stirring for 15 h at 25°C the mixture was diluted with 10 mL brine and 5 mL water. The organic phase was separated, dried with anhydrous Na₂SO₄ and concentrated under reduced pressure to give the desired alcohol which was used for the next step without further purification.

The crude alcohol (2 mmol) was suspended in anhydrous tetrahydrofuran (12 mL) and stirred. Activated 4A molecular sieves (4 g) and 5 mmol of pyridinium dichromate was added and the mixture was stirred for 3 h at 25°C. Another portion of pyridinium dichromate (5 mmol) was added and the mixture was stirred for 3 h. The mixture was filtered through silica gel and the filtrate was concentrated under reduced pressure to give the product which was purified by column chromatography with hexane-ethyl acetate (1:1) as eluting solvents.

3-Sulfamoyl-benzaldehyde:

White solid, yield (after 2 steps from 3-Sulfamoyl-benzoic acid) 43.4%; ¹HNMR (300 MHz, in DMSO-d₆) δ ppm δ 10.1 (s, 1H, CHO), 8.32 (s, 1H, Ar-H), 8.13 (t, J=6.9Hz, J=6.0Hz, 2H, Ar-H), 7.82 (t, J=7.8Hz, 1H, Ar-H), 7.55 (s, 2H, NH₂)

3-Formyl-N-methyl-benzenesulfonamide

White solid, yield (after 2 steps from 3-N-Methylsulfamoyl-benzoic acid) 42.5%, ¹HNMR (300 MHz, in DMSO-d₆) δ ppm δ 10.10 (s, 1H, CHO), 8.26 (s, 1H, Ar-H), 8.18 (d, J = 7.6 Hz, 1H, Ar-H), 8.07 (d, J = 7.7 Hz, 1H, Ar-H), 7.85 (t, J = 7.7 Hz, 1H, Ar-H), 7.65 (s, 1H, N-H), 2.44 (s, 3H, Me)

4-Formyl-N-methyl-benzenesulfonamide:

White solid, yield (after 2 steps from 4-N-Methylsulfamoyl-benzoic acid) 38.9%, ¹HNMR (300 MHz, in DMSO-d₆) δ ppm δ 10.09 (s, 1H, CHO), 8.18-8.06 (m, 2H, Ar-H), 7.97 (d, J = 8.3 Hz, 2H, Ar-H), 7.68 (s, 1H, NH), 2.44 (s, 3H, Me).

3-Formyl-N,N-dimethyl-benzenesulfonamide, N-ethyl-3-formyl-benzenesulfonamide, 3-formyl-N-propyl-benzenesulfonamide and 3-formyl-N-isopropyl-benzene-sulfonamide were oils and were used without further purification for the next step of reaction.

2.6.6. Synthesis of 5,6-difluoro-oxindole

The method of Cervena *et al.*¹⁷² was followed. To a stirred solution of 3,4-difluoroaniline (10 mmol) in toluene (5 mL) and pyridine (10 mmol) maintained at 5-10°C was added chloroacetyl chloride (10 mmol) in toluene (5 mL) dropwise. The mixture was allowed to stand overnight at room temperature. The organic layer was then separated and the residue

was mixed with water (60 mL). The separated solid product was recrystallized from toluene to give *N*-(3,4-difluorophenyl) chloroacetamide as a light purple solid, yield 84.3%; ¹HNMR (300 MHz, CDCl₃) δ ppm δ 8.24 (s, 1H, NH), 7.63 (td, J=8.1 Hz, 1H, Ar-H), 7.16-7.12 (m, 2H, Ar-H), 4.19 (s, 2H, COCH₂Cl).

A mixture of *N*-(3,4-difluorophenyl) chloroacetamide (14 mmol) and aluminum chloride (54 mmol) was stirred and heated to 200-210 °C in a silicon oil bath for 4.5 h. On cooling, 40 mL of ice cold hydrochloric acid was added to the reaction mixture. The solid residue was removed by vacuum filtration and purified by column chromatography with hexane-ethyl acetate (1:1) as eluting solvent to give 5,6-difluoro-oxindole as a beige solid, yield 40.7%; ¹HNMR (300 MHz, in DMSO-d₆) δ ppm δ 10.46 (s, 1H, NH), 7.33 (t, J=8.7 Hz, 1H, Ar-H), 6.82 (q, J=6.9 Hz, 1H, Ar-H), 3.47 (s, 2H, ArCH₂CO).

2.6.7. Synthesis of 1-methyl-oxindole and 6-chloro-1-methyl-oxindole

The method of Liégault *et al.*¹⁷³ was followed. A suspension of sodium hydride (2mmol, 60 % dispersion in mineral oil) in toluene (4 mL) was heated to 100 °C in an atmosphere of argon. A solution of the oxindole (2 mmol) in toluene was added to the stirred mixture and stirring was continued for 1 h at 100°C. Neat dimethylsulphate (2 mmol) was added dropwise and the mixture was stirred for 2 h at 100°C. On cooling, the mixture was thoroughly washed with distilled water and the aqueous phase was extracted with ethyl acetate. The organic phase was dried with anhydrous Na₂SO₄, concentrated under reduced pressure and purified by column chromatography with hexane-ethyl acetate (3:1) as eluting solvent.

1-Methyl-oxindole:

White solid, yield 45.2%, ¹HNMR (300 MHz, in DMSO-d₆) δ ppm δ 7.27 (t, J=7.8Hz, J=7.5Hz, 2H, Ar-H), 6.98 (q, J=15.8, 2H, Ar-H), 3.53 (s, 2H, ArCH₂CO), 3.11 (s, 3H, *N*-Me).

6-Chloro-1-methyl-oxindole:

Light pink solid, yield 76.7%, ¹HNMR (300 MHz, in DMSO-d₆) δ ppm δ 7.24 (d, J=7.8Hz, 1H, Ar-H), 7.10 (s, 1H, Ar-H), 7.05 (d, J=7.8Hz, 1H, Ar-H), 3.54 (s, 2H, ArCH₂CO), 3.11 (s, 3H, *N*-Me)

2.6.8. General procedure for the synthesis of 3-phenylimino-2-indolones

(8-2, 8-4, 8-6, 8-7)

The method of Konkel *et al.*¹⁵² was followed with some modification. Briefly, a mixture of isatin/substituted isatin (3 mmol) and 3-(trifluoromethyl)aniline (15 mmol) was heated in a sealed 10 mL vial on the microwave synthesizer for 15 minutes at 140 °C. On cooling, the product was filtered and washed with cold methanol to give the desired product as an orange or red solid.

Chapter 3: Investigations into the growth inhibitory activities of Series 1-8 compounds on malignant liver cancer cell lines

3.1. Introduction

This chapter describes the growth inhibitory activities of the Series 1-8 compounds on a panel of malignant liver cancer cell lines. Compounds were evaluated for their half maximal growth inhibitory concentrations (IC₅₀) on a colorimetric tetrazolium (MTT) assay. Investigations were first carried out on HuH7 cells and compounds that had low micromolar to submicromolar IC₅₀ values were shortlisted for further screening on two other malignant liver cells (HepG2, Hep3B) and a non-malignant cell line (diploid primary human fibroblasts, IMR90).¹⁷⁴ Selected potent compounds were investigated for the induction of apoptosis in HuH7 cells.

3.2. Materials and Methods

3.2.1. Reagents

3-(4,5)-Dimethylthiazolium(-z-y1)-3,5-di-phenyltetrazoliumromide (MTT) was purchased from Duchefa Biochemie (Denmark). Penicillin G and streptomycin were from Sigma–Aldrich. Cell culture media were from Sigma–Aldrich (Singapore). Test compounds were prepared in DMSO (ACS grade, purchased from NUS Laboratory Supply) at 10 mM as stock solutions and stored at room temperature (25°C). Annexin V-FITC apoptosis detection kit was purchased from Sigma–Aldrich (Singapore). The following were purchased from Santa Cruz Biotechnology (CA, USA): rabbit monoclonal antibodies to PARP and caspase 3; goat anti-rabbit-horse radish peroxidase (HRP) conjugate and goat anti-mouse HRP. Rabbit monoclonal antibodies to cleaved caspase 3 were purchased from Cell Signaling (MA, USA). Fetal bovine serum (FBS) and mouse monoclonal antibodies to β-actin were purchased from Invitrogen Life Technologies (CA, USA).

3.2.2. Cell Lines and cell culture.

Hep3B was a gift from Dr Ho Han Kiat, Department of Pharmacy, NUS. HuH7 was purchased from Japanese Collection of Research Bioresources Cell Bank (Japan). HepG2 and IMR90 were purchased from American Type Culture Collection (VA, USA).

HuH7, HepG2 and Hep3B cells were cultured in Dulbecco's Modified Eagle Medium (DMEM, high glucose, with HEPES) with 10% v/v fetal bovine serum (FBS), 100 mg/L penicillin G and 100 mg/L streptomycin. IMR 90 cells were cultured in EMEM (Eagle's Minimum Essential Medium), with 10% v/v FBS and 100 mg/L penicillin G. The cells were sub-cultured when the following densities in a T75 mL flask were reached: HuH7 and HepG2: $60\text{-}80 \times 10^5$ cells; Hep3B: $35\text{-}40 \times 10^5$ cells; IMR 90: 10×10^5 cells. Cells were maintained within 2-10 passages for experiments.

3.2.3. MTT assay for determination of cell growth inhibition

The antiproliferative activities of the compounds were determined by the MTT assay. The assay monitored the conversion of a tetrazolium dye MTT to its insoluble purple colored formazan product. This conversion was catalyzed by NAD(P)H dependent cellular oxidoreductases found in viable /proliferating cells. Thus, loss of cell viability or non-proliferating cells would result in less formazan, the formation of which was monitored by visible spectroscopy (570 nm)

An aliquot of cells in media (200 μL , 3×10^4 cells/mL of HuH7, 3.75×10^4 cells/mL of HepG2, 5.5×10^4 cells/mL of Hep3B, or 2×10^4 cells/mL of IMR 90) were added to each well in a 96-well microtitre plate. After 24 h incubation at 37° C, 5% CO₂, the cells formed an adherent layer on the floor of the well. The media was removed from each well and replaced by fresh media (200 μL) containing a known concentration of test compound. The final concentration of DMSO in each well was maintained at 0.5% v/v or 1% v/v, depending on compound solubility. The test compounds were incubated with the cells for another 72 h at 37° C, 5% CO₂. After this time, the media was removed and replaced with FBS free media

(200 μ L) and MTT (50 μ L of 2 mg/mL solution in phosphate buffer saline, pH 7.4). The phosphate buffer saline comprised 10 mM phosphate buffer and 137 mM NaCl. After incubation (3 h) at 37° C, 5% CO₂, the supernatant was removed from each well and a solution of 200 μ L DMSO and 25 μ L Sorenson buffer (0.1 M glycine, 0.1 M NaCl, adjusted to pH 10.5 with 0.1 M NaOH) was added to dissolve the formazan crystals. Vehicle controls were cells grown in 0.5 or 1% v/v DMSO/media for 72 h, 37 ° C, 5% CO₂ while blank controls were wells that contained 200 μ L DMSO and 25 μ L Sorenson buffer. Absorbances were measured at 570 nm on a microplate reader (Tecan Infinite 200). The % viability of cells at a given concentration of test compound was determined from the expression:

$$\text{Percentage Cell Viability} = \frac{[\text{Absorbance_Compound}] - [\text{Absorbance_Blank}]}{[\text{Absorbance_Vehicle Control}] - [\text{Absorbance_Blank}]} \times 100$$

where Absorbance_Compound = absorbance of wells containing cells and test compound, Absorbance_Vehicle Control = absorbance of vehicle control (cells + DMSO/media) and Absorbance_Blank = Absorbance of blank control (DMSO/media).

Each concentration of test compound was evaluated at least 3 times on separate occasions, using two different stock solutions. The IC₅₀ (concentration required to reduce cell viability to 50% of that observed in control/untreated cells) was determined from the sigmoidal curve obtained by plotting percentage viability versus logarithmic concentration of test compound using GraphPad Prism 5 (San Diego, USA).

3.2.4. Detection of Apoptosis by flow cytometry

The Annexin V-FITC Apoptosis Detection Kit (Sigma Aldrich) was used following the manufacturer's instructions. Briefly, HuH7 cells were seeded at a density of 3.0 \times 10⁵ cells/mL in each well of a 6-well plate and treated with a known concentration of test compound for 48 h, 37°C, 5% CO₂. Cells were trypsinized, centrifuged at 500 g for 5 min, the cell pellet rinsed with chilled PBS and resuspended in 1 \times binding buffer at a density of 10⁶ cells per mL. Annexin V-FITC conjugate protein (5 μ L) and propidium iodide (PI) solution (1 μ L) were

added to an aliquot (500 μ L) of cell suspension and incubated on ice for 10 min. Cells were then immediately analyzed by cell cytometry. Flow cytometry was carried out using fluorescence activated cell sorting on BD LSR Fortessa Flow Cytometry Analyser (Beckton Dickinson, USA). Unstained treated cells, treated cells stained with AnnexinV-FITC and treated cells stained with PI were used for calibration and compensation. 10000 cells were read for each sample determination. At least three repetitions were made for each test concentration.

3.2.5. Preparation of HuH7 cell lysates

HuH7 cells were incubated with test compounds for 48 h, 37°C, 5% CO₂. After this time, the adherent cells were gently scraped from the walls of the petri dish with a cell scraper. The cell suspension was centrifuged at 500 g for 5min, supernatant was discarded and the cell pellet was washed twice with 1×PBS. The washed cells (10⁶) were dissolved in 70 μ L lysis buffer (20 mM Tris pH 7.4, 250 mM NaCl, 2 mM EDTA pH 8.0, 0.1% Triton X-100, 0.01 mg/ml aprotinin, 0.005 mg/ml leupeptin, 0.4 mM PMSF, and 4 mM NaVO₄) and incubated at 0°C for at least 20 min. After the incubation, the lysates were spun at 13 300 g for 10 min to remove the cell debris. 3 μ L of the supernatant was retained for protein determination (Section 3.2.6) while the remaining solution was served as solvent to dilute the 4×SDS solution (0.2 M Tris pH 6.8, 0.28 M SDS, 40 % v/v glycerol, 0.59 M β -mercaptoethanol, 50 mM EDTA, 1.1 mM bromophenol blue) to give 1×SDS solution which was then deactivated at 99°C, 5 min and subsequently stored for no more than 1 week at -80°C.

3.2.6. Protein quantification

Protein quantification was carried out using the Bradford Protein Assay Kit (Bio-Rad Laboratories Inc, CA, USA). The cell lysate was diluted 200-fold with Milli-Q water and 160 μ L of the diluted solution was mixed with 40 μ L of Bradford dye in a 96-well transparent plate. The standard curve was prepared in a similar way using bovine serum albumin (BSA) solution at the concentration range from 25 μ g/mL to 0 μ g/mL. The solutions were incubated at 25°C, 10 min and their absorbances were read at 595 nm on a Tecan Plate Reader. Protein

concentration of lysate was determined from the BSA standard curve. At least three absorbance readings were obtained for each concentration of BSA or cell lysate.

3.2.7. Sodium dodecyl sulfate - polyacrylamide gel electrophoresis (SDS-PAGE)

Cell lysates were separated on the SDS-PAGE Bio-Rad Mini-Protean II system (Bio-Rad Laboratories Inc, CA, USA). Briefly, SDS-polyacrylamide gels were cast using a Mini-Protean gel caster. Resolving gels (10% or 15%) were prepared and allowed to set for 30 min. Stacking gels were prepared and allowed to set for another 30 min before being assembled in the electrophoresis chamber. The inner and outer chambers of the unit were filled with 1× SDS-PAGE running buffer (25mM Tris-base, 192 mM glycine, 0.1% SDS w/v). Protein 1×SDS solutions were then loaded into the wells and electrophoresis was carried out at 25 °C at a constant current of 10 mA through each stacking gel and increased to 20 mA through each resolving gel. After electrophoresis, the gels were subjected to Western blotting (Section 3.2.8).

3.2.8. Western blotting

After electrophoresis, separated protein samples were transferred to nitrocellulose membranes using the wet transelectroblotting system (Bio-Rad Laboratories Inc, CA, USA) at a constant voltage of 90V, 2 h, 4°C using ice-cold 1× transfer buffer (48 mM Tris-base, 37mM Glycine, 10% MeOH v/v). Membranes were blocked with blocking buffer for 30 min at 25 °C and then incubated with primary antibodies at appropriate dilutions in 2.5% BSA in TBST (50 mM Tris, 150 mM NaCl, 0.1% Tween 20) solution overnight at 4°C. Membranes were then washed thrice with TBST (10 min per wash), incubated for 1 hr with secondary antibodies in TBST at 25 °C, and followed by washing in TBST (thrice, 10 min per wash). The immunoreactive bands were detected by the ECL reagent (GE Healthcare, Little Chalfont, UK) using Bio-Rad Universal Hood II Gel Doc. If needed, the membranes were stripped with

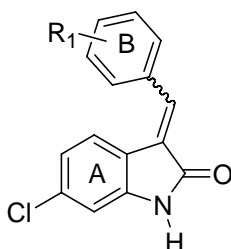
stripping buffer, blocked with blocking buffer for 30 min at 25 °C, and re-probed with other antibodies.

3.3. Results

3.3.1. Growth inhibitory activities of Series 1-8 on HuH7 cells

The growth inhibitory activities of Series 1-8 compounds were first evaluated for their IC₅₀ on HuH7 cells. Based on the working hypothesis that the synthesized compounds would have RTK inhibitory activity, like **47** (**1-10** in Table 3-1), a kinase inhibitor sorafenib was included as a positive control. Its IC₅₀ was found to be 5.4 ± 0.5 μM on HuH7. The growth inhibitory activities of Series 1-8 were discussed in the following paragraphs. Compounds that did not reduce cell viability by more than 50% at 30 μM and those that had no activity at the highest soluble concentration were not explored further. Growth inhibitory activities of Series 1 compounds

Table 3-1: IC₅₀ of Series 1 compounds on HuH7 cells. Mean ± SD for n= 3 determinations.



No	R ₁	IC ₅₀ (μM)	No	R ₁	IC ₅₀ (μM)
1-1	H	17.5 ± 3.5	1-14	3'OCF ₃	5.1 ± 0.7
1-2	2'F	N.A. ^a	1-15	4'OCF ₃	10.1 ± 1.7
1-3	3'F	10.0 ± 0.9	1-16	3'SO ₂ Me	10.8 ± 3.7
1-4	4'F	12.9 ± 1.0	1-17	3'SO ₂ NH ₂	3.1 ± 0.2
1-5	3'Me	11.0 ± 0.3	1-18	3'SO ₂ NHMe	0.97 ± 0.09
1-6	2'OMe	>30	1-19	3'CN	7.4 ± 0.3
1-7	3'OMe	12.2 ± 0.6	1-20	3'SO ₂ NMe ₂	4.9 ± 0.4
1-8	4'OMe	>30	1-21	4'SO ₂ NHMe	15.3 ± 0.6
1-9	2'CF ₃	N.A. ^a	1-22	3'SO ₂ NHEt	0.70 ± 0.03
1-10	3'CF ₃	0.46 ± 0.16	1-23	3'SO ₂ NHPr	0.28±0.09
1-11	4'CF ₃	11.0 ± 1.8	1-24	3'SO ₂ NHiPr	1.9 ± 0.3
1-12	3'4'F	16.7 ± 3.4	1-25	3'NHSO ₂ Me	7.4 ± 0.2
1-13	2'OCF ₃	N.A. ^a			

^aNo activity at the highest soluble test concentration

Series 1 compounds were designed to investigate the structural importance of the 3'-CF₃ of **47** (**1-10** in Series 1). IC₅₀ values of the 25 members in this series, the largest among the investigated series, ranged from 0.23 μM to >30 μM, an 80 fold (or more) variation in inhibitory activity. The striking variation in IC₅₀ arising from a single modification underscored a special role for the substitution on phenyl ring B on growth inhibitory activity. Key SAR trends in Series 1 are as follows:

(i) There was a clear preference for substitution at the 3' position of ring B, irrespective of the stereoelectronic or lipophilic character of the substituent. Thus, the growth inhibitory activities of 3'-F (mildly lipophilic, electron withdrawing), 3'-OMe (polar, electron withdrawing), 3'-CF₃ (lipophilic, electron withdrawing), 3'-SO₂NHCH₃ (polar, electron withdrawing) exceeded that of 2' and/or 4' regioisomers. As the preference for the 3' position was noted early, the subsequent series were populated with more 3'-substituted analogs.

(ii) Among the 3'-substituted analogs, activity decreased in the following order:

3'-CF₃ (**47**, most active) > 3'-SO₂NH₂ > 3'-OCF₃ > 3'-CN, 3'-NHSO₂CH₃ > 3'F > 3'-SO₂CH₃ > 3-Me > 3-OMe (**1-7**, least active)

This sequence did not include the functionalized aminosulfonyl derivatives (**1-18**, **1-20** to **1-24**) which are discussed separately in the following paragraph. Table 3-2 lists the IC₅₀ and Hammett σ_m values of these substituents.¹⁶⁸

Table 3-2: σ_m values and IC₅₀ values of 3'-substituents on phenyl ring B of Series1

Substituent (Cpd No)	σ _m	IC ₅₀ μM	Substituent (Cpd No)	σ _m	IC ₅₀ μM	Substituent (Cpd No)	σ _m	IC ₅₀ μM
CF ₃ (47 , 1-10)	0.43	0.46	CN (1-19)	0.56	7.3	SO ₂ Me (1-16)	0.52	10.8
SO ₂ NH ₂ (1-17)	0.46	3.1	NHSO ₂ Me (1-25)	0.20	7.4	CH ₃ (1-5)	-0.07	11.1
OCF ₃ (1-14)	0.38	5.1	F (1-3)	0.34	10.0	O Me (1-7)	0.12	12.2

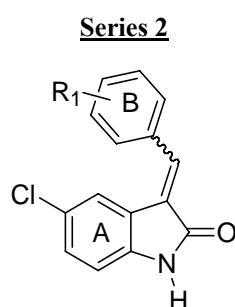
Although the top ranking compounds (**47**, **1-17**, **1-14**) had electron withdrawing groups on ring B, there was no apparent correlation between the magnitude of electron withdrawal and IC₅₀. Nitrile CN (σ_m 0.56) and methylsulfonyl SO₂Me (σ_m 0.52) were strongly electron

withdrawing but were not highly ranked in terms of IC₅₀. The least active compounds were Me (**1-5**) and OMe (**1-7**) analogs. Methyl Me is weakly electron donating (σ_m -0.07) but OMe (σ_m 0.12) is electron withdrawing because of its meta location. Taken together, the electronic nature of the ring B substituent is deemed to have a minor influence on activity.

(iii) The most potent compound in Series 1 was the 3'-*N*-n-propylaminosulfonyl analog **1-23** (IC₅₀ 0.28 μ M). Specific structural requirements for the aminosulfonyl side chain were evident: First, the aminosulfonyl moiety must be *N*-substituted. The aminosulfonyl SO₂NH₂ analog **1-17** (IC₅₀ 3.1 μ M) was only weakly active. Second, mono *N*-substitution was preferred to di-*N,N*-substitution. The *N,N*-dimethylaminosulfonyl analog (**1-20**, IC₅₀ 4.9 μ M) was 5x less potent than the mono substituted counterpart (**1-18**, IC₅₀ 0.97 μ M). Third, homologous extension of the mono *N*-substituent (methyl \rightarrow ethyl \rightarrow propyl) had a positive impact on activity, but branching of the alkyl side chain (**1-24**, IC₅₀ 1.9 μ M) was not helpful. Lastly, "reversing" the *N*-methylaminosulfonyl side chain (**1-18**, IC₅₀ 0.97 μ M) to methylsulfonylamino (**1-25**, IC₅₀ 7.4 μ M) caused a significant loss in potency, highlighting the singular importance of retaining the *N*-monosubstituted aminosulfonyl motif.

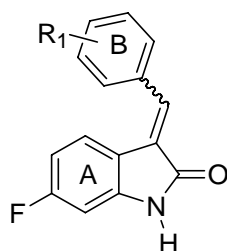
3.3.1.1. Growth inhibitory activities of Series 2, 3 and 4 compounds

Table 3-3: IC₅₀ of Series 2,3 and 4 compounds on HuH7 cells. Mean \pm SD for n= 3 determinations.



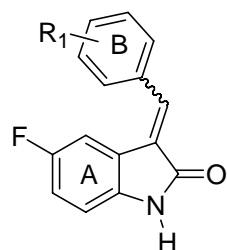
No	R ₁	IC 50 (μ M) \pm S.D	No	R ₁	IC 50 (μ M)
2-1	H	21.3 \pm 2.2	2-9	3'4'F	11.4 \pm 1.5
2-2	2'F	>30	2-10	3'OCF ₃	3.8 \pm 0.3
2-3	3'F	15.1 \pm 2.9	2-11	3'SO ₂ Me	6.5 \pm 0.5
2-4	4'F	12.7 \pm 2.8	2-12	3'SO ₂ NH ₂	9.7 \pm 1.6
2-5	3'OMe	>30	2-13	3'CN	10.4 \pm 2.0
2-6	2'CF ₃	>30	2-14	3'SO ₂ NHMe	3.1 \pm 0.1
2-7	3'CF ₃	0.81 \pm 0.11	2-15	3'SO ₂ NHPr	7.4 \pm 0.3
2-8	4'CF ₃	7.9 \pm 1.5	2-16	3'NH ₂ SO ₂ Me	11.4 \pm 0.8

Series 3



No	R ₁	IC 50 (μM)	No	R ₁	IC 50 (μM)
3-1	H	N.A. ^a	3-8	3'OCF ₃	7.5 ± 0.2
3-2	2'F	N.A. ^a	3-9	3'SO ₂ Me	12.7 ± 1.5
3-3	3'F	N.A. ^a	3-10	3'SO ₂ NHMe	0.48 ± 0.01
3-4	4'F	N.A. ^a	3-11	3'SO ₂ NHEt	0.39 ± 0.07
3-5	2'CF ₃	>30	3-12	3'SO ₂ NHPr	0.093±0.029
3-6	3'CF ₃	1.4 ± 0.1	3-13	3'SO ₂ NHiPr	2.3 ± 0.1
3-7	4'CF ₃	8.4 ± 0.3	3-14	3'NHSO ₂ Me	15.3 ± 1.1

Series 4



No	R ₁	IC 50 (μM)	No	R ₁	IC 50 (μM)
4-1	H	21.4 ± 1.7	4-10	3'CF ₃	4.0 ± 0.5
4-2	2'F	>30	4-11	4'CF ₃	9.3 ± 1.0
4-3	3'F	13.3 ± 2.3	4-12	3'4'F	15.3 ± 0.2
4-4	4'F	13.2 ± 0.4	4-13	3'OCF ₃	5.2 ± 0.6
4-5	2'Me	>30	4-14	3'SO ₂ Me	5.2 ± 0.6
4-6	3'Me	20.8 ± 0.4	4-15	3'CN	7.4 ± 1.1
4-7	4'Me	16.4 ± 4.2	4-16	3'SO ₂ NHMe	1.2 ± 0.0
4-8	3'OMe	11.7 ± 1.1	4-17	3'SO ₂ NHPr	1.43 ± 0.27
4-9	2'CF ₃	>30	4-18	3'NHSO ₂ Me	18.6 ± 1.8

^aNo activity at the highest soluble test concentration

Series 2, 3 and 4 explored the replacement of 6-Cl in Series 1 with 6-F (Series 3) and moving the halogens (Cl, F) from position 6 to position 5 (Series 2,4). IC₅₀ values are given in Table 3-3 and for ease of comparison, IC₅₀ values of substituents common to the Series are collated in Table 3-4.

Table 3-4: IC₅₀ values of ring B 3'-substituents (R₁) in Series 1-4

R ₁	IC ₅₀ on HUH7 cells (μM)			
	Series 1 (6-Cl)	Series 2 (5-Cl)	Series 3 (6-F)	Series 4 (5-F)
H	17.5	21.3	NA ^a	21.4
3'-F	10.0	15.1	NA ^a	13.3
3'-CF ₃	0.46	0.81	1.4	4.1
3'-OCF ₃	5.1	3.8	7.5	5.2
3'-SO ₂ Me	10.8	6.5	12.7	5.2

3'-SO ₂ NH ₂	3.1	9.7	Not done ^b	Not done ^b
3'-SO ₂ NHMe	0.97	3.1	0.48	1.2
3'-SO ₂ NHPr	0.28	7.4	0.093	1.43

^a No activity at the highest soluble test concentration.

^b Not done because compound was not synthesized.

As seen from Table 3-4, changes in activity brought about by these modifications were largely dependent on the nature of the 3' substituent. Nonetheless, some SAR trends could be gathered. First, with the exception of trifluoromethoxy (3'-OCF₃) and methylsulfonyl (3'-SO₂Me), substitution at position 6 on ring A (6-Cl, 6-F) was preferred to position 5 (5-Cl, 5-F) for the same ring B substitution. Second, the 6-F analog was superior to its 6-Cl counterpart in compounds that had the *N*-substituted aminosulfonyl group on ring B, namely **3-10** (SO₂NHMe) and **3-12** (SO₂NHPr), but not in compounds that had CF₃, OCF₃ or SO₂Me. Thus, 6-F on ring A and an *N* substituted aminosulfonyl group on ring B was associated with good activity. In contrast, 6-Cl on ring A may be combined with either 3'CF₃ or 3' *N*-substituted aminosulfonyl with retention of good activity.

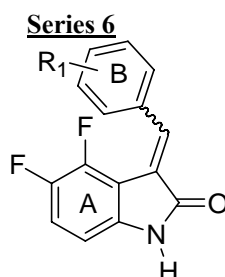
Next, the results were analyzed to determine if the SAR trends observed in Series 1 also prevailed in Series 2-4. First, based on the few relevant comparisons available (F, CF₃, Me), no consistent preference for the 3' regioisomer was noted. Intriguingly, it was only observed for CF₃ but not F or methyl in Series 2-4. Second, the activity advantage associated with the *N*-methyl to *N*-propyl conversion was only evident in Series 3, but not in Series 2 and 4. Interestingly, the indolinone rings in Series 2 and 4 were 5-substituted, whereas those in Series 1 and 3 were 6-substituted. Thus, there was limited cross over in SAR established in Series 1 to Series 2-4 in spite of their structural similarity.

3.3.1.2. Growth inhibitory activities of Series 6 and 7 compounds

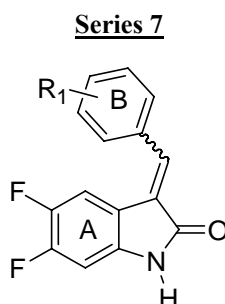
As discussed in Section 2.4, Series 6 compounds were assigned as predominant *Z* isomers (except **6-5**, **6-9**) whereas Series 7 compounds were assigned as predominant *E* isomers. However, racemization during biological testing would result in *E/Z* mixtures of Series 6 and 7 compounds. Based on the time dependent course of racemization of **6-6** (Section 2.4), it is assumed that Series 6 compounds would have a greater proportion of *Z* isomers whereas

Series 7 would have near equal proportions of *E* and *Z* forms. IC₅₀ of Series 6 and 7 compounds are given in Table 3-5.

Table 3-5: IC₅₀ of Series 6 and 7 compounds on HuH7 cells. Mean ± SD for n= 3 determinations.



No	R ₁	IC ₅₀ (μM)	No	R ₁	IC ₅₀ (μM)
6-1	H	>30	6-7	4'CF ₃	>30
6-2	2'F	16.9 ± 1.7	6-8	3'OCF ₃	2.9 ± 0.3
6-3	3'F	15.9 ± 1.1	6-9	3'SO ₂ Me	>30
6-4	4'F	14.0 ± 0.7	6-10	3'SO ₂ NHMe	16 ± 3
6-5	2'CF ₃	>30	6-11	3'SO ₂ NHPr	13.4 ± 2.2
6-6	3'CF ₃	0.54 ± 0.07	6-12	3'NHSO ₂ Me	2.4 ± 0.4



No	R ₁	IC ₅₀ (μM)	No	R ₁	IC ₅₀ (μM)
7-1	H	>30	7-7	4'CF ₃	10.6 ± 0.7
7-2	2'F	>30	7-8	3'OCF ₃	5.6 ± 0.3
7-3	3'F	19 ± 3	7-9	3'SO ₂ Me	13.9 ± 2.0
7-4	4'F	N.A. ^a	7-10	3'SO ₂ NHMe	2.8 ± 0.2
7-5	2'CF ₃	>30	7-11	3'SO ₂ NHPr	3.6 ± 0.9
7-6	3'CF ₃	0.84 ± 0.17	7-12	3'NHSO ₂ Me	15 ± 2

^a No activity at the highest soluble test concentration.

It can be seen from Table 3-5 that there was no consistent regioisomeric preference for the 3' position. Only two ring B substituents (CF₃, F) were available for comparison and the results showed that 3'CF₃ but not 3'F was preferred in both Series. Series 6 and 7 were also examined to determine if the *N*-methyl to *N*-propyl extension in the substituted aminosulfonyl side chain resulted in improved activity. This was not observed in either series.

Table 3-6 compares the IC₅₀ values of 3'-substituted Series 6 and 7 compounds with that of their mono-F analogs in Series 3 and 4. The activity advantage of difluoro substitution was observed only for 3'CF₃ and not for the other groups on ring B. 3' CF₃ was in fact the preferred ring B substituent in the di-fluorinated Series 6 and 7, whereas the 3' *N*-substituted aminosulfonyl side chains were preferred in the mono-fluorinated Series 3 and 4.

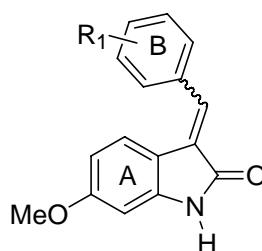
Table 3-6: IC₅₀ values of ring B 3'-substituents (R₁) in Series 1-4

R ₁	IC ₅₀ on HUH7 cells (μM)			
	Series 6 (4,5-F)	Series 7(5,6-F)	Series 3(6-F)	Series 4 (5-F)
H	>30	>30	NA ^a	21
3'-F	16	19	NA ^a	13
3'-CF ₃	0.54	0.84	1.4	4.1
3'-OCF ₃	2.9	5.6	7.5	5.2
3'-SO ₂ Me	>30	14	13	5.2
3'-SO ₂ NHMe	16	2.8	0.48	1.2
3'-SO ₂ NHPr	13.4	3.6	0.093	1.4

3.3.1.3. Growth inhibitory activities of Series 5 compounds

The Series 5 compounds which were substituted with 6-MeO on ring A had exceptionally potent activity. Of the 10 compounds in this series, half of them had submicromolar IC₅₀ on HuH7. The most potent compound was the *N*-methylaminosulfonyl analog **5-9** (IC₅₀ 34 nM). The regiosomeric preference for position 3' over position 4' was observed for CF₃ and F, and the improvement in activity on going from *N*-methyl to *N*-propyl was also apparent.

Table 3-7: IC₅₀ values of Series 5 compounds. Mean ± SD for n= 3 determinations.



No	R ₁	IC ₅₀ (μM)	No	R ₁	IC ₅₀ (μM)
5-1	H	0.77 ± 0.07	5-6	3'CF ₃	1.2 ± 0.1
5-2	2'F	0.49 ± 0.05	5-7	4'CF ₃	>30
5-3	3'F	0.71 ± 0.07	5-8	3'SO ₂ NHMe	0.17 ± 0.02
5-4	4'F	5.4 ± 0.1	5-9	3'SO ₂ NHPr	0.034 ± 0.008
5-5	2'CF ₃	7.0 ± 0.8	5-10	3'NHSO ₂ Me	2.4 ± 0.4

A characteristic feature of the growth inhibitory activity the Series 5 compounds was the failure of high concentrations of test compound to completely abolish cell viability. Thus the dose response curve had a characteristic “hanging” appearance. It would seem that a subpopulation of “susceptible” cells were readily killed by the test compound, leaving behind a core of “resistant” cells that remained viable even at relatively high concentrations of test compound.

Practically, the “hanging” dose response curve raised concerns over the determination of IC₅₀. The approach adopted here was to take the concentration corresponding to the mid-point of the higher and lower “flat” portions of the curve. To confirm if this was a viable approach, the GI₅₀ values of several series 5 compounds were also determined.

Briefly, GI₅₀ is a parameter used by the National Cancer Institute (NCI) to quantify the growth inhibitory activity of a test compound.¹⁷⁵ Unlike IC₅₀, GI₅₀ takes into consideration the cell count at time zero. Thus GI₅₀ is the concentration of test compound at which $100 \times (T - T_0) / (C - T_0) = 50$, where T = absorbance of the test well which contains test compound and cells after 72 h incubation, C = absorbance of control well which contains only cells after 72 h of incubation and T₀ = absorbance of control well which contains cells at time 0 (at the point of compound addition to other wells). T, C and T₀ were also corrected for absorbance due to the vehicle used in the assay.

The NCI protocol proposed that if after 72 hours, some concentrations of test compound had absorbances lower than T₀, it would signal that the test compound was cytotoxic. Cytotoxicity was quantified in terms of LC₅₀ (lethal concentration 50), which is the concentration at which $T = \frac{1}{2} T_0$ [or $100 \times (T - T_0) / (C - T_0) = -50$]. If LC₅₀ could not be determined, then the compound was deemed to be antiproliferative (cytostatic) and the test concentration at which $T = T_0$ was designated “TGI”, which is the highest concentration at which the test compound arrested cell growth.

Figure 3-1 shows the curve for determination of GI₅₀ of a representative Series 5 compound. The GI₅₀ (29 nM) compared favorably with IC₅₀ (34 nM). In general, GI₅₀ values were lower

than IC_{50} values. The dose response curve of **5-9** showed that from 0.1 to 10 μM , cell viability remained relatively constant, before declining at extremely high concentrations (Figure 3-2A). If the latter concentrations were ignored, **5-9** would be deemed to have a cytostatic component in its growth inhibitory profile. The curve for determination of GI_{50} is given in Figure 3-2B. Similar observations applied to several other Series 5 compounds whose GI_{50} values were also determined. However, IC_{50} values were reported in Table 3-7 to keep in step with the other Series.

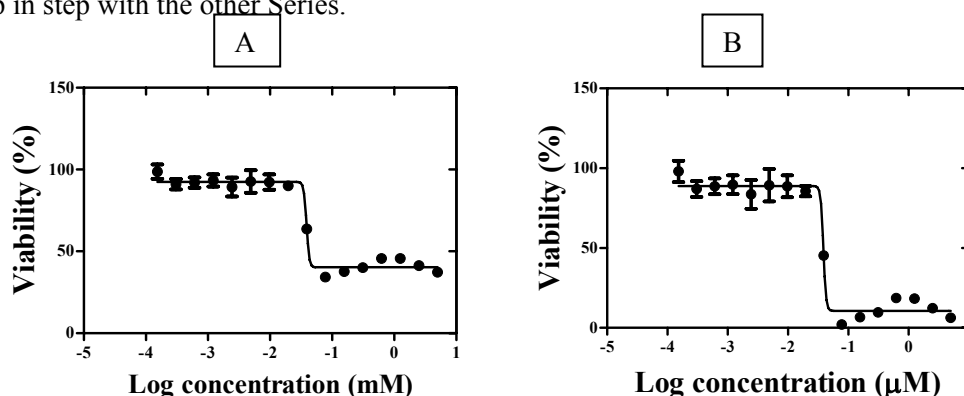


Figure 3-1: Dose response curves of determination of (A) IC_{50} and (B) GI_{50} of **5-9** on HuH7 cells, 72 h incubation.

When **3-12** was tested for its GI_{50} value, it was apparent that it was predominantly cytotoxic (Figure 3-3). GI_{50} of **3-12** was 60 nM as compared to IC_{50} of 94 nM.

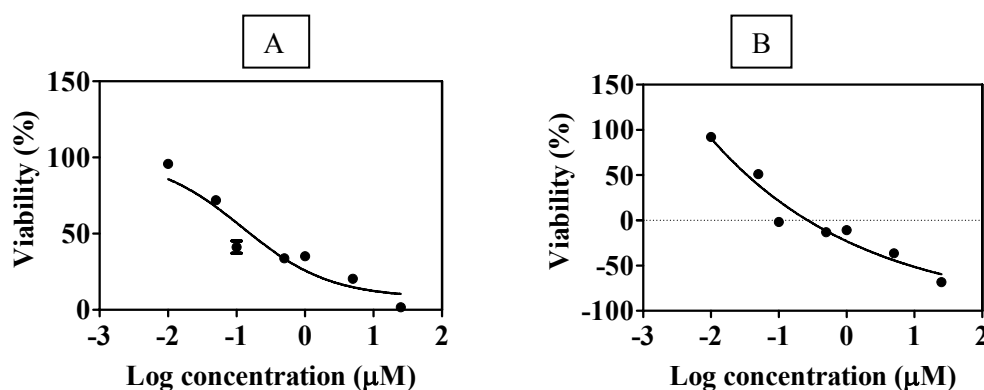
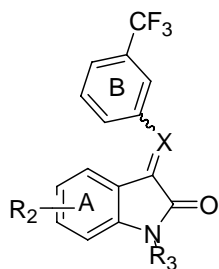


Figure 3-2: Dose response curves of determination of (A) IC_{50} and (B) GI_{50} of **3-12** on HuH7 cells, 72 hr incubation.

3.3.1.4. Growth inhibitory activities of Series 8 compounds

Table 3-8: IC_{50} of Series 8 compounds on HuH7 cells. Mean \pm SD for $n=3$ determinations.

Series 8



No	R ₂	R ₃	X	IC ₅₀ (μM)
8-1	H	H	CH	5.6 ± 0.1
8-2	H	H	N	>30
8-3	H	CH ₃	CH	6.7 ± 1.2
8-4	5Cl	H	N	20 ± 4
8-5	5F	H	N	23 ± 5
8-6	6Cl	H	N	20 ± 2
8-7	6Cl	CH ₃	CH	1.1 ± 0.2
8-8	6Cl	Et	CH	2.5 ± 0.3
8-9	6Cl	Bn	CH	0.93 ± 0.12

^a IC₅₀ could not be determined due to poor solubility of test compound

Series 8 was designed to report on the SAR of the exocyclic methine (=CH-) bond and substitution on the indolinone nitrogen. Replacing the exocyclic methine (=CH-) for azomethine (=N-) resulted in a significant drop in activity and this was consistently observed in Series 1 (6-Cl), Series 2 (5-Cl) and Series 4 (5-F). (Figure 3-4).

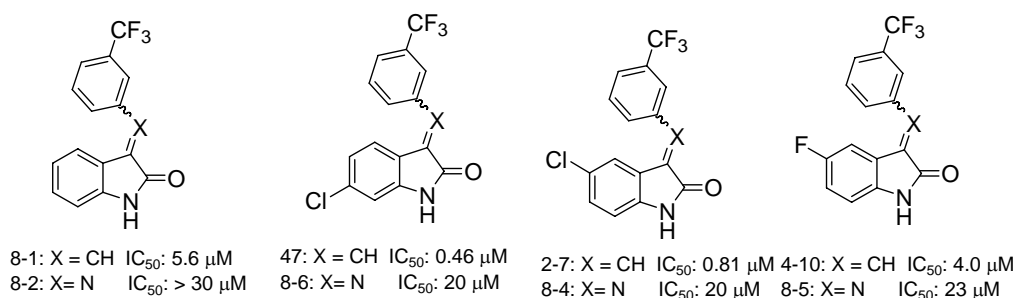


Figure 3-3: Comparison of IC₅₀ values of benzylidene indolinones and phenyliminoindolinones.

Substitution on the lactam N showed that *N*-substitution did not improve activity. No specific trend was apparent when the potencies of the *N*-methyl, *N*-ethyl and *N*-benzyl analogs were compared. (Figure 3-5).

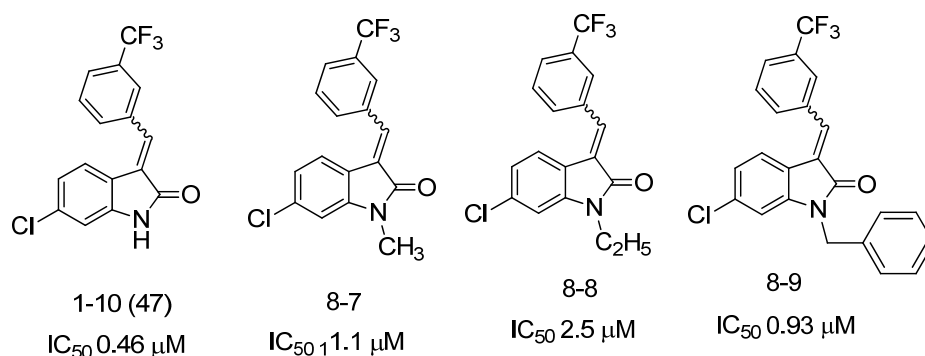


Figure 3-4: IC₅₀ values of 47 and its *N*-substituted analogs

3.3.2. Growth inhibitory properties of selected compounds on Hep3B and HepG2

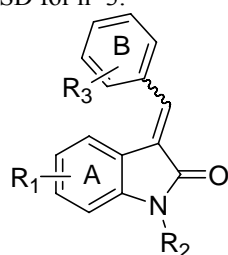
In the next stage of the investigation, selected compounds were investigated on two other liver cancer cell lines, HepG2 and Hep3B. Most of the selected compounds had IC₅₀ values of approximately 1 μM or lower on HuH7 cells. The rest were less potent but had ring B substituents (CF₃, SO₂NHMe, SO₂NHPr) that were associated with potent activity. Hence they were included for establishing SAR.

Mention should be made of the differences between the liver cell lines HuH7, HepB2 and HepG2. Unlike Hep3B and HuH7, HepG2 is a hepatoblastoma cell line.¹⁷⁶ Whereas HCC is associated with known environmental risk factors, inherited factors contribute more to the pathogenesis of hepatoblastoma.¹⁷⁷ The p53 gene which is the most frequently mutated gene in HCC¹⁷⁸⁻¹⁸¹ is wild-type in HepG2 but has altered structure and function in HuH7 and Hep3B.¹⁷⁹ Levels of p53 were exceptionally high in HuH7 presumably due to the complexation of the mutant p53 with heat shock proteins.¹⁷⁹ A major portion of the p53 gene was deleted in Hep3B and this deletion was accompanied by the absence of p53 transcripts and p53 protein in this cell line.¹⁷⁹ Hep3B cells were also unusual in that their genome contained hepatitis B virus (HBV) DNA.¹⁸² Thus, Hep3B cells expressed HBx, a protein encoded by HBV that is critically involved in HBV-induced HCC.¹⁸³

As seen from the results in Table 3.9, except for the *N*-benzyl analog **8-9**, the test compounds were consistently less potent on HepG2 cells. Growth inhibitory activities on HuH7 and

Hep3B were broadly comparable, with a few exceptions (3-12, 5-1, 5-6, 5-8, 5-9, 8-8) where IC_{50} values differed by 2-fold or greater. Sorafenib was equipotent on all 3 cell lines. The diminished activity on HepG2 compared to HuH7/Hep3B may imply that cells with mutated p53 were more susceptible to the test compounds.

Table 3-9: IC₅₀ of selected compounds on HepG2 and Hep3B cells. IC₅₀ on HuH7 cells were included for comparison. IC₅₀ values are mean ± SD for n=3.



Code	R ₁	R ₂	R ₃	IC ₅₀ (μM)		
				HuH7	Hep3B	HepG2
47 (1-10)	6Cl	H	3'CF ₃	0.46±0.06	0.96±0.22	0.94±0.18
1-17	6Cl	H	3'SO ₂ NH ₂	3.1 ± 0.2	7.6±0.2	9.8 ± 1.7
1-18	6Cl	H	3'SO ₂ NHMe	1.0 ± 0.1	1.0±0.1	3.6±0.3
1-20	6Cl	H	3'SO ₂ NMe ₂	4.9 ± 0.4	5.3±0.5	7.9 ± 0.6
1-22	6Cl	H	3'SO ₂ NHEt	0.7±0.03	1.4±0.2	4.0±0.6
1-23	6Cl	H	3'SO ₂ NHPr	0.28±0.09	0.32±0.08	1.5±0.1
1-24	6Cl	H	3'SO ₂ NHiPr	1.9±0.3	1.6±0.2	5.5±1.0
2-7	5Cl	H	3'CF ₃	0.8±0.1	0.8±0.1	1.5±0.06
2-14	5Cl	H	3'SO ₂ NHMe	3.1 ± 0.07	5.40±0.3	10 ± 0.2
2-15	5Cl	H	3'SO ₂ NHPr	7.4 ± 0.3	5.7 ± 0.3	10 ± 1.
3-10	6F	H	3'SO ₂ NHMe	0.48 ± 0.01	1.1±0.2	2.8 ± 0.6
3-11	6F	H	3'SO ₂ NHEt	0.39±0.07	0.51±0.06	1.6±0.2
3-12	6F	H	3'SO ₂ NHPr	0.093±0.029	0.36 ± 0.13	0.80±0.14
3-13	6F	H	3'SO ₂ NHiPr	2.3±0.06	1.7 ± 0.3	4.2±0.5
4-16	5F	H	3'SO ₂ NHMe	1.2± 0.02	2.4 ± 0.4	9.1 ± 0.3
4-17	5F	H	3'SO ₂ NHPr	1.4 ± 0.3	0.77 ± 0.13	5.2± 0.5
5-1	6OMe	H	H	0.77±0.07	3.2±0.7	1.5 ± 0.1
5-2	6OMe	H	2'F	0.49±0.05	0.91±0.09	1.84 ± 0.18
5-3	6OMe	H	3'F	0.71±0.07	1.2±0.3	1.3± 0.2
5-6	6OMe	H	3'CF ₃	1.2±0.05	4.1±0.1	1.1 ± 0.2
5-8	6OMe	H	3'SO ₂ NHMe	0.17 ± 0.02	0.31 ± 0.06	0.22 ± 0.01
5-9	6OMe	H	3'SO ₂ NHPr	0.034 ± 0.008	0.56 ± 0.11	0.19 ± 0.074
6-6	4,5F	H	3'CF ₃	0.54±0.07	0.43±0.09	0.96±0.11
6-11	4,5F	H	3'SO ₂ NHPr	13.4 ± 2.2	13.6 ± 0.7	17.6 ± 1.2
7-6	5,6F	H	3'CF ₃	0.84±0.17	0.45±0.07	0.69 ± 0.02
7-10	5,6F	H	3'SO ₂ NHMe	2.8±0.2	2.8±0.2	5.5±0.4
7-11	5,6F	H	3'SO ₂ NHPr	3.6 ± 0.9	2.7 ± 0.5	8.8 ± 1.0
8-7	6Cl	Me	3'CF ₃	1.1±0.2	0.9±0.1	1.7 ± 0.06
8-8	6Cl	Et	3'CF ₃	2.5±0.3	0.58 ± 0.021	2.12 ± 0.35
8-9	6Cl	Bn	3'CF ₃	0.93±0.12	0.78 ± 0.16	0.71 ± 0.06
					IC ₅₀ (μM)	
				HuH7	Hep3B	HepG2
			Sorafenib	5.4 ± 0.5	5.8 ± 0.5	5.6 ± 0.2

As seen from Table 3-9, the potent compounds against HuH7 (IC₅₀ ≤ 1 μM) were **47**(0.46 μM), **1-18** (1.0 μM), **1-22** (0.7 μM), **1-23** (0.28μM), **2-7** (0.81 μM), **3-10** (0.48 μM), **3-11** (0.39 μM), **3-12** (0.09 μM), **5-1** (0.77 μM), **5-2** (0.49 μM), **5-3** (0.71 μM), **5-8** (0.17 μM), **5-9** (34 nM), **6-6**(0.70 μM), **7-6** (0.84 μM) and **8-9** (0.93 μM).

Fourteen compounds were found to have IC₅₀ ≤ 1 uM on Hep3B: **47**(0.96 μM), **1-18** (1.0 μM), **1-23** (0.32 μM), **2-7** (0.77 μM), **3-11** (0.51 μM), **3-12** (0.36 μM) **4-17** (0.77 μM), **5-2**

(0.91 μM), **5-8** (0.31 μM), **5-9** (0.56 μM), **6-6**(0.43 μM), **7-6** (0.45 μM), **8-7** (0.91 μM), **8-8** (0.58 μM) and **8-9** (0.78 μM). There was considerable overlap between the two lists, with **47**, **1-18**, **2-7**, **3-11**, **3-12**, **5-2**, **5-8**, **5-9**, **6-6**, **7-6** and **8-9** common to both.

Analysis of the 3' substituents in potent HuH7 compounds revealed that there were more compounds with 3'*N*-substituted aminosulfonyl side chains than 3' CF_3 (8 versus 5). In contrast, among the potent Hep3B compounds, Hep3B compounds revealed that there were equal compounds with 3' CF_3 on ring B to those with 3' *N*-substituted aminosulfonyl (7 versus 7).

Table 3-10: 3' Substituents in potent HuH7 and Hep3B compounds ($\text{IC}_{50} \leq 1 \mu\text{M}$)

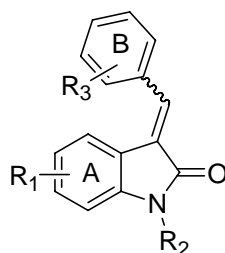
Potent compounds against HuH7			Potent compounds against Hep3B		
3' CF_3	3' SO_2NHR	Others	3' CF_3	3' SO_2NHR	Others
47	1-18	5-1	47	1-18	5-2
2-7	1-22	5-2	2-7	1-23	
6-6	1-23	5-3	6-6	3-12	
7-6	3-10		7-6	3-12	
8-9	3-11		8-7	4-17	
	3-12		8-8	5-8	
	5-8		8-9	5-9	
	5-9				

3.3.3. Growth inhibitory properties and selectivity ratios of selected

compounds on IMR 90 cell

In order to assess the selective growth inhibitory activity of the test compounds, the compounds were evaluated on non-malignant diploid primary human fibroblast cells (IMR90). Ideally, screening for selective activity should be carried out on primary human hepatocytes¹⁸⁴ or non-malignant liver cell lines such as THLE-2 or THLE-3, for a more accurate comparison with malignant liver cells. Unfortunately, hepatocytes are not readily replicable and normal liver cells are difficult to culture. IMR90 cells are commonly employed for investigating the selective activity of anti-cancer drugs.¹⁸⁵ Hence they were used here as a representative non-malignant cell line. $\text{IC}_{50 \text{ IMR90}}$ values and selectivity ratios calculated from $\text{IC}_{50 \text{ IMR90}} / \text{IC}_{50 \text{ HCC}}$ for each HCC cell line are listed in Table 3-11.

Table 3-11: IC₅₀ of selected compounds on non-malignant human fibroblast cells IMR90 (mean ± SD for n=3 determinations). Selectivity ratios (IC₅₀ IMR90 / IC₅₀ HCC) were calculated for each compound from IC₅₀ values in Table 3-9.



Code	R ₁	R ₂	R ₃	IMR90 IC ₅₀ (μM)	Selectivity Ratios ^a		
					HuH7	Hep3B	HepG2
1-10	6Cl	H	3'CF ₃	9.2 ± 0.9	20	9.6	9.8
1-17	6Cl	H	3'SO ₂ NH ₂	9.2 ± 0.6	3.0	1.2	0.9
1-18	6Cl	H	3'SO ₂ NHMe	2.1 ± 0.4	3.9	2.0	0.59
1-20	6Cl	H	3'SO ₂ NMe ₂	6.0 ± 0.2	1.2	1.2	0.76
1-22	6Cl	H	3'SO ₂ NHEt	3.5 ± 0.8	5.0	2.6	0.88
1-23	6Cl	H	3'SO ₂ NHPr	0.6 ± 0.09	2.1	1.8	0.38
1-24	6Cl	H	3'SO ₂ NHiPr	1.8 ± 0.2	0.9	1.1	0.3
2-7	5Cl	H	3'CF ₃	9.1 ± 1.1	11	12	3.6
2-14	5Cl	H	3'SO ₂ NHMe	6.6 ± 0.3	2.1	1.2	0.6
3-10	6F	H	3'SO ₂ NHMe	10.4 ± 0.2	21	9.6	3.8
3-11	6F	H	3'SO ₂ NHEt	0.99 ± 0.14	2.5	1.9	0.61
3-12	6F	H	3'SO ₂ NHPr	0.83 ± 0.06	8.9	2.3	1.1
3-13	6F	H	3'SO ₂ NHiPr	3.1 ± 0.4	1.4	1.9	0.73
4-16	5F	H	3'SO ₂ NHMe	9.9 ± 0.6	8.4	4.2	1.1
5-1	6OMe	H	H	2.1 ± 0.3	2.7	0.94	1.4
5-2	6OMe	H	2'F	0.56 ± 0.05	1.1	0.62	0.30
5-3	6OMe	H	3'F	1.2 ± 0.07	1.7	0.99	0.93
5-6	6OMe	H	3'CF ₃	1.8 ± 0.1	1.5	0.44	1.6
5-8	6OMe	H	3'SO ₂ NHMe	0.13 ± 0.02	0.8	0.42	0.59
6-6	4,5F	H	3'CF ₃	8.1 ± 0.7	15	19	8.4
7-6	5,6F	H	3'CF ₃	8.5 ± 0.6	10	19	12
7-10	5,6F	H	3'SO ₂ NHMe	7.7 ± 0.2	2.8	2.8	1.4
8-7	6Cl	Me	3'CF ₃	11 ± 0.5	9.5	12	6.3
8-8	6Cl	Et	3'CF ₃	15.2 ^b	6.1	26	7.2
8-9	6Cl	Bn	3'CF ₃	9.76 ^b	10.5	12	14
Sorafenib				11 ± 2	2.1	1.9	1.9

^a Selectivity ratio is calculated from IC₅₀ IMR 90 / IC₅₀ HCC cell line. ^b IC₅₀ value based on two replicates.

Compounds that selectively curtailed the viability of HCC cell lines have ratios > 1.0. As seen from Table 3-11, most compounds were selectively more potent against HuH7 and Hep3B than HepG2.

Earlier, potent compounds against HuH7 and Hep3B were identified based on their IC₅₀ values (≤ 1 μM) (Table 3-10). The selectivity ratios of these compounds are collated in Table 3-12. It was gratifying to note most of the compounds had ratios ≥ 2. Interestingly,

compounds with 3'CF₃ on ring B (**47**, **2-7**, **6-6**, **7-6**, **8-7**, **8-8**, **8-9**) had larger ratios than compounds with *N*-substituted aminosulfonyl side chains (**1-18**, **1-23**, **3-11**, **5-8**).

Table 3-12: Selectivity ratios (SR) of potent compounds (IC₅₀ values ≤ 1 μM) against HuH7 and Hep3B.

Potent compounds against HuH7				Potent compounds against Hep3B			
<i>Cpd</i>	<i>SR</i> ^a	<i>Cpd</i>	<i>SR</i> ^a	<i>Cpd</i>	<i>SR</i> ^b	<i>Cpd</i>	<i>SR</i> ^b
47	20	5-2	1.1	47	9.6	5-9 ^c	-
1-18	1.6	5-3	1.7	1-18	2.0	6-6	18.8
1-22	5.0	5-8	0.8	1-23	1.8	7-6	19.0
1-23	1.6	5-9 ^c	-	2-7	11.9	8-7	11.9
2-7	11.3	6-6	15	3-11	1.9	8-8	26.4
3-10	21.7	7-6	10	3-12	2.3	8-9	12.5
3-11	2.5	8-9	10.5	4-17 ^c	-		
3-12	6.9			5-2	0.62		
5-1	2.7			5-8	0.4		

^a Selectivity ratio = IC₅₀ IMR90 / IC₅₀ HuH7

^b Selectivity ratio = IC₅₀ IMR90 / IC₅₀ Hep3B

^c Not determined

3.3.4. Investigations into the induction of apoptotic cell death of HuH7

cells by selected test compounds

Having identified compounds with potent effects on the viability of HuH7, it was of interest to determine if apoptosis was involved in the cell death phenomenon. Compounds **47**, **1-23**, **2-7**, **3-12**, **5-1**, **6-6**, **7-6** and **8-7** were selected for investigation (Figure 3-6). Of these, only the IC₅₀ of **8-7** (1.1 μM) exceeded 1 μM.

The induction of apoptotic cell death was investigated by flow cytometry using the Annexin V-FITC Apoptosis Detection Kit which contains propidium iodide (PI) and Annexin V tagged to fluorescein isothiocyanate (FITC). Briefly, the kit is designed to detect the translocation of phosphatidylserine residues from the inner to outer surface of the cell membrane during apoptosis. When attached to the outer surface of the membrane, the phosphatidylserine molecules bind to Annexin V and are detected by the fluorescence imparted by FITC. PI is a DNA intercalator but cannot permeate the intact membranes of live cells to intercalate with nuclear DNA. Thus only dead cells or those in late apoptosis are stained by PI. HuH7 cells were treated with test compound for 48 h, at a concentration close to or corresponding to its IC₅₀. Compounds **47**, **3-12**, **5-1** and **8-7** were tested over a range of concentrations. The cells were then harvested and stained with Annexin V / PI. Depending on the staining

characteristics, cells were distinguished as normal (not stained by Annexin –V or PI), in early apoptosis (stained by Annexin V but not PI) and in late apoptosis or necrosis (stained by both Annexin V and PI) (Table 3-13).

Table 3-13: Distribution of HuH7 into normal, apoptotic and necrotic categories on compound treatment, as assessed by FACS analysis. Mean \pm SD for n =3 determinations. ^a

Name	Concentration n (μ M)	Population (%)		
		Normal ^b	Apoptotic ^b	Necrotic ^b
Control^a	-	95.1 \pm 0.6	1.4 \pm 0.5	1.4 \pm 0.6
47	0.25	84.3 \pm 1.5	11.0 \pm 0.4	3.1 \pm 0.7
	0.5 ^c	82.8 \pm 3.6	13.6 \pm 4.2	2.2 \pm 0.7
	1	74.1 \pm 3.3	19.9 \pm 3.4	4.6 \pm 0.7
1-23	0.25 ^c	88.9 \pm 1.2	7.9 \pm 0.4	1.9 \pm 0.1
2-7	1.0 ^c	83.4 \pm 1.8	11.7 \pm 2.7	2.6 \pm 0.3
3-12	0.05	88.9 \pm 1.2	7.9 \pm 0.4	1.9 \pm 0.1
	0.12 ^c	87.3 \pm 1.3	9.1 \pm 0.3	2.2 \pm 0.3
	0.25	84.2 \pm 4.0	12.1 \pm 2.4	2.6 \pm 0.9
6-6	0.5	82.7 \pm 2.5	13.0 \pm 1.9	2.6 \pm 0.1
7-6	0.5	85.1 \pm 0.7	11.4 \pm 0.4	2.3 \pm 0.4
Control^a	-	85.3 \pm 5.1	2.1 \pm 2.0	4.4 \pm 3.9
5-1	0.5	77.2 \pm 1.5	9.6 \pm 4.2	9.9 \pm 4.3
	1 ^c	66.8 \pm 10.9	19.7 \pm 8.6	10.6 \pm 1.7
	2.5	56.1 \pm 20.1	29.6 \pm 15.5	10.7 \pm 6.6
	5	52.6 \pm 14.0	35.9 \pm 16.1	9.2 \pm 3.0
8-7	1 ^c	78.0 \pm 0.7	10.6 \pm 2.3	7.5 \pm 2.6
	2.5	73.8 \pm 7.2	12.1 \pm 4.7	11.2 \pm 3.6
	5	52.1 \pm 14.9	24.9 \pm 7.1	20.2 \pm 10.2
	10	47.2 \pm 11.9	28.7 \pm 10.6	21.2 \pm 3.8

^a Control cells were treated with media containing 0.5% v/v DMSO for 48 hr. ^b Proportion of normal, apoptotic and necrotic cells were deduced from cell populations in the lower left, lower right and upper right quadrants of the FACS diagram respectively. ^c Concentration corresponding to IC₅₀.

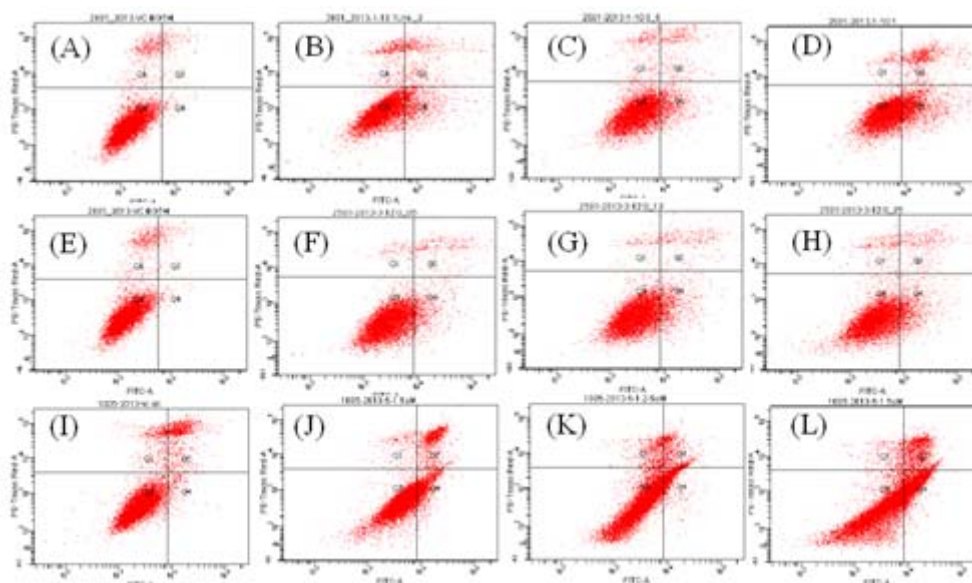


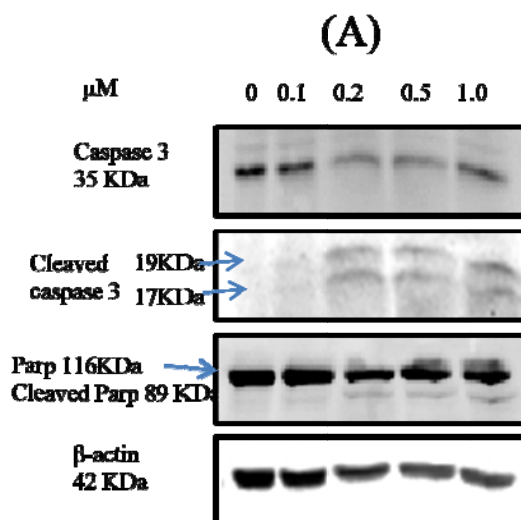
Figure 3-5: Representative figures showing FACS analysis of HuH7 cells treated with **47**, **3-12** and **5-1**. (A) Vehicle control for **47**; (B –D) : **47** at 0.25, 0.5, and 1.0 μ M respectively . (E) Vehicle control for

3-12 (F – H): **3-12** at 0.05, 0.12 and 0.25 μ M respectively (I) Vehicle control for **5-1**; (J - L): **5-1** at 0.5, 2.5, and 5 μ M respectively.

All the compounds induced apoptotic cell death in HuH7 cells, as seen from the increases in apoptotic cells under the present treatment conditions. A dose dependent increase in the proportion of apoptotic cells was observed for **47**, **3-12**, **5-1** and **8-7**. Interestingly, **5-1** which was deemed to have a cytostatic effect on HuH7 cells (Section 3.3.1.3), also induced apoptotic cell death. Thus there is support for the notion that a subpopulation of cells were susceptible to apoptosis.

Apoptosis was also investigated by monitoring apoptotic marker proteins (caspase 3, poly(ADP-ribose) polymerase, PARP) by immunoblotting. Caspase 3 is a cysteine protease that is normally present in its inactive state. It is an executioner (effector) caspase as signals from either the intrinsic and extrinsic apoptotic pathway would trigger its cleavage to the active state. Once activated, the effector caspases mediate the cleavage of key cellular proteins that lead to the typical morphological changes observed in cells undergoing apoptosis. The enzyme PARP is an important DNA repair enzyme and a substrate of caspase 3. The ability of PARP to repair DNA damage is prevented following the cleavage of PARP by caspase 3. Thus induction of apoptosis would be accompanied by elevated levels of cleaved caspase 3 and cleaved PARP.

Here, **3-12**, **5-1** and **8-7** were investigated for their effects on caspase 3 and PARP levels in HUH7 cells after 48 h of incubation at concentrations corresponding to IC_{50} , $2 \times IC_{50}$, $5 \times IC_{50}$ and $10 \times IC_{50}$.



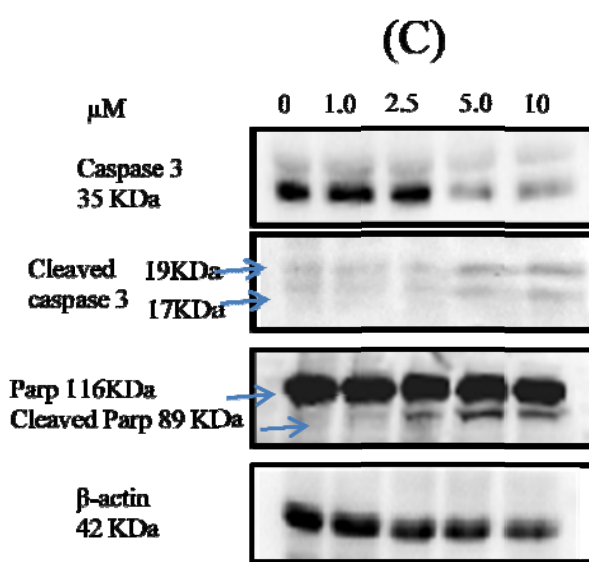
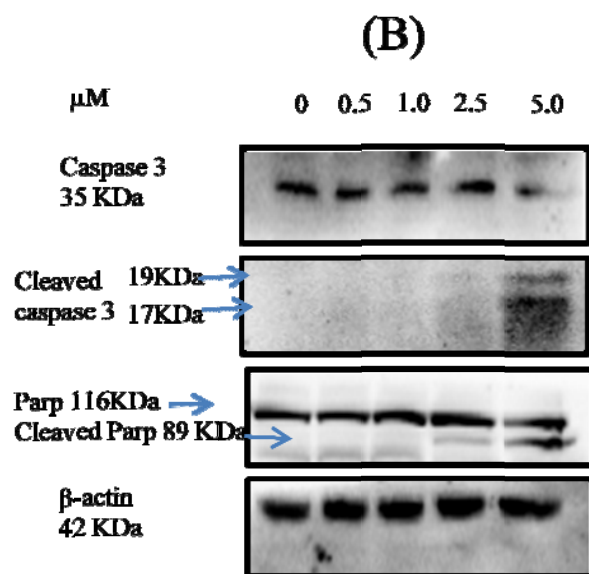


Figure 3-6: **3-12** (A), **5-1** (B) and **8-7** (C) induced apoptosis in HuH7 cells as seen from the increased levels of apoptotic markers cleaved caspase 3 and cleaved PARP induced by incubation with these compounds. Cells were treated with test compounds at stated concentrations 0.5 % DMSO (control) for 48 h. Cell lysates were prepared and caspase 3 (35 KDa), PARP (116 KDa), cleaved caspase 3 (19 and 17 KDa) and cleaved PARP (89 KDa) were probed by Western blot. β -actin (42 Kda) was the loading control. IC_{50} of **3-12**, **5-1** and **8-7** on HuH7 cells were 94 nM, 0.77 μM and 1.1 μM respectively.

As seen from Figure 3-7, the cleaved caspase 3 and cleaved PARP bands were seen in HuH7 cells treated with 0.2 μM **3-12** ($\sim 2 \times IC_{50}$). The appearance of the cleaved PARP band was observed at 2.5 μM **5-1** ($\sim 2 \times IC_{50}$) but the cleaved caspase 3 band was only evident at 5 μM **5-1**. Similarly, the cleaved PARP band was observed at 2.5 μM **8-7** ($\sim 2 \times IC_{50}$) but cleaved caspase 3 was observed in cells treated with a higher concentration of **8-7** (5 μM).

Based on dual staining of cells with Annexin V/PI and monitoring of apoptotic marker proteins, it was concluded that **3-12**, **5-1** and **8-7** induced apoptotic cell death in HuH7 cells.

3.4. Discussion

The structural alterations undertaken in this chapter were aimed at optimizing the HCC growth inhibitory activity of benzylideneindolinone scaffold, specifically that of the lead compound **47** whose structure-activity relationships (SAR) were largely unexplored. The desired outcomes of these modifications were to identify compounds with enhanced potency and selectivity for HCC, while retaining drug-like solubility and permeability profiles.

The structure activity relationships established in this chapter were essentially derived from HuH7 cells. It was revealing that most of the compounds tested on the panel of liver cancer cells (HuH7, Hep3B, HepG2) were more potent on HuH7 and Hep3B which were mutated p53 cell lines, than on HepG2 in which p53 was wild type. p53 is the most frequently mutated gene in HCC and the greater susceptibilities of cells bearing mutated p53 may suggest that signaling pathways associated with the loss of function or gain of a new function due to p53 mutations were targeted by these compounds. Several potent HuH7 compounds (**47**, **1-23**, **2-7**, **3-12**, **5-1**, **6-6**, **7-6**, **8-7**) induced apoptotic cell death, further underscoring the potential of these compounds for HCC.

Figure 3-7: Graphical summary of the effect of substituents on growth inhibitory potency of benzylidene indolinones on HuH7 cells. The vertical axis depicts substituents on ring A of the scaffold. The horizontal axis depicts substituents on ring B of the scaffold. The range of IC₅₀ values are color coded (most potent in red and least potent in black). N.A. = No activity at the highest soluble test concentration

The potency of compounds in Series 1-7 was dependent on the ring substituents. Figure 3-7 provides a graphical summary of substituent effects on potency. The most potent compounds were shown in red and least potent compound in black.

Several useful SAR insights were gleaned from the present investigations. First, the exocyclic methine (=C-) linking indolinone to phenyl ring B should be maintained as such. Replacing it with azomethine (=N-) was not tolerated as seen from the diminished activities of the Series 8 3-phenylimino indolin-2-ones. Second, *N*-substitution of the lactam in **47** was not helpful although the *N*-benzyl analog **8-9** maintained submicromolar IC₅₀ on HuH7, HepG2 and Hep3B. Compound **8-9** was in fact unique among the test compounds in having comparable activities on both HepG2 and Hep3B. Third, substitution on the phenyl ring B had a pronounced effect on growth inhibitory activity. The substantial variation (≥ 80 fold) in potency brought about by varying the ring B substituents in Series 1 clearly showed the immense influence of this single structural modification. Both the position and type of

substitution on ring B affected activity. There was a clear preference for substitution at 3' position on ring B in Series 1 but not in the other series (2-7) where regioisomeric preference depended more on the type of ring B substituent. Notwithstanding, 3'CF₃ isomer was consistently preferred in all Series (1-7). There was no apparent correlation between the electron withdrawing nature of the ring B substitution and growth inhibitory activity. Groups with greater electron withdrawing effects than CF₃ were not found to have greater activity. Possibly, an electron withdrawing group on ring B is an essential but not sufficient requirement for activity.

An important finding of this study related to the good growth inhibitory activity of compounds bearing *N*-substituted aminosulfonyl side chain on ring B. The most potent compounds on HuH7 (**3-12**, **5-9**) were substituted on ring B with *N*-*n*-propylaminosulfonyl groups. A robust SAR was observed for the *N*-substituted aminosulfonyl side chain, namely a distinct preference for mono *N*-substitution, an increase in growth inhibitory activity on homologation (H > *N*-methyl > *N*-ethyl > *N*-*n*-propyl), and the negative impact on potency imparted by branching (propyl → isopropyl) and reversal of the aminosulfonyl side chain (MeNHSO₂- → MeSO₂NH-).

Fewer modifications were made on the indolinone ring A, with substitutions limited to halogens (largely influenced by **47**) and methoxy. 6-Cl on ring A may be replaced by 6-F (Series 3) but switching from position 6 to position 5 (6Cl, 6F → 5Cl, 5F) was generally not recommended. Interestingly, the most active compounds in the mono-fluorinated series 3 (6-F) and 4 (5F) had *N*-methyl (**3-10**, **4-16**) or *N*-propylaminosulfonyl (**3-12**, **4-17**) on ring B. The same was true for Series 5 (6OMe on ring A).

Difluoro substitution of ring A was explored to provide insight on the contribution of *E/Z* isomerism to growth inhibitory activities. Series 6 (4,5-diF) was reasoned to be predominantly *Z*, while Series 7 (5,6-diF) was deemed to exist in equivalent proportions of *E* and *Z*. However, the apparent configurational preference in Series 6 did not appear to affect potencies. The most potent compounds in Series 6 and 7 (**6-6**, **7-6**) had comparable IC₅₀ values. Both were 3'CF₃ substituted on ring B.

The Series 5 compounds which were substituted with 6-MeO on ring A were unusual in having characteristic “hanging” dose response curves that were typical of cytostatic compounds. Nonetheless, one member (**5-1**) induced apoptosis in HuH7 cells, suggesting that the cell population may not exhibit homogenous responses to the Series 5 compounds and that only a subpopulation of the cells succumbed to apoptosis.

One of the aims in this investigation was to identify a suitable replacement for 3'CF₃ on ring B. The ideal group should impart potency and selectivity to the growth inhibitory profile, address the physicochemical deficits associated with 3'CF₃ and permit functionalization for expansion of the series. The 3'-N-substituted aminosulfonyl side chains have several of these desirable attributes. This side chain was encountered as frequently as 3'CF₃ in potent HuH7 and Hep3B compounds. A preference for the aminosulfonyl side chain was evident among the potent compounds in Series 3, 4 and 5. Compounds with 3' N substituted aminosulfonyl groups were anticipated to have greater solubilities and lower lipophilicity based on estimated values (Tables 2-1 to 2-3), thus providing the physicochemical advantage not found in 3'CF₃ compounds. Furthermore, the side chain may be modified by further homologation (presently not explored beyond propyl), cyclization or replacement by isosteric groups (ureido, amido).

The predominance of only 2 side chains CF₃ and *N*-propylaminosulfonyl – among the potent analogs identified in this chapter raised the question as to whether these groups could be remotely bioisosteric. A consideration of the binding interactions of CF₃ and the *N*-substituted aminosulfonyl side chain suggested that they share more similarities than differences. The *N*-substituted aminosulfonyl group is a H bond donor (NH) and H bond acceptor (-SO₂-). H bonding is desirable because it introduces substantial specificity to molecular interactions. In spite of its ability to function as a H bond acceptor, only 30% of sulfones and sulfonamides were found to act in this capacity.¹⁸⁶ Examination of sulfonyl containing ligands in the Protein Database (PDB) revealed that when situated in a hydrophobic environment, 36% were found to interact as H bond acceptors while 79% of the H bonded sulfonyl groups interacted simultaneously with a hydrophobic group.¹⁸⁶ These findings clearly pointed to a dual character for the weakly polar sulfonyl group, namely as a H bond acceptor and a

hydrophobic group. The CF₃ group also participates in a wide range of bonding interactions. The electron rich F atoms in CF₃ are electronegative and have low polarizabilities. Although not recognized as a classical H bond acceptor, interactions between CF and polar H atoms (OH, NH) are frequently encountered in the PDB and Cambridge Structural Database (CSD).¹⁸⁷ Thus C-F forms weak H bonds, with distances exceeding 3Å. C-F also participates in orthogonal multipolar interactions.¹⁸⁶ This interaction motif is characterized by a close orthogonal contact between two dipolar functionalities.¹⁸⁸ Thus C-F establishes dipolar interactions with C-H, C=O and positively charged guanidinium groups.¹⁸⁶ In addition, CF₃ is a lipophilic appendage (π 0.88) that readily fills hydrophobic cavities.

3.5. Summary

In summary, SAR for the growth inhibitory activities of benzylidene indolinones on HuH7 cells were established. Key findings are summarized in Figure 3-7.

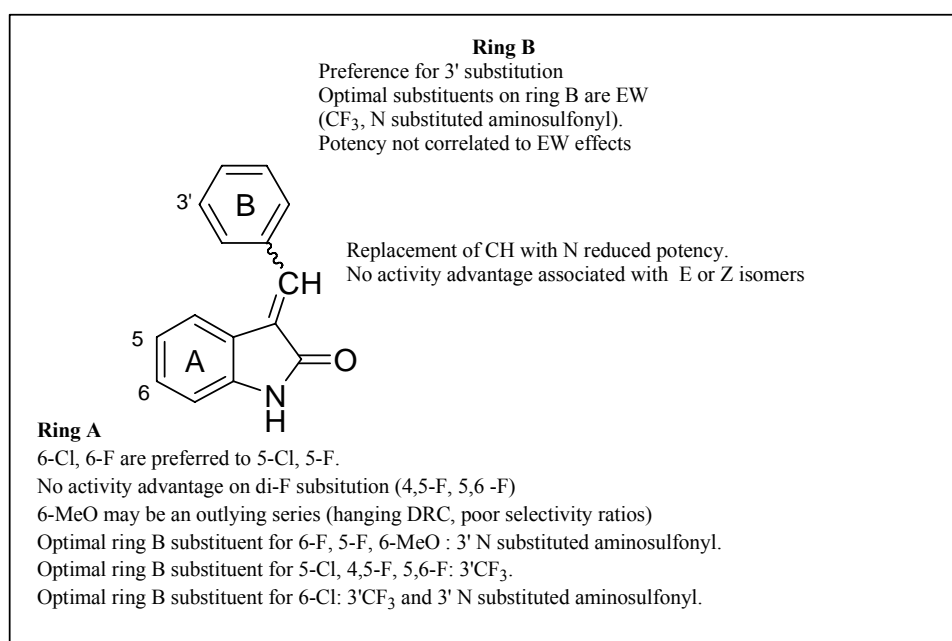


Figure 3-8: Summary of major SAR findings for the growth inhibitory activity of benzylidene indulines on HuH7 cells. EW: Electron withdrawing.

The 3'*N* substituted aminosulfonyl side chain was identified as a promising replacement for the 3'CF₃ group. It provides a rich source of molecular interactions (H bonding, hydrophobic), its polarity may translate to improved solubility and permeability, and it is amendable to structural variations.

Nearly ½ of the potent HuH7 analogs ($IC_{50} < 1 \mu M$) were substituted on ring B with the 3'-N-methyl or *N*-propylaminosulfonyl side chains. The more promising analogs like **3-10**, **3-12** selectively targeted HuH7 cells and were reasonably potent on Hep3B cells. Compound **3-12** induced apoptotic cell death in HuH7 cells.

Chapter 4 : Investigations into the sirtuin inhibitory activities of selected compounds from Series 1-8.

4.1. Introduction

This chapter describes the screening of selected compounds from Series 1-8 for sirtuin 1 (SIRT1) and sirtuin 2 (SIRT2) inhibitory activities. These investigations were motivated by two factors, namely evidence that the benzylideneindolinone scaffold is associated with sirtuin2 inhibitory activity (Section 1.6)^{117,118} and growing support for the notion that dysregulation of sirtuins is involved in the growth and progression of HCC (Section 1.5.3).^{110, 131-133, 135, 140} Having identified several benzylidene indolinones that potently diminish viability of the HCC cell lines HuH7 and Hep3B (Chapter 3), it was of interest to determine if these compounds were sirtuin inhibitors and if sirtuin inhibition contributed in any way to the loss in cell viability. To this end, selected potent members were screened for SIRT1 and SIRT2 inhibitory activity on an *in vitro* luminescence assay using human recombinant enzymes. The functional relevance of sirtuin inhibition was validated by monitoring levels of acetylated sirtuin substrates (p53, α -tubulin) and downstream apoptotic proteins in treated HuH7 cells. Molecular docking was carried out to probe the ligand-target interactions involved in the inhibitory process.

4.2. Materials and Methods

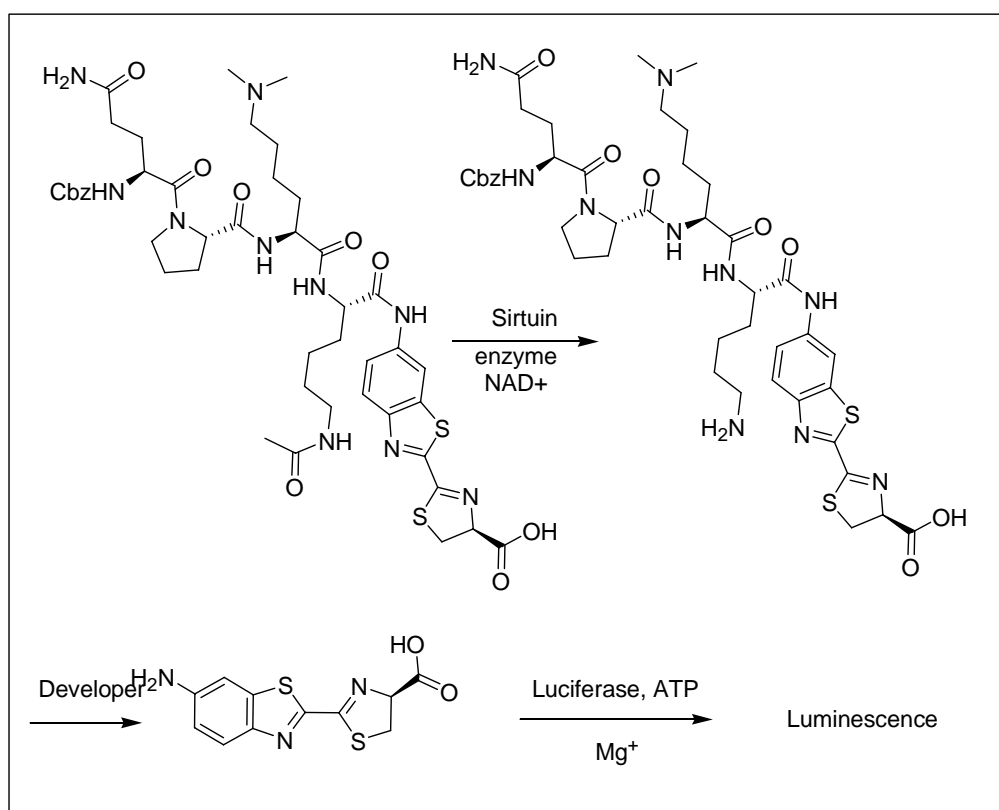
4.2.1. Reagents

AGK2 (2-Cyano-3-[5-(2,5-dichlorophenyl)-2-furanyl]-N-5-quinolinyl-2-propenamide) was from Torcris (Bristol, UK). Ex-527 (6-chloro-2,3,4,9-tetrahydro-1H carbazole-1-carboxamide) was from Sigma-Aldrich Inc (Singapore). Cell culture reagents (penicillin G, streptomycin, fetal bovine serum (FBS), culture media) were obtained from sources listed in Section 3.2.1. Stock solutions of test compounds were prepared as described in Section 3.2.1. Rabbit monoclonal antibodies to acetylated p53 (K382) and Bcl-2 were purchased from Cell Signaling Technology Inc (MA, USA). Mouse monoclonal antibodies to acetylated α -tubulin and α -tubulin were from Sigma-Aldrich Inc (Singapore). Mouse monoclonal antibodies to

p53, Bcl-xl, Bax, goat anti-rabbit-horse radish peroxidase (HRP) conjugate and goat anti-mouse HRP were from Santa Cruz Inc (CA, USA). Mouse monoclonal antibodies to β -actin were from Invitrogen Life Technologies (CA, USA).

4.2.2. Principle of sirtuin enzyme assay

sirtuin inhibitory activity was determined using the SIRT-Glo™ Assay Kit (G6450) from Promega (Singapore). Briefly, the assay is based on monitoring the rate at which the enzyme catalyzes the removal of the acetyl group from a luminogenic peptide substrate Z-QPK(Me₂)K(acetyl)-aminoluciferin.¹⁸⁹ The deacetylated substrate reacts with a protease in the Developer Reagent which removes aminoluciferin. In the presence of firefly luciferase, ATP and magnesium, aminoluciferin is oxidized to oxyluciferin with concurrent emission of light. In the presence of a sirtuin inhibitor, deacetylation of the substrate is prevented and this causes a corresponding loss in luminescence. Figure 4-1 summarizes the reaction steps involved in the assay procedure.



Scheme 4-1 Reaction involved in the sirtuin *in vitro* enzyme assay.

4.2.3. Measurement of sirtuin activity

SIRT 1 and SIRT2 activities were determined using the SIRT-Glo™ Assay Kit (G6450, Promega) following manufacturer's instructions. Assays were carried out on a 384-well with human recombinant SIRT 1 (Se239) and SIRT 2 (Se251) enzymes from Biomol International / Enzo Life Sciences (NY, USA). The amount of enzyme to be used in the assay was determined by measuring the signal-to-noise ratio of serially diluted enzyme in SIRT-GLO™ Buffer solution. The concentration of enzyme corresponding to a mid-range linear portion of the signal to noise ratio vs concentration plot was selected. A representative plot is given in Figure 4-1 (A). In this way, enzyme concentration was fixed at 0.1 unit SIRT1 per well and 0.2 unit SIRT2 per well. Serially diluted inhibitor solutions (10 µL in SIRT-GLO™ Buffer solution, with 1 µL of DMSO) were added to each well in a white-wall 384 well plate followed by the sirtuin enzyme (10 µL in SIRT-GLO™ Buffer solution). The plate was agitated using the shaking function of the Tecan plate reader (Infinite 200) at 400 rpm for 30 min at room temperature (25 °C) after which 20 µL of SIRT-GLO™ Reagent solution was added per well and the contents mixed by shaking (400 rpm) for another 30 min, 25°C. Luminescence was read on a Tecan plate reader. Enzyme activity (%) was measured by the following expression:

$$\text{Enzyme activity (\%)} = \frac{[lum_compound] - [lum_blank]}{[lum_vehicle] - [lum_blank]} \times 100\%$$

where lum_compound = luminescence of wells containing enzyme and test compound, lum_vehicle = luminescence of wells containing enzyme only and lum_blank = luminescence of wells containing vehicle (SIRT Glo™ Buffer/Reagent).

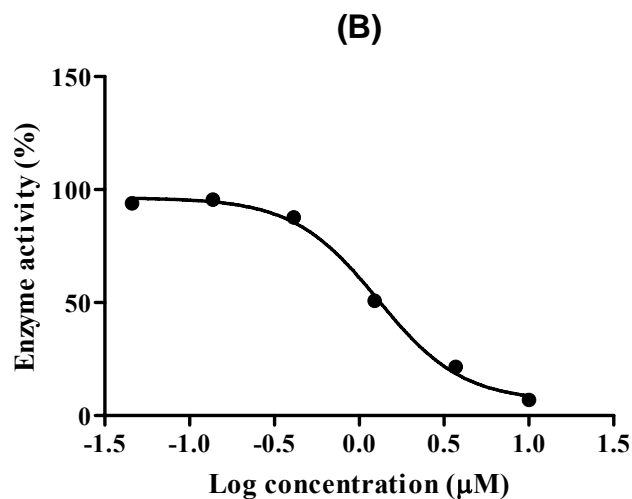
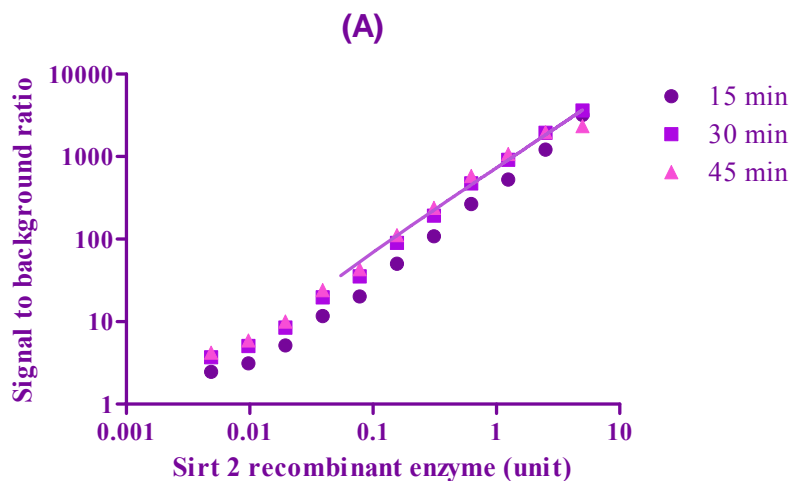


Figure 4-1 (A) Activity versus concentration of SIRT2 at different incubation times (15 min, 30 min, 45 min) (B) Representative dose response curve of **5-1** on SIRT1 activity

For the determination of IC_{50} (concentration required to inhibit 50% of enzyme activity), test compound was evaluated over a 300-fold concentration range, with at least 6 different concentrations tested. IC_{50} was determined from the sigmoidal curve obtained by plotting % enzyme activity versus logarithmic concentration of test compound on GraphPad Prism 5 (San Diego, USA). IC_{50} values were reported as mean \pm SD from $n=3$ separate determinations. A representative dose response curve for the determination of IC_{50} of **5-1** is given in Figure 4-1 (B).

4.2.4. Preparation of HuH7 or Hep G2 cell lysates

For detection of acetylated proteins, HuH7 or Hep G2 were incubated with test compounds for 12 h, 37°C, 5% CO₂. For detection of intrinsic apoptosis marker, HuH7 cells were incubated with test compounds for 48 h, 37°C, 5% CO₂. After this time, the adherent cells were processed using the method described in the Section 3.2.5.

4.2.5. Protein quantification

After obtaining the cell lysate, the protein quantification was conducted using the method described in the Section 3.2.6.

4.2.6. Sodium dodecyl sulfate - polyacrylamide gel electrophoresis (SDS-PAGE)

After protein quantification, cell lysates were separated on the SDS-PAGE Bio-Rad Mini-Protean II system (Bio-Rad Laboratories Inc, CA, USA). Each sample with the same protein amount were loaded on to separate lanes and were separate using the same method described in the Section 3.2.7. After electrophoresis, the gels were subjected to Western blotting (Section 4.2.7).

4.2.7. Western blotting

After electrophoresis, the gels were processed using the same method described in the Section 3.2.8.

4.2.8. Molecular Docking

The human SIRT2 enzyme was retrieved from the RCSB protein data bank (PDB ID: 3ZGV).¹⁹⁰ Water molecules were removed and the monomeric enzyme was processed for docking using LigX in the software Molecular Operating Environment (MOE, version 2011, Chemical Computing Group, Montreal, Canada). The *E* and *Z* structures of the test compounds were separately prepared for docking on MOE. Docking was carried out on GOLD v 5.2 (Cambridge Crystallographic Data Centre Software Ltd, Cambridge, UK) with

default GA settings. The binding pocket was defined by the atoms within 8 Å radius of co-crystallized ligand in 3ZGV (ADP-ribose). Docking was carried out without the reference ligand (ADP ribose). GOLD uses a genetic algorithm (GA) for docking flexible ligands into the binding pocket to explore the full range of ligand conformational flexibility.¹⁹¹ The GOLD Score was used as the fitness function for selection of the best docked conformations of test compounds in the binding pocket. For each molecule, the top 3 docked conformations were retained and analyzed graphically within MOE.

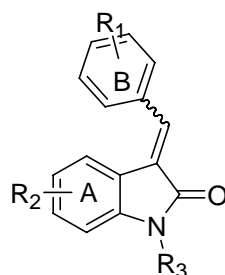
The human SIRT1 enzyme was retrieved from the RCSB protein data bank (PDB 4I5I).¹⁹² The protein was co-crystallized with NAD⁺ and an indole analog (R-2-chloro-5,6,7,8,9,10-hexahydrocyclohepta[b]indole-6-carboxamide). Both ligands were removed and the binding cavity was defined by the atoms within 8 Å radius of NAD⁺. The docking protocol described for SIRT2 was followed.¹⁹¹

4.3. Results

4.3.1. Inhibition of sirtuin activities by selected test compounds

In Chapter 3, compounds with IC₅₀ < 1 µM against HuH7 cells were identified (Table 3-10). These compounds were screened for SIRT2 inhibitory activity at 10 µM and those with < 50% activity at that concentration were investigated for their IC₅₀ concentrations. The results are given in Table 4-1. Based on the results, additional compounds were screened to provide a better understanding of the structural features affecting inhibitory activity.

The known SIRT2 inhibitor AGK2 was used as a positive control. Its IC₅₀ was found to be 8.1 µM, which was higher than the reported value of 3.5 µM.¹⁹³ The difference may be attributed to the assay kits employed. The reported method used a kit that was based on fluorescence detection unlike the present method which used a luminescence-based kit.

Table 4-1: Inhibition of SIRT2 and SIRT1 activities by potent HuH7 compounds ($IC_{50} \sim 1 \mu M$)

Compound No	R ₁	R ₂	R ₃	SIRT2 IC ₅₀ (μM)	SIRT1 IC ₅₀ (μM) Or Activity at 10 μM (shown as X% ± S.D.)
47	3' CF ₃	6-Cl	H	10.9±0.7	>50 μM
1-18	3'SO ₂ NHMe	6-Cl	H	24.7±2.4	91.1 %±7.6
1-22	3'SO ₂ NHEt	6-Cl	H	12.9±1.9	88.9 % ±2.6
1-23	3'SO ₂ NHPr	6-Cl	H	12.0±1.5	90.0 % ±7.2
1-24	3'SO ₂ NHPr _i	6-Cl	H	9.7±1.0	ND ^a
2-7	CF ₃	5-Cl	H	16.8±4.5	80.3% ±2.9
3-10	3'SO ₂ NHMe	6-F	H	46.0±8.2	82.7 % ±7.9
3-11	3'SO ₂ NHEt	6-F	H	12.2±3.2	88.1 % ±4.4
3-12	3'SO ₂ NHPr	6-F	H	12.6±2.1	78.4 % ±7.0
3-13	3'SO ₂ NHPr _i	6-F	H	9.2±1.9	ND ^a
5-1	H	6-MeO	H	1.5±0.4	1.3±0.1
5-2	2'F	6-MeO	H	3.0±0.4	4.1±0.68
5-3	3'F	6-MeO	H	1.8±0.2	4.1±0.7
5-4	4'F	6-MeO	H	1.3±0.1	1.0±0.1
5-5	2'CF ₃	6-MeO	H	3.4±0.1	5.7±0.7
5-6	3'CF ₃	6-MeO	H	2.9±0.1	>50μM
5-7	4'CF ₃	6-MeO	H	1.1±0.1	9.6±2.0
5-8	3'SO ₂ NHPr	6-MeO	H	9.9 ± 0.1	99%
6-6	3'CF ₃	4,5-F	H	24.5±6.7	99.8 % ±5.8
7-6	3'CF ₃	5,6-F	H	13.0±1.3	91.1% ±9.4
8-7	3'CF ₃	6-Cl	Me	3.4±0.1	>50 μM.
8-8	3'CF ₃	6-Cl	Et	3.1±0.2	>50 μM
8-9	3'CF ₃	6-Cl	Benzyl	0.97±0.10	>50 μM
	AGK2 ^b			8.1±1.2	
	EX-527 ^b				0.19±0.01

^a ND = Not determined ^b AGK2 and EX 527 are known SIRT 2 and SIRT1 inhibitors. IC₅₀ values were reported to be 3.5 μM¹⁹³ and 0.098 μM¹⁹⁴, respectively.

As seen from Table 4-1, most of the compounds were more potent than AGK2 or had comparable inhibitory activity. A notable few were less potent. Most of these compounds were those with *N*-methylaminosulfonyl (**1-18**, **3-10**) although extending the *N*-alkyl side chain in a homologous manner, from *N*-methyl to *N*-ethyl, *N*-propyl and *N*-isopropyl, resulted in a modest 2 to 4 fold improvement in inhibitory activity. Another compound with poor activity was the 4,5-difluoro substituted compound **6-6** (IC₅₀ 24.5 μM). Compound 6-6 was the least potent of the several 3'CF₃ analogs (**47**, **2-7**, **7-6**, **5-6**) listed in Table 4-1.

Potent inhibitors of SIRT2 ($IC_{50} < 5 \mu M$) were found in Series 5 and Series 8. One striking observation among the potent Series 5 compounds (**5-1 to 5-7**) was the narrow variation in IC_{50} values (1.1 μM to 3.4 μM). The 6-methoxyindolinone scaffold may conceivably have features that promote interaction with the sirtuin active site. Notwithstanding, a role for the benzylidene ring B should not be entirely discounted. Notably, the *N*-propylaminosulfonyl analog **5-8** (IC_{50} 9.9 μM) was comparatively less potent.

Strong inhibitory activities were also observed in the *N*-substituted analogs of **47** (**8-7**, **8-8** and **8-9**). Compared to **47** which had an unsubstituted lactam NH, substitution with methyl, ethyl and benzyl improved inhibitory activities by 3 to 10-fold. The *N*-methyl and *N*-ethyl analogs were equipotent ($IC_{50} \sim 3 \mu M$) but the *N*-benzyl analog **8-9** was significantly more potent (IC_{50} 0.9 μM).

The compounds were also evaluated for sirtuin 1 inhibitory activity. EX-527, a known SIRT 1 selective inhibitor, served as a positive control. Its IC_{50} was found to be 0.19 μM , as compared to the reported value of 0.1 μM .¹⁹⁴ The test compounds were found to have negligible sirtuin 1 inhibitory activity, with the notable exception of the Series 5 compounds (**5-1 to 5-5**) which maintained sirtuin 1 inhibitory activities that were broadly comparable to sirtuin 2. They were however significantly weaker inhibitors than EX527.

4.3.2. Validation of sirtuin inhibition by compounds 5-1 and 8-7 using

Western blot analysis

The functional relevance of sirtuin inhibition was explored by investigating the effects of **5-1** and **8-7** on the deacetylation of physiological substrates of SIRT1/2. Briefly, the test compound was incubated with HepG2 or HuH7 cells for 12 h, following which levels of acetylated p53 and α -tubulin were probed by Western blotting. p53 is a substrate of both SIRT1⁷² and SIRT2⁷⁴ while α -tubulin is a SIRT2 substrate.¹⁴⁴ Inhibition of sirtuin activity would result in higher levels of the acetylated substrate. The compounds were investigated at 2.5, 5, 10 and 25 μM . These concentrations were higher than their reported IC_{50} values (Table

3-9) but since shorter treatment times were employed for probing the acetylated proteins, higher concentrations may be required to demonstrate an effect.

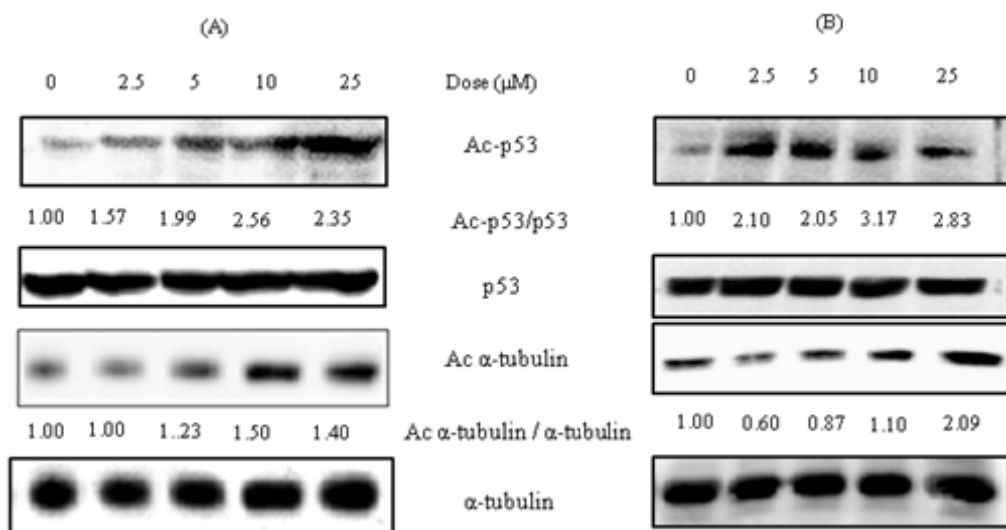


Figure 4-2: **5-1** induces hyper-acetylation of p53 and α -tubulin in (A) HepG2 and (B) HuH 7 cells after 12 h incubation. The ratios of acetylated (Ac) p53/p53 and acetylated (Ac) α -tubulin / α -tubulin were obtained in the following way. The intensities of the blots were quantified by densitometry and those obtained from untreated (control) cells were set at 1. At a given compound concentration, the intensity of the blot for the acetylated protein was compared to that of acetylated protein from untreated cells and expressed as x. Similarly, the intensity of the blot for the same protein (total) from treated cells was compared to total protein from untreated cells and expressed as y. The ratio of acetylated protein/total protein for cells treated at a given concentration of test compound was given by x/ y. x/y values were obtained for other concentrations. Increasing values were indicative of elevated levels of acetylated protein. Loading controls were p53 and α -tubulin.

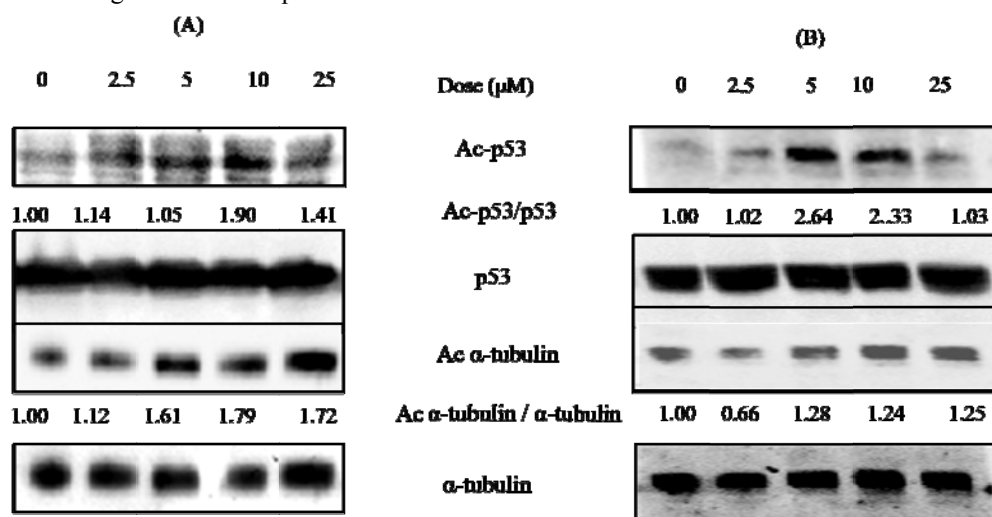


Figure 4-3: **8-7** induces hyper-acetylation of p53 and α -tubulin in (A) HepG2 and (B) HuH7 cells after 12 hr treatment. The ratios of acetylated (Ac) p53/p53 and acetylated (Ac) α -tubulin / α -tubulin were obtained as described in Figure 4-2. Loading controls were p53 and α -tubulin.

Compounds **5-1** and **8-7** increased the levels of acetylated p53 and acetylated α -tubulin in both HuH7 and HepG2 cells. Representative blots are shown in Figures 4-2 and 4-3. In

general, basal levels of acetylated p53 were lower than that of acetylated α -tubulin in untreated HuH7/HepG2 cells. This was due to the fact that only levels of p53 acetylated at Lys 382 were probed. Since Lys 382 constituted a small proportion of total acetylated p53, it was easier to demonstrate increases in acetylated p53 (K382) in treated cells. In contrast, basal levels of acetylated α -tubulin in control cells were high to start with and hence, dose dependent increases were more difficult to demonstrate (Figure 4-1A, Figure 4-2B).

Table 4-2 lists the maximum ratios of acetylated to total proteins obtained from compound-treated cells and the concentrations at which these peak ratios were obtained. The results showed that peak ratios of acetylated p53/total p53 were generally obtained at 10 μ M **5-1** and **8-7** (except for **8-7** on HuH7 cells). In contrast, concentrations at which peak ratios of acetylated α tubulin /total α tubulin were induced were less consistent (10 μ M, 25 μ M). It should be noted that increases in the acetylated protein were often evident at lower concentrations than those associated with the peak ratios. For example, **5-1** caused a two-fold increase in acetylated p53 at 2.5 μ M on both cell lines (Figure 4-2 A, B) although peak ratios were observed at 5 μ M.

Table 4-2: Peak ratios of acetylated protein/total protein induced by test compound (**5-1**, **8-7**) in HepG2 and HuH7 cells. The concentration at which these ratios were obtained are indicated in brackets.

	Compound	HepG2		HuH7	
Acetylated p53^a	5-1	1.7	(10 μ M)	3.1	(10 μ M)
		2.6	(10 μ M)	1.8	(10 μ M)
Total p53	8-7	1.3	(10 μ M)	2.6	(5 μ M)
		1.9	(10 μ M)	1.5	(25 μ M)
		1.5	(10 μ M)	2.1	(25 μ M)
Acetylated α tubulin^a	5-1	1.1	(25 μ M)	1.8	(5 μ M)
		1.8	(10 μ M)	1.1	(10 μ M)
Total α-tubulin	8-7	1.7	(25 μ M)	1.3	(10 μ M)

^a Ratios were obtained from two independent Western blots. The results of one attempt are given in Figure 4-1 and 4-2. The results of the 2nd attempt are given in the Appendix IV. The ratios were calculated as described in Figure 4-1.

sirtuins bind to and deacetylates activated p53. Inhibition of sirtuins would retain p53 in its transcriptionally active (acetylated) state, which is capable of triggering signaling pathways involved in apoptotic cell death. Both **5-1** and **8-7** have been shown to induce apoptosis in HuH7 cells (Section 3.3.4). They increased levels of cleaved caspase 3 and cleaved PARP as well as the proportion of cells in the apoptotic phase when investigated by double staining with Annexin V and PI. In order to obtain further evidence of compound-induced apoptosis,

the expression levels of the pro-apoptotic protein Bax and the anti-apoptotic proteins Bcl-2 and Bcl-xl were monitored in **5-1** treated HuH7 cells. Briefly, HuH7 cells were exposed to various concentrations of **5-1** for 48 h, after which levels of Bcl-2, Bcl-xl and Bax were probed by Western blotting. As shown in Figure 4-4, **5-1** (2.5 μ M) reduced levels of the anti-apoptotic proteins Bcl-xl, Bcl-2 and increased levels of the pro-apoptotic protein Bax.

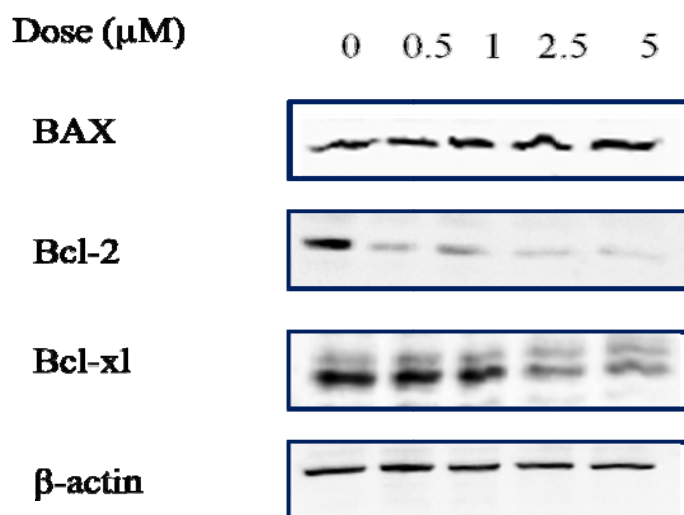


Figure 4-4: **5-1** decreased the expression of the pro-apoptotic protein Bax and increased the expression of anti-apoptotic proteins Bcl-2 and Bcl-xl in HuH7 cells. Cells were treated with **5-1** at stated concentrations, 0.5% DMSO (control) for 48 h. Cell lysates were prepared and Bcl-xl, Bcl-2, Bax were probed by Western blot. β -actin was the loading control.

4.3.3. Molecular docking of functionalized benzylidene indolinones in the

SIRT2 binding pocket

The variation in the inhibitory potencies of the test compounds may arise from different interaction modalities in the sirtuin binding pocket. Compounds with structural features that promote tight interactions within the binding pocket are more likely to be potent inhibitors while compounds that lack productive interactions with the binding pocket would conceivably be weaker inhibitors. Hence, molecular docking was undertaken to provide insight into the range of interactions associated with the benzylidene indolinone scaffold and their possible contributions to inhibition. The following compounds were investigated: **47**, **2-7**, **3-12**, **5-1**, **5-6**, **6-6**, **7-6**, **8-7**, **8-8** and **8-9**. Also included was the functionalized benzylideneindolinone, 6,7-dichloro-3-(4-nitrobenzylidene)indolin-2-one (III, Figure 1-8), previously identified by Huber et al as one of their more potent SIRT2 inhibitors.¹⁴³ Docking was carried out on

human SIRT2 (PDB 3ZGV) co-crystalized with ADP ribose¹⁹⁰ and human SIRT1 (PDB 4I5I) co-crystalized with NAD⁺ and an indole analog (R-2-chloro-5,6,7,8,9,10-hexahydrocyclohepta[b]indole-6-carboxamide) which is structurally related to the SIRT1 specific inhibitor EX527.¹⁹²

Sirtuins are known to share a highly conserved catalytic core domain but to differ in the length and sequences of the N and C-terminal segments.¹⁹⁵ The catalytic domain comprises a large Rossmann fold and a small domain that contains a zinc-binding ribbon module and a helical module that includes a flexible loop. The two modules are attached to the Rossmann fold through 4 linking loops, two for each module. These loops form a cleft between the small and large domains, within which are found the binding pockets for the co-factor NAD⁺ and the acetylated substrate. These two entities insert from opposite sides into a hydrophobic tunnel within the cleft where catalysis occurs. The NAD⁺ binding pocket is divided into 3 regions: Site A for the binding of the adenine moiety of NAD⁺, Site B for the ribose moiety connected to nicotinamide and Site C for the nicotinamide ring (Figure 4-5).

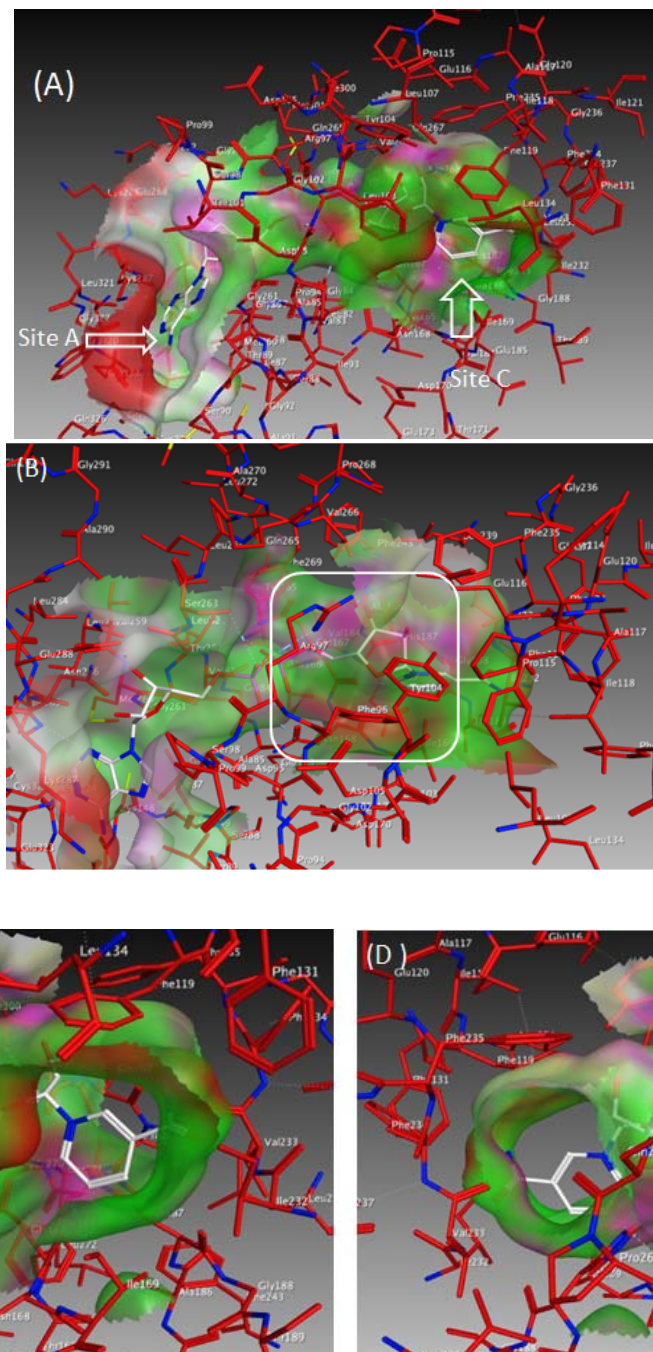


Figure 4-5: (A) Cofactor NAD⁺ in SIRT2 pocket (PDB 3ZGV). NAD⁺ was docked into the pocket as described in Section 4.2.5. Sites A (adenine binding pocket) and C (nicotinamide binding pocket) are indicated. (B) Site B (nicotinamide ribose binding pocket) is highlighted. Residues in the vicinity of Site B include Tyr 104, Arg 97, Phe 96, Asn 168. (C) Close up of Site C. Residues in the vicinity of Site C include Phe 119, Phe 123, Phe 131, Ile 232, Ile 169. (D) Close up of Substrate Channel which is on opposite side of Site B. Residues in the vicinity are His 187, Leu 239, Val 233, Phe 235. Color code of pocket: Green = Hydrophobic; Magenta = Polar; Red = Exposed.

4.3.3.1. Docking analysis of Z isomers of test compounds on SIRT2

Molecular docking showed that the Z isomers of the investigated compounds straddled the nicotinamide Site C, the substrate channel and ribose site B in such a way that the indolinone ring was positioned at sites B/C whereas the benzylidene ring B projected into the substrate channel/Site B. The exact locations were difficult to establish as the co-crystallization of the co-factor NAD⁺ with SIRT2 has not been achieved and there is some overlap between the residues lining Sites B and C, and Site C/substrate channel. Huber *et al*¹⁴³ reported that their benzylidene indolinones occupied Site C/substrate channel but they used a different SIRT2 crystal structure (PDB 1J8F).¹⁹⁶ Examination of the docking poses of the Z isomers (except those of **8-7**, **8-8**, **8-9**) revealed three characteristic interactions:

(i) H bonding interactions involving the lactam NH and carbonyl O of the indolinone ring. The lactam NH was H bonded to the phenolic OH of Tyr104 (N- - O), while the carbonyl O was H bonded to the guanidine side chain of Arg 97 (O- - N). The NH to Tyr 104 H bond was generally longer by ~ 0.6 Å than the carbonyl O to guanidine N of Arg 97. The length of H bonds varied among the compounds. For instance, in the ring B CF₃ analogs (**47**, **2-7**, **6-6**, **7-6**), the length of the N- -O bond ranged from 3.16 to 3.47 Å (Figure 4-6 A). The same bond was longer in **3-12** (N- -O 4.42 Å) (Fig 4-6 B) and shorter in the 6-methoxy analogs **5-1**, **5-6** (N- -O 2.97, 3.03 Å) (Fig 4-6 C). Compound **III** reported by Huber *et al*¹⁶ also displayed a long N- -O bond (4.42 Å) (Fig 4-6 D). The length of the NH to Tyr104 H bond changed in tandem with that of the carbonyl O to Arg 95 H bond. Thus they were shorter in the Series 5 compounds (O- - N 2.27 to 2.38 Å) and longer in **III** and **3-12** (O- - N 3.13 to 3.74 Å).

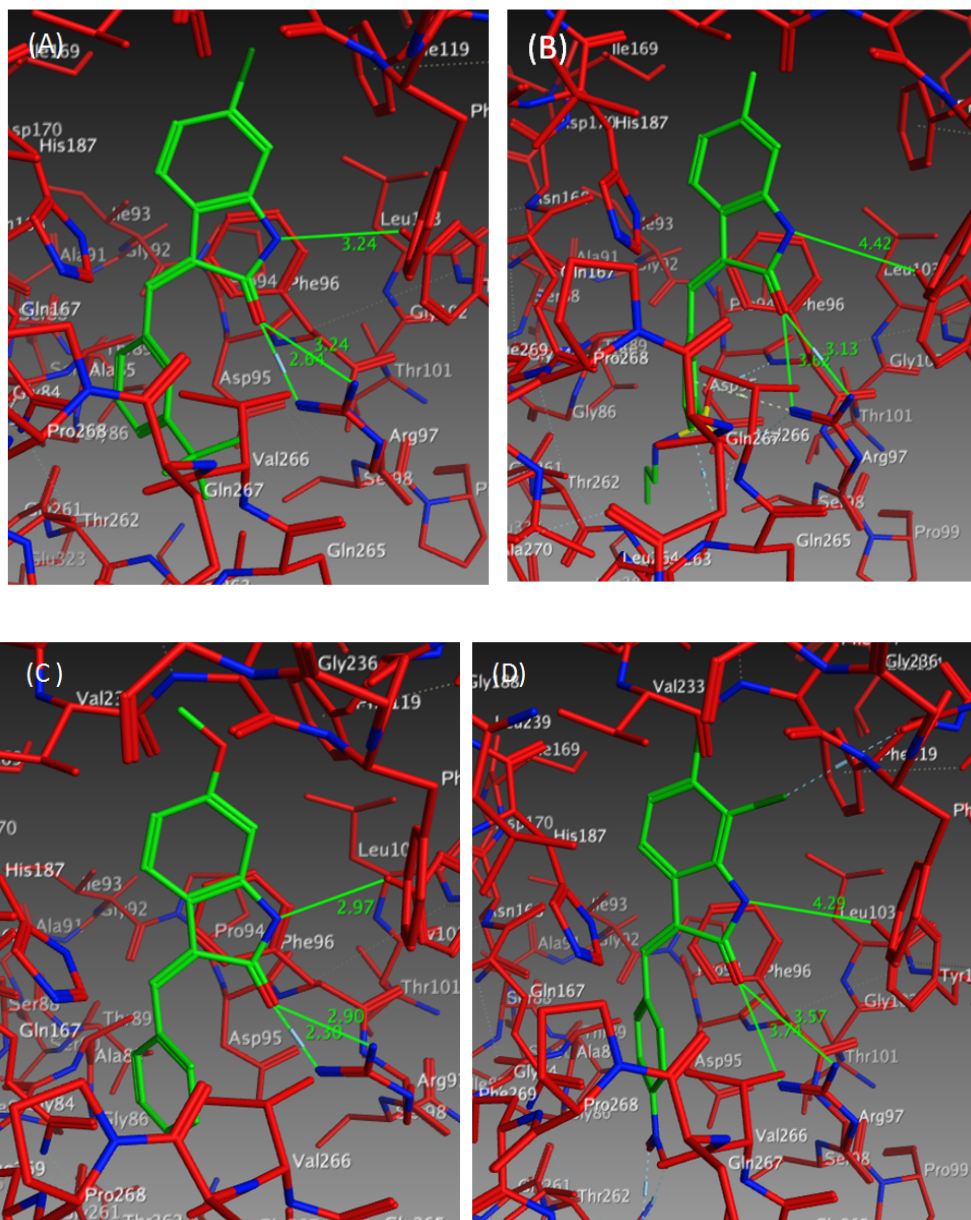


Figure 4-6: Bond lengths between lactam moiety (NHCO) of indolinone ring and residues Tyr 104 and Arg 97: (A) Compound 47; (B) Compound 3-12; (C) Compound 5-1; (D) Compound III. Compounds were examined in their Z configuration. Distances were measured between heavy atoms. H bonds are generally < 3.5 Å

(ii) $\pi \pi$ interactions between the indolinone ring and the phenyl ring of Phe 96. (Figure 4-7).

H bonds and $\pi \pi$ stacking interactions were involved in positioning the indolinone ring of the Z isomer at Site C.

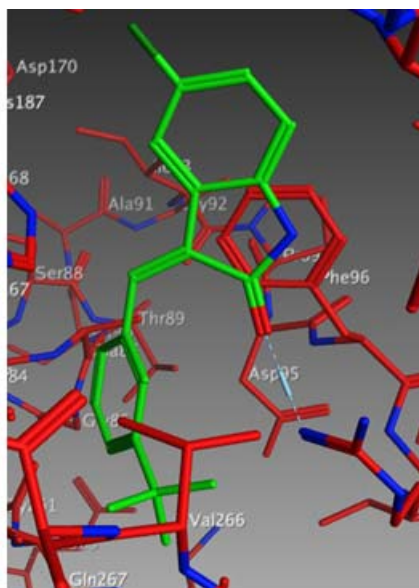


Figure 4-7 The indolinone ring is stacked against the phenyl ring of Phe 96 and well positioned for $\pi\pi$ interactions. Illustrated with compound **2-7**

(iii) Cationic π interactions between the benzylidene ring B and the positively charged guanidinium side chain of Arg 97. The benzylidene ring B was directed deeper into Site B, and in some test compounds (**3-12**, **5-1** and other Series 5 compounds) was well placed for cationic π interactions with Arg 97 (Fig 4-8). The strength of this interaction would depend on the electron density of the benzylidene ring and would be weaker in CF_3 substituted ring B analogs since the electron withdrawing CF_3 would arguably diminish the π electron density of ring B.

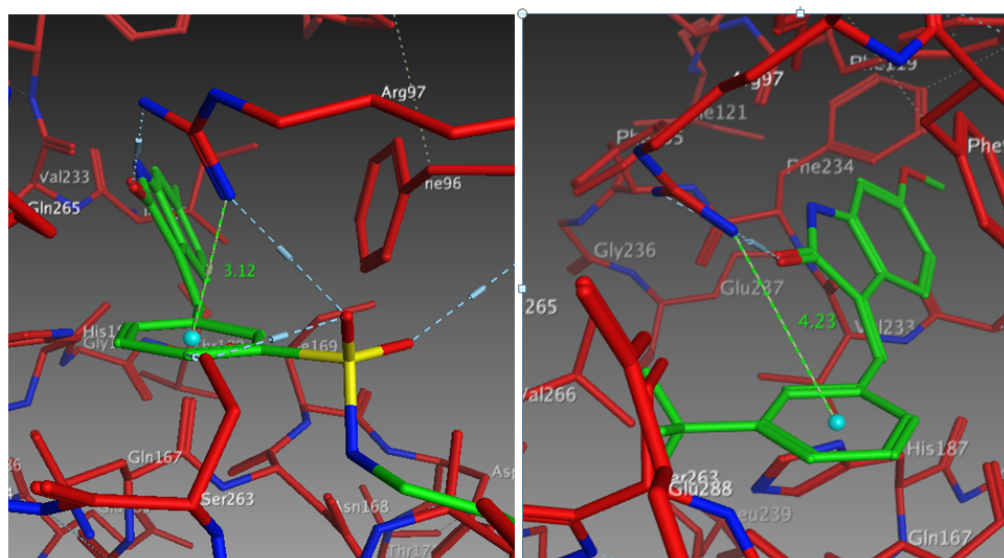


Figure 4-8: Cation- π interactions between benzylidene ring B and guanidinium side chain of Arg 97 as shown in (A) Compound **3-12** and (B) Compound **5-6**.

Notwithstanding its potential to weaken cation π interactions, the CF_3 group was a source of multipolar interactions with the binding pocket. As seen in Figure 4-9, one of the F atoms in $3'$ CF_3 of **47** was oriented almost orthogonally to the guanidinium side chain of Arg 97 while another F may form a similar interaction with the carbonyl C of Ser 263 (Figure 4-9).

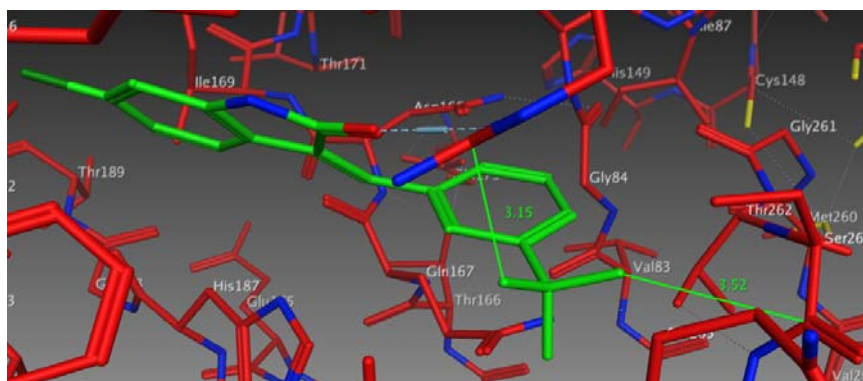


Figure 4-9: Orthogonal multipolar interactions are formed between C-F bonds in **47** and guanidinium side chain of Arg 97 and carbonyl O of Ser 263.

Mention was made of the variation in H bond lengths between the indolinone lactam moiety and Tyr104/Arg95. These variations could potentially account for differences in inhibitory potencies and thus were examined in greater detail. Compounds **3-12** and **III** were characterized by exceptionally long and weak H bonds. The docking pose of **3-12** suggested that this was largely due to the positioning of the *N*-propylaminosulfonyl side chain towards Site B of the NAD^+ binding pocket. In this orientation, the sulfonyl O atoms of this side chain was H bonded to Arg 97 (side chain guanidine), Ser 263 (OH) and Phe 96 (NH) (Figure 4-10 A), thus causing the molecule to be “pulled down” towards site B. Consequently, the usual H bond interactions of the indolinone ring A were weakened. When the docking pose of **3-12** was viewed concurrently with that of the co-crystallized ligand ADP ribose, a good overlap was observed between the sulfonyl moiety of **3-12** and the phosphoryl group ($\text{P}=\text{O}$) of ADP ribose (Figure 4-10 C), with both moieties involved in H bonding as H bond acceptors. The *N*-propyl side chain of **3-12** projected into a large cavity that could conceivably accommodate larger and bulkier *N*-substituents. Like **3-12**, **III** has a H bonding nitro group on its benzylidene ring. The docking pose of **III** revealed H bonding between the nitro group and

NH of Ser 263 (Figure 4-10 B). Consequently, the molecule was pulled down towards Site B, hence weakening the H bonding interactions of the indolinone ring.

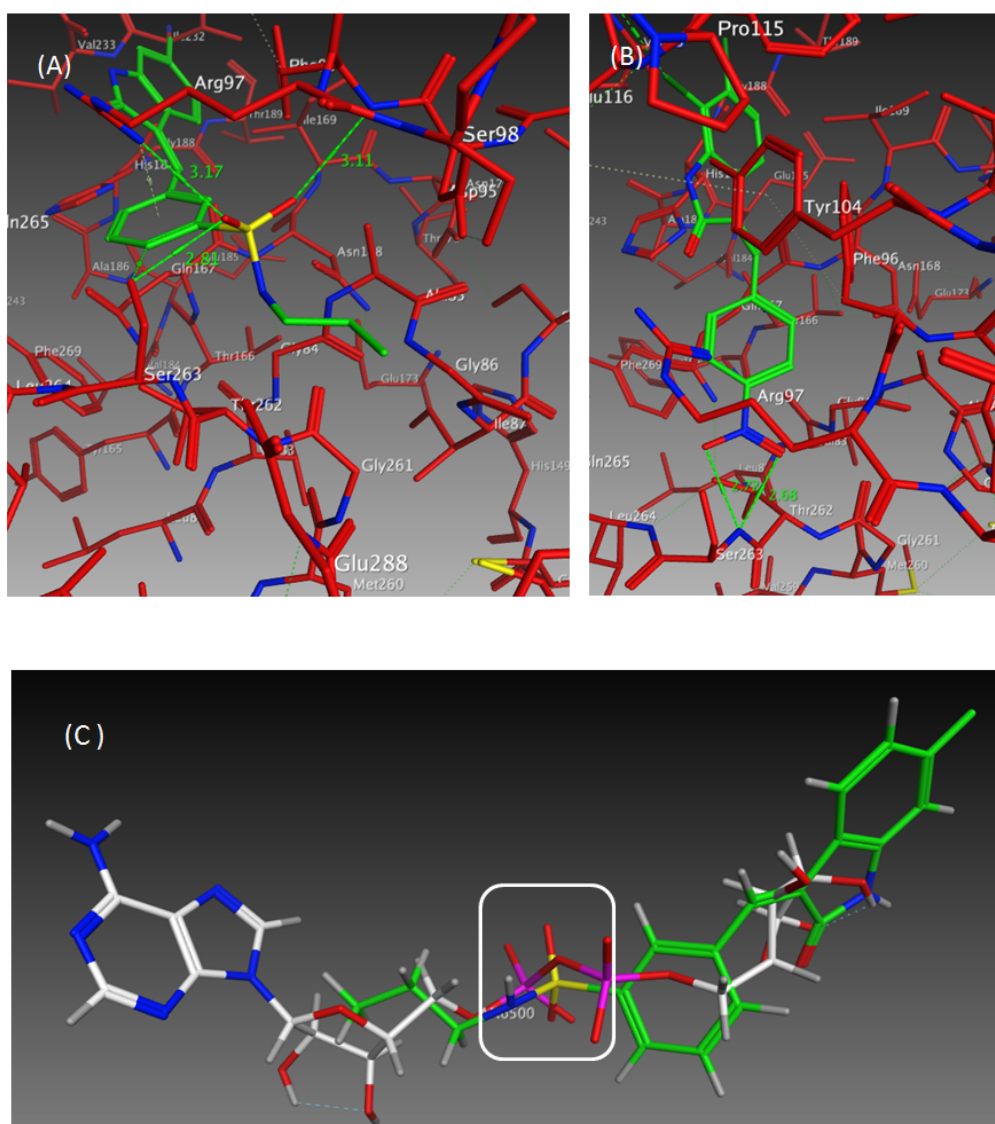


Figure 4-10: H bonding between (A) sulfonyl O atoms of **3-12** and Arg 97, Ser 263, Phe 96; (B) Nitro O atoms of **III** and Ser 263. (C) Overlap of **3-12** and ADP ribose in sirtuin 2 binding pocket (PDB 3ZGV). The residues in the pocket were removed to reveal overlap (bracketed) between SO₂ and PO₂ moieties in **3-12** and ADP ribose respectively.

In contrast to **3-12** and **III**, the Series 5 compounds were characterized by short H bonds. To analyze how the shortened H bonds could have affected the interactions of this class of compounds, the orientation of the 6-methoxy group was examined as this was the only moiety common to the potent Series 5 analogs. Except for **5-7**, the top ranked poses of the potent Series 5 compounds (**5-1** to **5-6**) showed that the 6-methoxy group was flanked by non-polar

residues Phe 119 and Ile 232 lining the substrate channel (Figure 4-11 A). Other ring A substituents (6-Cl, 5-Cl, 6-F) were also positioned in the substrate channel, but none approached the proximity observed with the methoxy group. It is tempting to propose that just as H bonding groups on ring B (**3-12**, **III**) pulled the molecule towards site B and disrupted the H bonding interactions of the indolinone ring, strong hydrophobic interactions by the methoxy group pulled the molecule towards the substrate channel and strengthened H bonding interactions of the indolinone ring. Curiously, **5-7** had a strikingly different orientation in the binding pocket (Figure 4-11 B) even though its SIRT2 IC₅₀ (1.1 μM) was not significantly different from the other Series 5 compounds. (Figure 4-11 B).

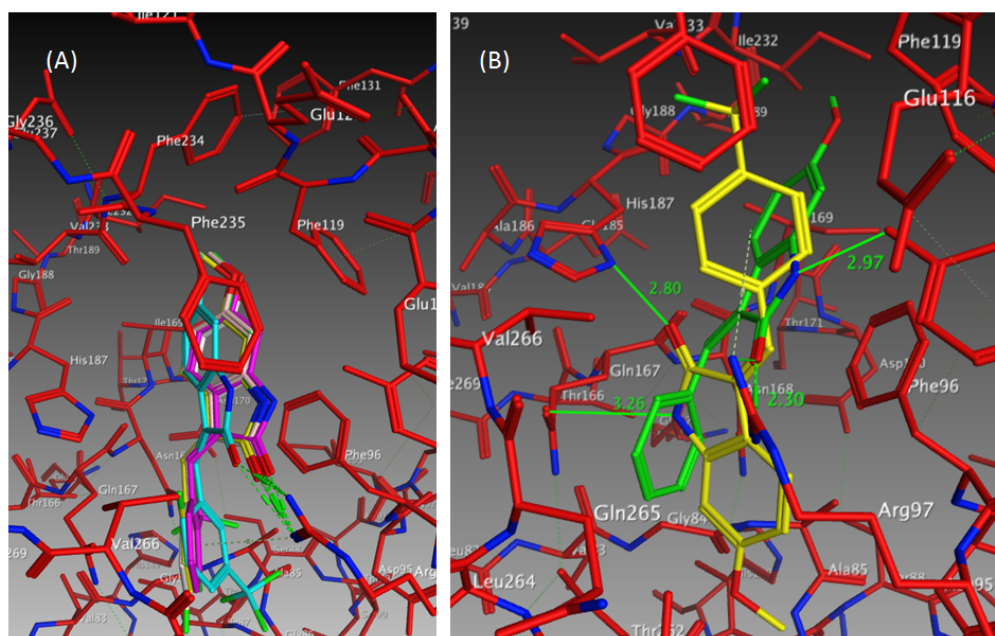


Figure 4-11: (A) Overlap of top poses of representative Series 5 compounds (shown in different colors) in SIRT2 pocket. The methoxy group is not involved in H bonding but the methyl is orientated towards the non-polar residues Phe 119, Ile 232, Val 233. (B) Pose of Compound **5-7** (in yellow) shows H bonding of the lactam NH to amide carbonyl of Gln 167 and lactam CO to NH of imidazole in His 187. The contrasting pose of **5-1** is shown in green.

Good SIRT2 inhibitory activity was also evident among the Series 8 compounds **8-7**, **8-8** and **8-9**. Substitution of the lactam N abolished the characteristic H bonding between NH and Tyr 104, but the H bond between the carbonyl O and Arg 95 remained intact. The loss in H bonding may have been compensated by the increase in hydrophobic interactions as the N

substituent was extended from methyl to ethyl and benzyl. Notably, the *N*-benzyl side chain of **8-9** was well positioned for $\pi\pi$ interactions with the phenyl ring of Phe 235 (Figure 4-12).

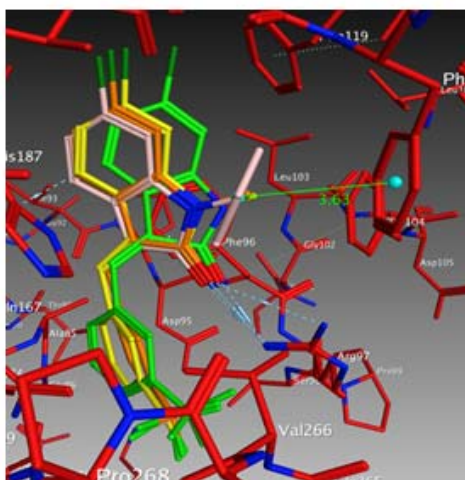


Figure 4-12 Overlap of best poses of compound **47** (green), **8-7** (yellow), **8-8** (orange) and **8-9** (pink). H bonding between lactam C=O and Arg 97 is maintained in Series 8 compounds. The benzyl ring of **8-9** stacks onto the phenyl ring of Phe 235.

The Series 8 compounds were substituted on the indolinone ring with 6-Cl and the benzylidene ring with 3'CF₃. Of these two features, the 6-Cl was likely to smaller contribute less to binding affinity. Like 6-methoxy, the chlorine atom was directed towards the substrate channel but the docking poses of the Series 8 and other 6-Cl compounds (Series 1) did not reveal any outstanding attractive or repulsive interactions involving the Cl group. Notably, there was no evidence of halogen bonding, which was in fact observed for the 7-Cl of **III** (Figure 4-13 A). Halogen bonding is a non-covalent interaction caused by the anisotropic charge distribution of halogens (except F) attached to electron withdrawing groups.¹⁹⁷⁻¹⁹⁹ This creates a positively charged region on the hind side of the halogen (σ hole) which attracts nucleophilic groups. The requirements for halogen bonding are bond lengths that are shorter than the sum of the van der Waal radii of the atoms involved and a C--X -- Y angle exceeding 120° (where X = halogen, Y = nucleophile). In **III**, 7-Cl formed a halogen bond with the carbonyl O of Phe 119, with a bond length of 3.5 Å (exceeding 3.27 Å which is the sum of van der waals radii of O and Cl) but a favorable subtended at Cl of 166°. (Figure 4-13 A)

In contrast, the contribution of the CF₃ substituted benzylidene ring to binding affinity in the Series 8 compounds was likely to exceed that of the 6-Cl on ring A. Depending on the orientation of the ring, interactions may involve CF₃ (orthogonal multipolar interactions), benzylidene ring (cation- π interactions) or both. In the case of **6-6 Z** however, the 4,5-difluoro substitution on ring A may have played some role in its poor SIRT2 inhibitory activity (IC₅₀ 24.9 μ M). The docking pose of **6-6** showed that 4-F was within 2.39 Å of the carbonyl O of Asn 168. (Figure 4-13 B). The electrostatic repulsion associated with the head-on F to O interaction could conceivably reduce the feasibility of this binding interaction which was particularly critical for **6-6** in view of its strong *Z* preference as discussed in Section 2.4.

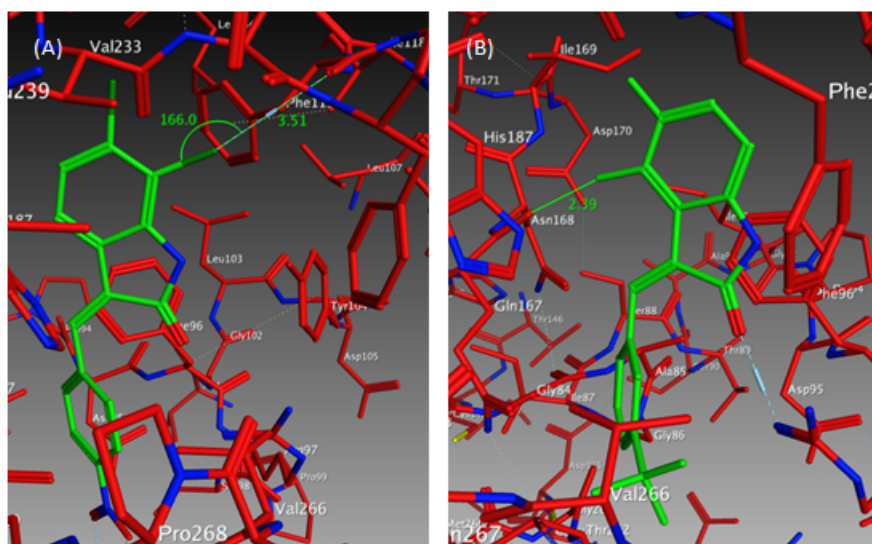


Figure 4-13: (A) 7-Cl of indolinone ring of Compound **III** is involved in halogen bond formation with carbonyl O of Phe 119. (B) 4-F of Compound **6-6** is oriented towards carbonyl O of Asn 168 (F- - O 2.39 Å) and head on orientation is likely to be destabilizing.

4.3.3.2. Docking analysis of *E* isomers of test compounds on SIRT2

Analyses of the docking poses of the *E* isomers of the benzylidene indolinones revealed that these isomers docked in Site B and the substrate channel but with significantly fewer interactions than their *Z* counterparts. Thus it was reasonable to conclude that the preferred configuration for docking was the *Z* isomer. Huber *et al*¹⁴³ reached a similar conclusion when they noted that their *E* isomers failed to display energetically favoring binding modes. Here we found comparable Gold Scores for both *E* and *Z* isomers but strikingly different docking

poses for the two isomers. This is illustrated in Figure 4-14 which compares the docking poses of *47E* and *47Z* in the SIRT2 binding pocket. The indolinone ring in the *E* isomer had made a complete “turn” such that the indolinone NH was H bonded to the amide C=O of Asn 168 located in Site B. An H bond between the indolinone C=O and CH of Asn 168 was flagged out by MOE but was discounted as this bond was likely to be weak.

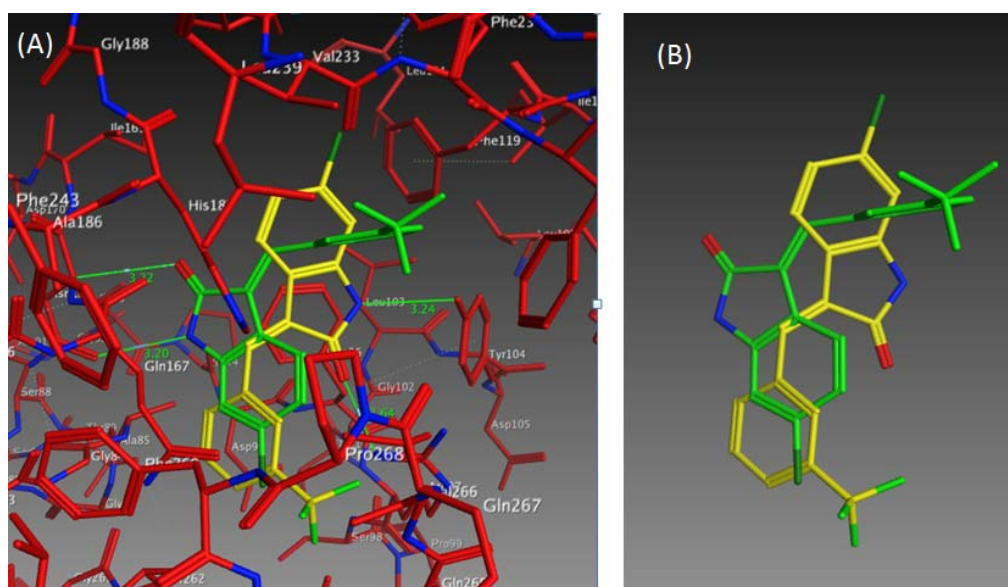


Figure 4-14: (A) Docking poses of **47Z** (yellow) and **47E** (green) in SIRT2 binding pocket. The lactam NH of **47E** establishes a H bond with carbonyl O of Asn 168 (NH - - O=C). The lactam carbonyl O of **47E** is recognized by MOE to form a H bond to CH of Asn 168. (B) Orientations of **47Z** (yellow) and **47E** (green) in SIRT2. Pocket residues have been removed.

The core interactions of the *E* benzylidene indolinones were (i) H bonding of the indolinone lactam NH and Asn 168. As a consequence of this orientation, the indolinone ring A was directed towards site B (Figure 4-15 A). No outstanding attractive or repulsive interactions involving the ring A substituent were noted, with the notable exception of the 6-methoxy of Series 5. H bonding was evident between the 6-methoxy oxygen and NH of Gly 84 (3.28 to 3.70 Å) (Figure 4-15 B). Additional interactions between the methoxy methyl and the side chain of Val 266, Pro 268 may serve to further strengthen interactions at this site (Figure 4-15 B).

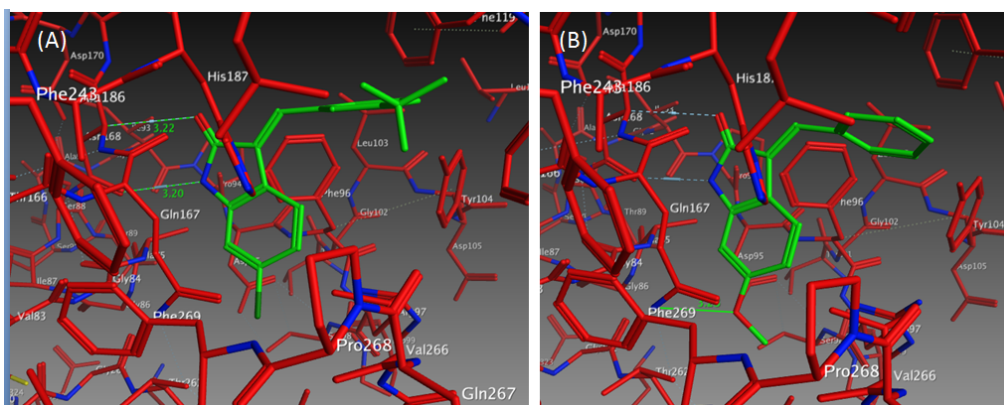


Figure 4-15: Docking poses of (A) Compound **47E** in SIRT2 binding pocket. Lactam NH is involved in H bonding (Asn 168). Indolinone ring A is directed towards Site B. (B) Compound **5-1E** in SIRT2 binding pocket. Methoxy O is involved in H bonding to amide side chain of Gln 167. Methyl group is oriented towards non polar residues Pro 268, Val 266.

(ii) Hydrophobic and van der waals interactions between the substituted benzylidene ring B and the non polar residues lining the substrate channel (Phe 119, Phe 235, Ile 232, Ile 169). An edge to side $\pi\pi$ interaction may also be possible in those compounds (**47E**) where Ring B was aligned almost orthogonally to Phe 235 (Figure 4-16).

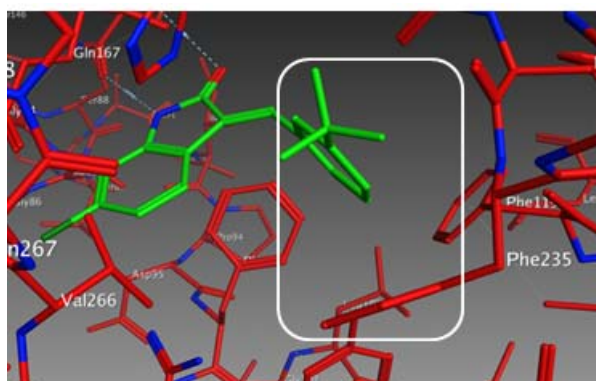


Figure 4-16: Edge to face $\pi\pi$ interactions(bracketed) between Ring B of **47E** and phenyl ring of Phe 235

While most of the *E* isomers maintained these core interactions, some exceptions were noted. These were compounds that had H bonding substituents on ring B, namely **3-12** and **III**. The highest ranked docking poses showed that the H bonding sidechains were directed towards site B. In **3-12**, the *N*-propylaminosulfonyl side chain was H bonded (via the sulfonyl O) to Ser 263 (NH) and Ala 85. In **III**, the 4-nitro moiety was H bonded to Ser 263 (NH) and Gln265. Consequently, the indolinone rings of **3-12** and **III** were not involved in H bonding interactions (Figure 4-17).

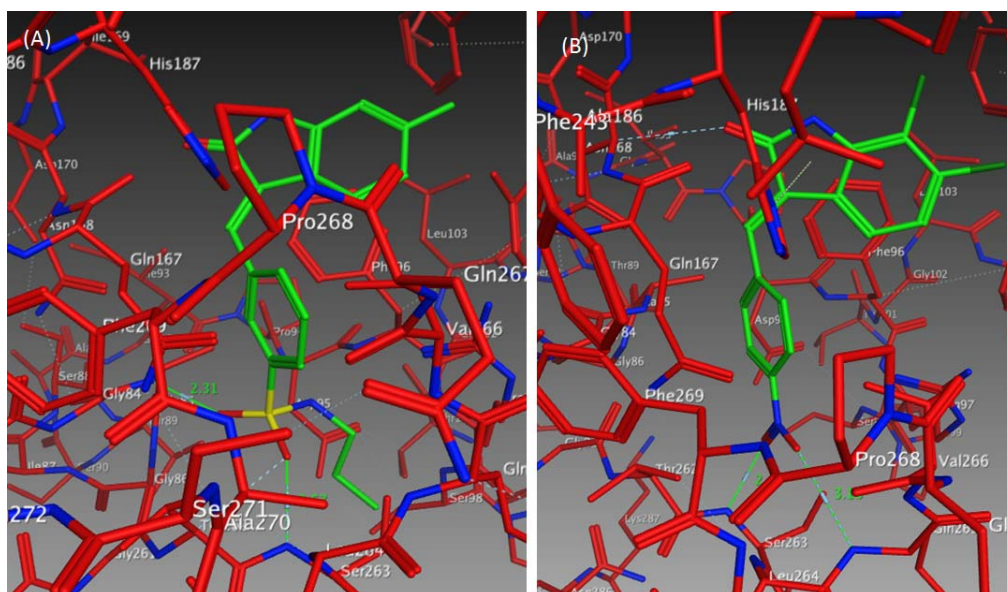


Figure 4-17: Docking poses of (A) Compound **3-12** and (B) Compound **III** in SIRT2 pocket. Both compounds have H bonding side chains on Ring B and their poses differ from that of compounds without this feature. The lactam in the indolinone ring A is not involved in H bonding.

The Series 8 compounds which were substituted on the lactam NH were another exception. The highest ranked poses of **8-7**, **8-8** and **8-9** showed that the indolinone ring was oriented towards the substrate channel, as observed in **3-12** and **III**. (Figure 4-18) The realignment may be explained by the loss of H bonding on *N*-substitution which was further compounded by the increasing bulk at the lactam N. In the realigned pose, the *N*-substituent was directed towards the more spacious lipophilic channel in the substrate binding site. Notably, *N*-benzyl of **8-9** was flanked by non-polar residues Ile 169 and Phe 233 (Figure 4-18)

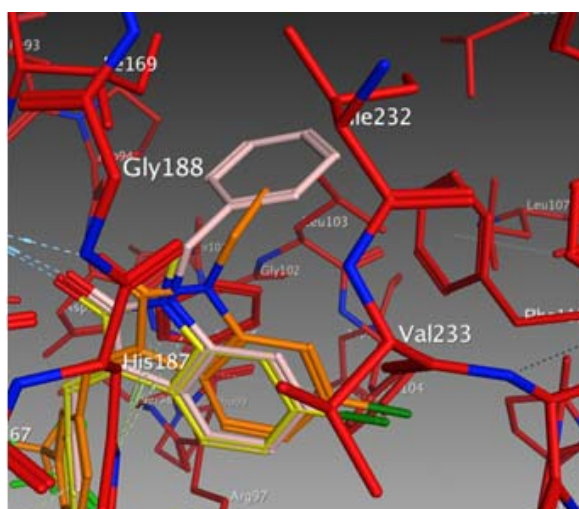


Figure 4-18 Overlap of best poses of compound **8-7** (yellow), **8-8** (orange) and **8-9** (pink) in SIRT 2 pocket. The *N*-substituent projects into the substrate channel which is lined by Phe232, Ile 119, among other residues.

4.3.4. Docking analysis of *Z* isomers and *E* isomers of test compounds on

SIRT1

The docking of the *Z* isomers on SIRT1 yielded inconclusive results. Based on the *in vitro* inhibitory activities, only selected Series 5 compounds demonstrated significant inhibition. However this could not be rationalized from their docking poses on the crystal structure, which were essentially similar to that observed for the other compounds. A possible reason may be that the SIRT1 crystal structure that was used for docking was co-crystallized with the co-factor NAD⁺ and an inhibitor (a 7-membered ring analog of EX527). The inhibitor was bound deep in the catalytic site, and consequently displaced the nicotinamide moiety of NAD⁺ from Site C, and forced NAD⁺ to assume an extended conformation. Therefore the binding cavity would be larger and could be less discriminating. If so, this could explain why the more potent Series 5 analogs had very similar docking poses as the less potent inhibitors like **47**, Series 3 and 8 compounds.

4.4. Discussion

The present investigations were undertaken to explore the sirtuin inhibitory potential of the benzylideneindolinone scaffold and to assess its contribution to cell growth inhibition. SIRT2 inhibition by several functionalized benzylidene indolineones had been reported earlier¹⁴³ and thus the main issue at hand was whether the structural modifications reported in this chapter had improved inhibitory potency. Unfortunately, the sirtuin inhibitory activities of the previously reported benzylidene indolinones (Figure 1-9) were not determined and thus the question as to whether they were more or less potent than the compounds tested here could not be completely addressed. Nonetheless, the sirtuin inhibitory potential of the benzylideneindolinone scaffold was clearly evident from the present findings. First, several compounds in Series 5 and 8 demonstrated potent SIRT2 inhibitory activities, exceeding that of the specific SIRT2 inhibitor AGK2. Second, the 40-fold variation in SIRT2 IC₅₀ values pointed to specific structural requirements for inhibition that could be further exploited to

improve inhibitory potency. Third, the 6-methoxy substituted benzylideneindolinones were unique in demonstrating equipotent inhibitory potencies on both SIRT1 and SIRT2, a property not found for other benzylidene indolinones, including those reported by Huber *et al.*

143

Analysis of the SIRT2 inhibitory activities of the test compounds revealed several interesting structure activity relationships. First, with regard to the Series 5 compounds, the observation that 7 of the 8 members had minimal variations in their IC₅₀ values (1.1 -3.4 μ M) in spite of having different ring B substituents (H, F, CF₃) implied that the Ring A methoxy had an overriding influence on activity. Support for this notion was provided by the docking poses of the *Z* isomers of these compounds. As described earlier, the methoxy group was favorably placed for hydrophobic and van der waals interactions in the substrate channel, which presumably led to tighter and stronger interactions between the rest of the molecule and the binding pocket. However **5-8** (N-propylaminosulfonyl on ring B) of Series 5 had weaker SIRT2 inhibitory activity. This side chain had been explored in compounds with different ring A substituents and the inhibitory activities of **5-8** fell within the same range of these other compounds. Notably, the SIRT2 inhibitory activity of **5-8** (9.9 μ M) was close to that of **1-23** (12.0 μ M) and **3-12** (12.6 μ M). A reasonable deduction was that these sulfonyl bearing ring B substituents had annulled the activity advantage associated with 6-methoxy group.

The second SAR observation pertained to compounds with 3'-CF₃ substituted benzylidene rings B. These included **47**, **2-7**, **6-6**, **7-6** and the potent Series 8 compounds (**8-7**, **8-8**, **8-9**). Compound **47**, from which these compounds were derived, was comparable to AGK2 in terms of sirt2 inhibitory activity. Replacing the 6-Cl of **47** with 5-Cl (**2-7**), 4,5-F (**6-6**) and 5,6-F (**7-6**) had limited impact on inhibitory activity, suggesting that the interactions of the CF₃ substituted benzylidene ring B were more important than those of the indolinone ring. Examination of the docked poses of these compounds showed that the CF₃ substituted benzylidene ring B, unlike the Cl and F groups on ring A, was a rich source of multipolar and cation π interactions. These interactions together with the hydrophobic / $\pi\pi$ stacking

interactions associated with the *N*-substituted lactam moiety could have accounted for the potent SIRT2 inhibitory activities of the Series 8 compounds.

Third, the preference for the *Z* configuration of benzylideneindolines for binding to the SIRT2 binding pocket was evident from the present results. A similar conclusion was reached by Huber *et al.*¹⁶ The *E* isomers established few productive interactions with the binding pocket. In contrast, the docking poses of the *Z* isomers were characterized by a host of binding modalities including H bonding, $\pi\pi$, cation π , non-polar and multipolar interactions.

The docking pose of **III** reported by Huber *et al.*¹⁴³ could not be reproduced in the present investigation. This was likely due to the different SIRT 2 crystal structures used for docking. Huber *et al.*¹⁴³ docked their compounds on to the apoenzyme of SIRT2 (PDB 1JKF) whereas docking was carried out here on a SIRT2 structure that was co-crystalized with a ligand ADP-Ribose (PDB 3ZGV). The presence of the ligand would affect the size and shape of the binding cavity, and very likely the poses of docked structures.

Although molecular docking had provided valuable insight into the structure activity trends associated with SIRT2 inhibition of the test compounds, the empirical nature of the approach should not be overlooked. The inhibitory activities of some compounds could not be readily explained by their docking poses. These were the homologs of *N*-alkylaminosulfonyl side chains (**3-11**, **3-13**) whose inhibitory activities improved with extension of the *N*-alkyl side chain. These trends could not be rationalized from their docking poses. Similarly, docking on SIRT1 proved to be disappointing. These caveats reflect the pitfalls associated with molecular docking and highlight the need for further verification by additional investigations like site selective mutation of key residues proposed to be involved in the interactions and deriving co-crystalized complexes of the enzyme with one of the test compounds. The limitations of the static docking techniques employed in the software should not be overlooked either. Investigators have proposed that the conformational freedom of the flexible loop region in Site C of the co-factor binding pocket of SIRT2 may play a critical role in substrate

binding,²⁰⁰ but the contribution of this feature could not be assessed by the current docking approach.

The functional relevance of the *in vitro* sirtuin inhibitory activities of **5-1** and **8-7** were confirmed by monitoring their effects on two physiological substrates of sirtuins, p53 and α -tubulin. Western blot analysis showed that both compounds efficiently induced the acetylation of p53 and α tubulin in HepG2 and HuH7 cell lysates. These increases were observed at 2.5 -10 μ M (acetylated p53) and 5-25 μ M (acetylated α -tubulin) for both compounds on HepG2 and HuH7. Although these concentrations were higher than the growth inhibitory IC₅₀ of **5-1** and **8-7**, they may be justified by the different time points employed in these experiments (12 h in Western blot versus 72 h in cell viability assays).

Hyperacetylation of p53 at Lys 382 has been reported to enhance p53 stability by inhibiting its ubiquitination by Mdm2.²⁰¹ It also led to the activation of the cell cycle regulator p21²⁰² and pro-apoptotic mediators BAX²⁰³ and PUMA.²⁰⁴ Hence, a consequence of the acetylation of p53 would be the induction of apoptotic cell death and this was indeed found to be true for **5-1** and **8-7**. Both compounds increased the proportion of HuH7 cells in the apoptotic phase when probed by Annexin V staining. They also increased the expression of apoptotic marker proteins (cleaved caspase 3, cleaved PARP). Compound **5-1** also induced changes in the levels of Bcl2, Bcl-xl and BAX that were congruent with the induction of apoptosis. However, the question as to whether sirtuin inhibition was a major factor contributing to apoptotic cell death could not be addressed by these preliminary experiments. While the sequence of events (hyperacetylation of p53 \rightarrow activation of p53 \rightarrow induction of apoptosis) may provide support for this notion, the likelihood of **5-1** or **8-7** acting on other oncogenic targets should not be discounted.

In an earlier study, Peck *et al.*¹⁴¹ proposed that sirtuin inhibitors sirtinol and salermide induced apoptosis only in cell lines that had functional p53. If this was the case, differential effects should be observed in HuH7 (mutated p53) and HepG2 (WT p53). However, the present results showed that **5-1** and **8-7** promoted acetylation of p53 and α -tubulin on both

cell lines at comparable concentrations. Other investigators have maintained that there was no correlation between p53 status and sirtuin expression.¹³⁴ Clearly, this is an unresolved issue that warrants further investigation.

4.5. Summary

Taken together, potent SIRT2 inhibitors have been identified from a focused library of functionalized benzylidene indolinones. The most potent inhibitors were the benzylideneindolinones substituted at position 6 with methoxy (Series 5) and *N*-substituted analogs of **47** (Series 8). Several members in Series 5 were also found to be moderately active SIRT1 inhibitors. Inhibition by representative members (**5-1**, **8-7**) promoted the hyperacetylation of physiological sirtuin substrates (p53 and α -tubulin) and induced the apoptotic cascade in HuH7 cells. SAR for SIRT2 inhibition is summarized in Figure 4-18. Support for the differences in inhibitory activity was derived from molecular docking.

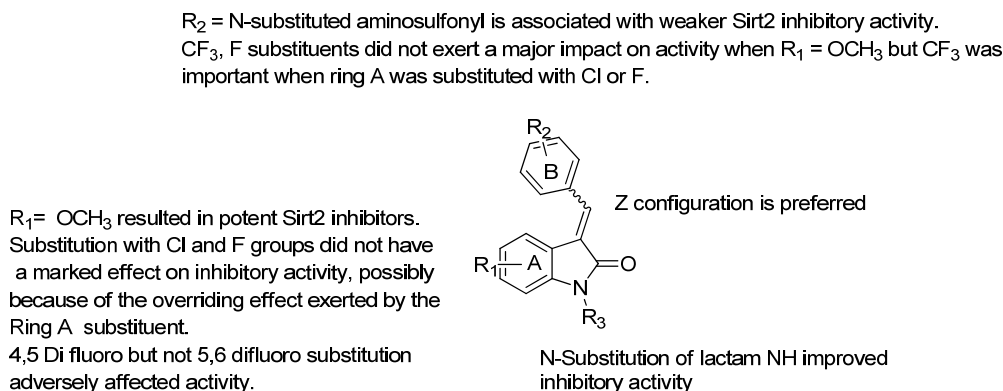


Figure 4-19: Summary of SAR for SIRT2 inhibitory activity.

Chapter 5: Investigations into the receptor tyrosine kinase (RTK) inhibitory activity of Compound 3-12.

5.1. Introduction

In this chapter, compound **3-12** was investigated for its ability to inhibit the phosphorylation of RTKs in HuH7 lysates. Inhibition of the identified RTKs were confirmed by demonstrating reductions in the protein levels of the affected RTKs by Western blotting or immunoprecipitation. The docking of **3-12** on a homology model of human FGFR4 was carried out to provide some insight into the interactions of **3-12** in the binding pocket of FGFR4 that could explain its inhibitory activity.

5.2. Experimental methods

5.2.1. Chemicals and Materials

Penicillin G and streptomycin were from Sigma-Aldrich Co (Singapore). Fetal bovine serum (FBS) was from Invitrogen Life Technologies (CA, USA). Cell culture media were from Sigma-Aldrich Co (Singapore). Stock solutions of **47** and **3-12** (10 mM) were prepared in DMSO (ACS grade, NUS Lab Supply) and stored at 25°C. Rabbit monoclonal antibodies to phosphorylated HER-3 (Tyr 1289), HER-3, FGFR 4, phosphorylated Akt (Ser 732), Akt and mouse monoclonal antibodies to phosphorylated tyrosine were purchased from Cell Signaling Technology, Inc. (MA, USA). Goat anti-rabbit-horse radish peroxidase (HRP) conjugate and goat anti-mouse HRP were purchased from Santa Cruz (CA, USA). Human phospho-receptor tyrosine kinase (RTK) array kit (Catalog No ARY001B) was purchased from RnD Systems Inc. (MN, USA). Blocking buffer for the immunoblot assay (Blocking One) was obtained from Nacalai Tesque Inc (Kyoto, Japan). Pierce Stripping Buffer was purchased from Thermo Scientific (MA, USA). Chemiluminescence reagent (ECL) used in the immunoblot assay was from GE Healthcare (Buckinghamshire, UK).

5.2.2. Preparation of HuH7 cell lysates

HuH7 cell lysates were prepared as described in Section 3.2.5.

5.2.3. Protein quantification

Protein quantification was carried out using the Bradford Protein Assay Kit (Bio-Rad Laboratories Inc, CA, USA) as described in Section 3.2.6.

5.2.4. Immunoprecipitation

Cell lysates were obtained as described in Section 5.2.2 and protein content was determined as described in Section 5.2.3. Pierce Protein A/G Plus Agarose beads were washed three times with immunoprecipitation (IP) buffer (25mM Tris-base, 150mM NaCl; pH 7.2). Cell lysates containing 1000 µg protein were gently agitated with FGFR4 total antibody (2 µL) overnight at 4 °C and then with pre-washed Pierce Protein A/G Plus Agarose beads for 3 hr at 25 °C. After this time, the suspension was centrifuged at 13,000 g for 5 min. The supernatant was discarded and the beads washed with IP buffer thrice after which they were deactivated with 50 µL 1×SDS at 99 °C for 5 min. The mixture was quickly centrifuged to give the supernatant which was separated on SDS PAGE as described in Section 5.2.5.

5.2.5. Sodium dodecyl sulfate - polyacrylamide gel electrophoresis (SDS-PAGE)

Cell lysates were separated as described in section 3.2.7. cell lysates were separated on the SDS-PAGE Bio-Rad Mini-Protean II system (Bio-Rad Laboratories Inc, CA, USA). Each sample with the same protein amount were loaded on to separate lanes and were separate using the same method described in the Section 3.2.7. After electrophoresis, the gels were subjected to Western blotting (Section 5.2.6).

5.2.6. Western blotting

Western blotting was carried out as described in Section 3.2.8.

5.2.7. Human receptor tyrosine kinase profiling

5.2.7.1. Principle of human phospho-receptor tyrosine kinase array

The array is an enzyme-linked immunosorbent assay carried out on nitrocellulose membranes instead of wells in a plate (Figure 5-1). Each nitrocellulose membrane was pre-spotted with a mixture containing antibodies (“capture antibodies”) to 49 different human RTK proteins. The nitrocellulose membranes were then incubated overnight with the drug-treated or control (untreated) HuH7 cell lysates. RTKs (phosphorylated and non-phosphorylated) in the cell lysates would bind to their cognate antibodies on the membrane but only the phosphorylated RTKs would be detected by chemiluminescence when the membranes were subsequently washed (to remove unbound material) and treated with a pan anti-phospho-tyrosine antibody conjugated to HRP.

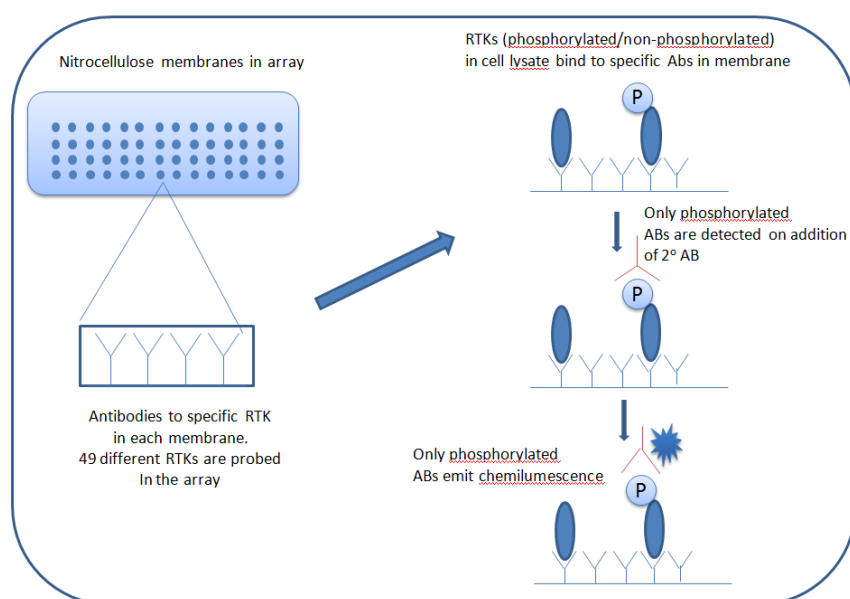


Figure 5-1 Cartoon depicting the principle underlying the detection of phosphorylated RTKs in the Phospho-RTK Array Kit (RTK : Receptor Tyrosine Kinases; AB = antibodies; P = phosphorylated)

5.2.7.2. Procedure

Simultaneous determination of multiple RTK phosphorylation was achieved with Human Phospho-RTK array. HuH7 cells were subjected to vehicle control, **47** (10 μM) or **3-12** (0.5 μM and 2 μM) for 24 hr. Cells harvesting, hybridization with RTK array and incubation with anti-phosphotyrosine were performed according to manufacturer’s instruction.

Briefly, the HuH7 cells were treated with the vehicle control or compounds for 24 hr, after which cells were collected, washed with 1× PBS twice, dissolved in Lysis Buffer 17 to give a final concentration of 10⁷ cells/mL. Protein content was determined as described in Section 5.2.3. Solutions containing cell lysates (800 µg protein) were prepared in 1.5 mL Array Buffer 1. The nitrocellulose membranes were blocked with Array Buffer 1 for 1 hr at 25°C and then incubated with the protein solution prepared from the cell lysates overnight at 4°C. The membranes were washed in Array Buffer 2 (thrice, 10 min per wash) and incubated with anti-phospho-tyrosine-HRP detection antibodies for 2hr at 25 °C. The membranes were then washed thrice (10 min per wash) with Array Buffer 2 and incubated with pro-chemiluminescence reagent for 5-10 minutes. The chemiluminescence signals were captured on Gel Doc and quantified by Image J (Version 1.47, NIH, Bethesda, Maryland) Signals from duplicate spots for each RTK were averaged and reported.

The alignment of the different antibodies on the array is given in Figure 5-2 and the RTKs detected by these antibodies are shown in Table 5-1.

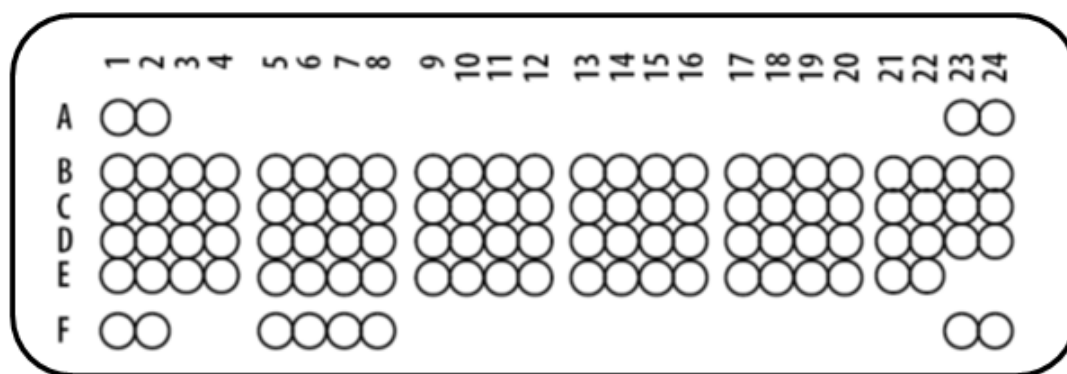


Figure 5-2: Coordinates of the antibody array

Table 5-1: RTKs corresponding to the coordinates in the antibody array

Coordinates	Receptor Family	RTK/control	Coordinates	Receptor Family	RTK/control
A1, A2	Reference Spots	—	D1, D2	Tie	Tie-2
A23, A24	Reference Spots	—	D3, D4	NGF R	TrkA
B1, B2	EGF R	EGF R	D5, D6	NGF R	TrkB
B3, B4	EGF R	HER 2	D7, D8	NGF R	TrkC
B5, B6	EGF R	HER 3	D9, D10	VEGF R	VEGF R1
B7, B8	EGF R	HER 4	D11, D12	VEGF R	VEGF R2
B9, B10	FGF R	FGF R1	D13, D14	VEGF R	VEGF R3
B11, B12	FGF R	FGF R2 α	D15, D16	MuSK	MuSK
B13, B14	FGF R	FGF R3	D17, D18	Eph R	EphA1
B15, B16	FGF R	FGF R4	D19, D20	Eph R	EphA2
B17, B18	Insulin R	Insulin R	D21, D22	Eph R	EphA3
B19, B20	Insulin R	IGF-1 R	D23, D24	Eph R	EphA4
B21, B22	Axl	Axl	E1, E2	Eph R	EphA6
B23, B24	Axl	Dtk	E3, E4	Eph R	EphA7
C1, C2	Axl	Mer	E5, E6	Eph R	EphB1
C3, C4	HGF R	HGF R	E7, E8	Eph R	EphB2
C5, C6	HGF R	MSP R	E9, E10	Eph R	EphB4
C7, C8	PDGF R	PDGF R α	E11, E12	Eph R	EphB6
C9, C10	PDGF R	PDGF R β	E13, E14	Insulin R	ALK
C11, C12	PDGF R	SCF R	E15, E16	—	DDR1
C13, C14	PDGF R	Flt-3	E17, E18	—	DDR2
C15, C16	PDGF R	M-CSF R	E19, E20	Eph R	EphA5
C17, C18	RET	c-Ret	E21, E22	Eph R	EphA10
C19, C20	ROR	ROR1	F1, F2	Reference Spots	
C21, C22	ROR	ROR2	F5, F6	Eph R	EphB3
C23, C24	Tie	Tie-1	F7, F8	—	RYK
			F23, F24	Control (-)	PBS

5.2.8. FGFR4 homology model and molecular docking

The FGFR4 homology model was built by Dr Jin Haixiao from Ningbo University, PRC. The homology model was based on the X-ray structure of the tyrosine kinase domain of human FGFR1 co-crystalized with an inhibitor SU 4984 ¹⁴⁶ (retrieved from RCSB Protein Data Bank; PDB code 1AGW, 2.40 Å resolution) and the primary sequence of FGFR4 ²⁰⁵ (retrieved from Universal Protein Resource, entry code AEO19721.1). The sequence of human FGFR4 and crystal structure of FGFR1 were aligned using the Align application in Molecular Operating Environment (MOE, version 2011, Chemical Computing Group, Montreal, Canada).

The *E* and *Z* structures of the **3-12** and **47** were separately prepared for docking on MOE. Docking was carried out on GOLD v 5.2 (Cambridge Crystallographic Data Centre Software Ltd, Cambridge, UK) with default GA settings. The binding pocket was defined by the atoms

within 6 Å radius of the co-crystallized ligand SU 4984 in 1AGW. Docking was carried out without the reference ligand (SU 4984). GOLD uses a genetic algorithm (GA) for docking flexible ligands into the binding pocket to explore the full range of ligand conformational flexibility.¹⁹¹ The GOLD Score was used as the fitness function for selection of the best docked conformations of test compounds in the binding pocket. For each molecule, the top 10 docked conformations were retained and analyzed graphically with MOE.

5.3. Results

5.3.1. Effects of **47** and **3-12** on the phosphorylated states of RTKs in

HuH7 cells

Although the original intent was to screen a larger number of compounds from Series 1-8 for inhibition of RTKs, this could not be realized because of the high cost of screening on the Human phospho-RTK antibody array. Consequently, it was decided that only 2 compounds could be screened. **3-12** was selected for its promising activity and drug like character (Chapter 6) and **47** was tested because it was the lead compound and was found to inhibit FGFR4 (among other RTKs) in HuH7 cells (unpublished results). Thus **47** served as a positive control.

Figure 5-3A shows the results from membranes exposed to lysates from untreated HuH7 cells. The levels of seven phosphorylated RTKs were elevated in untreated HuH7 cells. They were EGFR, ErbB2 (Her2), ErbB3 (Her 3), FGFR4, insulin receptor, Mer and RYK (receptor tyrosine kinase). When the cells were treated with **47** or **3-12**, phosphorylation either remained unchanged (reflected by no change in signal intensity) or was reduced (reduction in signal intensity) (Figure 5-3 B-D).

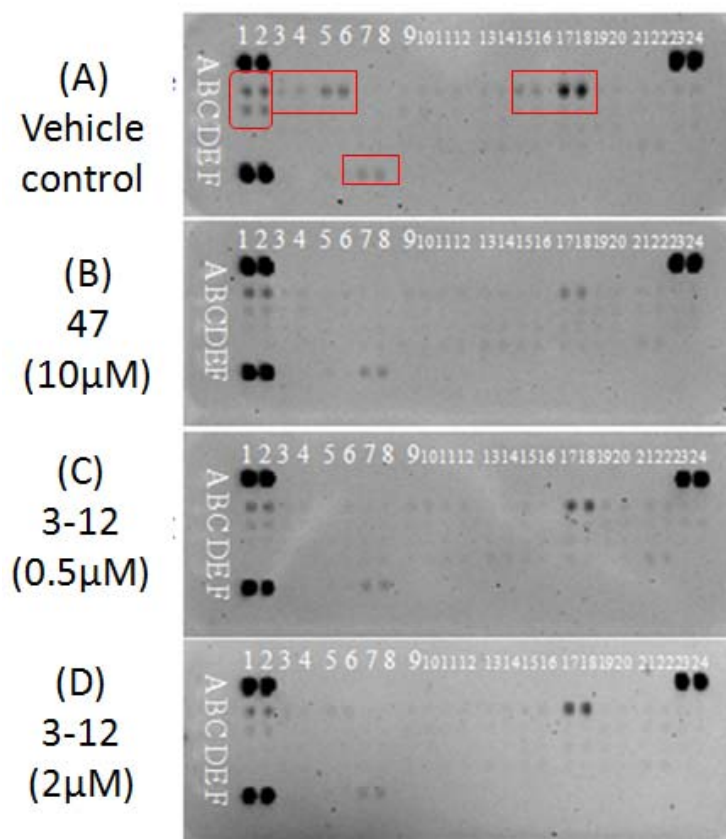


Figure 5-3: Intensity of blots obtained from (A) untreated HuH7 cells and HuH7 cells treated with (B) 47 at 10 μ M, (C) 3-12 at 0.5 μ M and (D) 3-12 at 2 μ M. Intense reference spots at the extreme left and right upper corners and extreme left lower corners of each blot indicated that the protocol was carried out correctly. Red brackets in (A) correspond to RTKs that were upregulated in untreated HuH7 cells. If test compound had no effect on the RTK, the intensities of the spots corresponding to the RTK in (A) would be unchanged in the treated membranes. If the test compound reduced the expression or inhibited the phosphorylation of the RTK, the intensity in the treated membranes would be lower than that observed in (A).

Table 5-2 summarizes the effects of 47 and 3-12 on the phosphorylated RTKs that were upregulated in HuH7 cells. Both compounds had a marked effect on the phosphorylation of HER3 and FGFR4 as seen from the greatly diminished signal intensities. Dose dependent reduction in signal intensity was however not evident. Notably, 3-12 was investigated at two concentrations (0.5 μ M, 2 μ M) but paradoxically, gave a stronger HER3 signal (34%) at the higher concentration (2 μ M). The signal intensities from the FGFR4 blots could not be distinguished in spite of the 4-fold difference in concentration of 3-12. Both compounds reduced the signal intensities of blots corresponding to HER-2, Insulin Receptor and Mer but the reductions were less pronounced than that of FGFR4 and HER3. Neither 47 nor 3-12 affected the phosphorylation of EGFR significantly.

Table 5-2: Effects of **47** and **3-12** on the intensities of blots (determined by densitometry) corresponding to phosphorylated RTKs that were upregulated in untreated HuH7 cells.

Kinase family	Receptor Tyrosine kinase	Coordinates on microarray ^a	Vehicle control ^b	Intensity of blot normalized against corresponding blot in control membrane ^c		
				47 (10 μ M)	3-12 (0.5 μ M)	3-12 (2 μ M)
EGF R	EGFR	B1,B2	100.00%	118 % (123%, 113%)	77% (81%, 74%)	90 % (90%, 89%)
EGF R	ErbB2(HER2)	B3,B4	100.00%	34 % (49%, 19%)	38% (41%, 35%)	42% (48%, 36%)
EGF R	ErbB3(HER3)	B5,B6	100.00%	4% (3.9%, 3.6%)	3% (3.1%, 2.4%)	34% (31%, 38%)
FGFR	FGFR4	B15, B16	100.00%	5% (5.5%, 3.9%)	7% (11%, 2.9%)	7% (11%, 3%)
Insulin R	Insulin R	B17,B18	100.00%	23% (23%, 23%)	62% (71%, 53%)	72% (70%, 75%)
AXI	Mer	C1,C2	100.00%	52% (56%, 48%)	52% (56%, 48%)	43% (43%, 43%)
-	RYK	F7,F8	100.00%	95% (104%, 85%)	93% (111%, 76%)	68% (48%, 87%)

^a Coordinates indicated location of the RTK antibody in the microarray membrane as shown in Figure 5-2. ^b These phosphorylated RTKs were identified in the membrane exposed to untreated HuH7 cells (Figure 5-3A). The intensities of the blots were assigned 100%. ^c The intensity of the corresponding blots in the treated membranes were normalized against the control blots and expressed as a %. Average of two readings.

To confirm that **3-12** reduced the phosphorylation of HER3 and FGFR4, the protein levels of HER3 and FGFR4 were monitored in HuH7 cells treated with a range of concentrations of **3-12** for the same time period. Both phosphorylated and total Her3 levels were monitored by Western blot whereas phosphorylated and total FGFR4 levels were probed by immunoprecipitation. **3-12** reduced levels of both phosphorylated Her3 and phosphorylated FGFR4. Reductions were observed at the lowest concentration (0.2 μ M) for phospho-HER3 and at a higher concentration (1 μ M) for phospho-FGFR4.

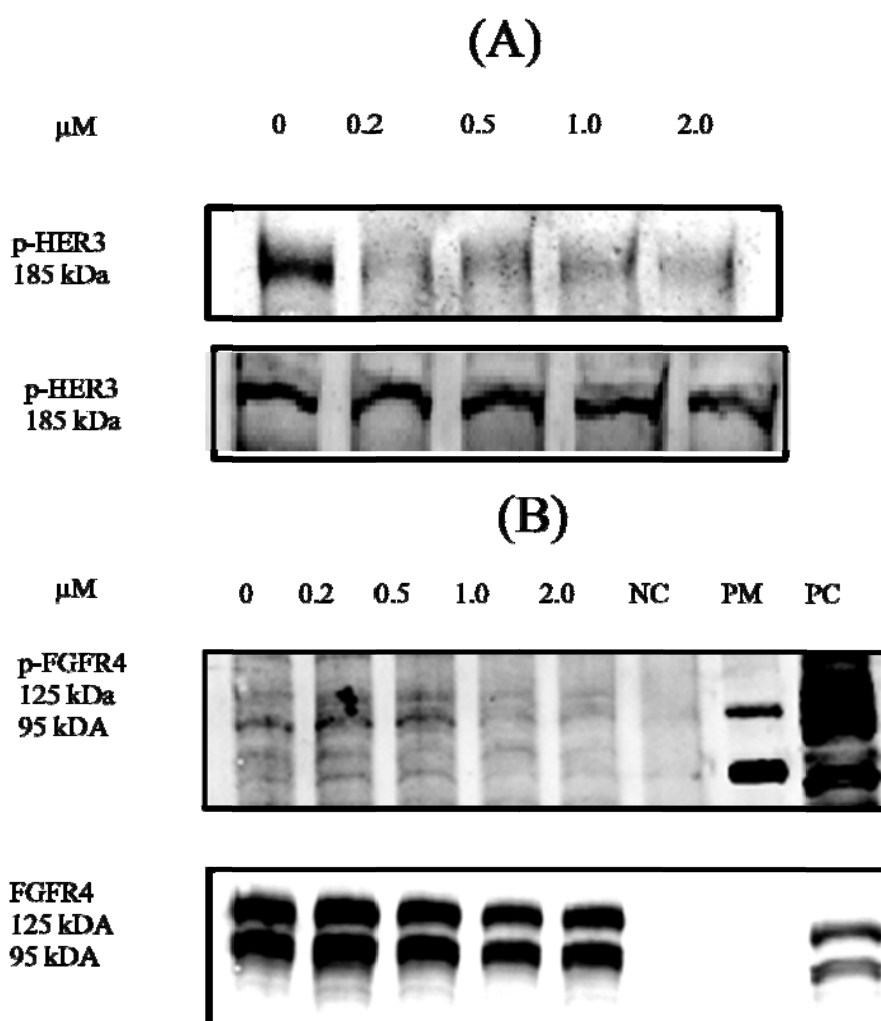


Figure 5-4: (A) **3-12** reduced the phosphorylation of HER3 at Tyr1289 in HuH7 cells after 24 h incubation. Total HER3 protein levels were unchanged under similar treatment conditions. (B) **3-12** reduced the phosphorylation of FGFR4 at all tyrosine sites in the protein. Total FGFR4 levels were unchanged on compound treatment. NC (Negative control): Cell lysates treated with non-specific IgG antibody during immunoprecipitation; PC (Positive control): Phospho-FGFR4: Cell lysates without immunoprecipitation, probed with phosphor-tyrosine antibody. FGFR4: Cell lysates without immunoprecipitation, probed with total FGFR4 antibody. PM (Protein Marker): Two protein markers 100kDa and 75 kDa (Biorad, Hercules, California) were used as guides to identify the bands in other lanes. p-FGFR4/FGFR4 is the ratio of the signal intensities of bands at 95 kDa, normalized against the ratio obtained in untreated cells.

The PI3K/AKT/mTOR signaling pathway is downstream to many receptor tyrosine kinases including HER3²⁰⁶ and FGFR4.²⁰⁷ Since **3-12** inhibited the phosphorylation of HER3 and FGFR4, it was expected to curtail signaling along this pathway. Hence, levels of phospho-Akt were probed in HuH7 cells treated with **3-12**. As shown in Figure 5-5, **3-12** reduced levels of phospho-Akt over a range of concentrations (0.2 – 2.0 μM).

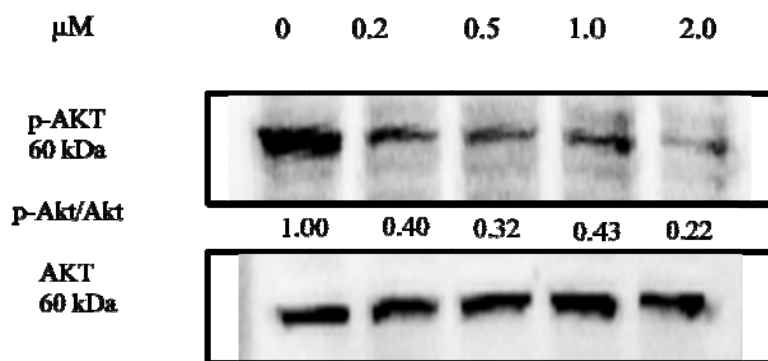


Figure 5-5: **3-12** reduced the phosphorylation of Akt in HuH7 treated cells (24 h, 37°C, 5% CO₂). Phospho-Akt and total Akt levels were probed by Western blotting. Loading control was total Akt. p-Akt/Akt is the ratio of the signal intensities of respective bands, normalized against the ratio obtained in untreated cells.

5.3.2. Molecular docking of **3-12** in a homology model of human FGFR4

The crystal structure of the same domain in FGFR4 has not been solved. Thus a homology model of FGFR4 was constructed based on FGFR1. FGFR1 has close sequence homology to FGFR4, with 55% homology overall and 74% for the ATP binding site.²⁰⁸

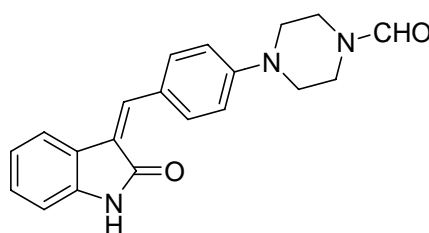


Figure 5-6: Structure of SU 4984 (4-[4-(2-oxo-1,2-dihydroindol-3-ylidenemethyl)-phenyl]-piperazine-1-carbaldehyde)

The docking pose of SU 4984 (Z isomer) was first examined in the homology model. It was found to form H bonds with the hinge region of the ATP binding site. The lactam NH was directed to Glu 563 and the lactam carbonyl towards Ala 561 (Figure 5-7 A, C, D). The benzylidene phenyl ring established CH- π interactions with Leu 473. The piperazinyl ring projected out of the binding pocket towards the open solvent phase, as shown in Figure 5-7B.

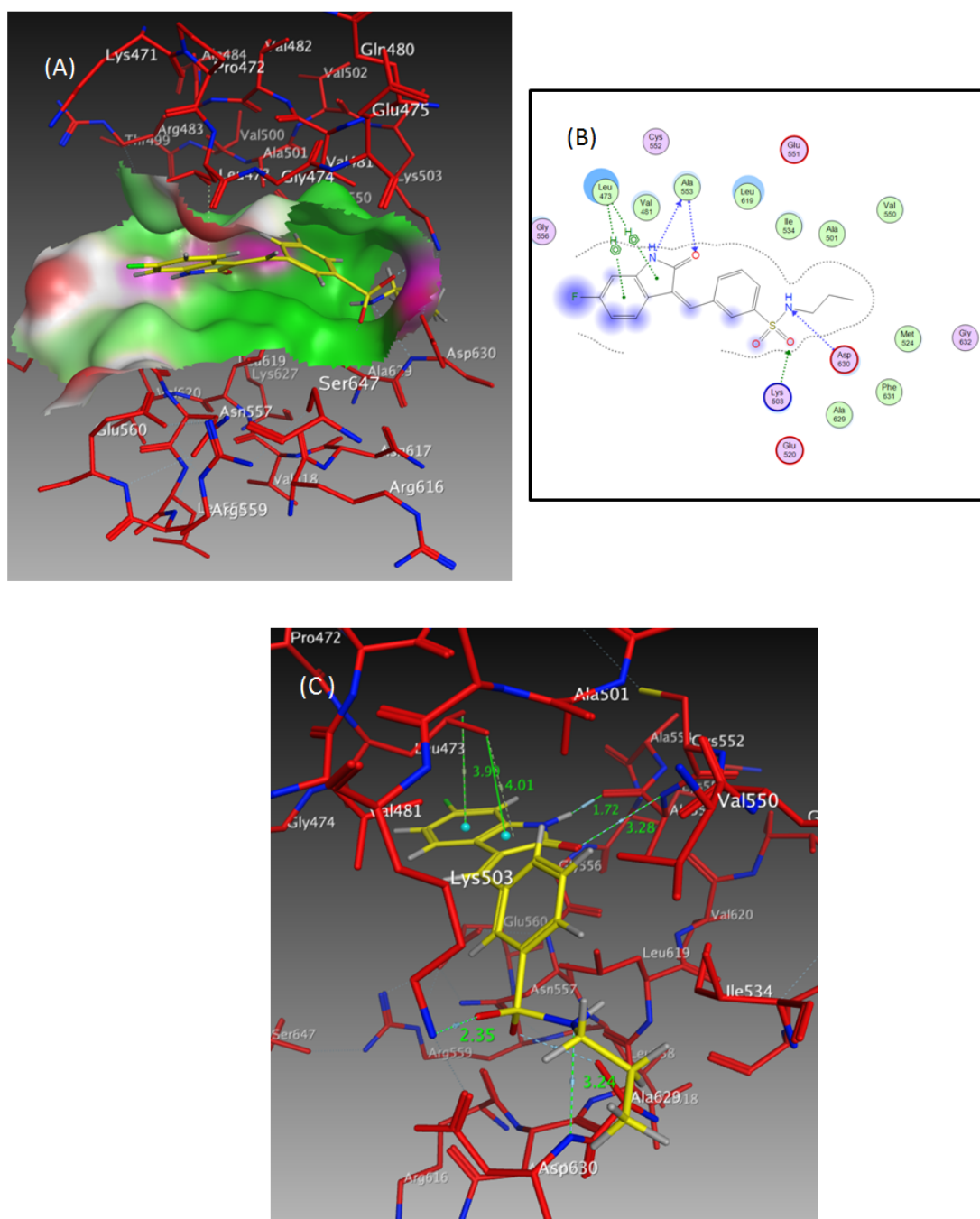


Figure 5-8: Docking pose of **3-12Z** in the FGFR4 binding pocket. (A) The indolinone ring of **3-12Z** is directed towards the solvent pocket. The binding pocket is color coded as follows: Green = hydrophobic; Magenta = polar, Red = exposed. (B) Ligand interaction map of **3-12Z** (MOE2011). (C) Close up of **3-12Z** at the hinge region, showing interactions with Ala 563 and Leu 473 (CH- π interactions). The aminosulfonyl side chain was H bonded to Lys 503 and Asp 630.

Compound **3-12E** (Figure 5-9) assumed a similar orientation to **3-12Z**. The sulfonylamino side chain on the benzylidene ring was H bonded to Asp639 and Lys 503 (through the sulfonyl O) and the lactam on the indolinone ring was H bonded to Ala 563. The indolinone ring in the *E* isomer was almost orthogonal to the same ring in **3-12Z**.

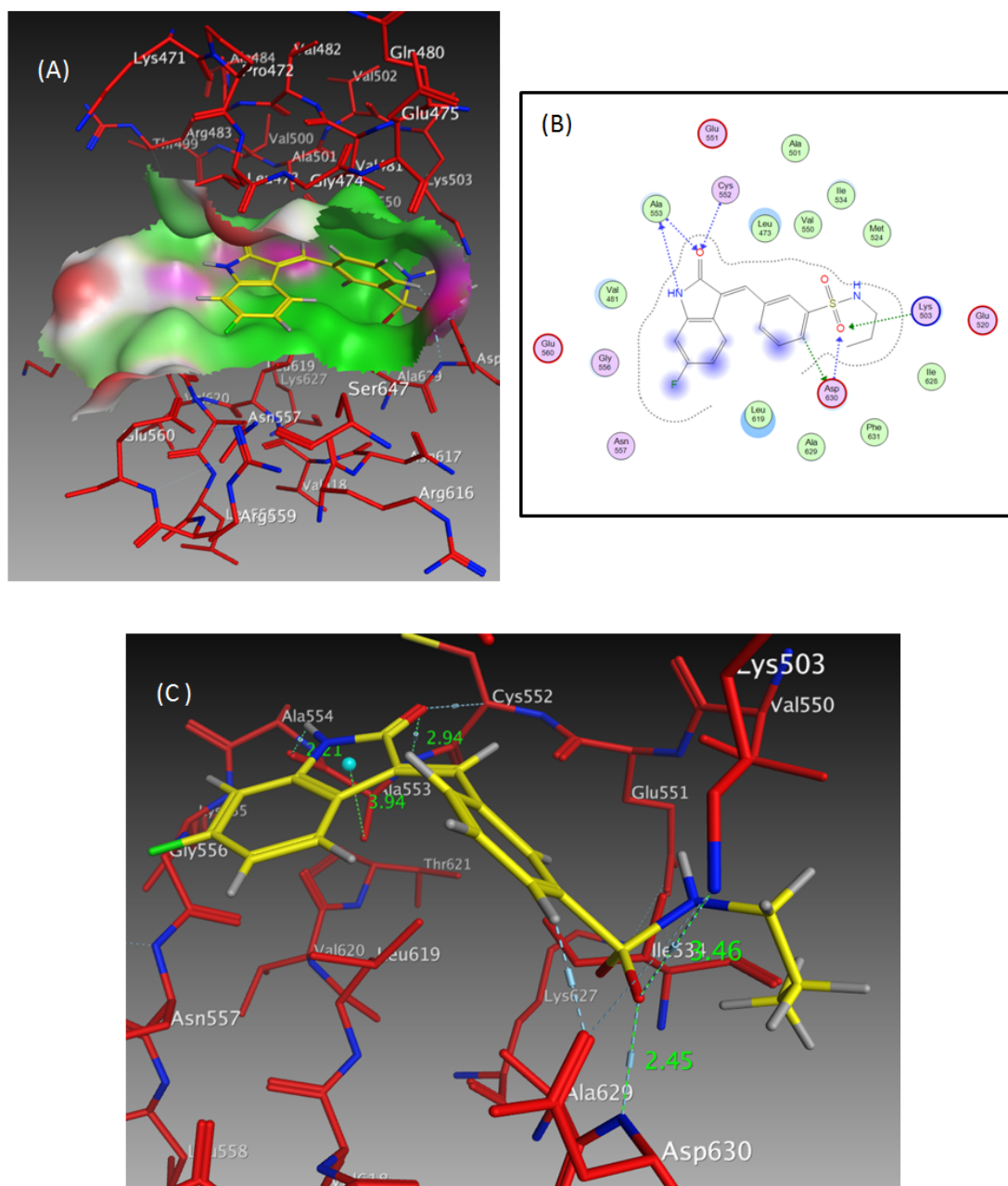


Figure 5-9: Docking pose of **3-12E** in the FGFR4 binding pocket. (A) The indolinone ring of **3-12E** is directed towards the solvent pocket. The binding pocket is color coded as follows: Green = hydrophobic; Magenta = polar, Red = exposed. (B) Ligand interaction map of **3-12E** (MOE 2011). (C) Close up of **3-12E** at the hinge region, showing interactions with Ala 563, Lys 503, Asp 630. The NH of the sulfonylamino side chain is not involved in H bonding.

The orientation of **47Z** and **47E** were also examined in the FGFR4 binding pocket. The binding pose of **47E** closely resembled that of SU 4984. The lactam moiety in **47E** was H bonded to Ala 563 and Glu 561, and a CH- π interaction between the indolinone ring and Val481 was evident (Figure 5-10). The benzylidene ring was oriented towards the solvent phase.

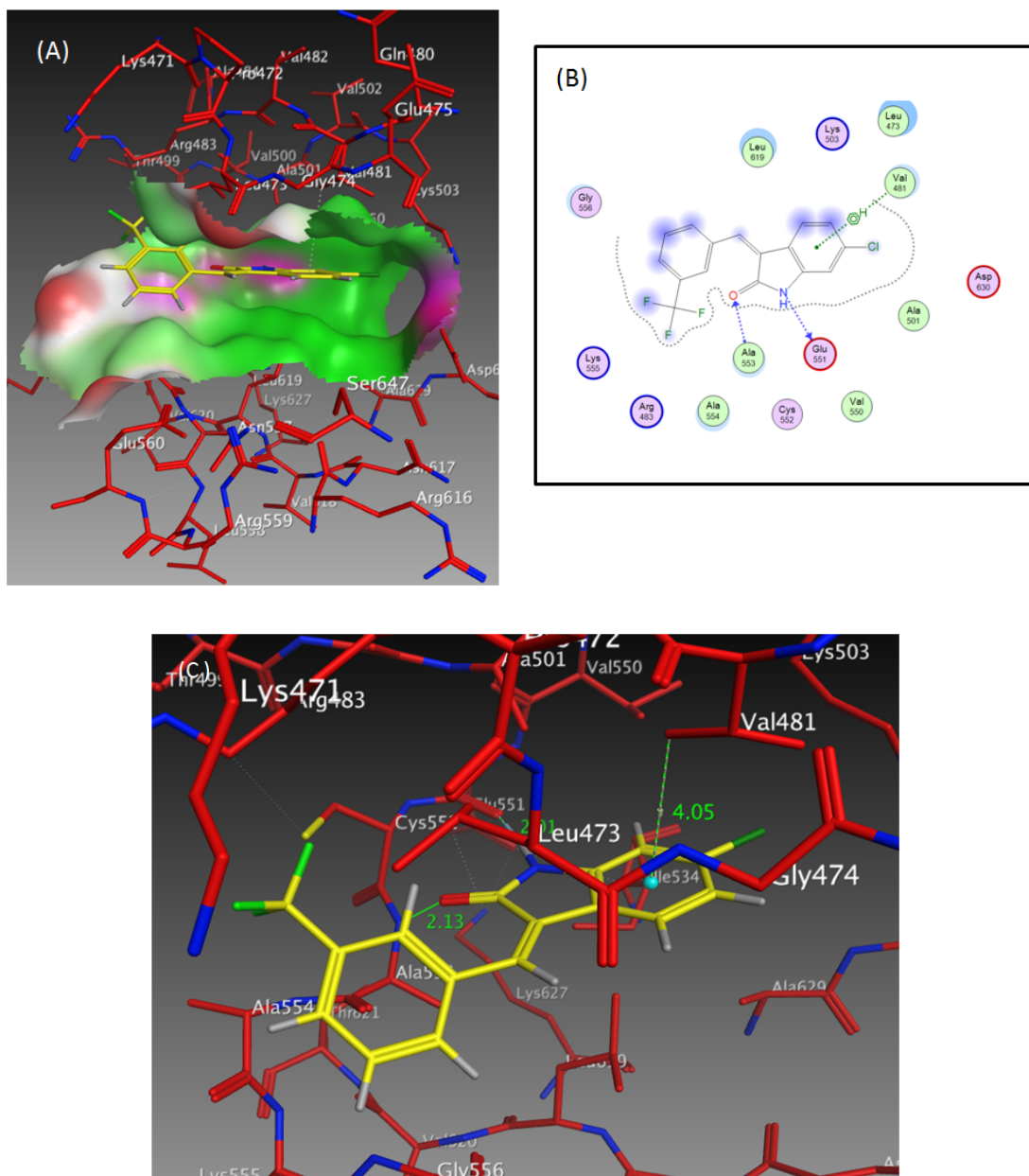


Figure 5-10: Docking pose of **47Z** in the FGFR4 binding pocket. (A) The benzylidene ring of **47Z** is directed towards the solvent phase. The binding pocket is color coded as follows: Green = hydrophobic; Magenta = polar, Red = exposed. (B) Ligand interaction map of **47Z** (MOE 2011). (C) Close up of **47Z** at the hinge region, showing interactions with Ala 563, Glu561, Val 481.

Compound **47E** had a similar orientation (Figure 5-11) except that the benzylidene ring was not extended along the length of the binding pocket but projected “out” of the pocket as depicted in Figure 5-11C.

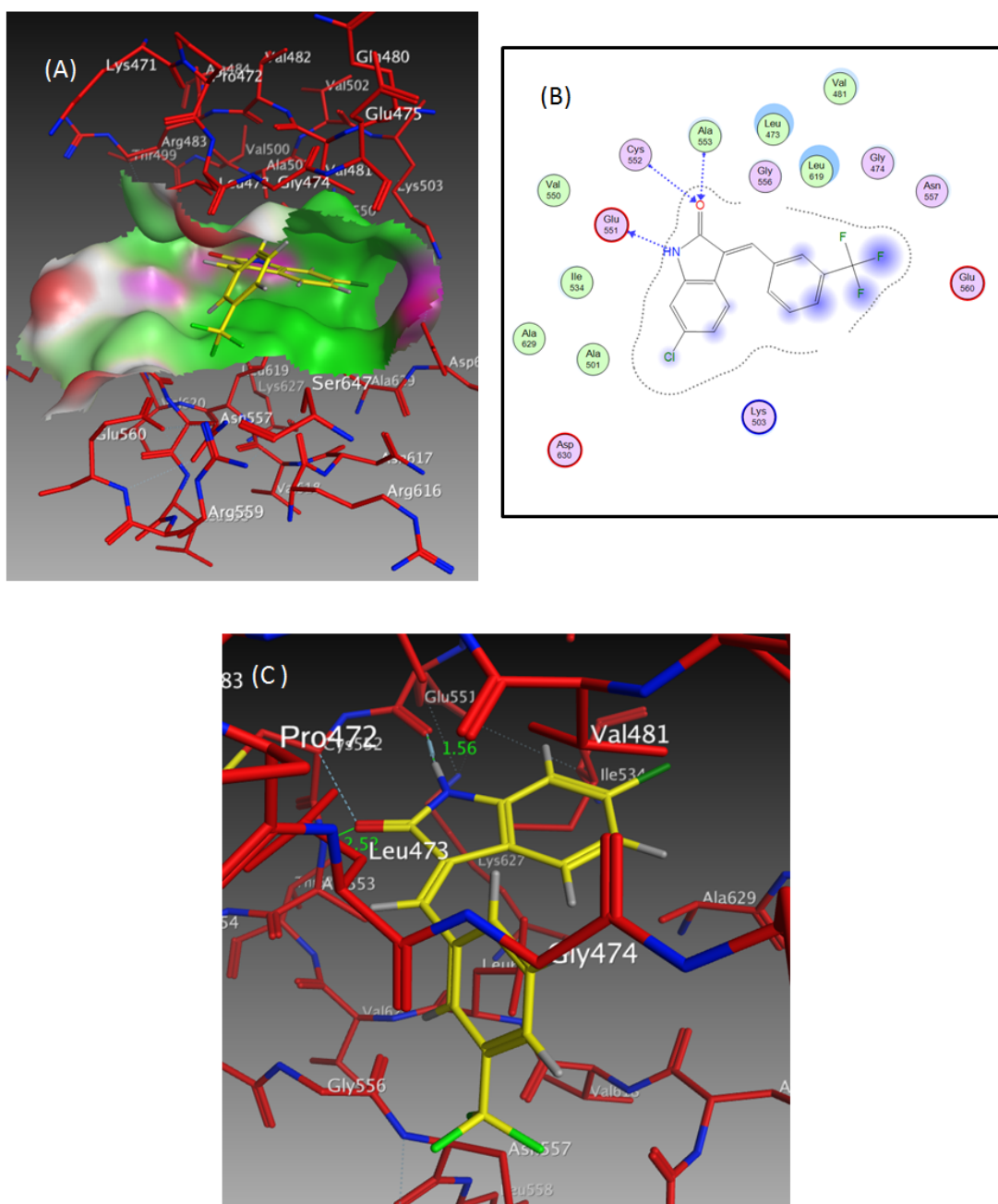


Figure 5-11: Docking pose of **47E** in the FGFR4 binding pocket. (A) The benzylidene ring of **47E** is directed towards the solvent phase. The binding pocket is color coded as follows: Green = hydrophobic; Magenta = polar, Red = exposed. (B) Ligand interaction map of **47E** (MOE 2011). (C) Close up of **47E** at the hinge region, showing interactions with Ala 563, Glu561.

5.4. Discussion

Compound **3-12** was identified in Chapter 3 as one of the more potent and selective compounds affecting the viability of HuH7 cells. Although not the “best” compound, **3-12** had some advantageous features such as better solubility and permeability than the lead

compound **47** (described in Chapter 6). The presence of the *N*-propylaminosulfonyl side chain was another positive feature as the latter would offer opportunities for structural modification, thus addressing a key concern of **47** which was its under-functionalized state.

Evaluation of **47** and **3-12** on the human phospho-RTK array identified two RTKs (HER3 and FGFR4) in HuH7 cells whose phosphorylations were significantly reduced by both compounds. **47** was previously investigated for inhibition of RTKs using a similar platform. In that study, HER3 and FGFR4 were among the RTKs (insulin receptor, IGF-1R, Tyro3, EphA2, Met, RON) inhibited by **47**. The present study confirmed that **47** inhibited the phosphorylation of HER3 and FGFR4 in HuH7 cells. It also identified other RTKs (HER2, insulin receptor, Mer) that were inhibited by **47**, of which only insulin receptor was flagged out in the earlier study by Ho *et al.* (unpublished data). A possible reason may be the different experimental conditions employed in that study. For example, Ho *et al.* used serum starved HuH7 cells which were not used here.

The inhibition of HER3 and FGFR4 by **3-12** were detected at lower concentrations (0.5 μ M, 2 μ M) than **47** but this need not imply that **3-12** was more potent than **47** as this platform was more useful as a qualitative (and not quantitative) indicator of inhibition. Moreover **47** was investigated at only 1 concentration and its effects were not investigated at lower concentrations. However, it was encouraging to note that **3-12** reduced phosphorylation of HER3 and FGFR4 at low to sub-micromolar concentrations (0.5 μ M, 2 μ M).

HER3 is a member of the EGFR family and higher levels of HER3 have been found in HCC tissue samples (84%) compared to non-malignant tissue (38%).²⁰⁹ HER3 signaling is unique in that HER3 lacks intrinsic tyrosine kinase activity and can only trigger downstream signaling pathways when it forms a dimer with the HER2 isoform.²¹⁰ Heterodimerization and transphosphorylation activates HER3, promotes its binding to PI3K and signaling along the PI3K/Akt/mTOR pathway.²⁰⁶ Tyrosine kinase inhibitors (TKIs) directed towards HER2 were found to be ineffective against HER2 driven tumors because of a compensatory shift in HER3 phosphorylation-dephosphorylation equilibrium (promoting phosphorylation at the expense of dephosphorylation) that is driven by Akt mediated negative feedback signaling.²¹¹ The present

finding that **3-12** reduced the phosphorylation of both HER2 and HER3 is therefore interesting. It may be that **3-12** is able to inhibit HER2-HER3 heterodimer formation or the transphosphorylation of these kinases.

FGFR4 is the only isoform of FGFR expressed at high levels in hepatocytes²¹² and the liver has the highest transcript expression of FGFR 4 compared to other major organs.²¹³ Ho *et al.*²¹⁴ reported that inhibition of FGFR4 activity in HuH7 cells with PD173074 (a low micromolar non-selective inhibitor of FGFR) blocked proliferation to a greater extent than other HCC cells that have lower levels of FGFR4. FGFR4 was found to modulate α -fetoprotein (AFP) secretion in HCC cell lines, with AFP levels declining on FGFR4 silencing and increasing when HepG2 cells (a HCC cell line with low basal levels of AFP) were stimulated with FGF19 (a ligand of FGFR4). The authors concluded that FGFR4 contributed significantly to HCC progression by modulating AFP secretion, proliferation and anti-apoptosis.²¹⁴ The present findings have identified **47** and **3-12** as inhibitors of FGFR4. Both compounds inhibited the viability of HuH7 cells (high FGFR4 levels) to a greater degree than HepG2 cells (low FGFR4 levels). **3-12** induced apoptosis and reduced FGFR4 protein levels in HuH7 cells at comparable (0.5 μ M-2 μ M). Investigations should be directed to interrogating the specificity (FGFR4 versus other isoforms) and mechanistic aspects of the inhibition.

Molecular docking provided some support for the notion that **3-12** interacted with the binding pocket of FGFR4. Based on a homology model of FGFR4, both *E* and *Z* isomers of **3-12** adopted poses in the hinge region of FGFR4 which were reinforced by H bonding between the indolinone lactam NHCO and Ala 561. The presence of the *N*-propylaminosulfonyl side chain on the benzylidene ring of **3-12** had a significant influence on the docking poses as its ability to form H bonds directed the side chain away from the solvent exposed regions of the binding pocket. This was in contrast to the benzylideneindolinone SU 4984, the co-crystallized ligand of the FGFR1 X-ray structure (PDB 1AGW) that was used to build the homology model in this chapter. The pose of SU4984 in homology model showed striking similarities to its pose in the FGFR1 pocket (Figure 5-12). The lactam moiety of SU 4984 was H bonded to

Ala and Gly residues in the hinge region, and the polar piperazinyl side chain was directed towards the exposed solvent phase.

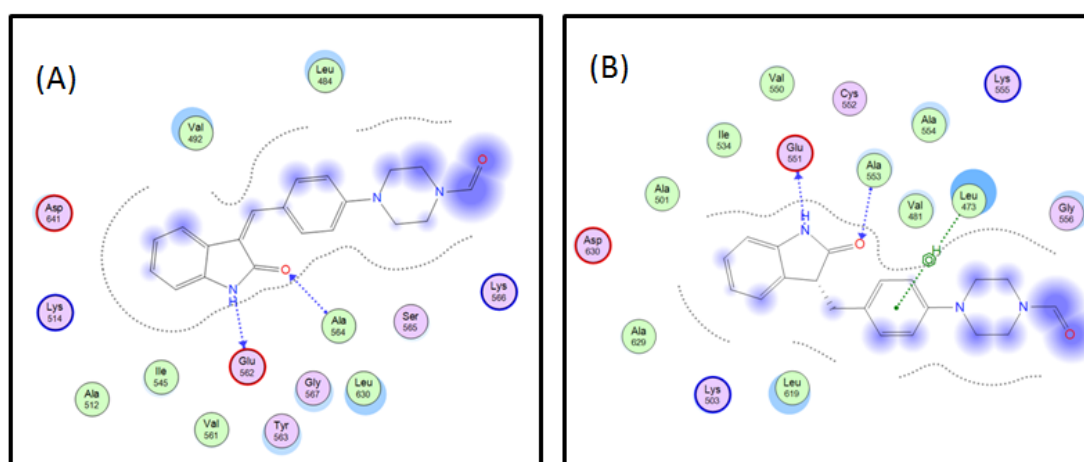


Figure 5-12: Orientation of SU 4984 in (A) FGFR1 (PDB 1AGW) and (B) FGFR4 homology model. The blue coloration depicts parts of the molecule that are solvent exposed.

The *N*-propylaminosulfonyl side chain of **3-12** may be less polar in spite of its H bonding potential and this could have directed it away from solvent exposed regions of the binding pocket. Interestingly, both **3-12Z** and **3-12E** assumed very similar orientations at the hinge region. H bonding to the hinge region occurred via Ala 561, and the *N*-propylsulfonylamino side chain in both isomers were H bonded to the same residues (Lys 503, Asp 630). There was however an additional CH π interaction between the indolinone ring of **3-12 Z** and Leu 473 that was not observed in **3-12E**.

The docking poses of **47E** and **47Z** were strikingly similar to that of SU 4984 in that the lactam moiety was involved in H bonding at the hinge region (Ala 561, Glu 563) the benzylidene ring was directed towards the exposed solvent. In this regard, the lipophilic CF₃ substituted benzylidene ring may not be well placed for interaction with solvent. Potential multipolar interactions between the C-F bonds and residues flanking CF₃ were not obvious from the top ranked poses of **47Z** and **47E**. Based on an analysis of interactions in the docked poses, **3-12** was deemed a stronger inhibitor of FGFR4 than **47**. *In vitro* IC₅₀ determinations on FGFR4 would be required to determine if **3-12** is truly more potent than **47** on FGFR4.

5.5. Summary

Compound **3-12** was found to inhibit the phosphorylation of several RTKs (EGFR, HER2, HER3, FGFR4, insulin receptor, Mer and RYK) in HuH7 cells. The investigations which were carried out on a Human Phospho-RTK antibody array kit at 0.5 and 2 μ M **3-12**, identified HER3 and FGFR4 to be inhibited to a greater extent than the other RTKs. The functional relevance of the inhibition was further confirmed by immunoblotting/immunoprecipitation which showed that **3-12** reduced phospho-FGFR4 and phospho-HER3 protein levels in HuH7 cell lysates at comparable concentrations. Molecular docking on a homology model of FGFR4 showed that **3-12** adopted favorable poses at the hinge region of FGFR4. Both the indolinone ring and the *N*-propylaminosulfonyl side chains were involved in productive binding interactions, in contrast to **47** where only the indolinone ring was involved in H bonding to the FGFR4 binding pocket.

Chapter 6: Investigation of the drug-like properties of selected benzylidene indolinones

6.1. Introduction

This chapter describes the investigation of drug-like properties of selected benzylidene indolinones. The objective was to provide a comparison of these properties in the newly identified benzylidene indolinones with potent growth inhibitory properties vis-à-vis the lead compound 47. The properties investigated were aqueous solubility at pH 7.4, permeability assessed by the parallel artificial membrane permeability assay (PAMPA), *in vitro* microsomal stability, light scattering properties, *in vivo* maximum tolerated dose in mice, cytotoxicities and genotoxicity potential on cell based assays. Of these properties, the PAMPA permeability, cytotoxicity and genotoxicity assays were carried out by the Drug Development Unit of the National University of Singapore. *In vivo* evaluation in mice was carried out by a collaborator at the National Cancer Centre, Singapore. The other properties were determined by the candidate

6.2. Materials and Methods

6.2.1. Determination of aqueous solubility

Determination of aqueous solubility was carried out on Multiscreen[®] Solubility filter plates (Millipore-MSSLBPC10) following the manufacturer's protocol (PC2445EN00, Millipore Corporation). Briefly, various concentrations of the test compound were prepared in Universal buffer (pH 7.4)/acetonitrile/DMSO. The UV absorbance of these solutions were obtained at a pre-determined wavelength and used to construct a calibration curve for the test compound. Next, a stock solution of the test compound in DMSO was prepared at a concentration that was estimated to exceed the solubility of the compound (that is, the saturating concentration). If the concentration was incorrectly estimated, the experimental

solubilities after 3 h or 24 h agitation would be close to that concentration but if it was correct, the experimentally determined solubilities would be lower. If the estimation was incorrect, a higher starting concentration would then be prepared. The stock solution was diluted with Universal buffer (pH 7.4), dispensed into wells in the filter plate, and agitated for 3 hr and 24 hr at room temperature (25 °C). Final concentration of DMSO per well was kept at 1% v/v. At the end of this time, the suspension was filtered on a manifold, the filtrate diluted with acetonitrile to give the same solvent composition used to prepare the calibration solutions. The absorbance of the diluted filtrate was read on a microplate reader (Tecan Infinite™ M200) at the predetermined wavelength (λ_{max} of 262 nm for **1-18** and λ_{max} of 322 nm for **3-10**) and the concentration of the filtrate (equivalent to the solubility of the test compound) was determined from the calibration curve. The concentrations of **47**, **1-23**, **3-12** and **7-6** were determined by LC–MS because of their low solubilities. LCMS determinations were made on an Agilent 1200 Series HPLC linked to a AB Sciex Instruments 3200 Q TRAP LC/MS/MS. Separations were carried out on a Phenomenex Luna column [3u, C₁₈(2), 100 A, 5 × 4.6 mm] with p-(dipropylsulfamoyl)benzoic acid (Sigma Aldrich, Singapore) as internal standard. Quantification was based on the ratio of the peak area of daughter-mother ion peak of sample over daughter-mother ion peak of the internal standard, normalized against the same ratio obtained from the calibration curve. The solubility determinations were carried out in triplicates using two different stock solutions

6.2.2. Determination of *in vitro* stability of compound 47, 1-23, 3-12, and 7-

6 in the presence of rat male liver microsomes

The test compound was incubated with pooled male rat liver microsomes (BD Gentest Corporation, MA, USA) in a mixture (total volume 500 μ L) comprising rat liver microsomes (0.3 mg microsome protein/mL), test compound (3 μ M) and phosphate buffer (0.1 M, pH 7.4, containing 1 mM EDTA). The mixture was pre-incubated for 5 min, 37 °C in a shaking water bath, after which the reaction was started by adding 50 μ L of 10 mM NADPH (freshly prepared in phosphate buffer) to give a final concentration of 1 mM NADPH in the mixture. Aliquots of 50 μ L were withdrawn immediately on addition of NADPH (time 0) and then at 5, 15, 30 and 45 min. On removal of the sample, the reaction was quenched by addition of chilled acetonitrile (100 μ L) which also contained the internal standard (3-12 was internal standard for compound 47 and 7-6; 7-6 was the internal standard for 1-23 and 3-12) at 0.4 μ M. The mixture was then centrifuged at 10,000 *g* to remove protein and the content of the test compound in the supernatant was measured by LCMS.

For each test compound, the metabolic stability of a positive control, midazolam (Yichang Humanwell Pharmaceutical Co. Ltd, Hubei, PRC), a known cytochrome P450 substrate, was concurrently determined to evaluate the adequacy of the experimental conditions. The internal standard used for the LCMS quantification of midazolam was *N*-ethyl-*N*-[5-(4-methylsulfonylphenyl)-1-octyl-1*H*-indol-3-yl]methyl ethanamine at 2 μ M. The stability of the test compound to microsomal degradation in the absence of NADPH was also monitored.

Analysis was carried out by LC-MS-MS on a 1200 HPLC instrument (Agilent Technologies, Palo Alto, CA, USA) coupled to a Q TrapTM 3200 hybrid triple quadrupole linear ion trap mass spectrometer (Applied Biosystems/MDS Sciex, Concord, Ontario, Canada) or a Shimadzu UFLC system (Shimadzu Scientific Instruments, Columbia, MD) coupled to a Q TrapTM 3200 hybrid triple quadrupole linear ion trap mass spectrometer (Applied Biosystems/MDS Sciex, Concord, Ontario, Canada) for the other compounds. Separations were made on a Phenomenex Luna column [3 μ , C₁₈(2), 100 A, 5 \times 4.6 mm] or Poroshell 120

EC-C18 column (3 X 75 mm, i.d., 2.7 μ M, Agilent Technologies, Palo Alto, CA, USA) with a Security Guard Cartridge (3.0 X 4 mm, Agilent Technologies, Palo Alto, CA, USA). Mobile phase was 0.1% formic acid in acetonitrile – water as mobile phase. Flow rate was set at 0.2 or 0.6 mL/min and the column temperature was 30° or 40 °C. 2 or 5 μ L full loop sample injection was used.

Data processing was performed on the Analyst™ 1.4.2 software package (Applied Biosystems, MA, USA). The corresponding multiple reaction monitoring (MRM) transition of the test compound was selected and used for peak configuration in Analyst 1.4.2 for semi-quantification. The peak areas of test compound at different time points were expressed as a % of the peak area of test compound at time 0 min (=100%). The resulting % test compound (average of 3 measurements with SD) was plotted against incubation time drug. *In vitro* half life ($T_{1/2}$ min) was calculated from Equation (1) where elimination constant k is the slope of the line obtained from a plot of \log_e (% Test compound) versus time.

Equation (1): $T_{1/2}=0.693/-k$ where k is the slope of the plot.

Estimated *in vitro* clearance was determined from Equation (2):

Equation (2): $CL_{int, in vitro} = V \times 0.693/T_{1/2}$, where V (μ L/mg) = volume of incubation mixture/amount of microsomal protein in the incubation mixture.

6.2.3. Assessment of aggregation tendency by dynamic light scattering

(DLS)

Stock solutions (10 mM) of test compounds were prepared in DMSO, diluted to 1 mM with DMSO and then serially diluted with potassium phosphate buffer (5mM, pH 7.4, pre-filtered before use) to give final concentrations of 1 μ M and 10 μ M. The final concentration of DMSO was maintained at 1% v/v. Measurements were carried out on the Malvern Instrument Zetasizer Nano ZS system equipped with a 4mW He-Ne laser at 633nm and detector angle of 90°. Three or more determinations of derived count rates (kilocounts per second, kcps) were obtained for each concentration of test compound from two separately prepared stock

solutions. Data collection was carried out using the software supplied with the instrument. Results were represented as mean \pm standard deviation. The positive control was benzyl benzoate (250 μ M) which gave a count rate of 1568 kcps (\pm 133). The vehicle (phosphate buffer, 1% DMSO) gave a reading of 16.3 ± 0.1 .

6.2.4. Determination of PAMPA permeability

The determinations of PAMPA permeability were done by Ms Yap Siew Qi from Drug Development Unit, NUS with the method described in Appendix V.

6.2.5. Determination of cytotoxicities of test compounds

The determinations of cytotoxicities of test compounds were done by Ms Ho Jia Pei from Drug Development Unit, NUS with the method described in Appendix V.

6.2.6. Determination of genotoxicities of test compounds

The determinations of genotoxicities of test compounds were done by Ms Ho Jia Pei from Drug Development Unit, NUS with the method described in Appendix V.

6.3. Results

6.3.1. Aqueous solubilities of compounds 47, 1-18, 1-23, 3-10, 3-12 and 7-6.

The aqueous solubilities of **47, 1-18, 1-23, 3-10, 3-12** and **7-6** were determined after 3 h and 24 h of agitation at 25 °C, pH7.4 (Table 6-1). Lower solubilities were recorded after 24 h possibly due to the longer agitation time which permitted equilibration to take place. The ranking of compounds based on their solubilities was of the order **3-10** (most soluble) > **1-18** > **3-12** > **1-23** > **7-6, 47** (least soluble) at both time points. Estimated solubilities showed a similar rank order as experimental solubilities.

Structurally, the most soluble compounds were those with the *N*-methylaminosulfonyl side chains on the benzylidene ring B (**1-18, 3-10**). The *N*-propyl homologs (**1-23, 3-12**) were less soluble. The least soluble compounds were those substituted with 3'-CF₃ on ring B. The better solubilities of compounds with *N*-alkylaminosulfonyl side chains were likely due to the H

bonding capability of the side chain. The *N*-alkyl substituent was also important. Thus, **1-18** and **3-10** which had shorter *N*-methyl side chains were more soluble than **3-12** and which had the longer propyl side chain. For the same side chain on ring B, better solubility was recorded for the 6-F analog compared to the 6Cl analog, likely due to the presence of the smaller and less lipophilic F. Thus, **3-10** and **3-12** were more soluble than **1-18** and **1-23** respectively. The poor solubilities of **47** and **7-6** were attributed to the absence of polar functionalities in their structures.

6.3.2. PAMPA permeabilities of compounds 47, 1-18, 1-23, 3-10, 3-12 and 7-6.

The *in vitro* permeabilities of compounds were determined on the parallel artificial membrane permeation assay (PAMPA) with 1% lecithin in dodecane as the simulated membrane barrier. The permeabilities were expressed in terms of P_e (effective permeability) and compared against control compounds (warfarin, caffeine, quinidien, carbamazepine, propranolol, verapamil) which have a range of PAMPA permeabilities ranging from poor (low P_e) to very good (high P_e). The P_e values of the test compounds are given in Table 6-1. As in the case of solubilities, there was a time dependent decline in P_e values for most compounds but the ranking of P_e values was largely the same at both time points. The P_e of **4-7** and **1-23** could not be determined at either time point (6h, 16 h) because of their poor solubilities. At the 6 h time point, **1-18** had the best permeability, followed by **3-10**, **3-12** and then **7-6**. When determined at the longer time point (16h), **1-18** and **7-6** were found to be the most permeable with P_e values falling between that of quinidine and carbamazepine, which had “average” permeabilities. Compounds **3-10** and **3-12** were next with P_e values comparable to that of quinidine. The paradoxical increase in the permeability of **7-6** with time came about because the P_e of **7-6** did not change significantly with time, unlike the other compounds whose P_e values were almost halved when agitation time was extended.

The permeation of substances across a lipid barrier is most commonly a passive diffusion process that occurs without the expenditure of energy and is largely driven by the presence of

a concentration or electrochemical gradient. The net diffusion of a solute down a concentration gradient is described by Fick's Law²¹⁵ and given by the expression (3)

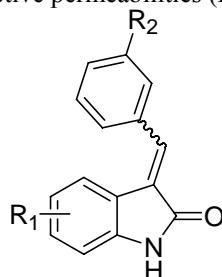
$$J = \frac{D \cdot P(C_{\text{out}} - C_{\text{in}})}{H}$$

where J = net flux (or net rate of diffusion); D= diffusion coefficient of solute in the membrane; A = Surface area; H = thickness of membrane; P = partition coefficient of solute and $C_{\text{out}} - C_{\text{in}}$ = concentration gradient across the membrane.

Assuming that thickness H and surface area A are constant values, the rate of diffusion (permeability) is essentially determined by lipophilicity and aqueous solubility of the solute. Lipophilicity determines the partition coefficient P and diffusion coefficient D. It is directly correlated to P but inversely correlated to D. Permeability is also dependent on solubility of the compound which determines the concentration gradient that is the driving force of diffusion across the membrane. Therefore, for good permeability, compounds must be sufficiently soluble in order to establish a large concentration gradient as well as adequately lipophilic to drive diffusion across the membrane. Very lipophilic compounds would be hampered by poor solubility and a small diffusion coefficient D.

With this background, the permeabilities of some test compounds may be rationalized as follows: The poor permeabilities of **47** and **7-6** were primarily due to their poor solubilities. In contrast, **1-18** owed its good permeability to its "optimal" balance of solubility and lipophilicity. Changing *N*-methyl of **1-18** to *N*-propyl (**1-23**) increased lipophilicity and diminished solubility, hence resulting in a non-determinable P_e . On the hand, replacing 6-Cl in **1-18** with the smaller fluorine atom (**3-10**) reduced lipophilicity and increased solubility, causing its P_e to diminish. There is no good explanation for the unexpected improvement in the permeability of **7-6** with longer agitation time. It was unusual given that **7-6** was no more soluble than the poorly permeable **47** and probably less lipophilic (based on clogP values) than **47**.

Table 6-1: Aqueous solubilities and effective permeabilities (P_e) of selected benzylidene indolinones



Cpd No.	R_1	R_2	Solubility pH7.4, 25°C (μM) ^a		Estimated solubility (μM) ^b	PAMPA P_e ($\times 10^{-6}$ cm/s) ^a	
			6 h	24 h		6 h ^c	16 h ^d
47	6Cl	CF ₃	0.12 ± 0.00	0.09 ± 0.00	3.4	N.A.	N.A.
1-18	6Cl	SO ₂ NHMe	25.4 ± 0.03	6.6 ± 0.6	13.6	11.91 ± 0.59	6.65 ± 0.34
1-23	6Cl	SO ₂ NHPr	0.54 ± 0.10	0.20 ± 0.04	7.9	N.A.	N.A.
3-10	6F	SO ₂ NHMe	113 ± 23	19.0 ± 1.2	76.0	6.11 ± 0.21	3.34 ± 0.28
3-12	6F	SO ₂ NHPr	1.59 ± 0.24	1.27 ± 0.25	15	6.25 ± 1.21	2.40 ± 0.30
7-6	5,6F	CF ₃	0.09 ± 0.02	0.13 ± 0.03	2.7	5.38 ± 0.66	6.11 ± 0.98

^a Mean ± SD of at least n=3 determinations

^b Estimated solubilities (pH 7.4) were determined on ACDLabs, Solubility DB, Version 6.00

^c P_e ($\times 10^{-6}$ cm/s) of positive controls, 6 hr: warfarin (1.92 ± 0.09), caffeine (1.71 ± 0.16), quinidine (2.88 ± 0.37), carbamazepine (9.07 ± 0.96), propranolol (13.09 ± 0.10), verapamil (22.61 ± 0.35)

^d P_e ($\times 10^{-6}$ cm/s) of positive controls, 16 hr: warfarin (1.89 ± 0.09), caffeine (1.76 ± 0.08), quinidine (3.32 ± 0.15), carbamazepine (8.99 ± 0.27), propranolol (9.47 ± 0.22), verapamil (12.19 ± 0.13)

6.3.3. *In vitro* metabolic stability of 47, 1-23, 3-12 and 7-6.

The *in vitro* metabolic stabilities of the compounds were investigated by monitoring the time dependent loss of the parent compound when incubated with rat (male) liver microsomes (Table 6-2 and Figure 6-1). Compounds **1-23** and **3-12** were cleared as rapidly as the positive control midazolam while **47** and **7-6** were more stable to microsomal metabolism. The deduced half-lives were of the order **7-6** (35 min) > **47** (29 min) > midazolam (8.1 min) > **1-23** (6.6 min) > **3-12** (5.8 min). The shorter the half-life, the more rapid the clearance and accordingly, **1-23** and **3-12** were predicted to be cleared more rapidly than **7-7** and **47**. The metabolic susceptibilities of **1-23** and **3-12** were likely due to the *N*-propylaminosulfonyl side chain that was common to both compounds. *N*-Dealkylation of the side chain, a Phase 1 metabolic reaction, would result in the loss of the parent compound. In contrast, the CF₃

group in **47** and **7-6** was generally resistant to Phase I metabolism and could have contributed to the stability to microsomal oxidation reactions.

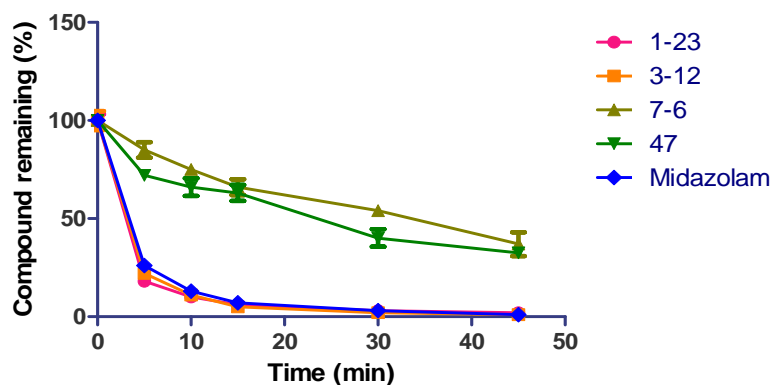


Figure 6-1 Percentages of test compounds and positive control midazolam relative to initial amounts ($t = 0$) in rat liver microsomes on incubation at 37 °C for 5, 15, 30 and 45 min. The percentages of remaining compound are expressed as the mean \pm SD ($n = 3$).

Table 6-2: Estimated half-lives ($T_{1/2}$) and clearance values of test compounds deduced from a plot of \log_e (% compound) versus time.

Compound	$T_{1/2}$ (min)	$CL_{int, in vitro}$ (uL/min/mg)
47	28.6 \pm 2.6	81.1 \pm 7.7
1-23	6.6 \pm 0.4	350 \pm 24
3-12	5.8 \pm 0.03	396 \pm 2
7-6	35.1 \pm 3.0	66.0 \pm 5.0
Midazolam	8.1 \pm 1.1	290 \pm 38

6.3.4. *In vitro* cytotoxicities and genotoxicities of **47**, **1-23**, **3-12** and **7-6**.

The cytotoxicities of the compounds were investigated by the 24 hr viability assay on two non-malignant murine cell lines TAMH and HL-1 (Table 6-3). Compound **47** had the highest IC_{50} values on both TAMH and HL-1 cells whereas the other compounds had IC_{50} values that exceeded 5 μ M. Compared to IC_{50} values obtained on non-malignant human fibroblast cells IMR90 (Section 3.3.3), the values obtained on the murine cells were higher, except for **7-6** on

TAMH cells. Two reasons could have accounted for the observed differences, namely specie variations (murine versus human) and the time of incubation (24 h versus 72 h). It may be that the cytotoxicities of the test compounds are observed after a longer incubation period.

Table 6-3 IC₅₀ values of test compounds on mouse hepatocyte (TAMH) and mouse cardiomyocyte (HL-1) cells after 24 h incubation. Values obtained on human fibroblast IMR90 (72 h incubation) are also listed.

Compound	Growth Inhibitory IC ₅₀ (μM)		
	TAMH (24h)	HL-1(24h)	IMR90 (72 h)
47	68.0 ^a	45.4 ^a	9.2 ± 0.9
1-23	8.2 ± 0.9	10.8 ± 1.0	0.58±0.09
3-12	11.0 ± 0.9	17.6 ± 0.8	0.83±0.06
7-6	5.1 ± 0.4	15.6 ± 0.8	8.5 ± 0.6

^a Based on average of two determinations. The other readings were mean ± SD (n = 3).

The genotoxicities of **1-23**, **3-12** and **7-6** were investigated in the Ames Test using two mutated strains (TA98 and TA100) of *Salmonella typhimurium*. Both strains had point mutations such that the presence of histidine in the growth media was required for their proliferation. When exposed to a mutagen, the strains underwent mutations that permitted growth in a histidine-deficient media.^{216,217} As shown in Table 6-4, the test compounds at two concentrations (1 mM and 10 μM) did not promote the growth of TA98 and TA100. In contrast, proliferation of TA98 and TA100 were strongly induced in the presence of the known mutagen 2-aminoanthracene.

Table 6-4: Number of TA98 and TA 100 colonies observed in the presence of test compounds (1 mM, 10 μ M) after 48 h of incubation. The numbers of colonies were based on the average of the counts of the colonies from two replicates.

Compound	Number of colonies	
	TA98	TA100
DMSO	39.5	9.5
2-aminoanthracene (19 μ M)	936.5	568.5
1-23 (1 mM)	9	19
1-23 (10 μ M)	4	7
3-12 (1 mM)	3	16
3-12 (10 μ M)	28	15.5
7-6 (1 mM)	16	10.5
7-6 (10 μ M)	51	12.5

6.4. Aggregate formation by test compounds

Several compounds are known to form aggregates in aqueous media which led to their ability to inhibit a wide variety of enzymes^{218, 219}. The non-specific inhibition was attributed to the association of the enzyme onto the surfaces of the aggregates, leading to a reduction in available enzyme and misinterpretation of the data as being due to specific enzyme inhibition.²¹⁸ Aggregators are commonly characterized by low solubility, high lipophilicity and extended conjugation in their structures.²¹⁹ As some of these properties are characteristic of the present series of compounds, there was concern that aggregate formation could have contributed to the sirtuin and kinase inhibitory properties of the compounds.

Various experimental approaches have been used to identify compounds that form aggregates. Here, the formation of aggregates was monitored by light scattering. Compounds that form soluble or colloidal aggregates normally exist as particles of 30-1000 nm diameter that can be detected by light scattering.²²⁰ Briefly, the method involves measuring the light scattering capacity of a known concentration of test compound in aqueous 5 mM phosphate buffer with ion strength at 30 mM (containing 1% v/v DMSO). In the presence of aggregates, the solutions would give a high count rate (measured in kilocounts per sec, kcps). Count rate of 10 μ M or 1 μ M of the compound solution were recorded. Benzyl benzoate (at 250 μ M), a known aggregator was used as a positive control.^{221, 222} The light scattering measurements of the test compounds are given in Table 6-5.

Table 6-5: Dynamic light scattering (DLS) count rates of test compounds in phosphate buffer (pH 7.4) containing 1% DMSO. Results are given as mean \pm SD of n=3 determinations.

Compound	DLS count rate (kcps)		Estimated solubility (μ M) ^a
	DLS count rate at 10 μ M	DLS count rate at 1 μ M	
47	94.8 \pm 18.1	17.6 \pm 0.8	3.4
3-12	16.0 \pm 0.2	15.8 \pm 0.0	15
5-1	16.1 \pm 0.2	16.1 \pm 0.3	81
5-6	119.3 \pm 16.8	16.1 \pm 0.6	10
8-8	323 \pm 68	19.1 \pm 1.0	2.1
8-9	426 \pm 104	20.3 \pm 2.3	0.08
Phosphate buffer (pH7.4) containing 1% DMSO	16.3 \pm 0.1		-
Benzyl benzoate (250 μM)	1568 \pm 133		-

^a Estimated solubilities at pH 7.4 were determined with ACD Labs Version 12.00, Toronto, Canada.

The results showed that test compounds at 1 μ M had negligible light scattering effects, with DLS count rates that were no different from that of the buffer/DMSO media used to dissolve the compounds. An increase in concentration of 3-12 and 5-1 to 10 μ M did not increase count rates but increases were observed for **47**, **5-6**, **8-8** and **8-9** at 10 μ M. However these rates were low compared to the positive control benzyl benzoate (<1000) and more importantly, were not pharmacologically relevant for compounds like **5-6**, **8-8** and **8-9** which had SIRT2 IC₅₀ values of \sim 1-3 μ M. When the estimated solubilities of the compounds in Table 6-5 were compared with their light scattering properties, it was observed that higher scattering values were associated with less soluble compounds. Although estimated solubilities were used here, the correlation may be valid as estimated and experimental solubility rankings were fairly well correlated as shown in Section 6.3.1.

6.4.1. Maximum tolerated dose of 3-12 in mice

The maximum tolerated dose of **3-12** was determined in Balb/c nude mice (female). The protocol involved administering **3-12** at doses 30, 50, and 60 mg/kg twice a week for 15 days. The compound was administered in DMSO by intraperitoneal (IP) injection. Control mice were similarly treated with DMSO. Body weight, food and water consumption of the animals were monitored daily throughout the period of dosing (15 days). As seen from Figure 6-2, **3-12** was well tolerated at 30 mg/kg with regard to body weight, food and water consumption

(no significant difference from control, 1-way ANOVA with Dunnett's post hoc). At a higher dose of 50 mg/kg, **3-12** did not induce changes in food and water consumption but caused a significant loss in weight in treated animals ($p < 0.01$). When administered at the highest dose of 60 mg/kg, **3-12** caused significant reduction in weight and food consumption.

Reductions in body weight and food/water consumption are important parameters for determining the maximum tolerated dose in mice. According to guidelines on drug treatment in mice,²²³ a reduction in weight (20% weight lost) and drop in water/feed consumption by 25% to 40% within 72 hours were deemed as "mild" effects induced by the compound. The response classified as moderate if the test compound caused 20% - 25 % weight loss and less than 60% reduction in food/water consumption within 72 hours. By this criteria, **3-12** was categorized as having only mild effects on the treated animals, since it did not reduce food/water consumption by more than 40% at the end of the treatment period, at all 3 doses. After 15 days, weight loss was also not more than 10% at all 3 doses of **3-12**.

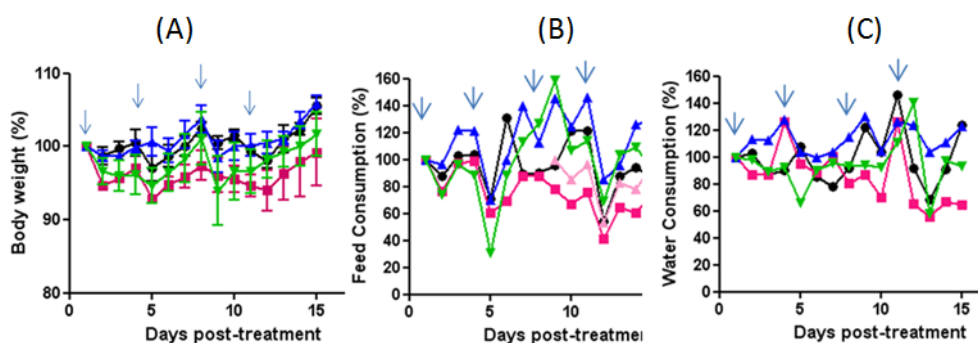


Figure 6-2: Changes in (A) body weight, (C) % feed consumption and (C) % water consumption of Balb-c mice treated with **3-12** at 60 mg/kg (red square / pink triangle), 50 mg/kg (green inverted triangle) and 30 mg /kg (blue triangle). Untreated animals (n=3) are indicated by black circles. Three mice were treated at each dose. Arrow indicates administration of **3-12**, IP in DMSO solution. Mean and SD of n=3 animals.

6.5. Discussion

The objective of this chapter was to compare the "drug-like" properties of selected benzylidene indolinones with potent growth inhibitory properties on HCC with that of the lead compound **47**. A simple definition of "druglike" in the context that it is normally used would be "orally available and relatively nontoxic in humans".²²⁴ Oral bioavailability is

determined by the fraction of administered drug that reaches the systemic circulation as intact (unchanged) drug. It is a function of the fraction of dose that is absorbed after oral administration and escapes intestinal/hepatic metabolism.²²⁵ Hence, solubility, permeability and susceptibility to microsomal metabolism would be useful indicators of oral bioavailability. To this end, the aqueous solubilities and PAMPA permeabilities of **47**, **1-18**, **1-23**, **3-10**, **3-12** and **7-6** were monitored. These compounds were found to have submicromolar IC₅₀ values on HuH7, with **1-23** and **3-12** more potent than **47**. Thus, there was considerable interest in the druglike properties of **1-23** and **3-12**.

In terms of solubility, both **1-23** and **3-12** were more soluble than **47** but **3-12** was more soluble than **1-23**. Both compounds were substituted on ring B with the H bonding *N*-propylaminosulfonyl side chain but **3-12** was fluorinated (6-F on ring A), unlike **1-23** which had the more lipophilic chloro substituted ring A. The poor solubility of **1-23** was likely due to its chlorinated ring A. Reducing *N*-propyl to *N*-methyl greatly improved aqueous solubilities as seen in **1-18** and **3-10**. These compounds should be considered as viable alternatives to **1-23** and **3-12**. This notion was further reinforced by their PAMPA permeabilities. Compounds **1-18**, **3-10** and **3-12** had significantly higher permeabilities than **47**. Disappointingly, the permeability of **1-23** was indeterminable due to its poor solubility.

Notwithstanding its good solubilities and permeabilities, **3-12** was found to be highly susceptible to microsomal metabolism. This was attributed to the *N*-dealkylation of the *N*-propylaminosulfonyl side chain in **3-12**. Compound **1-23** which had the same *N*-propylaminosulfonyl side chain as **3-12** was also metabolically unstable while **47** and **7-6** which lacked metabolic hotspots in their structures were stable in the presence of liver microsomes. Further investigations should be directed towards identifying the metabolites of **3-12** and **1-23** and to determine if they retain growth inhibitory activities.

Another requirement of a druglike compound is that it should be relatively nontoxic in humans. Only clinical data could provide the required evidence but for preliminary assessments, cell based and animal data are commonly used. Hence, **3-12** was examined for cytotoxicity and genotoxicity on cell based assays and its acute toxicity was assessed in mice.

These investigations support the view that **3-12** had minimal toxicity. It was not cytotoxic or mutagenic and was well tolerated in mice at doses up to 60 mg/kg. No fatalities were observed during acute dosing in mice. Compounds **47**, **1-23** and **7-6** were also found to lack cytotoxicities on the murine cell lines. Neither were they mutagenic on the Ames Test (**47** was not tested).

An assessment of aggregation formation among selected compounds (**47**, **5-1**, **3-12**, **8-8**, **8-9**, **5-6**) showed that this tendency was negligible at 1 μ M. However light scattering was more pronounced for some compounds (**8-8**, **8-9**, **5-6**) at 10 μ M, notably those with poorer (estimated) solubilities. Even then the levels of light scattering were low at the higher concentration. For compounds like **3-12**, **5-1**, **8-9** which demonstrated FGFR4 /SIRT2 inhibitory activities at concentrations < 3 μ M, it was reasonable to conclude that the observed inhibitions were specific and not induced by aggregate formation.

6.6. Summary

Taken together, benzylideneindolinones that were more druglike than the lead compound **47**, based on some but not all criteria, had been identified. These were compounds with the *N*-alkylaminosulfonyl side chains on ring B, notably **1-18**, **3-10** and **3-12**. They had better solubilities and PAMPA permeabilities than **47** due to the presence of the H bonding *N*-alkylaminosulfonyl side chain but as shown for **3-12**, were more susceptible to microsomal metabolism. **3-12** and other benzylidene indolinones were found to lack acute toxicity on murine liver and heart cells, and were not mutagenic. The propensity to form aggregates was not pronounced for **3-12**, **5-1** and **8-7** which had potent enzyme (SIRT2/FGF4) inhibitory activities. Compound **3-12** was well tolerated in mice possibly up to a dose of 60 mg/kg (IP, twice weekly for 2 weeks). Thus **3-12** constitute a good starting point for future structural elaboration.

Chapter 7: Conclusions

In this thesis, the candidate tested the hypothesis that structural elaboration of compound **47** would provide a means of uncovering drug-like compounds with greater potency and selectivity on hepatocellular carcinoma (HCC), and that the enhanced potency would involve kinase or sirtuin inhibition, or possibly, inhibition of both targets. To this end, 115 compounds across 8 series of functionalized benzylideneindolinones were designed, synthesized and evaluated for their effects on the viability of liver cancer cell lines (HuH7, Hep3B, HepG2). The focus of the design strategy was to enhance the drug-like character of the lead compound **47**, notably its poor solubility and excessive lipophilicity. The approach was to vary substitution at two sites of the scaffold, namely the indolinone ring A and the benzylidene ring B. The core lactam moiety in the indolinone ring was retained in view of its acknowledged role in kinase inhibition, and possibly sirtuin inhibition.

The structural modifications reported in this investigation, while admittedly limited in scope and range, allowed a comprehensive structure activity relationship to be deduced. Figure 7-1 summarizes the key SAR insights with respect to HuH7 cells which were investigated more extensively than the other hepatoma cells.

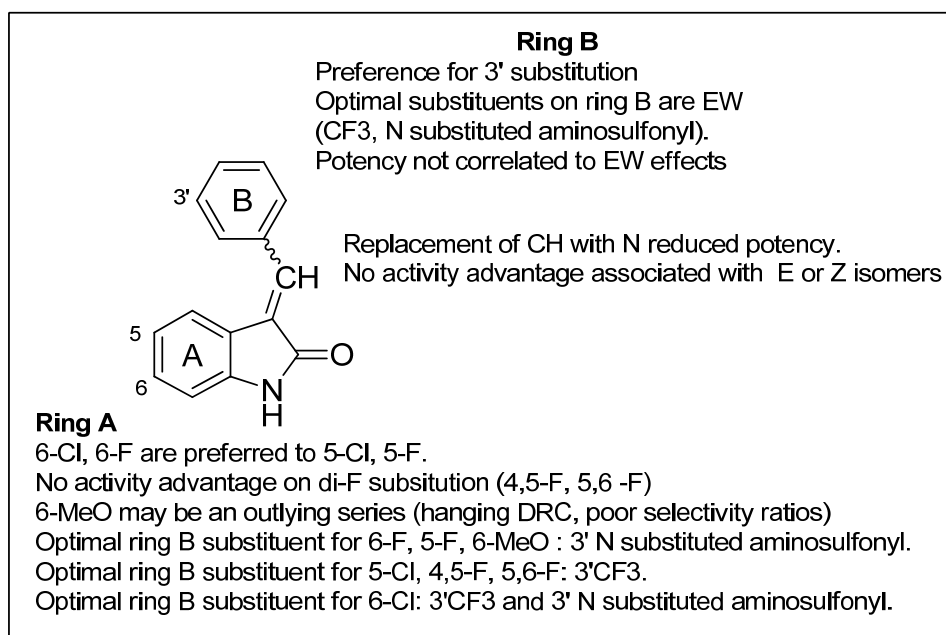


Figure 7-1: Summary of major SAR findings for the growth inhibitory activity of benzylidene indolinones on HuH7 cells. EW : Electron Withdrawing.

Among the modifications made to address the solubility-lipophilicity balance, replacing 6-Cl on ring A of **47** with fluoro (Series 3) or methoxy (Series 5) and substituting 3'CF₃ on ring B of **47** with the *N*-substituted aminosulfonyl side chain were prescient because the more potent compounds identified in this thesis were those with *N*-propylaminosulfonyl side chains in Series 3 (**3-11**, **3-12**) or Series 5 (**5-8**, **5-9**). Some compounds with CF₃ on ring B did not fare badly either, notably **6-6**, **7-6** and **8-9**. In view of their association with good potency, it was tempting to propose a bioisoteric relationship between the *N*-substituted aminosulfonyl side chain and the CF₃ moiety. There were however some differences between them. Compounds with CF₃ groups were well represented among the potent (IC₅₀ < 1 μM) analogs against Hep3B cells and were selectively more potent against hepatoma cells (HuH7, Hep3B) than the non-malignant IMR90 cells. In contrast, compounds with *N*-alkylaminosulfonyl side chains were generally more potent on HuH7 cells and were less selective on hepatoma cells compared to non-malignant IMR90 cells. As to whether compounds with greater growth inhibitory potencies than **47** were also endowed with better drug like properties, this was found to be true for compounds with *N*-substituted aminosulfonyl side chains. They were

more soluble and had better PAMPA permeabilities than the CF₃ containing compounds. Preliminary assessment of the *in vivo* toxicity of **3-12** in mice showed that it was well tolerated up to 50 mg/kg (twice weekly for 2 weeks, IP). Unfortunately **3-12** was found to be readily metabolized by human microsomes *in vitro*, with predicted half life and clearance that were significantly shorter than those estimated for the CF₃ substituted compounds **47** and **7-6**. However, genotoxic potential, cytotoxicity and aggregate formation were negligible for the investigated compounds regardless of their ring B substitution.

Taken together, the investigations reported in this thesis reinforced the notion that it was possible to improve on the growth inhibitory potencies and drug-like properties of **47** by structural modification. Replacing CF₃ of **47** with an *N*-substituted aminosulfonyl side chain was found to be particularly promising in terms of enhancing growth inhibitory potencies on hepatoma cells (Hep3B, HuH7), improving solubility and PAMPA permeability. It has limited aggregation potential and was not associated with genotoxic or cytotoxic activities. The side chain was however hampered by its metabolic susceptibility and modest selectivity when compared against non-malignant cell lines.

The other hypothesis tested in this thesis was related to the possible mode of action of these newly identified potent analogs on hepatoma cells. The growth inhibitory effects of representative potent analogs (**47**, **1-23**, **2-7**, **3-12**, **5-1**, **6-6**, **7-6**, **8-5**) induced apoptosis in HuH7 cells. Apoptosis was observed in compound-treated cells investigated by Annexin V-PI FACS analysis and in immunoblotting experiments that monitored changes in apoptotic marker proteins (caspase3, PARP). In view of the historical association of benzylidene indolinones with kinase inhibition, a representative *N*-substituted aminosulfonyl analog **3-12** was screened for inhibition of RTKs in HuH7 cells and was indeed found to significantly inhibit two RTKs (HER3, FGFR4). The functional significance of the inhibition was confirmed in experiments that showed decreases in phospho-protein levels in **3-12** treated HuH7 cells. Molecular docking on a FGFR4 homology model provided insight on the interactions of **3-12** and in particular its aminosulfonyl side chain, in the ATP binding pocket.

Compound 47 was also found to inhibit HER3 and FGFR4 but may be less potent than **3-12** in this regard. The binding pose of **47** in the FGFR4 pocket showed fewer productive interactions at the ATP binding site due to its under-functionalized state.

Benzylideneindolinones have been reported to be inhibitors of SIRT2 and this led to the hypothesis that the sirtuin inhibition may be involved in the growth inhibitory activities of the investigated compounds. The results showed that **3-12** and other analogs with *N*-substituted aminosulfonyl side chains inhibited SIRT2 at IC₅₀ concentrations that were comparable to that of AGK2, a known SIRT2 inhibitor. However more potent inhibition was associated with the Series 5 compounds (6-methoxy on ring A, H/F/CF₃ on ring B) and Series 8 compounds that were *N*-alkyl/arylalkyl analogs of **47**. Only the Series 5 compounds demonstrated *in vitro* SIRT1 inhibitory activities, but were less potent than the established SIRT1 inhibitor EX527. The functional relevance of sirtuin inhibition was validated in experiments that showed that **5-1** and **8-7** inhibited the deacetylation of nonhistone sirtuin substrates p53 and α -tubulin in HuH7 and HepG2 cells. A consequence of inhibiting p53 deacetylation was apoptosis and this was found to be true for **5-1** and **8-7**. Both compounds increased the proportion of HuH7 cells in the apoptotic phase when probed by Annexin V staining, increased the expression of apoptotic marker proteins (cleaved caspase 3, cleaved PARP) and in the case of **5-1**, induced changes in levels of Bcl2, Bcl-xl and BAX that were congruent with the induction of apoptosis. Molecular docking of the test compounds on the SIRT2 binding pocket provided support for the notion that (i) *Z* isomers were more potent inhibitors than *E* isomers and (ii) the benzylidene indolinone scaffold straddled across Sites B,C and the substrate channel. Notwithstanding the useful insight provided by the docking analysis, the empirical and qualitative nature of the exercise should not be overlooked. Thus molecular docking could not rationalize the SIRT1 inhibitory activities of the Series 5 compounds and in the case of some SIRT2 inhibitors, docking poses could not be reconciled with the levels of inhibition observed. That the benzylidene indolinone binds to more than one site of the sirtuin might explain the conflict between the molecular docking and empirical SAR. A kinetic study could be

undertaken to determine the type inhibition (competitive or non competitive) associated with the benzylidene indolinones with respect to the acetylated substrate and cosubstrate NAD⁺. This would provide greater insight into the binding mode of benzylidene indolinones.

The question as to whether kinase inhibition or sirtuin inhibition contributed to the potent growth inhibitory activities of benzylidene indolinones could not be conclusively addressed in this report. Certainly, the ability of **3-12** to inhibit FGFR4 and HER3 in HuH7 cells at concentrations (0.2-1 μ M) that were broadly comparable to its growth inhibitory concentrations was encouraging. However, including more compounds with varying potencies (and not just **3-12** and **47**) would have provided a better idea of the FGFR4 inhibitory potential of the benzylideneindolinone scaffold. Determining the *in vitro* IC₅₀ or for FGFR4 inhibition would be a useful means of quantifying the levels of inhibition. The kinetic study of benzylidene indolinone to FGFR4 would validate the molecular docking. With regard to sirtuin inhibition, it would help if selected compounds were tested on stably transfected HuH7 or other HCC cell lines in which SIRT1 or SIRT2 have been silenced. If **5-1**, **8-7** or other potent SIRT2 inhibitors failed to curtail proliferation of these modified cell lines, it would provide proof of concept that sirtuins are critical targets of these compounds.

In conclusion, the thesis has shown that structural elaboration of compound **47** was a viable means of identifying drug-like compounds with potent growth inhibitory activities on HCC. Two oncogenic proteins (FGFR4, SIRT2) were identified as plausible targets of this scaffold in HCC. These findings provide a useful platform for future investigations which should focus on (i) establishing *in vivo* efficacies of promising compounds in xenograft models, (ii) a better understanding of the metabolic susceptibility of compounds with the promising *N*-substituted aminosulfonyl side chain, (iii) in depth mode of action studies to validate the roles of FGFR4 and SIRT2 as target proteins of benzylidene indolinones and (iv) more extensive structural elaboration of the scaffold to enhance potency and drug-like profiles.

Reference

1. Ferlay, J.; Shin, H.; Bray, F.; Forman, D.; Mathers, C.; Parkin, D. Cancer Incidence and Mortality Worldwide: IARC Cancer Base No. 10 [Internet]. In 2010.
2. Perz, J. F.; Armstrong, G. L.; Farrington, L. A.; Hutin, Y. J. F.; Bell, B. P. The contributions of hepatitis B virus and hepatitis C virus infections to cirrhosis and primary liver cancer worldwide. *Journal of Hepatology* **2006**, *45*, 529-538.
3. Bray, F.; Ren, J.-S.; Masuyer, E.; Ferlay, J. Global estimates of cancer prevalence for 27 sites in the adult population in 2008. *International Journal of Cancer* **2013**, *132*, 1133-1145.
4. Parkin, D. M. The global health burden of infection-associated cancers in the year 2002. *International Journal of Cancer* **2006**, *118*, 3030-3044.
5. Izuno, K.; Fujiyama, S.; Yamasaki, K.; Sato, M.; Sato, T. Early detection of hepatocellular carcinoma associated with cirrhosis by combined assay of des-gamma-carboxy prothrombin and alpha-fetoprotein: a prospective study. *Hepatogastroenterology*. **1995**, *42*, 387-93.
6. Singal, A.; Volk, M. L.; Waljee, A.; Salgia, R.; Higgins, P.; Rogers, M. A. M.; Marrero, J. A. Meta-analysis: surveillance with ultrasound for early-stage hepatocellular carcinoma in patients with cirrhosis. *Alimentary Pharmacology & Therapeutics* **2009**, *30*, 37-47.
7. Mazzaferro, V.; Regalia, E.; Doci, R.; Andreola, S.; Pulvirenti, A.; Bozzetti, F.; Montalto, F.; Ammatuna, M.; Morabito, A.; Gennari, L. Liver transplantation for the treatment of small hepatocellular carcinomas in patients with cirrhosis. *New England Journal of Medicine* **1996**, *334*, 693-700.
8. Llovet, J. M.; Fuster, J.; Bruix, J. Intention-to-treat analysis of surgical treatment for early hepatocellular carcinoma: Resection versus transplantation. *Hepatology* **1999**, *30*, 1434-1440.
9. Yao, F. Y.; Bass, N. M.; Nikolai, B.; Davern, T. J.; Kerlan, R.; Wu, V.; Ascher, N. L.; Roberts, J. P. Liver transplantation for hepatocellular carcinoma: Analysis of survival according to the intention-to-treat principle and dropout from the waiting list. *Liver Transplantation* **2002**, *8*, 873-883.
10. Sato, S.; Shiratori, Y.; Imamura, M.; Teratani, T.; Obi, S.; Koike, Y.; Imai, Y.; Yoshida, H.; Shiina, S.; Omata, M. Power Doppler signals after percutaneous ethanol injection therapy for hepatocellular carcinoma predict local recurrence of tumors: a prospective study using 199 consecutive patients. *Journal of Hepatology* **2001**, *35*, 225-234.
11. Cao, H.; Phan, H.; Yang, L.-X. Improved chemotherapy for hepatocellular carcinoma. *Anticancer Research* **2012**, *32*, 1379-1386.
12. Voiculescu, M.; Winkler, R. E.; Moscovici, M.; Neuman, M. G. Chemotherapies and targeted therapies in advanced hepatocellular carcinoma: from laboratory to clinic. *Journal of Gastrointestinal and Liver Diseases* **2008**, *17*, 315-322.
13. Asghar, U.; Meyer, T. Are there opportunities for chemotherapy in the treatment of hepatocellular cancer? *Journal of Hepatology* **2012**, *56*, 686-695.
14. Balsano, C.; Avantaggiati, M. L.; Natoli, G.; De Marzio, E.; Will, H.; Perricaudet, M.; Levrero, M. Full-length and truncated versions of the hepatitis B virus (HBV) X protein (pX) transactivate the cmyc protooncogene at the transcriptional level. *Biochemical and Biophysical Research Communications* **1991**, *176*, 985-992.
15. Twu, J.-S.; Lai, M.-Y.; Chen, D.-S.; Robinson, W. S. Activation of Protooncogene C-jun by the X Protein of Hepatitis B Virus. *Virology* **1993**, *192*, 346-350.
16. Chirillo, P.; Falco, M.; Puri, P. L.; Artini, M.; Balsano, C.; Levrero, M.; Natoli, G. Hepatitis B virus pX activates NF-kappa B-dependent transcription through a Raf-independent pathway. *Journal of Virology* **1996**, *70*, 641-646.
17. Bann, J.; Schneider, R. J. Hepatitis B virus HBx protein activates Ras-GTP complex formation and establishes a Ras, Raf, MAP kinase signaling cascade. *Proceedings of the National Academy of Sciences of the United States of America* **1994**, *91*, 10350-10354.
18. Lee, Y.-H.; Yun, Y. HBx protein of hepatitis B virus activates Jak1-STAT signaling. *Journal of Biological Chemistry* **1998**, *273*, 25510-25515.
19. Murata, M.; Matsuzaki, K.; Yoshida, K.; Sekimoto, G.; Tahashi, Y.; Mori, S.; Uemura, Y.; Sakaida, N.; Fujisawa, J.; Seki, T. Hepatitis B virus X protein shifts human hepatic

- transforming growth factor (TGF) - β signaling from tumor suppression to oncogenesis in early chronic hepatitis B. *Hepatology* **2009**, 49, 1203-1217.
- 20.Miyaki, M.; Sato, C.; Sakai, K.; Konishi, M.; Tanaka, K.; Muraoka, M.; Kikuchi - Yanoshita, R.; Nadaoka, Y.; Kanda, H.; Kitagawa, T. Malignant transformation and EGFR activation of immortalized mouse liver epithelial cells caused by HBV enhancer - X from a human hepatocellular carcinoma. *International Journal of Cancer* **2000**, 85, 518-522.
- 21.Lee, M.-O.; Choi, Y.-H.; Shin, E.-C.; Kang, H.-J.; Kim, Y.-M.; Jeong, S.-Y.; Seong, J. K.; Yu, D.-Y.; Cho, H.; Park, J. H. Hepatitis B virus X protein induced expression of interleukin 18 (IL-18): a potential mechanism for liver injury caused by hepatitis B virus (HBV) infection. *Journal of Hepatology* **2002**, 37, 380-386.
- 22.Fukutomi, T.; Zhou, Y.; Kawai, S.; Eguchi, H.; Wands, J. R.; Li, J. Hepatitis C virus core protein stimulates hepatocyte growth: Correlation with upregulation of wnt - 1 expression. *Hepatology* **2005**, 41, 1096-1105.
- 23.Yamanaka, T.; Kodama, T.; Doi, T. Subcellular localization of HCV core protein regulates its ability for p53 activation and p21 suppression. *Biochemical and Biophysical Research Communications* **2002**, 294, 528-534.
- 24.Ito, Y.; Sasaki, Y.; Horimoto, M.; Wada, S.; Tanaka, Y.; Kasahara, A.; Ueki, T.; Hirano, T.; Yamamoto, H.; Fujimoto, J. Activation of mitogen - activated protein kinases/extracellular signal - regulated kinases in human hepatocellular carcinoma. *Hepatology* **1998**, 27, 951-958.
- 25.Kolch, W., Kotwaliwale, A., Vass, K., Janosch, P. The role of Raf kinases in malignant transformation. *Expert Reviews in Molecular Medicine* **2002**, 1-18.
- 26.Hwang, Y. H.; Choi, J. Y.; Kim, S.; Chung, E. S.; Kim, T.; Koh, S. S.; Lee, B.; Bae, S. H.; Kim, J.; Park, Y. M. Over-expression of c-raf-1 proto-oncogene in liver cirrhosis and hepatocellular carcinoma. *Hepatology Research* **2004**, 29, 113-121.
- 27.Zhou, Q.; Lui, V. W.; Yeo, W. Targeting the PI3K/Akt/mTOR pathway in hepatocellular carcinoma. *Future Oncology* **2011**, 7, 1149-1167.
- 28.Ueki, T.; Fujimoto, J.; Suzuki, T.; Yamamoto, H.; Okamoto, E. Expression of hepatocyte growth factor and its receptor c-met proto-oncogene in hepatocellular carcinoma. *Hepatology* **1997**, 25, 862-866.
- 29.Datta, S. R.; Dudek, H.; Tao, X.; Masters, S.; Fu, H.; Gotoh, Y.; Greenberg, M. E. Akt phosphorylation of BAD couples survival signals to the cell-intrinsic death machinery. *Cell* **1997**, 91, 231-241.
- 30.Hu, T. H.; Huang, C. C.; Lin, P. R.; Chang, H. W.; Ger, L. P.; Lin, Y. W.; Changchien, C. S.; Lee, C. M.; Tai, M. H. Expression and prognostic role of tumor suppressor gene PTEN/MMAC1/TEP1 in hepatocellular carcinoma. *Cancer* **2003**, 97, 1929-1940.
- 31.Chen, K.-F.; Chen, H.-L.; Tai, W.-T.; Feng, W.-C.; Hsu, C.-H.; Chen, P.-J.; Cheng, A.-L. Activation of phosphatidylinositol 3-kinase/Akt signaling pathway mediates acquired resistance to sorafenib in hepatocellular carcinoma cells. *Journal of Pharmacology and Experimental Therapeutics* **2011**, 337, 155-161.
- 32.Blivet-Van Eggelpoël, M.-J.; Chettouh, H.; Fartoux, L.; Aoudjehane, L.; Barbu, V.; Rey, C.; Priam, S.; Housset, C.; Rosmorduc, O.; Desbois-Mouthon, C. Epidermal growth factor receptor and HER-3 restrict cell response to sorafenib in hepatocellular carcinoma cells. *Journal of Hepatology* **2012**, 57, 108-115.
- 33.van Malenstein, H.; Verslype, C.; Windmolders, P.; Libbrecht, L.; Nevens, F.; van Pelt, J. 261 Long-term sorafenib exposure in hepatocellular cancer cell lines: resistance, risk of rebound growth and epithelial to mesenchymal transition. *Journal of Hepatology* **2011**, 54, Supplement 1, S107-S108.
- 34.Shimizu, S.; Takehara, T.; Hikita, H.; Kodama, T.; Tsunematsu, H.; Miyagi, T.; Hosui, A.; Ishida, H.; Tatsumi, T.; Kanto, T. Inhibition of autophagy potentiates the antitumor effect of the multikinase inhibitor sorafenib in hepatocellular carcinoma. *International Journal of Cancer* **2012**, 131, 548-557.
- 35.Bareford, M. D.; Park, M. A.; Yacoub, A.; Hamed, H. A.; Tang, Y.; Cruickshanks, N.; Eulitt, P.; Hubbard, N.; Tye, G.; Burrow, M. E. Sorafenib enhances pemetrexed cytotoxicity

through an autophagy-dependent mechanism in cancer cells. *Cancer Research* **2011**, 71, 4955-4967.

36. Degenhardt, K.; Mathew, R.; Beaudoin, B.; Bray, K.; Anderson, D.; Chen, G.; Mukherjee, C.; Shi, Y.; Gelinas, C.; Fan, Y. Autophagy promotes tumor cell survival and restricts necrosis, inflammation, and tumorigenesis. *Cancer Cell* **2006**, 10, 51-64.

37. Mathew, R.; Karp, C. M.; Beaudoin, B.; Vuong, N.; Chen, H.-Y.; Bray, K.; Reddy, A.; Bhanot, G.; Gelinas, C. Autophagy suppresses tumorigenesis through elimination of p62. *Cell* **2009**, 137, 1062-1075.

38. Yang, Z. J.; Chee, C. E.; Huang, S.; Sinicrope, F. A. The Role of Autophagy in Cancer: Therapeutic Implications. *Molecular Cancer Therapeutics* **2011**, 10, 1533-1541.

39. Zhang, Y.; Wei, W.; Cheng, N.; Wang, K.; Li, B.; Jiang, X.; Sun, S. Hepatitis C virus-induced up-regulation of microRNA-155 promotes hepatocarcinogenesis by activating Wnt signaling. *Hepatology* **2012**, 56, 1631-1640.

40. Srisuttee, R.; Koh, S. S.; Kim, S. J.; Malilas, W.; Boonying, W.; Cho, I.-R.; Jhun, B. H.; Ito, M.; Horio, Y.; Seto, E. Hepatitis B virus X (HBX) protein upregulates β -catenin in a human hepatic cell line by sequestering SIRT1 deacetylase. *Oncology reports* **2012**, 28, 276-282.

41. Cha, M.-Y.; Kim, C.-M.; Park, Y.-M.; Ryu, W.-S. Hepatitis B virus X protein is essential for the activation of Wnt/ β -catenin signaling in hepatoma cells. *Hepatology* **2004**, 39, 1683-1693.

42. Cheng, A.; Kang, Y.; Lin, D.; Park, J.; Kudo, M.; Qin, S.; Omata, M.; Pitman Lowenthal, S.; Lanzalone, S.; Yang, L. Phase III trial of sunitinib (Su) versus sorafenib (So) in advanced hepatocellular carcinoma (HCC). *Journal of Clinical Oncology* **2011**, 29, 4000.

43. Cainap, C.; Qin, S.; Huang, W.; Chung, I.; Pan, H.; Cheng, Y. Phase III trial of linifanib versus sorafenib in patients with advanced hepatocellular carcinoma (HCC). *J Clin Oncol* **2013**, 31, 249.

44. Johnson, P.; Qin, S.; Park, J.-W.; Poon, R. T.; Raoul, J.-L.; Philip, P. A.; Hsu, C.-H.; Hu, T.-H.; Heo, J.; Xu, J. In *Brivanib (BRI) versus sorafenib (SOR) as first-line therapy in patients with unresectable, advanced hepatocellular carcinoma (HCC): results from the phase 3 BRISK-FL study*, Hepatology, 2012; Wiley-blackwell 111 river st, hoboken 07030-5774, NJ USA: 2012; pp 1519-1520.

45. Zhu, A. X.; Rosmorduc, O.; Evans, J.; Ross, P.; Santoro, A.; Carrilho, F. J.; M.-A., L.; Jensen, M.; Meinhardt, G.; Kang, Y.-K. a phase III, randomized, double-blind, placebo-controlled trial of sorafenib plus erlotinib in patients with hepatocellular carcinoma (HCC). In *ESMO 2012*, 2012.

46. Kaposi-Novak, P.; Lee, J.-S.; Gómez-Quiroz, L.; Coulouarn, C.; Factor, V. M.; Thorgeirsson, S. S. Met-regulated expression signature defines a subset of human hepatocellular carcinomas with poor prognosis and aggressive phenotype. *Journal of Clinical Investigation* **2006**, 116, 1582-1595.

47. Rimassa, L. Tivantinib (ARQ 197) versus placebo in patients (Pts) with hepatocellular carcinoma (HCC) who failed one systemic therapy: Results of a randomized controlled phase II trial (RCT). In *2012 ASCO Annual Meeting*, 2012.

48. Yau, T. C.; Sukeepaisarnjaroen, W.; Yee Chao; Yen, C.-J.; Lausoontornsiri, W.; Chen, P.-J.; Sanpajit, T.; Lencioni, R.; Camp, A. C.; Donna S Cox; Kallender, H.; Ottesen, L. H.; Poon, R. T.-P. A phase I/II study of foretinib, an oral multikinase inhibitor targeting MET, RON, AXL, TIE-2, and VEGFR in advanced hepatocellular carcinoma (HCC). In *2012 ASCO Annual Meeting* 2012.

49. Villanueva, A.; Chiang, D. Y.; Newell, P.; Peix, J.; Thung, S.; Alsinet, C.; Tovar, V.; Roayaie, S.; Minguez, B.; Sole, M.; Battiston, C.; van Laarhoven, S.; Fiel, M. I.; Di Feo, A.; Hoshida, Y.; Yea, S.; Toffanin, S.; Ramos, A.; Martignetti, J. A.; Mazzaferro, V.; Bruix, J.; Waxman, S.; Schwartz, M.; Meyerson, M.; Friedman, S. L.; Llovet, J. M. Pivotal Role of mTOR Signaling in Hepatocellular Carcinoma. *Gastroenterology* **2008**, 135, 1972-1983.e11.

50. Althoff, E. Novartis study of Afinitor® in advanced liver cancer does not meet primary endpoint of overall survival. <http://www.novartis.com/newsroom/media-releases/en/2013/1721562.shtml>

- 51.Knox, J. J.; Qin, R.; Strosberg, J. R.; Andreas, K.; El-Khoueiry, A. B.; Bekaii-Saab, T. B.; Erlichman, C.; Rochester, M. C. A phase II trial of temsirolimus (TEM) and bevacizumab (BEV) in patients with advanced hepatocellular carcinoma (HCC). In *2012 ASCO Annual Meeting*
- 52.Butcher, E. C. Can cell systems biology rescue drug discovery? *Nature Reviews Drug Discovery* **2005**, *4*, 461-467.
- 53.Bell, S. D.; Botting, C. H.; Wardleworth, B. N.; Jackson, S. P.; White, M. F. The interaction of Alba, a conserved archaeal chromatin protein, with Sir2 and its regulation by acetylation. *Science* **2002**, *296*, 148-151.
- 54.Tissenbaum, H. A.; Guarente, L. Increased dosage of a sir-2 gene extends lifespan in *Caenorhabditis elegans*. *Nature* **2001**, *410*, 227-230.
- 55.De Ruijter, A.; Van Gennip, A.; Caron, H.; Kemp, S.; van Kuilenburg, A. Histone deacetylases (HDACs): characterization of the classical HDAC family. *Biochemical Journal* **2003**, *370*, 737-749.
- 56.Sauve, A. A.; Celic, I.; Avalos, J.; Deng, H.; Boeke, J. D.; Schramm, V. L. Chemistry of Gene Silencing: The Mechanism of NAD⁺-Dependent Deacetylation Reactions. *Biochemistry* **2001**, *40*, 15456-15463.
- 57.Borra, M. T.; Langer, M. R.; Slama, J. T.; Denu, J. M. Substrate specificity and kinetic mechanism of the Sir2 family of NAD⁺-dependent histone/protein deacetylases. *Biochemistry* **2004**, *43*, 9877-9887.
- 58.Sauve, A. A.; Schramm, V. L. Sir2 regulation by nicotinamide results from switching between base exchange and deacetylation chemistry. *Biochemistry* **2003**, *42*, 9249-9256.
- 59.Jackson, M. D.; Denu, J. M. Structural identification of 2'- and 3'-O-acetyl-ADP-ribose as novel metabolites derived from the Sir2 family of β -NAD⁺-dependent histone/protein deacetylases. *Journal of Biological Chemistry* **2002**, *277*, 18535-18544.
- 60.Dancy, B. C.; Ming, S. A.; Papazyan, R.; Jelinek, C. A.; Majumdar, A.; Sun, Y.; Dancy, B. M.; Drury III, W. J.; Cotter, R. J.; Taverna, S. D. Azalysine analogues as probes for protein lysine deacetylation and demethylation. *Journal of the American Chemical Society* **2012**, *134*, 5138-5148.
- 61.Haigis, M. C.; Sinclair, D. A. Mammalian sirtuins: biological insights and disease relevance. *Annual Review of Pathology* **2010**, *5*, 253.
- 62.Guarente, L. sirtuins, aging, and medicine. *New England Journal of Medicine* **2011**, *364*, 2235-2244.
- 63.Vaquero, A.; Scher, M.; Lee, D.; Erdjument-Bromage, H.; Tempst, P.; Reinberg, D. Human SIRT1 interacts with histone H1 and promotes formation of facultative heterochromatin. *Molecular Cell* **2004**, *16*, 93-105.
- 64.Vaquero, A.; Scher, M. B.; Lee, D. H.; Sutton, A.; Cheng, H.-L.; Alt, F. W.; Serrano, L.; Sternglanz, R.; Reinberg, D. SIRT2 is a histone deacetylase with preference for histone H4 Lys 16 during mitosis. *Genes & development* **2006**, *20*, 1256-1261.
- 65.Scher, M. B.; Vaquero, A.; Reinberg, D. SIRT3 is a nuclear NAD⁺-dependent histone deacetylase that translocates to the mitochondria upon cellular stress. *Genes & development* **2007**, *21*, 920-928.
- 66.McCord, R. A.; Michishita, E.; Hong, T.; Berber, E.; Boxer, L. D.; Kusumoto, R.; Guan, S.; Shi, X.; Gozani, O.; Burlingame, A. L. SIRT6 stabilizes DNA-dependent protein kinase at chromatin for DNA double-strand break repair. *Aging (Albany NY)* **2009**, *1*, 109.
- 67.Barber, M. F.; Michishita-Kioi, E.; Xi, Y.; Tasselli, L.; Kioi, M.; Moqtaderi, Z.; Tennen, R. I.; Paredes, S.; Young, N. L.; Chen, K. SIRT7 links H3K18 deacetylation to maintenance of oncogenic transformation. *Nature* **2012**.
- 68.Michishita, E.; McCord, R. A.; Boxer, L. D.; Barber, M. F.; Hong, T.; Gozani, O.; Chua, K. F. Cell cycle-dependent deacetylation of telomeric histone H3 lysine K56 by human SIRT6. *Cell Cycle* **2009**, *8*, 2664-2666.
- 69.Bird, A. W.; David, Y. Y.; Pray-Grant, M. G.; Qiu, Q.; Harmon, K. E.; Megee, P. C.; Grant, P. A.; Smith, M. M.; Christman, M. F. Acetylation of histone H4 by Esa1 is required for DNA double-strand break repair. *Nature* **2002**, *419*, 411-415.

70. Megee, P. C.; Morgan, B. A.; Mittman, B. A.; Smith, M. M. Genetic analysis of histone H4: essential role of lysines subject to reversible acetylation. *Science* **1990**, *247*, 841-845.
71. Fraga, M. F.; Ballestar, E.; Villar-Garea, A.; Boix-Chornet, M.; Espada, J.; Schotta, G.; Bonaldi, T.; Haydon, C.; Roper, S.; Petrie, K. Loss of acetylation at Lys16 and trimethylation at Lys20 of histone H4 is a common hallmark of human cancer. *Nature genetics* **2005**, *37*, 391-400.
72. Vaziri, H.; Dessain, S. K.; Eaton, E. N.; Imai, S.-I.; Frye, R. A.; Pandita, T. K.; Guarente, L.; Weinberg, R. A. hSIR2/SIRT1 Functions as an NAD-Dependent p53 Deacetylase. *Cell* **2001**, *107*, 149-159.
73. Luo, J.; Nikolaev, A. Y.; Imai, S.-i.; Chen, D.; Su, F.; Shiloh, A.; Guarente, L.; Gu, W. Negative control of p53 by Sir2 α promotes cell survival under stress. *Cell* **2001**, *107*, 137-148.
74. van Leeuwen, I. M. M.; Higgins, M.; Campbell, J.; McCarthy, A. R.; Sachweh, M. C. C.; Navarro, A. M.; Lain, S. Modulation of p53 C-Terminal Acetylation by mdm2, p14ARF, and Cytoplasmic SIRT2. *Molecular Cancer Therapeutics* **2013**, *12*, 471-480.
75. Li, S.; Banck, M.; Mujtaba, S.; Zhou, M.-M.; Sugrue, M. M.; Walsh, M. J. p53-induced growth arrest is regulated by the mitochondrial SIRT3 deacetylase. *PLoS One* **2010**, *5*, e10486.
76. Brunet, A.; Sweeney, L. B.; Sturgill, J. F.; Chua, K. F.; Greer, P. L.; Lin, Y.; Tran, H.; Ross, S. E.; Mostoslavsky, R.; Cohen, H. Y.; Hu, L. S.; Cheng, H.-L.; Jedrychowski, M. P.; Gygi, S. P.; Sinclair, D. A.; Alt, F. W.; Greenberg, M. E. Stress-Dependent Regulation of FOXO Transcription Factors by the SIRT1 Deacetylase. *Science* **2004**, *303*, 2011-2015.
77. Motta, M. C.; Divecha, N.; Lemieux, M.; Kamel, C.; Chen, D.; Gu, W.; Bultsma, Y.; McBurney, M.; Guarente, L. Mammalian SIRT1 represses forkhead transcription factors. *Cell* **2004**, *116*, 551-563.
78. Wang, F.; Chan, C.; Chen, K.; Guan, X.; Lin, H.; Tong, Q. Deacetylation of FOXO3 by SIRT1 or SIRT2 leads to Skp2-mediated FOXO3 ubiquitination and degradation. *Oncogene* **2011**, *31*, 1546-1557.
79. Jing, E.; Gesta, S.; Kahn, C. R. SIRT2 regulates adipocyte differentiation through FoxO1 acetylation/deacetylation. *Cell Metabolism* **2007**, *6*, 105-114.
80. Jacobs, K. M.; Pennington, J. D.; Bisht, K. S.; Aykin-Burns, N.; Kim, H.-S.; Mishra, M.; Sun, L.; Nguyen, P.; Ahn, B.-H.; Leclerc, J. SIRT3 interacts with the daf-16 homolog FOXO3a in the mitochondria, as well as increases FOXO3a dependent gene expression. *International Journal of Biological Sciences* **2008**, *4*, 291.
81. Yeung, F.; Hoberg, J. E.; Ramsey, C. S.; Keller, M. D.; Jones, D. R.; Frye, R. A.; Mayo, M. W. Modulation of NF- κ B-dependent transcription and cell survival by the SIRT1 deacetylase. *EMBO J* **2004**, *23*, 2369-2380.
82. Rothgiesser, K. M.; Erener, S.; Waibel, S.; Lüscher, B.; Hottiger, M. O. SIRT2 regulates NF- κ B-dependent gene expression through deacetylation of p65 Lys310. *Journal of cell science* **2010**, *123*, 4251-4258.
83. Kawahara, T. L. A.; Michishita, E.; Adler, A. S.; Damian, M.; Berber, E.; Lin, M.; McCord, R. A.; Ongaiqui, K. C. L.; Boxer, L. D.; Chang, H. Y.; Chua, K. F. SIRT6 Links Histone H3 Lysine 9 Deacetylation to NF- κ B-Dependent Gene Expression and Organismal Life Span. *Cell* **2009**, *136*, 62-74.
84. Menssen, A.; Hydbring, P.; Kapelle, K.; Vervoorts, J.; Diebold, J.; Lüscher, B.; Larsson, L.-G.; Hermeking, H. The c-MYC oncoprotein, the NAMPT enzyme, the SIRT1-inhibitor DBC1, and the SIRT1 deacetylase form a positive feedback loop. *Proceedings of the National Academy of Sciences of the United States of America* **2012**, *109*, E187-E196.
85. Jang, K. Y.; Noh, S. J.; Lehwald, N.; Tao, G.-Z.; Bellovin, D. I.; Park, H. S.; Moon, W. S.; Felsher, D. W.; Sylvester, K. G. SIRT1 and c-Myc promote liver tumor cell survival and predict poor survival of human hepatocellular carcinomas. *PLoS One* **2012**, *7*, e45119.
86. Liu, P.; Xu, N.; Malyukova, A.; Scarlett, C.; Sun, Y.; Zhang, X.; Ling, D.; Su, S.; Nelson, C.; Chang, D. The histone deacetylase SIRT2 stabilizes Myc oncoproteins. *Cell Death & Differentiation* **2012**.
87. Laemmle, A.; Lechleiter, A.; Roh, V.; Schwarz, C.; Portmann, S.; Furer, C.; Keogh, A.; Tschan, M. P.; Candinas, D.; Vorburger, S. A. Inhibition of SIRT1 impairs the accumulation

and transcriptional activity of HIF-1 α protein under hypoxic conditions. *PLoS One* **2012**, *7*, e33433.

88. Zhong, L.; D'Urso, A.; Toiber, D.; Sebastian, C.; Henry, R. E.; Vadysirisack, D. D.; Guimaraes, A.; Marinelli, B.; Wikstrom, J. D.; Nir, T.; Clish, C. B.; Vaitheesvaran, B.; Iliopoulos, O.; Kurland, I.; Dor, Y.; Weissleder, R.; Shirihai, O. S.; Ellisen, L. W.; Espinosa, J. M.; Mostoslavsky, R. The Histone Deacetylase SIRT6 Regulates Glucose Homeostasis via Hif1 α . *Cell* **2010**, *140*, 280-293.

89. Wang, C.; Chen, L.; Hou, X.; Li, Z.; Kabra, N.; Ma, Y.; Nemoto, S.; Finkel, T.; Gu, W.; Cress, W. D. Interactions between E2F1 and SIRT1 regulate apoptotic response to DNA damage. *Nature cell biology* **2006**, *8*, 1025-1031.

90. Cohen, H. Y.; Miller, C.; Bitterman, K. J.; Wall, N. R.; Hekking, B.; Kessler, B.; Howitz, K. T.; Gorospe, M.; de Cabo, R.; Sinclair, D. A. Calorie restriction promotes mammalian cell survival by inducing the SIRT1 deacetylase. *Science* **2004**, *305*, 390-392.

91. Sundaresan, N. R.; Samant, S. A.; Pillai, V. B.; Rajamohan, S. B.; Gupta, M. P. SIRT3 is a stress-responsive deacetylase in cardiomyocytes that protects cells from stress-mediated cell death by deacetylation of Ku70. *Molecular and cellular biology* **2008**, *28*, 6384-6401.

92. Yuan, Z.; Zhang, X.; Sengupta, N.; Lane, W. S.; Seto, E. SIRT1 regulates the function of the Nijmegen breakage syndrome protein. *Molecular Cell* **2007**, *27*, 149-162.

93. Yamamori, T.; DeRicco, J.; Naqvi, A.; Hoffman, T. A.; Mattagajasingh, I.; Kasuno, K.; Jung, S.-B.; Kim, C.-S.; Irani, K. SIRT1 deacetylates APE1 and regulates cellular base excision repair. *Nucleic Acids Research* **2010**, *38*, 832-845.

94. Fan, W.; Luo, J. SIRT1 regulates UV-induced DNA repair through deacetylating XPA. *Molecular Cell* **2010**, *39*, 247-258.

95. Li, K.; Casta, A.; Wang, R.; Lozada, E.; Fan, W.; Kane, S.; Ge, Q.; Gu, W.; Orren, D.; Luo, J. Regulation of WRN protein cellular localization and enzymatic activities by SIRT1-mediated deacetylation. *Journal of Biological Chemistry* **2008**, *283*, 7590-7598.

96. Gerhart-Hines, Z.; Rodgers, J. T.; Bare, O.; Lerin, C.; Kim, S.-H.; Mostoslavsky, R.; Alt, F. W.; Wu, Z.; Puigserver, P. Metabolic control of muscle mitochondrial function and fatty acid oxidation through SIRT1/PGC-1 α . *The EMBO journal* **2007**, *26*, 1913-1923.

97. Picard, F.; Kurtev, M.; Chung, N.; Topark-Ngarm, A.; Senawong, T.; Machado de Oliveira, R.; Leid, M.; McBurney, M. W.; Guarente, L. SIRT1 promotes fat mobilization in white adipocytes by repressing PPAR- γ . *Nature* **2004**, *429*, 771-776.

98. Li, X.; Zhang, S.; Blander, G.; Tse, J. G.; Krieger, M.; Guarente, L. SIRT1 deacetylates and positively regulates the nuclear receptor LXR. *Molecular Cell* **2007**, *28*, 91-106.

99. Kemper, J. K.; Xiao, Z.; Ponugoti, B.; Miao, J.; Fang, S.; Kanamaluru, D.; Tsang, S.; Wu, S.-Y.; Chiang, C.-M.; Veenstra, T. D. FXR Acetylation Is Normally Dynamically Regulated by p300 and SIRT1 but Constitutively Elevated in Metabolic Disease States. *Cell metabolism* **2009**, *10*, 392-404.

100. Yu, E. J.; Kim, S.-H.; Heo, K.; Ou, C.-Y.; Stallcup, M. R.; Kim, J. H. Reciprocal roles of DBC1 and SIRT1 in regulating estrogen receptor α activity and co-activator synergy. *Nucleic Acids Research* **2011**, *39*, 6932-6943.

101. Hallows, W. C.; Lee, S.; Denu, J. M. sirtuins deacetylate and activate mammalian acetyl-CoA synthetases. *Proceedings of the National Academy of Sciences of the United States of America* **2006**, *103*, 10230-10235.

102. Asher, G.; Gatfield, D.; Stratmann, M.; Reinke, H.; Dibner, C.; Kreppel, F.; Mostoslavsky, R.; Alt, F. W.; Schibler, U. SIRT1 regulates circadian clock gene expression through PER2 deacetylation. *Cell* **2008**, *134*, 317-328.

103. Bosch-Presegué, L.; Raurell-Vila, H.; Marazuela-Duque, A.; Kane-Goldsmith, N.; Valle, A.; Oliver, J.; Serrano, L.; Vaquero, A. Stabilization of Suv39H1 by SIRT1 is part of oxidative stress response and ensures genome protection. *Molecular Cell* **2011**, *42*, 210-223.

104. Bouras, T.; Fu, M.; Sauve, A. A.; Wang, F.; Quong, A. A.; Perkins, N. D.; Hay, R. T.; Gu, W.; Pestell, R. G. SIRT1 deacetylation and repression of p300 involves lysine residues 1020/1024 within the cell cycle regulatory domain 1. *Journal of Biological Chemistry* **2005**, *280*, 10264-10276.

105. Black, J. C.; Mosley, A.; Kitada, T.; Washburn, M.; Carey, M. The SIRT2 deacetylase regulates autoacetylation of p300. *Molecular Cell* **2008**, *32*, 449-455.
106. Wang, J.; Chen, J. SIRT1 regulates autoacetylation and histone acetyltransferase activity of TIP60. *Journal of Biological Chemistry* **2010**, *285*, 11458-11464.
107. Yi, J.; Luo, J. SIRT1 and p53, effect on cancer, senescence and beyond. *Biochimica et Biophysica Acta (BBA)-Proteins and Proteomics* **2010**, *1804*, 1684-1689.
108. Nie, Y.; Erion, D. M.; Yuan, Z.; Dietrich, M.; Shulman, G. I.; Horvath, T. L.; Gao, Q. STAT3 inhibition of gluconeogenesis is downregulated by SIRT1. *Nature Cell Biology* **2009**, *11*, 492-500.
109. Firestein, R.; Blander, G.; Michan, S.; Oberdoerffer, P.; Ogino, S.; Campbell, J.; Bhimavarapu, A.; Luikenhuis, S.; de Cabo, R.; Fuchs, C. The SIRT1 deacetylase suppresses intestinal tumorigenesis and colon cancer growth. *PLoS One* **2008**, *3*, e2020.
110. Chen, J.; Chan, A. W. H.; To, K.-F.; Chen, W.; Zhang, Z.; Ren, J.; Song, C.; Cheung, Y.-S.; Lai, P. B. S.; Cheng, S.-H.; Ng, M. H. L.; Huang, A.; Ko, B. C. B. SIRT2 overexpression in hepatocellular carcinoma mediates epithelial to mesenchymal transition by protein kinase B/glycogen synthase kinase-3 β / β -catenin signaling. *Hepatology* **2013**, *57*, 2287-2298.
111. Kume, S.; Haneda, M.; Kanasaki, K.; Sugimoto, T.; Araki, S.-i.; Ishiki, K.; Isono, M.; Uzu, T.; Guarente, L.; Kashiwagi, A. SIRT1 inhibits transforming growth factor β -induced apoptosis in glomerular mesangial cells via Smad7 deacetylation. *Journal of Biological Chemistry* **2007**, *282*, 151-158.
112. Bauer, I.; Grozio, A.; Lasigliè, D.; Basile, G.; Sturla, L.; Magnone, M.; Sociali, G.; Soncini, D.; Caffa, I.; Poggi, A. The NAD⁺-dependent histone deacetylase SIRT6 promotes cytokine production and migration in pancreatic cancer cells by regulating Ca²⁺ responses. *Journal of Biological Chemistry* **2012**, *287*, 40924-40937.
113. Nakagawa, T.; Lomb, D. J.; Haigis, M. C.; Guarente, L. SIRT5 Deacetylates carbamoyl phosphate synthetase 1 and regulates the urea cycle. *Cell* **2009**, *137*, 560-570.
114. Lombard, D. B.; Alt, F. W.; Cheng, H.-L.; Bunkenborg, J.; Streeper, R. S.; Mostoslavsky, R.; Kim, J.; Yancopoulos, G.; Valenzuela, D.; Murphy, A. Mammalian Sir2 homolog SIRT3 regulates global mitochondrial lysine acetylation. *Molecular and Cellular Biology* **2007**, *27*, 8807-8814.
115. Haigis, M. C.; Mostoslavsky, R.; Haigis, K. M.; Fahie, K.; Christodoulou, D. C.; Murphy, A. J.; Valenzuela, D. M.; Yancopoulos, G. D.; Karow, M.; Blander, G. SIRT4 inhibits glutamate dehydrogenase and opposes the effects of calorie restriction in pancreatic β cells. *Cell* **2006**, *126*, 941-954.
116. Martínez-Redondo, P.; Vaquero, A. The Diversity of Histone Versus Nonhistone sirtuin Substrates. *Genes & Cancer* **2013**.
117. Roth, M.; Chen, W. Sorting out functions of sirtuins in cancer. *Oncogene* **2013**.
118. Sebastián, C.; Satterstrom, F. K.; Haigis, M. C.; Mostoslavsky, R. From sirtuin Biology to Human Diseases: An Update. *Journal of Biological Chemistry* **2012**, *287*, 42444-42452.
119. Van Meter, M.; Mao, Z.; Gorbunova, V.; Seluanov, A. SIRT6 overexpression induces massive apoptosis in cancer cells but not in normal cells. *Cell Cycle* **2011**, *10*, 3153-3158.
120. Sebastián, C.; Zwaans, B. M.; Silberman, D. M.; Gymrek, M.; Goren, A.; Zhong, L.; Ram, O.; Truelove, J.; Guimaraes, A. R.; Toiber, D. The histone deacetylase SIRT6 is a tumor suppressor that controls cancer metabolism. *Cell* **2012**, *151*, 1185-1199.
121. Yuan, J.; Minter-Dykhouse, K.; Lou, Z. A c-Myc-SIRT1 feedback loop regulates cell growth and transformation. *The Journal of Cell Biology* **2009**, *185*, 203-211.
122. Lim, J.-H.; Lee, Y.-M.; Chun, Y.-S.; Chen, J.; Kim, J.-E.; Park, J.-W. sirtuin 1 modulates cellular responses to hypoxia by deacetylating hypoxia-inducible factor 1 α . *Molecular Cell* **2010**, *38*, 864-878.
123. Hanahan, D.; Weinberg, Robert A. Hallmarks of Cancer: The Next Generation. *Cell* **2011**, *144*, 646-674.
124. Finley, L. W.; Carracedo, A.; Lee, J.; Souza, A.; Egia, A.; Zhang, J.; Teruya-Feldstein, J.; Moreira, P. I.; Cardoso, S. M.; Clish, C. B. SIRT3 opposes reprogramming of cancer cell metabolism through HIF1 α destabilization. *Cancer Cell* **2011**, *19*, 416-428.

125. Bell, E.; Emerling, B.; Ricoult, S.; Guarente, L. SIRT3 suppresses hypoxia inducible factor 1 α and tumor growth by inhibiting mitochondrial ROS production. *Oncogene* **2011**, *30*, 2986-2996.
126. Hanahan, D.; Weinberg, R. A. The Hallmarks of Cancer. *Cell* **2000**, *100*, 57-70.
127. Jin, Y.-H.; Kim, Y.-J.; Kim, D.-W.; Baek, K.-H.; Kang, B. Y.; Yeo, C.-Y.; Lee, K.-Y. SIRT2 interacts with 14-3-3 β/γ and down-regulates the activity of p53. *Biochemical and Biophysical Research Communications* **2008**, *368*, 690-695.
128. Li, Y.; Matsumori, H.; Nakayama, Y.; Osaki, M.; Kojima, H.; Kurimasa, A.; Ito, H.; Mori, S.; Katoh, M.; Oshimura, M. SIRT2 down - regulation in HeLa can induce p53 accumulation via p38 MAPK activation - dependent p300 decrease, eventually leading to apoptosis. *Genes to Cells* **2011**, *16*, 34-45.
129. Wang, F.; Nguyen, M.; Qin, F.; Tong, Q. SIRT2 deacetylates FOXO3a in response to oxidative stress and caloric restriction. *Aging cell* **2007**, *6*, 505-514.
130. Zhao, Y.; Yang, J.; Liao, W.; Liu, X.; Zhang, H.; Wang, S.; Wang, D.; Feng, J.; Yu, L.; Zhu, W.-G. Cytosolic FoxO1 is essential for the induction of autophagy and tumour suppressor activity. *Nature cell biology* **2010**, *12*, 665-675.
131. Chen, J.; Zhang, B.; Wong, N.; Lo, A. W. I.; To, K.-F.; Chan, A. W. H.; Ng, M. H. L.; Ho, C. Y. S.; Cheng, S.-H.; Lai, P. B. S.; Yu, J.; Ng, H.-K.; Ling, M.-T.; Huang, A.-L.; Cai, X.-F.; Ko, B. C. B. sirtuin 1 Is Upregulated in a Subset of Hepatocellular Carcinomas where It Is Essential for Telomere Maintenance and Tumor Cell Growth. *Cancer Research* **2011**, *71*, 4138-4149.
132. Portmann, S.; Fahrner, R.; Lechleiter, A.; Keogh, A.; Overney, S.; Laemmle, A.; Mikami, K.; Montani, M.; Tschan, M. P.; Candinas, D.; Stroka, D. Antitumor Effect of SIRT1 Inhibition in Human HCC Tumor Models *In vitro* and *In vivo*. *Molecular Cancer Therapeutics* **2013**, *12*, 499-508.
133. Chen, H.-C.; Hsu, H.-C. SIRT1 promotes tumorigenesis and resistance to chemotherapy in hepatocellular carcinoma and its expression predicts poor prognosis. *Ann Surg Oncol* **2012**, *19*, 2011-2019.
134. Choi, H. N.; Bae, J. S.; Jamiyandorj, U.; Noh, S. J.; Park, H. S.; Jang, K. Y.; Chung, M. J.; Kang, M. J.; Lee, D. G.; Moon, W. S. Expression and role of SIRT1 in hepatocellular carcinoma. *Oncology Reports* **2011**, *26*, 503-510.
135. Wang, R.-H.; Sengupta, K.; Li, C.; Kim, H.-S.; Cao, L.; Xiao, C.; Kim, S.; Xu, X.; Zheng, Y.; Chilton, B. Impaired DNA damage response, genome instability, and tumorigenesis in SIRT1 mutant mice. *Cancer Cell* **2008**, *14*, 312-323.
136. Oyagbemi, A.; Azeez, O.; Saba, A. Hepatocellular carcinoma and the underlying mechanisms. *African Health Sciences* **2010**, *10*, 93.
137. Yamakuchi, M.; Ferlito, M.; Lowenstein, C. J. miR-34a repression of SIRT1 regulates apoptosis. *Proceedings of the National Academy of Sciences of the United States of America* **2008**, *105*, 13421-13426.
138. Jung-Hynes, B.; Ahmad, N. Role of p53 in the anti-proliferative effects of SIRT1 inhibition in prostate cancer cells. *Cell Cycle* **2009**, *8*, 1478-1483.
139. Srisuttee, R.; Koh, S. S.; Malilas, W.; Moon, J.; Cho, I.-R.; Jhun, B. H.; Horio, Y.; Chung, Y.-H. SIRT1 sensitizes hepatocellular carcinoma cells expressing hepatitis B virus X protein to oxidative stress-induced apoptosis. *Biochemical and Biophysical Research Communications* **2012**, *429*, 45-50.
140. Xie, H. J.; Jung, K. H.; Nam, S. W. Overexpression of SIRT2 contributes tumor cell growth in hepatocellular carcinomas. *Molecular & Cellular Toxicology* **2011**, *7*, 367-374.
141. Peck, B.; Chen, C.-Y.; Ho, K.-K.; Di Fruscia, P.; Myatt, S. S.; Coombes, R. C.; Fuchter, M. J.; Hsiao, C.-D.; Lam, E. W.-F. SIRT inhibitors induce cell death and p53 acetylation through targeting both SIRT1 and SIRT2. *Molecular Cancer Therapeutics* **2010**, *9*, 844-855.
142. Trapp, J.; Jochum, A.; Meier, R.; Saunders, L.; Marshall, B.; Kunick, C.; Verdin, E.; Goekjian, P.; Sippl, W.; Jung, M. Adenosine Mimetics as Inhibitors of NAD⁺-Dependent Histone Deacetylases, from Kinase to sirtuin Inhibition. *Journal of Medicinal Chemistry* **2006**, *49*, 7307-7316.

143. Huber, K.; Schemies, J. r.; Uciechowska, U.; Wagner, J. M.; Rumpf, T.; Lewrick, F.; Süß, R.; Sippl, W.; Jung, M.; Bracher, F. Novel 3-Arylideneindolin-2-ones as Inhibitors of NAD⁺-Dependent Histone Deacetylases (sirtuins). *Journal of Medicinal Chemistry* **2009**, *53*, 1383-1386.
144. North, B. J.; Marshall, B. L.; Borra, M. T.; Denu, J. M.; Verdin, E. The Human Sir2 Ortholog, SIRT2, Is an NAD⁺-Dependent Tubulin Deacetylase. *Molecular Cell* **2003**, *11*, 437-444.
145. Suenkel, B.; Fischer, F.; Steegborn, C. Inhibition of the human deacylase sirtuin 5 by the indole GW5074. *Bioorganic & Medicinal Chemistry Letters* **2012**.
146. Mohammadi, M.; McMahon, G.; Sun, L.; Tang, C.; Hirth, P.; Yeh, B. K.; Hubbard, S. R.; Schlessinger, J. Structures of the tyrosine kinase domain of fibroblast growth factor receptor in complex with inhibitors. *Science* **1997**, *276*, 955-960.
147. Sun, L.; Tran, N.; Tang, F.; App, H.; Hirth, P.; McMahon, G.; Tang, C. Synthesis and biological evaluations of 3-substituted indolin-2-ones: A novel class of tyrosine kinase inhibitors that exhibit selectivity toward particular receptor tyrosine kinases. *Journal of Medicinal Chemistry* **1998**, *41*, 2588-2603.
148. Xiong, X.; Zhang, Y.; Gao, X.; Dong, Z.; Li, L.; Ji, C.; Fu, L.; Luo, X.; Liu, H.; Mei, C. B5, a novel pyrrole-substituted indolinone, exerts potent antitumor efficacy through G2/M cell cycle arrest. *Investigational New Drugs* **2010**, *28*, 26-34.
149. R Prakash, C.; Raja, S. Indolinones as Promising Scaffold as Kinase Inhibitors: A Review. *Mini Reviews in Medicinal Chemistry* **2012**, *12*, 98-119.
150. Roth, G. J.; Heckel, A.; Colbatzky, F.; Handschuh, S.; Kley, J. r.; Lehmann-Lintz, T.; Lotz, R.; Tontsch-Grunt, U.; Walter, R.; Hilberg, F. Design, synthesis, and evaluation of indolinones as triple angiokinase inhibitors and the discovery of a highly specific 6-methoxycarbonyl-substituted indolinone (BIBF 1120). *Journal of Medicinal Chemistry* **2009**, *52*, 4466-4480.
151. Roth, G. J.; Heckel, A.; Brandl, T.; Grauert, M.; Hoerer, S.; Kley, J. T.; Schnapp, G.; Baum, P.; Mennerich, D.; Schnapp, A. Design, synthesis, and evaluation of indolinones as inhibitors of the transforming growth factor β receptor I (TGF β RI). *Journal of Medicinal Chemistry* **2010**, *53*, 7287-7295.
152. Konkel, M. J.; Lagu, B.; Boteju, L. W.; Jimenez, H.; Noble, S.; Walker, M. W.; Chandrasena, G.; Blackburn, T. P.; Nikam, S. S.; Wright, J. L.; Kornberg, B. E.; Gregory, T.; Pugsley, T. A.; Akunne, H.; Zoski, K.; Wise, L. D. 3-arylimino-2-indolones are potent and selective galanin GAL(3) receptor antagonists. *Journal of Medicinal Chemistry* **2006**, *49*, 3757-3758.
153. Christensen, M. K.; Erichsen, K. D.; Trojel-Hansen, C.; Tjørnelund, J.; Nielsen, S. J.; Frydenvang, K.; Johansen, T. N.; Nielsen, B.; Sehested, M.; Jensen, P. B.; Ikaunieks, M.; Zaichenko, A.; Loza, E.; Kalvinsh, I.; Björklund, F. Synthesis and Antitumor Effect *in vitro* and *in vivo* of Substituted 1,3-Dihydroindole-2-ones. *Journal of Medicinal Chemistry* **2010**, *53*, 7140-7145.
154. Kim, M. H.; Tshako, A. L.; Co, E. W.; Aftab, D. T.; Bentzien, F.; Chen, J.; Cheng, W.; Engst, S.; Goon, L.; Klein, R. R.; Le, D. T.; Mac, M.; Parks, J. J.; Qian, F.; Rodriguez, M.; Stout, T. J.; Till, J. H.; Won, K.-A.; Wu, X.; Michael Yakes, F.; Yu, P.; Zhang, W.; Zhao, Y.; Lamb, P.; Nuss, J. M.; Xu, W. The design, synthesis, and biological evaluation of potent receptor tyrosine kinase inhibitors. *Bioorganic & Medicinal Chemistry Letters* **2012**, *22*, 4979-4985.
155. Zou, H.; Zhang, L.; Ouyang, J.; Giulianotti, M. A.; Yu, Y. Synthesis and biological evaluation of 2-indolinone derivatives as potential antitumor agents. *European Journal of Medicinal Chemistry* **2011**, *46*, 5970-5977.
156. Chiang, C.-C.; Lin, Y.-H.; Lin, S. F.; Lai, C.-L.; Liu, C.; Wei, W.-Y.; Yang, S.-c.; Wang, R.-W.; Teng, L.-W.; Chuang, S.-H.; Chang, J.-M.; Yuan, T.-T.; Lee, Y.-S.; Chen, P.; Chi, W.-K.; Yang, J.-Y.; Huang, H.-J.; Liao, C.-B.; Huang, J.-J. Discovery of Pyrrole-Indoline-2-ones as Aurora Kinase Inhibitors with a Different Inhibition Profile. *Journal of Medicinal Chemistry* **2010**, *53*, 5929-5941.

157. Andreani, A.; Granaiola, M.; Locatelli, A.; Morigi, R.; Rambaldi, M.; Varoli, L.; Calonghi, N.; Cappadone, C.; Farruggia, G.; Stefanelli, C.; Masotti, L.; Nguyen, T. L.; Hamel, E.; Shoemaker, R. H. Substituted 3-(5-Imidazo[2,1-b]thiazolylmethylene)-2-indolinones and Analogues: Synthesis, Cytotoxic Activity, and Study of the Mechanism of Action(1). *Journal of Medicinal Chemistry* **2012**, *55*, 2078-2088.
158. Henise, J. C.; Taunton, J. Irreversible Nek2 Kinase Inhibitors with Cellular Activity. *Journal of Medicinal Chemistry* **2011**, *54*, 4133-4146.
159. Luo, Y.; Xiao, F.; Qian, S.; He, Q.; Lu, W.; Yang, B. Synthesis and evaluation of novel 5-sulfonyl-indolin-2-ones as potent cytotoxic agents. *MedChemComm* **2011**, *2*, 1054-1057.
160. Zhang, W.; Go, M.-L. Functionalized 3-benzylidene-indolin-2-ones: Inducers of NAD(P)H-quinone oxidoreductase 1 (NQO1) with antiproliferative activity. *Bioorganic & Medicinal Chemistry* **2009**, *17*, 2077-2090.
161. Yang, X.; Zhang, Y.; Zhang, L.; Zhang, L.; Mao, J. Silencing alpha-fetoprotein expression induces growth arrest and apoptosis in human hepatocellular cancer cell. *Cancer letters* **2008**, *271*, 281-293.
162. Cheng, W.; Tseng, C. J.; Lin, T. T.; Cheng, I.; Pan, H. W.; Hsu, H. C.; Lee, Y. M. Glypican-3-mediated oncogenesis involves the Insulin-like growth factor-signaling pathway. *Carcinogenesis* **2008**, *29*, 1319-26.
163. Hopfner, M.; Huether, A.; Sutter, A. P.; Baradari, V.; Schuppan, D.; Scherubl, H. Blockade of IGF-1 receptor tyrosine kinase has antineoplastic effects in hepatocellular carcinoma cells. *Biochem Pharmacol* **2006**, *71*, 1435-48.
164. Scharf, J. G.; Braulke, T. The role of the IGF axis in hepatocarcinogenesis. *Horm Metab Res* **2003**, *35*, 685-93.
165. Lee, C. F.; Ling, Z. Q.; Zhao, T.; Fang, S. H.; Chang, W. C.; Lee, S. C.; Lee, K. R. Genomic-wide analysis of lymphatic metastasis-associated genes in human hepatocellular carcinoma. *World J Gastroenterol* **2009**, *15*, 356-65.
166. Hafizi, S.; Dahlback, B. Gas6 and protein S. Vitamin K-dependent ligands for the Axl receptor tyrosine kinase subfamily. *FEBS J* **2006**, *273*, 5231-44.
167. Hughes, J. D.; Blagg, J.; Price, D. A.; Bailey, S.; DeCrescenzo, G. A.; Devraj, R. V.; Ellsworth, E.; Fobian, Y. M.; Gibbs, M. E.; Gilles, R. W.; Greene, N.; Huang, E.; Krieger-Burke, T.; Loesel, J.; Wager, T.; Whiteley, L.; Zhang, Y. Physicochemical drug properties associated with *in vivo* toxicological outcomes. *Bioorganic & Medicinal Chemistry Letters* **2008**, *18*, 4872-4875.
168. Wolff, M. E. Burger's Medicinal Chemistry and Drug Discovery. In *Principles and Practice*, Wolff, M. E., Ed. Wiley interscience: 1995; Vol. I, pp 507-509.
169. Rzepa, H. In *Anatomy of an arrow-pushing tutorial: reducing a carboxylic acid*.
170. Brown, H. C.; Heim, P.; Yoon, N. M. Selective reductions. XV. Reaction of diborane in tetrahydrofuran with selected organic compounds containing representative functional groups. *Journal of the American Chemical Society* **1970**, *92*, 1637-1646.
171. Shen, W.; Barr, K.; Oslob, J. D.; Zhong, M. Preparation of substituted isoquinolines as modulators of cellular adhesion. WO2005044817A1, 2005.
172. Cervena, I.; Metysova, J.; Protiva, M. Fluorinated analogs of the tricyclic neuroleptics - 2,3-difluoro derivative of clorothepin. *European Journal of Medicinal Chemistry* **1980**, *15*, 330-332.
173. Liégault, B. t.; Petrov, I.; Gorelsky, S. I.; Fagnou, K. Modulating Reactivity and Diverting Selectivity in Palladium-Catalyzed Heteroaromatic Direct Arylation Through the Use of a Chloride Activating/Blocking Group. *The Journal of Organic Chemistry* **2010**, *75*, 1047-1060.
174. Nichols, W.; Murphy, D.; Cristofalo, V.; Toji, L.; Greene, A.; Dwight, S. Characterization of a new human diploid cell strain, IMR-90. *Science* **1977**, *196*, 60-63.
175. http://dtp.nci.nih.gov/docs/compare/compare_methodology.html
176. López-Terrada, D.; Cheung, S. W.; Finegold, M. J.; Knowles, B. B. Hep G2 is a hepatoblastoma-derived cell line. *Human Pathology* **2009**, *40*, 1512-1515.

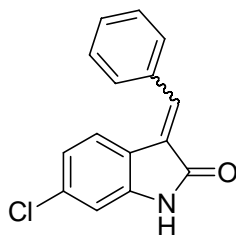
- 177.Hsu, I. C.; Tokiwa, T.; Bennett, W.; Metcalf, R. A.; Welsh, J. A.; Sun, T.; Harris, C. C. p53 gene mutation and integrated hepatitis B viral DNA sequences in human liver cancer cell lines. *Carcinogenesis* **1993**, *14*, 987-992.
- 178.Hsu, I.; Metcalf, R.; Sun, T.; Welsh, J.; Wang, N.; Harris, C. Mutational hot spot in the p53 gene in human hepatocellular carcinomas. **1991**.
- 179.Bressac, B.; Galvin, K. M.; Liang, T. J.; Isselbacher, K. J.; Wands, J. R.; Ozturk, M. Abnormal structure and expression of p53 gene in human hepatocellular carcinoma. *Proceedings of the National Academy of Sciences of the United States of America* **1990**, *87*, 1973-1977.
- 180.Bressac, B.; Puisieux, A.; Kew, M.; Volkmann, M.; Bozcall, S.; Bella Mura, J.; de la Monte, S.; Carlson, R.; Blum, H.; Wands, J. p53 mutation in hepatocellular carcinoma after aflatoxin exposure. *The Lancet* **1991**, *338*, 1356-1359.
- 181.Oda, T.; Tsuda, H.; Scarpa, A.; Sakamoto, M.; Hirohashi, S. p53 gene mutation spectrum in hepatocellular carcinoma. *Cancer Research* **1992**, *52*, 6358-6364.
- 182.Knowles, B. B.; Howe, C. C.; Aden, D. P. Human hepatocellular carcinoma cell lines secrete the major plasma proteins and hepatitis B surface antigen. *Science* **1980**, *209*, 497-499.
- 183.Lee, J. H.; Ku, J. L.; Park, Y. J.; Lee, K. U.; Kim, W. H.; Park, J. G. Establishment and characterization of four human hepatocellular carcinoma cell lines containing hepatitis B virus DNA. *World Journal of Gastroenterology* **1999**, *5*, 289-295.
- 184.Wilkening, S.; Stahl, F.; Bader, A. Comparison of primary human hepatocytes and hepatoma cell line hepg2 with regard to their biotransformation properties. *Drug Metabolism and Disposition* **2003**, *31*, 1035-1042.
- 185.Song, M.-S.; Lee, S.-W. Cancer-selective induction of cytotoxicity by tissue-specific expression of targeted trans-splicing ribozyme. *FEBS Letters* **2006**, *580*, 5033-5043.
- 186.Bissantz, C.; Kuhn, B.; Stahl, M. A Medicinal Chemist's Guide to Molecular Interactions. *Journal of Medicinal Chemistry* **2010**, *53*, 5061-5084.
- 187.Dunitz, J. D.; Taylor, R. Organic fluorine hardly ever accepts hydrogen bonds. *Chemistry-A European Journal* **1997**, *3*, 89-98.
- 188.Paulini, R.; Müller, K.; Diederich, F. Orthogonal multipolar interactions in structural chemistry and biology. *Angewandte Chemie International Edition* **2005**, *44*, 1788-1805.
- 189.Halley, F.; Reinshagen, J.; Ellinger, B.; Wolf, M.; Niles, A. L.; Evans, N. J.; Kirkland, T. A.; Wagner, J. M.; Jung, M.; Gribbon, P. A Bioluminogenic HDAC Activity Assay Validation and Screening. *Journal of Biomolecular Screening* **2011**, *16*, 1227-1235.
- 190.Moniot, S.; Schutkowski, M.; Steegborn, C. Crystal structure analysis of human SIRT2 and its ADP-ribose complex. *Journal of Structural Biology* **2013**.
- 191.Verdonk, M. L.; Cole, J. C.; Hartshorn, M. J.; Murray, C. W.; Taylor, R. D. Improved protein-ligand docking using GOLD. *Proteins* **2003**, *52*, 609-623.
- 192.Zhao, X.; Allison, D.; Condon, B.; Zhang, F.; Gheyi, T.; Zhang, A.; Ashok, S.; Russell, M.; MacEwan, I.; Qian, Y.; Jamison, J. A.; Luz, J. G. The 2.5 Å Crystal Structure of the SIRT1 Catalytic Domain Bound to Nicotinamide Adenine Dinucleotide (NAD⁺) and an Indole (EX527 Analogue) Reveals a Novel Mechanism of Histone Deacetylase Inhibition. *Journal of Medicinal Chemistry* **2013**, *56*, 963-969.
- 193.Outeiro, T. F.; Kontopoulos, E.; Altmann, S. M.; Kufareva, I.; Strathearn, K. E.; Amore, A. M.; Volk, C. B.; Maxwell, M. M.; Rochet, J.-C.; McLean, P. J. sirtuin 2 inhibitors rescue α -synuclein-mediated toxicity in models of Parkinson's disease. *Science* **2007**, *317*, 516-519.
- 194.Napper, A. D.; Hixon, J.; McDonagh, T.; Keavey, K.; Pons, J.-F.; Barker, J.; Yau, W. T.; Amouzegh, P.; Flegg, A.; Hamelin, E. Discovery of indoles as potent and selective inhibitors of the deacetylase SIRT1. *Journal of Medicinal Chemistry* **2005**, *48*, 8045-8054.
- 195.Yuan, H.; Marmorstein, R. Structural Basis for sirtuin Activity and Inhibition. *Journal of Biological Chemistry* **2012**, *287*, 42428-42435.
- 196.Finnin, M. S.; Donigian, J. R.; Pavletich, N. P. Structure of the histone deacetylase SIRT2. *Nature Structural & Molecular Biology* **2001**, *8*, 621-625.
- 197.Auffinger, P.; Hays, F. A.; Westhof, E.; Ho, P. S. Halogen bonds in biological molecules. *Proceedings of the National Academy of Sciences of the United States of America* **2004**, *101*, 16789-16794.

- 198.Voth, A. R.; Khuu, P.; Oishi, K.; Ho, P. S. Halogen bonds as orthogonal molecular interactions to hydrogen bonds. *Nature Chemistry* **2009**, 1, 74-79.
- 199.Lu, Y.; Liu, Y.; Xu, Z.; Li, H.; Liu, H.; Zhu, W. Halogen bonding for rational drug design and new drug discovery. *Expert Opinion on Drug Discovery* **2012**, 7, 375-383.
- 200.Huhtiniemi, T.; Wittekindt, C.; Laitinen, T.; Leppänen, J.; Salminen, A.; Poso, A.; Lahtela-Kakkonen, M. Comparative and pharmacophore model for deacetylase SIRT1. *Journal of Computer-Aided Molecular Design* **2006**, 20, 589-599.
- 201.Li, M.; Luo, J.; Brooks, C. L.; Gu, W. Acetylation of p53 inhibits its ubiquitination by Mdm2. *Journal of Biological Chemistry* **2002**, 277, 50607-50611.
- 202.Zhao, Y.; Lu, S.; Wu, L.; Chai, G.; Wang, H.; Chen, Y.; Sun, J.; Yu, Y.; Zhou, W.; Zheng, Q. Acetylation of p53 at lysine 373/382 by the histone deacetylase inhibitor depsipeptide induces expression of p21Waf1/Cip1. *Molecular and Cellular Biology* **2006**, 26, 2782-2790.
- 203.Yamaguchi, H.; Woods, N. T.; Piluso, L. G.; Lee, H.-H.; Chen, J.; Bhalla, K. N.; Monteiro, A.; Liu, X.; Hung, M.-C.; Wang, H.-G. p53 acetylation is crucial for its transcription-independent proapoptotic functions. *Journal of Biological Chemistry* **2009**, 284, 11171-11183.
- 204.Iyer, N. G.; Chin, S.-F.; Ozdag, H.; Daigo, Y.; Hu, D.-E.; Cariati, M.; Brindle, K.; Aparicio, S.; Caldas, C. p300 regulates p53-dependent apoptosis after DNA damage in colorectal cancer cells by modulation of PUMA/p21 levels. *Proceedings of the National Academy of Sciences of the United States of America* **2004**, 101, 7386-7391.
- 205.Marshall, A. D.; van der Ent, M. A.; Grosveld, G. C. PAX3 - FOXO1 and FGFR4 in alveolar rhabdomyosarcoma. *Molecular Carcinogenesis* **2012**, 51, 807-815.
- 206.Holbro, T.; Beerli, R. R.; Maurer, F.; Koziczak, M.; Iii, C. F. B.; Hynes, N. E. The ErbB2/ErbB3 Heterodimer Functions as an Oncogenic Unit: ErbB2 Requires ErbB3 to Drive Breast Tumor Cell Proliferation. *Proceedings of the National Academy of Sciences of the United States of America* **2003**, 100, 8933-8938.
- 207.Stadler, C. R.; Knyazev, P.; Bange, J.; Ullrich, A. FGFR4 GLY388 isotype suppresses motility of MDA-MB-231 breast cancer cells by EDG-2 gene repression. *Cellular Signalling* **2006**, 18, 783-794.
- 208.Kostrzewa, M.; Müller, U. Genomic structure and complete sequence of the human FGFR4 gene. *Mammalian Genome* **1998**, 9, 131-135.
- 209.Ito, Y.; Takeda, T.; Sakon, M.; Tsujimoto, M.; Higashiyama, S.; Noda, K.; Miyoshi, E.; Monden, M.; Matsuura, N. Expression and clinical significance of erb-B receptor family in hepatocellular carcinoma. *British Journal of Cancer* **2001**, 84, 1377.
- 210.Guy, P. M.; Platko, J. V.; Cantley, L. C.; Cerione, R. A.; Iii, K. L. C. Insect Cell-Expressed p180erbB3 Possesses an Impaired Tyrosine Kinase Activity. *Proceedings of the National Academy of Sciences of the United States of America* **1994**, 91, 8132-8136.
- 211.Sergina, N. V.; Rausch, M.; Wang, D.; Blair, J.; Hann, B.; Shokat, K. M.; Moasser, M. M. Escape from HER-family tyrosine kinase inhibitor therapy by the kinase-inactive HER3. *Nature* **2007**, 445, 437-441.
- 212.Kan, M.; Wu, X.; Wang, F.; McKeegan, W. L. Specificity for Fibroblast Growth Factors Determined by Heparan Sulfate in a Binary Complex with the Receptor Kinase. *Journal of Biological Chemistry* **1999**, 274, 15947-15952.
- 213.Lin, B. C.; Wang, M.; Blackmore, C.; Desnoyers, L. R. Liver-specific Activities of FGF19 Require Klotho beta. *Journal of Biological Chemistry* **2007**, 282, 27277-27284.
- 214.Ho, H. K.; Pok, S.; Streit, S.; Ruhe, J. E.; Hart, S.; Lim, K. S.; Loo, H. L.; Aung, M. O.; Lim, S. G.; Ullrich, A. Fibroblast growth factor receptor 4 regulates proliferation, anti-apoptosis and alpha-fetoprotein secretion during hepatocellular carcinoma progression and represents a potential target for therapeutic intervention. *Journal of Hepatology* **2009**, 50, 118-127.
- 215.Camenisch, G.; Folkers, G.; van de Waterbeemd, H. Review of theoretical passive drug absorption models: Historical background, recent developments and limitations. *Pharmaceutica Acta Helveticae* **1996**, 71, 309-327.

216. McCann, J.; Spingarn, N. E.; Kobori, J.; Ames, B. N. Detection of carcinogens as mutagens: bacterial tester strains with R factor plasmids. *Proceedings of the National Academy of Sciences of the United States of America* **1975**, *72*, 979-983.
217. Maron, D. M.; Ames, B. N. Revised methods for the Salmonella mutagenicity test. *Mutation Research/Environmental Mutagenesis and Related Subjects* **1983**, *113*, 173-215.
218. McGovern, S. L.; Helfand, B. T.; Feng, B.; Shoichet, B. K. A specific mechanism of nonspecific inhibition. *Journal of Medicinal Chemistry* **2003**, *46*, 4265-4272.
219. Seidler, J.; McGovern, S. L.; Doman, T. N.; Shoichet, B. K. Identification and prediction of promiscuous aggregating inhibitors among known drugs. *Journal of Medicinal Chemistry* **2003**, *46*, 4477-4486.
220. Giannetti, A. M.; Koch, B. D.; Browner, M. F. Surface plasmon resonance based assay for the detection and characterization of promiscuous inhibitors. *Journal of Medicinal Chemistry* **2008**, *51*, 574-580.
221. Thompson, M. J.; Louth, J. C.; Ferrara, S.; Sorrell, F. J.; Irving, B. J.; Cochrane, E. J.; Meijer, A.; Chen, B. N. Structure-Activity Relationship Refinement and Further Assessment of Indole-3-glyoxylamides as a Lead Series against Prion Disease. *Chemmedchem* **2011**, *6*, 115-130.
222. Thompson, M. J.; Louth, J. C.; Greenwood, G. K.; Sorrell, F. J.; Knight, S. G.; Adams, N. B.; Chen, B. Improved 2, 4 - Diarylthiazole - Based Antiprion Agents: Switching the Sense of the Amide Group at C5 Leads to an Increase in Potency. *ChemMedChem* **2010**, *5*, 1476-1488.
223. Baumans, V.; Brain, P. F.; Brugère, H.; Clausing, P.; Jeneskog, T.; Perretta, G. Pain and distress in laboratory rodents and lagomorphs: Report of the Federation of European Laboratory Animal Science Associations (FELASA) Working Group on Pain and Distress accepted by the FELASA Board of Management November 1992. *Laboratory Animals* **1994**, *28*, 97-112.
224. Rydzewski, R. Turning Hits into Drugs. In *Real World Drug Discovery: a Chemist's Guide to Biotech and Pharmaceutical Research*, Elsevier: 2008; p 289.
225. Rautio, J.; Kumpulainen, H.; Heimbach, T.; Oliyai, R.; Oh, D.; Järvinen, T.; Savolainen, J. Prodrugs: design and clinical applications. *Nature Reviews Drug Discovery* **2008**, *7*, 255-270.
226. Wang, Y.; Guziec, F. S. A Convenient Reductive Deamination (Hydrodeamination) of Aromatic Amines. *The Journal of Organic Chemistry* **2001**, *66*, 8293-8296.
227. Billen, D.; Boyle, J.; Critcher, D. J.; Gethin, D. M.; Hall, K. T.; Kyne, G. M.; Pfizer, I. Substituted arylpyrazoles. **2006**.
228. Kerns, E. H.; Di, L.; Petusky, S.; Farris, M.; Ley, R.; Jupp, P. Combined application of parallel artificial membrane permeability assay and Caco-2 permeability assays in drug discovery. *Journal of Pharmaceutical Sciences* **2004**, *93*, 1440-1453.
229. Avdeef, A.; Bendels, S.; Di, L.; Faller, B.; Kansy, M.; Sugano, K.; Yamauchi, Y. PAMPA—critical factors for better predictions of absorption. *Journal of Pharmaceutical Sciences* **2007**, *96*, 2893-2909.

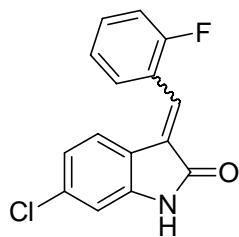
Appendix I: Characterization of synthesized analogues

(*E*)-3-Benzylidene-6-chloro-1,3-dihydro-indol-2-one (1-1):



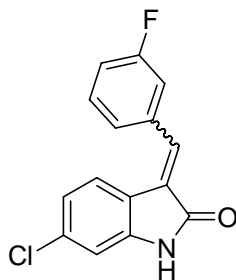
Yellow solid, yield: 11.8%; melting point: 197.0°C; ¹H NMR (300 MHz, in DMSO-d₆): δ 10.8 (br s, 1H), 7.68- 7.75 (m, 3H), 7.47- 7.55 (m, 4H), 6.84-6.92 (m, 2H); ¹³C NMR (75 MHz, in DMSO-d₆): δ 168.5, 144.2, 136.7, 134.1, 131.9, 129.9, 129.3, 128.8, 126.5, 123.5, 120.9, 119.7, 110.1; MS (APCI): *m/z* 256.0, 258.0 [M+H]⁺.

(*E*)-6-Chloro-3-(2-fluoro-benzylidene)-1,3-dihydro-indol-2-one, (1-2):



Yellow solid, yield: 50.2%; melting point: 239.6°C; ¹H NMR (300 MHz, in DMSO-d₆): δ 10.8 (br s, 1H, NH), 7.74 (t, J = 8 Hz, 1H), 7.52- 7.58 (m, 2H), 7.32- 7.41 (m, 2H), 7.22 (d, J = 7.80 Hz, 1H), 6.89-6.91 (m, 2H); ¹³C NMR (75 MHz, in DMSO-d₆): δ 168.0, 159.6, 144.4, 134.5, 132.1, 130.4, 128.6, 128.2, 124.7, 123.9, 122, 121, 119.5, 116, 110.1; MS (APCI): *m/z* 274.2, 276.2 [M+H]⁺.

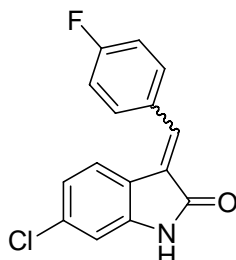
(*E*)-6-Chloro-3-(3-fluoro-benzylidene)-1,3-dihydro-indol-2-one (1-3):



Yellow solid, yield: 36.6%; melting point: 224.3°C; ¹H NMR (300 MHz, in DMSO-d₆): δ 10.8 (br s, 1H), 7.63 (s, 1H), 7.47- 7.58 (m, 3H), 7.42 (d, J = 8.7 Hz, 1H), 7.29- 7.34 (m, 1H),

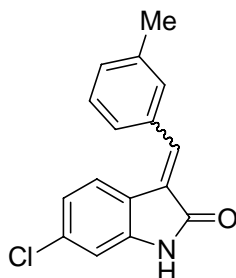
6.90- 6.92 (m, 2H); ^{13}C NMR (75 MHz, in DMSO- d_6): δ 168.3, 163.7, 160.4, 144.4, 136.5, 134.9, 134.4, 130.8, 127.5, 125.2, 123.6, 120.9, 119.4, 116.5, 115.9, 110.1; MS (APCI): m/z 274.2, 276.2 $[\text{M}+\text{H}]^+$.

(E)-6-Chloro-3-(4-fluoro-benzylidene)-1,3-dihydro-indol-2-one (1-4):



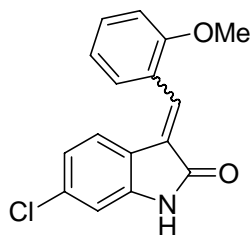
Yellow solid, yield: 42.86%; melting point: 224.4°C; ^1H NMR (300 MHz, in DMSO- d_6): δ 10.8 (br s, 1H), 7.72-7.78 (m, 2H), 7.64 (s, 1H), 7.47 (d, 2H), 7.23 (d, $J = 8.1$ Hz, 1H), 7.31-7.38 (m, 2H), 6.84- 6.92 (m, 2H); ^{13}C NMR (75 MHz, in DMSO- d_6): δ 169.6, 145.3, 136.7, 135.2, 133, 132.8, 131.7, 131.6, 127.6, 124.6, 122, 120.7, 117.2, 116.9, 111.2; MS (APCI): m/z 274.2, 276.2 $[\text{M}+\text{H}]^+$.

(E)-6-Chloro-3-(3-methyl-benzylidene)-1,3-dihydro-indol-2-one (1-5):



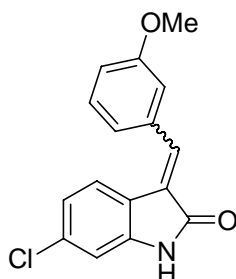
Yellow solid, yield: 3.70%; melting point: 197.3 °C; ^1H NMR (300 MHz, in DMSO- d_6): δ 10.8 (br s, 1H), 7.63 (s, 1H), 7.48-7.51 (m, 3H), 7.41 (t, $J = 8.1$ Hz, 1H), 7.29-7.33 (m, 1H), 6.89-6.91 (m, 2H), 2.36 (s, 3H); ^{13}C NMR (75 MHz, in DMSO- d_6): δ 169.6, 145.3, 142.9, 139.2, 137.9, 135.1, 131.7, 130.9, 129.8, 127.4, 124.6, 122, 120.9, 111.1, 21.9; MS (APCI): m/z 270.0, 272.0 $[\text{M}+\text{H}]^+$

(E)-6-Chloro-3-(2-methoxy-benzylidene)-1,3-dihydro-indol-2-one (1-6):



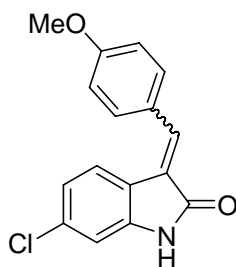
Yellow solid, yield: 61.40 %, melting point: 241.1 °C; ¹H NMR (300 MHz, in DMSO-d₆): δ 10.7 (br s, 1H), 7.68 (s, 1H), 7.65 (d, J = 7.5 Hz, 1H), 7.50 (t, J = 7.5 Hz, 1H), 7.37 (d, J = 8.1 Hz, 1H), 7.17 (d, J = 8.4 Hz, 1H, H-4), 7.08 (t, J = 7.2 Hz, 1H), 6.88-6.91 (m, 2H), 3.85 (s, 3H); ¹³C NMR (75 MHz, in DMSO-d₆): δ 169.6, 158.7, 145.1, 134.9, 133.6, 133.1, 130.6, 127.3, 124.6, 123.6, 121.9, 121.4, 121.1, 112.7, 111.0, 56.7 ; MS (APCI): *m/z* 286.0, 288.0 [M+H]⁺.

(E)-6-Chloro-3-(3-methoxy-benzylidene)-1,3-dihydro-indol-2-one (1-7):



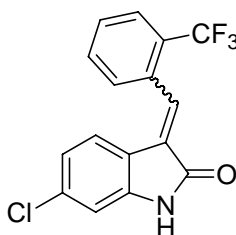
Yellow solid, yield 29.8%; melting point: 199.6 °C; ¹H NMR (300 MHz, in DMSO-d₆): δ 10.8 (br s, 1H), 7.65 (s, 1H), 7.53 (d, J = 8.4, 1H), 7.47 (d, J = 8.1 Hz, 1H), 7.24-7.28 (m, 2H), 7.06 (d, J = 8.4 Hz, 1H), 6.85-6.95 (m, 2H), 3.80 (s, 3H); ¹³C NMR (75 MHz, in DMSO-d₆): δ 169.6, 160.4, 145.4, 137.6, 136.5, 135.2, 131.1, 127.7, 124.8, 122.6, 122, 120.8, 117, 115.3, 111.2, 56.3; MS (APCI): *m/z* 286.0, 288.0 [M+H]⁺.

(E)-6-Chloro-3-(4-methoxy-benzylidene)-1,3-dihydro-indol-2-one (1-8):



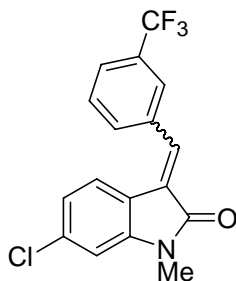
Yellow solid, yield 40.4%; melting point: 225.5 °C; ¹H NMR (300 MHz, in DMSO-d₆): δ10.8 (br s, 1H), 7.62-7.72 (m, 4H), 7.09 (d, J=8.7 Hz, 2H), 6.89-6.95 (m, 2H), 3.85 (s, 3H); ¹³C NMR (75 MHz, in DMSO-d₆): δ168.8, 160.7, 143.9, 136.9, 133.5, 126.3, 124.3, 123.2, 120.1, 120, 114.3, 109.9, 55.3; MS (APCI): *m/z* 286.2, 288.2 [M+H]⁺.

(E)-6-Chloro-3-(2-trifluoromethyl-benzylidene)-1,3-dihydro-indol-2-one (1-9):



Yellow solid, yield: 40.3%; melting point: 209.4 °C; ¹H NMR (300 MHz, in DMSO-d₆): δ10.9 (br s, 1H), 7.91 (d, J = 7.8 Hz, 1H), 7.68-7.81 (m, 4H), 6.88 (s, 1H), 6.75- 6.84 (m, 2H); ¹³C NMR (75 MHz, in DMSO-d₆): δ 167.7, 144.5, 134.7, 132.9, 132.8, 131.6, 130.1, 129.8, 129.3, 127.1, 126.7, 126.43, 126.36, 123.8, 121.1, 119.2, 110.3; MS (APCI): *m/z* 323.9, 325.9 [M+H]⁺.

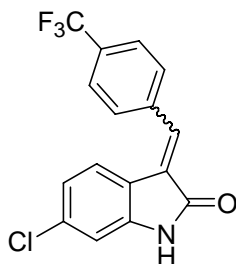
(E) 6-Chloro-1-methyl-3-(3-trifluoromethyl-benzylidene)-1,3-dihydro-indol-2-one (1-10):



Yellow solid, yield 16.6%; melting point: 209.7 °C; ¹H NMR (300 MHz DMSO-d₆), δ 7.98 (d, J=7.8 Hz, 2H), 7.85-7.72 (m, 3H), 7.29 (d, J=8.1 Hz, 1H), 7.17 (s, 1H), 6.91 (d, J=8.1 Hz, 1H),

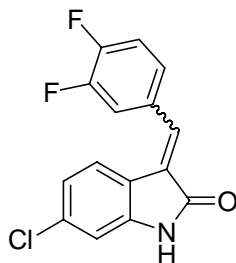
3.19 (s, 3H); ^{13}C NMR (75 MHz, DMSO- d_6)*, δ 167.0, 145.7, 143.4, 135.2, 135.1, 134.9, 134.4, 133.9, 132.9, 130.0, 129.3, 127.1, 126.3, 125.9, 125.9, 123.0, 122.3, 121.5, 121.4, 121.2, 118.6, 109.5, 26.2, 26.0. MS (APCI): m/z 338.4, 340.4 $[\text{M}+1]^+$.

(E)-6-Chloro-3-(4-trifluoromethyl-benzylidene)-1,3-dihydro-indol-2-one (1-11):



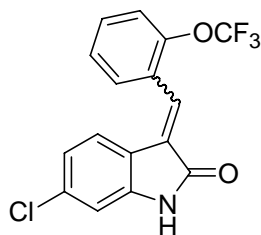
Yellow solid, yield: 29.2%; melting point: 217.1 $^{\circ}\text{C}$; ^1H NMR (300 MHz, in DMSO- d_6): δ 10.8 (br s, 1H), 7.86-7.92 (m, 4H), 7.70 (s, 1H), 7.40 (d, $J = 8.7$ Hz, 1H), 6.88-6.90 (m, 2H); ^{13}C NMR (75 MHz, in DMSO- d_6): δ 169.3, 145.7, 139.5, 135.7, 133.1, 131, 129.3, 126.8, 124.9, 124.3, 122.1, 120.4, 111.3; MS (APCI): m/z 324.0, 326.0 $[\text{M}+1]^+$.

(E)-6-Chloro-3-(3,4-difluorobenzylidene) 1,3-dihydro-indolin-2-one (1-12):



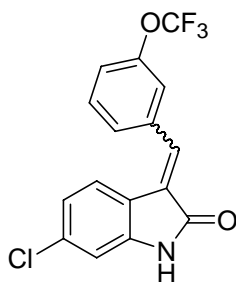
Yellow solid, yield: 41%; melting point: 226.2 $^{\circ}\text{C}$; ^1H NMR (300 MHz, in DMSO- d_6): δ 10.78 (s, 1H), 7.76 (t, $J=8.7$ Hz, 1H), 7.58 (s, 3H), 7.41 (d, $J=8.1$ Hz, 1H), 6.89 (d, $J=8.4$ Hz, 2H); ^{13}C NMR (75 MHz, in DMSO- d_6): δ 168.2, 144.4, 134.4, 134.1, 131.7, 127.4, 126.5, 126.5, 126.4, 123.7, 121.0, 119.3, 118.6, 118.3, 118.2, 117.9, 110.1; MS (APCI): m/z 292.2, 294.2 $[\text{M}+1]^+$.

(E)-6-Chloro-3-(2-trifluoromethoxy-phenylidene)-1,3-dihydro-indolin-2-one (1-13):



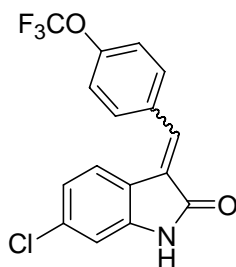
Yellow solid, yield 73.6%; melting point: 207.7 °C; ¹H NMR (300 MHz DMSO-d₆) δ 10.86 (s, 1H), 7.81 (d, J = 7.0 Hz, 1H), 7.69-7.48 (m, 4H), 7.12 (d, J = 8.0 Hz, 1H), 6.88 (d, J = 7.9 Hz, 2H); ¹³C NMR (75 MHz, DMSO-d₆)*, δ 167.8, 166.3, 146.4, 146.1, 144.5, 142.6, 134.7, 134.0, 132.2, 131.8, 131.5, 130.5, 129.1, 129.0, 128.2, 127.9, 127.7, 126.8, 126.6, 125.1, 123.7, 122.5, 121.9, 121.7, 121.2, 121.1, 120.6, 119.3, 118.3, 114.8, 110.2, 109.5; MS (APCI): *m/z* 340.4, 342.2 [M+H]⁺

(E)-6-Chloro-3-(3-trifluoromethoxy-phenylidene)-1,3-dihydro-indol-2-one (1-14):



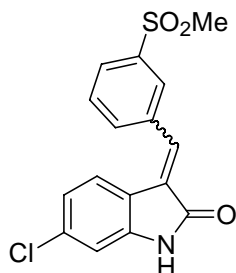
Yellow solid, yield 57.1%; melting point: 194.0 °C; ¹H NMR (300 MHz, DMSO-d₆) δ 10.8(s, 1H), 7.72-7.62 (m, 4H), 7.48 (d, =7.8Hz, 1H), 7.33 (d, J=8.1 Hz, 1H), 6.89 (d, J=7.8 Hz, 2H); ¹³C NMR (75 MHz, DMSO-d₆)*, δ 168.2, 166.9, 148.5, 148.1, 144.5, 142.2, 136.5, 135.8, 135.6, 134.6, 134.5, 133.6, 131.2, 130.9, 130.1, 128.2, 127.9, 127.2, 123.5, 123.4, 123.3, 122.7, 122.1, 121.8, 121.7, 121.5, 121.0, 120.9, 119.4, 118.4, 118.3, 110.2, 109.5; MS (APCI): *m/z* 340.5, 342.5 [M+1]⁺.

(E)-6-Chloro-3-(4-trifluoromethoxy-benzylidene)-1,3-dihydro-indol-2-one (1-15):



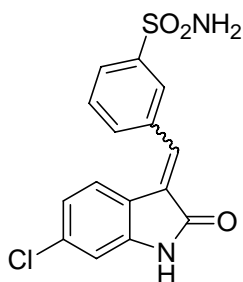
Yellow solid, yield 83.0%; melting point: 194.0 °C; ^1H NMR (300 MHz DMSO- d_6), δ 10.80 (s, 1H), 7.80 (t, $J=9.0$ Hz, 2H), 7.65 (s, 1H), 7.50 (q, $J=16.5$ Hz, 3H), 6.90 (d, $J = 7.1$ Hz, 2H); ^{13}C NMR (75 MHz, DMSO- d_6)*, δ 168.4, 166.9, 149.3, 148.9, 144.4, 142.0, 135.8, 134.8, 134.4, 133.9, 133.3, 132.8, 131.4, 127.2, 126.4, 123.6, 123.5, 121.7, 121.4, 121.1, 121.0, 120.9, 120.3, 119.4, 118.3, 110.2, 109.4; MS (APCI): m/z 340.4, 342.5 $[\text{M}+\text{H}]^+$.

(E)-6-Chloro-3-(3-methanesulfonyl-benzylidene)-1,3-dihydro-indol-2-one (1-16):



Yellow solid, yield 45.5%; melting point: 218.1 °C ^1H NMR (300 MHz DMSO- d_6), δ 10.83 (s, 1H), 8.22 (s, 1H), 8.02 (d, $J = 7.6$ Hz, 2H), 7.80 (t, $J = 7.8$ Hz, 1H), 7.72 (s, 1H), 7.35 (d, $J = 8.7$ Hz, 1H), 6.89 (d, $J = 6.2$ Hz, 2H), 3.29 (s, 1H); ^{13}C NMR (75 MHz, DMSO- d_6), δ 168.2, 144.6, 141.3, 135.4, 134.6, 134.3, 134.0, 130.1, 128.1, 127.7, 127.4, 123.6, 121.0, 119.3, 110.2, 43.3; MS (APCI): m/z 334.3, 336.3 $[\text{M}+\text{H}]^+$.

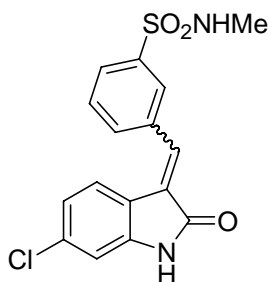
(E) 3-(6-Chloro-2-oxo-1,2-dihydro-indol-3-ylidenemethyl)-benzene-sulfonamide (1-17):



Yellow solid, yield 47.8%; melting point: 271.4°C; ¹HNMR (300 MHz DMSO-d₆), δ 10.8 (s, 1H), 8.13 (s, 1H), 7.90 (t, J=7.8 Hz, J=6.6Hz, 2H), 7.49 (s, 2H), 7.28 (d, J=8.1 Hz, 1H), 6.91 (d, J=8.1 Hz, 1H);

¹³CNMR (75 MHz, DMSO-d₆), δ 168.2, 144.5, 144.5, 134.9, 134.7, 134.6, 132.5, 129.7, 127.8, 126.5, 125.8, 123.6, 121.0, 119.3, 110.2. MS (APCI): *m/z* 335.3, 337.3 [M+1]⁺.

(E)-3-(6-Chloro-2-oxo-1,2-dihydro-indol-3-ylidene)methyl-N-methylbenzenesulfonamide (1-18):

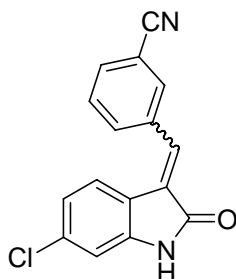


Yellow solid, yield 22.9%; melting point: 183.4°C; ¹HNMR (400 MHz DMSO-d₆), δ 10.84 (s, 1H), 8.04 (s, 1H), 7.92(d, J=7.6 Hz, 1H), 7.85 (d, J=7.6 Hz, 1H), 7.75 (t, J=7.6 Hz, 1H), 7.71 (d, 1H), 7.58 (s, 1H), 7.32(d, J=8 Hz, 1H), 6.92 (d, J=1.6 Hz, 1H), 6.90 (dd, J=8.4 Hz, 1H), 2.46 (s, 3H);

¹³CNMR (100MHz, DMSO-d₆), δ 168.3, 144.6, 140.0, 135.3, 134.8, 134.7, 133.1, 130.1, 128.0, 127.7, 126.9, 123.6, 121.1, 119.4, 110.4, 28.7;

MS (APCI): *m/z* 350.1, 352.1 [M+1]⁺.

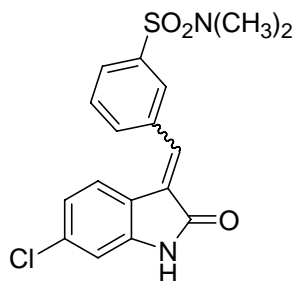
(E) 3-(6-Chloro-2-oxo-1,2-dihydro-indol-3-ylidenemethyl)-benzonitrile (1-19):



Yellow solid, yield 57.0%; melting point: 221.5°C; ¹H NMR (300 MHz DMSO-d₆), δ 10.8 (s, 1H), 8.10 (s, 1H), 7.99 (d, J=7.8 Hz, 1H), 7.91 (d, J=7.8 Hz, 1H), 7.71 (t, J=7.8 Hz, 1H), 7.63 (s, 1H), 7.28 (d, J=8.7 Hz, 1H), 6.88 (d, J=7.2 Hz, 2H);

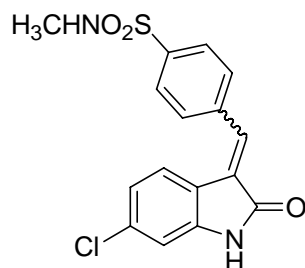
¹³C NMR (75 MHz, DMSO-d₆), δ 168.3, 144.6, 135.6, 134.8, 134.1, 133.6, 133.1, 132.7, 130.1, 128.3, 123.8, 121.2, 119.4, 118.4, 112.1, 110.4; MS (APCI): *m/z* 281.5, 283.5 [M+1]⁺.

(E)-3-(6-Chloro-2-oxo-1,2-dihydro-indol-3-ylidenemethyl)-N,N-dimethylbenzenesulfonamide(1-20):



Yellow solid, yield 22.9%; melting point: 222.0 °C; ¹H NMR (400 MHz, DMSO-d₆) 10.79 (s, 1H), 8.78 (s, 1H), 8.50 (d, J = 7.7 Hz, 1H), 7.98 (s, 1H), 7.89-7.65 (m, 3H), 7.06 (d, J = 8.1 Hz, 1H), 6.88 (d, J = 16.9 Hz, 1H), 2.67 (s, 6H); ¹³C NMR (101 MHz, DMSO-d₆), δ 166.8, 142.2, 135.6, 135.5, 134.9, 134.6, 133.6, 130.1, 129.2, 128.7, 127.4, 123.3, 121.7, 121.0, 109.5, 40.1, 38.8; MS (ACPI): *m/z* 361.5, 363.5 [M-H]⁻.

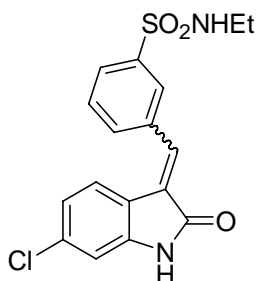
(E)-4-(6-Chloro-2-oxo-1,2-dihydro-indol-3-ylidenemethyl)-N-methyl-benzenesulfonamide (1-21):



Yellow solid, yield 40.7%; melting point: 235.7 °C; ¹H NMR (400 MHz, DMSO-d₆) δ 11.10-10.52 (br, 1H), 7.88 (s, 4H), 7.68 (s, 1H), 7.44-7.38 (m, 1H), 6.91 (dd, *J* = 6.9, 2.0 Hz, 2H), 2.46 (d, *J* = 8.9 Hz, 3H)

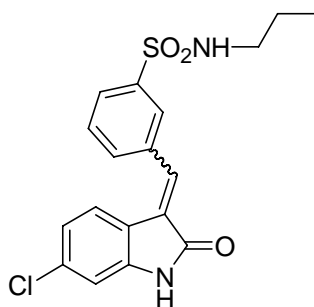
¹³C NMR (100 MHz, DMSO-d₆), δ 168.4, 144.6, 140.0, 138.2, 134.8, 134.7, 132.1, 130.1, 128.3, 127.2, 126.4, 124.0, 121.3, 119.4, 110.4, 28.8; MS (ESI): *m/z* 347.1, 349.1 [M-H]⁻.

(E)-3-(6-Chloro-2-oxo-1,2-dihydro-indol-3-ylidenemethyl)-N-ethyl-benzenesulfonamide (1-22) :



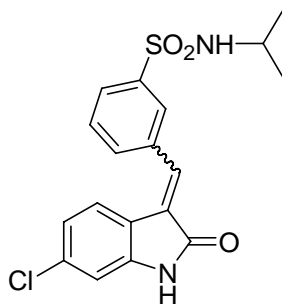
Orange red solid, yield 3.59% (after 3 steps) ; melting point: 194.8 °C; ¹H NMR (400 MHz, DMSO-d₆), δ 10.84 (s, 1H), 8.05 (s, 1H), 7.90 (dd, *J* = 18.7, 7.8 Hz, 2H), 7.77-7.62 (m, 3H), 7.33 (d, *J* = 8.2 Hz, 1H), 6.99-6.80 (m, 2H), 2.83 (dd, *J* = 6.7, 3.9 Hz, 2H), 0.98 (t, *J* = 7.2 Hz, 3H); ¹³C NMR (100 MHz, DMSO-d₆), δ 168.2, 144.6, 141.2, 135.2, 134.8, 134.7, 132.9, 130.0, 128.0, 127.4, 126.7, 123.5, 121.0, 119.4, 110.3, 37.6, 14.8. MS (ESI): *m/z* 361.2, 363.2 [M-H]⁻.

(E)-3-(6-Chloro-2-oxo-1,2-dihydro-indol-3-ylidenemethyl)-N-propylbenzenesulfonamide (1-23)



Orange solid, Yield 20.9% (after 3 steps); melting point: 197.5 °C; ¹H NMR (400 MHz, DMSO-d₆), δ 10.84 (s, 1H), 8.05 (s, 1H), 7.95-7.80 (m, 2H), 7.81-7.62 (m, 3H), 7.33 (d, J = 8.2 Hz, 1H), 6.96-6.80 (m, 2H), 2.75 (t, J = 7.1 Hz, 2H), 1.47-1.28 (m, 2H), 0.79 (t, J = 7.4 Hz, 3H); ¹³C NMR (100 MHz, DMSO-d₆), δ 168.2, 144.5, 141.3, 135.2, 134.7, 134.6, 132.9, 129.9, 127.9, 127.3, 126.6, 123.5, 120.9, 119.3, 110.2, 44.3, 22.4, 11.0. MS (ESI): *m/z* 375.3, 377.3 [M-H]⁻.

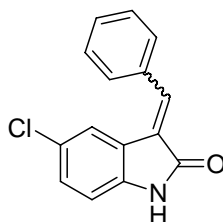
(E/Z) 3-(6-Chloro-2-oxo-1,2-dihydro-indol-3-ylidenemethyl)-N-isopropylbenzenesulfonamide (1-24) :



Yellow solid; yield 5.72 (after 3 steps), melting point: 178.5 °C; ¹H NMR (400 MHz, DMSO-d₆), δ 10.81 (s, 1H), 8.02 (s, 1H), 7.88-7.82 (m, 2H), 7.74-7.63 (m, 3H), 7.28 (d, J = 8.27 Hz, 1H), 6.90 (d, J = 1.93 Hz, 1H), 6.86-6.80 (m, 1H), 3.29-3.22 (m, 1H), 0.92 (d, J = 6.54 Hz, 6H); ¹³C NMR (100 MHz, DMSO-d₆)#, δ 172.2, 168.4, 144.6, 142.5, 136.0, 135.2, 134.9, 134.8, 132.9, 130.1, 129.4, 129.2, 128.0, 127.4, 126.6, 123.6, 121.1, 119.5, 110.5, 45.5, 42.2,

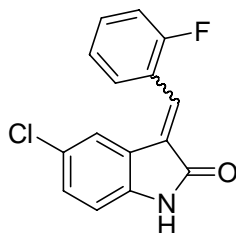
23.3, 21.1. MS (ESI): m/z 375.3, 377.3 [M-H]⁻.

(E)-3-Benzylidene-5-chloro-1,3-dihydro-indol-2-one (2-1):



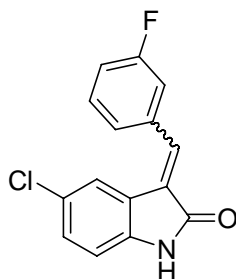
Orange solid, yield: 62.8%; melting point: 208.0°C; ¹H NMR (300 MHz, in DMSO-d₆): δ 10.8 (br s, 1H), 7.73 (s, 1H, H), 7.70 (d, J = 7 Hz, 2H), 7.54-7.59 (m, 3H), 7.51 (d, J = 2.1 Hz, 1H, H-4), 7.29 (d, J = 8.4 Hz, 1H), 6.90 (d, J = 8.4 Hz, 1H); ¹³C NMR, (75 MHz, in DMSO-d₆): δ 168.3, 141.7, 137.7, 134, 130.1, 129.6, 129.2, 128.9, 126.9, 124.9, 122.5, 121.7, 111.5; MS (APCI): m/z 256.1, 258.1 [M+H]⁺.

(E)-5-Chloro-3-(2-fluorobenzylidene)-1,3-dihydro-indol-2-one (2-2):



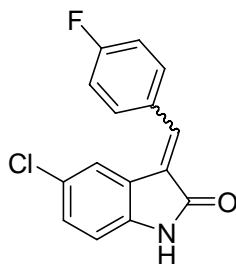
Orange solid, yield 89.4%; melting point: 237.4°C; ¹H NMR (300 MHz DMSO-d₆) δ 10.8 (br s, 1H), 7.74 (t, J = 7.5 Hz, 1H), 7.62 (s, 1H), 7.51-7.60 (m, 1H), 7.35-7.43 (m, 2H), 7.28 (d, J = 8.1 Hz, 1H), 7.13 (d, J = 2.1 Hz, 1H), 6.89 (d, J = 8.4 Hz, 1H); ¹³C NMR, (75 MHz, in DMSO-d₆): δ 168.8, 162.3, 159.0, 143.0, 141.0, 133.5, 133.4, 131.6, 131.1, 130, 126.2, 125.8, 123.3, 123.2, 123, 122.8, 117.4, 117.1, 112.6; MS (APCI): m/z 273.9, 275.9 [M+H]⁺.

(E)-5-Chloro-3-(3-fluorobenzylidene)-1,3-dihydro-indol-2-one (2-3)



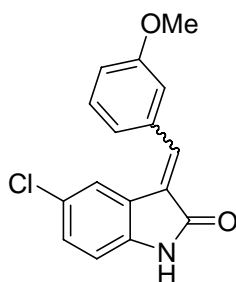
Orange solid, yield 37.0%; melting point: 209.5°C; ¹H NMR (300 MHz, DMSO-d₆) δ 10.8 (br s, 1H), 7.69 (s, 1H), 7.53-7.60 (m, 3H), 7.37 (d, J = 9 Hz, 1H), 7.33 (s, 1H), 7.30 (d, J = 1.8 Hz), 6.90 (d, J = 8.4 Hz, 1H); ¹³C NMR, (75 MHz, in DMSO-d₆): δ 168.0 , 162.1 , 141.8 , 136.4 , 135.9 , 130.9 , 129.9 , 127.8 , 125.1 , 124.9 , 122.1 , 121.9 , 116.7 , 115.8 , 111.5; MS (APCI): *m/z* 273.9, 275.9 [M+H]⁺.

(E)-5-Chloro-3-(4-fluorobenzylidene)-1,3-dihydro-indol-2-one (2-4):



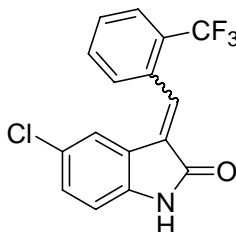
Orange solid, yield 63.0%; melting point: 215.6°C; ¹H NMR (300 MHz, DMSO-d₆) δ 10.8 (br s, 1H), 7.74-7.79 (m, 2H), 7.69 (s, 1H), 7.36-7.42 (m, 2H), 7.26-7.32 (m, 2H), 6.88 (d, J=8.4 Hz, 1H); ¹³C NMR, (75 MHz, in DMSO-d₆): δ 167.9, 142.0, 139.9, 138.5, 138.3, 135.5, 132.1, 130.1, 129.8, 128.4, 125.7, 125.0, 122.0, 111.6; MS (APCI): *m/z* 273.9, 275.9 [M+H]⁺.

(E)-5-Chloro-3-(3-methoxybenzylidene)-dihydro-indol-2-one (2-5):



Orange solid, yield 79.0%; melting point: 211.6°C; ¹H NMR (300 MHz, DMSO-d₆) δ 10.8 (br s, 1H), 7.69 (s, 1H), 7.44-7.50 (m, 2H), 7.25-7.30 (m, 3H), 7.08 (d, J = 8.4 Hz, 1H), 6.89 (d, J= 8.4 Hz, 1H), 3.81 (s, 3H), ¹³C NMR, (75 MHz, in DMSO-d₆): δ 169.3, 160.4, 142.8, 138.6, 136.4, 131.1, 130.1, 128.1, 125.9, 123.5, 123.1, 122.5, 117.2, 115.2, 112.6, 56.3. MS (APCI): *m/z* 285.9, 287.9 [M+H]⁺.

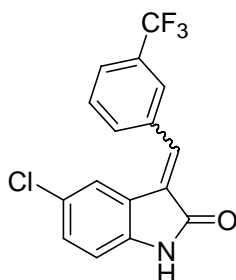
(E)-5-Chloro-3-(2-trifluoromethylbenzylidene)-1,3-dihydro-indol-2-one (2-6):



Orange solid, yield 50.8%; melting point: 209.4°C; ¹H NMR (300 MHz DMSO-d₆) δ 10.9 (br

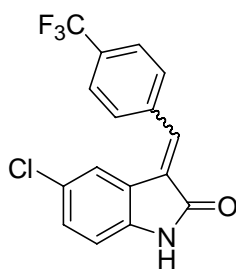
s, 1H), 7.94 (d, J = 7.5 Hz, 1H), 7.74-7.84 (m, 4H), 7.28 (dd, J = 10 Hz, J= 1.8 Hz, 1H), 6.89 (d, J=8.1 Hz, 1H), 6.64 (d, J = 2.1 Hz, 1H); ¹³C NMR, (75 MHz, in DMSO-d₆): δ 167.5 , 142.0 , 133.0 , 132.8 , 132.7 , 130.2 , 130.1 , 129.6 , 127.1 , 126.7 , 126.6 , 126.5 , 125.7 , 125.1 , 122.1 , 122.0 , 111.8; MS (APCI): *m/z* 323.8, 325.8 [M+H]⁺.

(E)-5-Chloro-3-(3-(trifluoromethyl)benzylidene)-1,3-dihydro-indol-2-one (2-7):



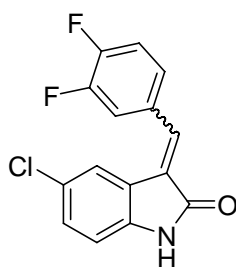
Orange solid, yield 38.5%; melting point: 192.4°C; ¹H NMR (300 MHz, DMSO-d₆) δ 10.8 (s, 1H), 7.99-8.06 (m, 2H), 7.70-7.88 (m, 3 H), 7.26-7.32 (m, 2H), 6.90 (d, J =8.4 Hz, 1H). ¹³C NMR (75 MHz, DMSO-d₆)*, δ 167.9, 166.7, 141.9, 139.7, 135.6, 135.5, 135.1, 133.0, 130.0, 129.3, 128.3, 126.3, 125.7, 125.6, 124.9, 122.0, 111.6. MS (APCI): *m/z* 323.9, 325.9 [M+1]⁺.

(E)-5-Chloro-3-(4-trifluoromethylbenzylidene)-1,3-dihydro-indol-2-one (2-8):



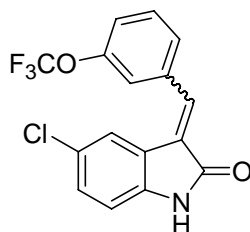
Orange solid, yield 38.5%; melting point: 212.4°C; ¹H NMR (300 MHz, DMSO-d₆) δ 10.8 (br s, 1H), 7.91 (t, J = 9 Hz, 4H), 7.75 (s, 1H), 7.28-7.33 (m, 2H), 6.91 (d, J = 8.4 Hz, 1H); ¹³C NMR, (75 MHz, in DMSO-d₆): δ 167.7 , 142.0 , 139.9 , 138.3 , 135.3 , 132.1 , 130.1 , 129.8 , 129.4 , 128.4 , 125.7 , 125.0 , 122.1 , 121.9 , 111.6; MS (APCI): *m/z* 323.9, 325.9 [M+H]⁺.

(E)-5-Chloro-3-(3,4-difluoro-benzylidene)-1,3-dihydro-indol-2-one (2-9):



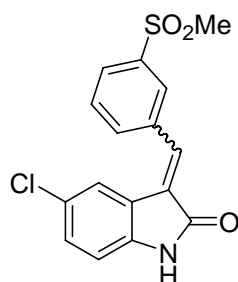
Orange solid, yield: 51%; melting point: 189.0°C; ¹H NMR (300 MHz, DMSO-d₆): δ 10.82 (s, 1H), 8.86 (m, 1H), 8.01 (br, 1H), 7.89 (d, J=1.8 Hz, 1H), 7.55 (q, J=8.7 Hz, 1H), 7.23 (dd, J=1.8 Hz, 1H), 6.32 (d, J=8.4 Hz, 1H); ¹³C NMR, (75 MHz, in DMSO-d₆)*: δ 166.8, 152.3, 152.1, 148.9, 147.1, 147.0, 139.5, 136.2, 131.4, 131.3, 131.3, 131.3, 130.3, 128.6, 126.4, 126.3, 125.5, 120.2, 120.0, 119.9, 117.5, 117.2, 110.8; MS (APCI): *m/z* 292.2, 294.2 [M+H]⁺.

(E)-5-Chloro-3-(3-trifluoromethoxy-benzylidene)-1,3-dihydro-indol-2-one (2-10):



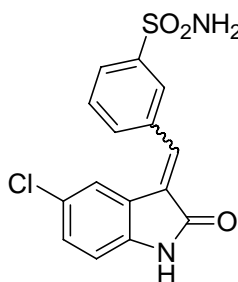
Orange solid, yield 13.5%; melting point: 175.7 °C; ¹H NMR (300 MHz DMSO-d₆) δ 10.79 (s, 1H), 7.70 (s, 4H), 7.50 (s, 1H), 7.29 (d, J = 7.2 Hz, 2H), 6.89 (d, J = 8.4 Hz, 1H); ¹³C NMR (75 MHz, DMSO-d₆)* δ 167.9, 166.7, 148.4, 148.1, 141.9, 139.7, 136.3, 135.7, 135.5, 131.3, 131.0, 130.1, 130.0, 128.9, 128.4, 128.2, 127.3, 126.3, 125.5, 125.0, 123.3, 122.9, 122.4, 122.1, 121.8, 121.3, 120.2, 118.3, 111.6, 110.9; MS (APCI): *m/z* 340.5, 342.5 [M+H]⁺.

(E)-5-Chloro-3-(3-methanesulfonyl-benzylidene)-1,3-dihydro-indol-2-one (2-11) :



Orange solid, yield 49.1%; melting point: 238.4 °C; ¹HNMR (300 MHz DMSO-d₆) δ 10.8 (s, 1H), 8.25 (s, 1H), 8.02 (d, J=6.9 Hz, 2H), 7.77-7.85 (m, 2H), 7.31 (s, 2H), 6.91 (d, J=7.8 Hz, 1H), 3.29 (s, 3H); ¹³CNMR (75 MHz, DMSO-d₆) δ 167.9, 142.0, 141.3, 135.4, 135.2, 134.2, 130.1, 128.4, 127.9, 127.3, 125.1, 122.0, 121.9, 111.7, 43.3; MS (APCI): *m/z* 334.4, 336.4 [M+1]⁺.

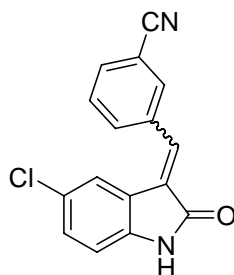
E/Z 3-(5-Chloro-2-oxo-1,2-dihydro-indol-3-ylidenemethyl)-benzenesulfonamide (2-12):



Orange solid, yield 17.9%; melting point: 235.1 °C; ¹HNMR (300 MHz DMSO-d₆) δ 10.8 (s, 1H), 8.12 (s, 1H), 7.84 (t, J=9.0 Hz, J=9.6 Hz, 2H), 7.75 (t, J=7.5 Hz, J=7.8 Hz, 2H), 7.47 (br, 1H), 7.32-7.29 (m, 2H), 6.92 (d, J=8.1 Hz, 1H); ¹³CNMR (75 MHz, DMSO-d₆) δ 168.0, 166.7, 144.7, 144.2, 141.9, 139.8, 136.9, 135.8, 134.8, 134.2, 132.5, 130.2, 129.7, 129.0, 128.8, 128.2, 127.5, 127.3, 126.7, 126.4, 125.9, 125.6, 125.3, 122.0, 120.4, 111.7.

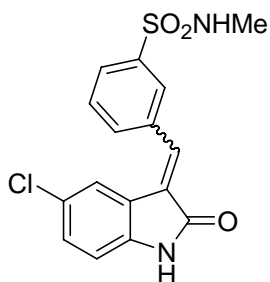
MS (ESI): *m/z* 335.1, 337.1[M+1]⁺.

(E) 3-(5-Chloro-2-oxo-1,2-dihydro-indol-3-ylidenemethyl)-benzonitrile (2-13):



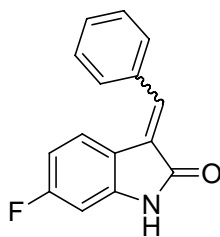
Orange solid, yield, 67.7%; melting point: 265.3 °C; ¹H NMR (300 MHz DMSO-d₆), δ 10.84 (s, 1H), 8.87 (s, 1H), 8.45 (d, J=7.8 Hz, 1 H), 7.95-7.89 (m, 2H), 7.82 (s, 1H), 7.29 (d, J=8.1 Hz, 1H), 6.85 (d, J=8.1 Hz, 1H); ¹³C NMR (75 MHz, DMSO-d₆)#, δ 166.6, 139.8, 136.2, 135.4, 134.7, 134.6, 133.4, 129.5, 129.1, 128.5, 127.8, 126.1, 125.6, 122.0, 120.3, 118.5, 112.0, 111.3, 111.0; MS (APCI): *m/z* 281.5, 283.5 [M+H]⁺.

(E)-3-(5-Chloro-2-oxo-1,2-dihydro-indol-3-ylidenemethyl)-N-methylbenzenesulphonamide (2-14):



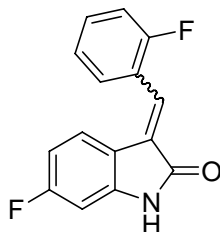
Orange solid, yield 29.3%; melting point: 215.0 °C; ¹H NMR (400 MHz, DMSO-d₆) 10.81 (s, 1H), 8.07 (s, 1H), 7.91 (dd, J = 17.4 Hz, 2H), 7.84-7.74 (m, 2H), 7.61 (q, J = 4.5 Hz, 1H), 7.37-7.20 (m, 2H), 6.91 (d, J = 8.3 Hz, 1H), 2.48 (d, J = 4.8 Hz, 3H); ¹³C NMR (100 MHz, DMSO-d₆), δ 166.6, 139.7, 139.5, 136.6, 135.1, 134.4, 129.8, 129.2, 128.9, 128.0, 127.4, 126.3, 125.5, 120.3, 110.9, 28.6; MS (ACPI): *m/z* 347.5, 349.5 [M-H]⁻;

(E)-3-Benzylidene-6-fluoro-1,3-dihydro-indol-2-one (3-1):



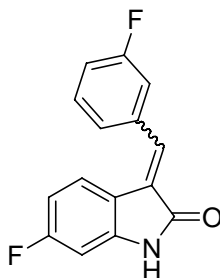
Pale yellow solid, yield: 14.6%; melting point: 186.1 °C; ¹HNMR (300 MHz, in DMSO-d₆): δ 10.7 (br s, 1H), 7.61 (d, J = 6.9 Hz, 1H), 7.57 (s, 1H), 7.41-7.50 (m, 4H), 6.58-6.73 (m, 2H); ¹³NMR (75 MHz, DMSO-d₆), δ 169.9 , 144.9 , 136.4 , 134.5 , 132.2 , 130.5 , 129.6 , 128.8 , 126.9 , 124.5 , 117.8 , 108.3 , 98.9. MS (APCI): *m/z* 240.2 [M+H]⁺.

(E)-6-Fluoro-3-(2-fluoro-benzylidene)-1,3-dihydro-indol-2-one (3-2):



Pale yellow solid, yield: 54.7%; melting point: 237.1 °C; ¹HNMR (300 MHz, in DMSO-d₆), δ 10.8 (br s, 1H), 7.74 (t, J = 7.5 Hz, 1H), 7.54-7.57 (m, 1H), 7.52 (s, 1H), 7.33-7.41 (m, 2H), 7.24 (d, J = 6.3 Hz, 1H), 6.65-6.72 (m, 2H); ¹³NMR (75 MHz, DMSO-d₆), δ 168.5, 165.0, 161.5, 157.9, 145.0, 132.0, 130.4, 128.7, 127.1, 124.8, 122.1, 117.1, 116.1, 107.8, 98.3; MS (APCI): *m/z* 258.3 [M+H]⁺.

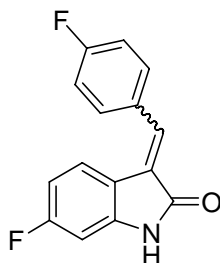
(E)-6-Fluoro-3-(3-fluoro-benzylidene)-1,3-dihydro-indol-2-one (3-3):



Pale yellow solid, yield 23.6%; melting point: 196.7 °C; ¹HNMR (300 MHz DMSO-d₆) δ 10.8 (br s, 1H, NH), 7.55 (s, 1H), 7.41-7.53 (m, 4H), 7.23-7.29 (m, 1H), 6.65-6.70 (m, 1H), 6.59-6.62 (m, 1H); ¹³CNMR (75 MHz, DMSO-d₆), δ 168.6, 167.2, 163.7, 145, 144.9, 142.3, 136.6,

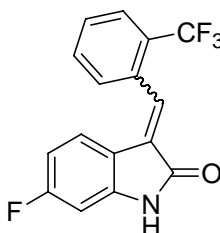
133.7, 130.8, 127.5, 125.1, 117.0, 115.9, 115.6, 107.8, 107.5, 98.4, 89.0; MS (APCI): m/z , 258.2 $[M+H]^+$.

(E)-6-Fluoro-3-(4-fluorobenzylidene)-1,3-dihydro-indol-2-one (3-4):



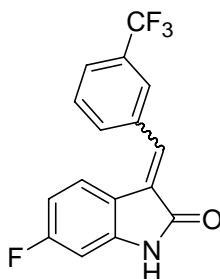
Pale yellow solid, Yield: 27.5%; melting point: 221.2 °C; $^1\text{H NMR}$ (300 MHz, in DMSO-d_6), δ 10.8 (br s, 1H), 7.76 (dd, $J_1 = 14$ Hz, $J_2 = 6$ Hz), 7.59 (s, 1H), 7.50 (t, $J = 6.3$ Hz, 1H), 7.36 (t, $J = 8.7$ Hz), 6.65-6.71 (m, 2H); $^{13}\text{C NMR}$ (75 MHz, DMSO-d_6), δ 168.8, 164.4, 161.1, 144.8, 134.3, 131.6, 130.6, 126.5, 123.8, 117.1, 115.8, 107.4, 98.1; MS (APCI): m/z 258.2 $[M+H]^+$.

(E)-6-Fluoro-3-(2-trifluoromethylbenzylidene)-1,3-dihydro-indol-2-one (3-5):



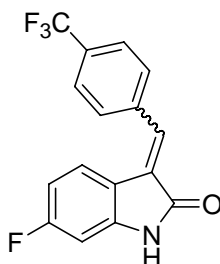
Pale yellow solid, yield 45.8%; melting point: 192.8 °C; $^1\text{H NMR}$ (300 MHz DMSO-d_6) δ 10.6 (br s, 1H), 7.91 (d, $J = 7.5$ Hz), 7.76-7.84 (m, 2H), 7.66- 7.73 (m, 2H), 6.78 (dd, $J = 14$ Hz, $J = 5.7$ Hz, 1H), 6.70 (dd, $J = 12$ Hz, $J = 2.1$ Hz, 1H), 6.56-6.63 (m, 1H); $^{13}\text{C NMR}$ (75 MHz, DMSO-d_6) δ 168.1, 163.4, 145.0, 133.0, 130.2, 129.8, 126.8, 126.5, 126.4, 125.7, 124.3, 116.8, 107.8, 98.4; MS (APCI): m/z 308.0 $[M+H]^+$.

(E)-6-Fluoro-3-(3-trifluoromethyl-benzylidene)-1,3-dihydro-indol-2-one (3-6):



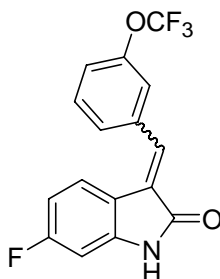
Pale yellow solid, yield 24.0 %; melting point: 163.4 °C; ¹HNMR (300 MHz DMSO-d₆) δ 10.8 (s, 1H), 7.98 (d, J = 6.9 Hz, 2H), 7.82 (d, J = 7.5 Hz, 1H), 7.75 (t, J = 7.8 Hz, 1H), 7.66 (s, 1H), 7.33 (dd, J = 14 Hz, J = 5.4 Hz, 1H), 6.66-6.71 (m, 2H); ¹³CNMR (75 MHz, DMSO-d₆)*, δ 168.5, 164.9, 161.7, 145.2, 145.0, 135.4, 133.35, 133.31, 132.8, 129.9, 129.3, 128, 125.9, 125.7, 123.9, 123.7, 122.1, 116.9, 116.9, 107.7, 107.4, 98.5, 98.1; (APCI): *m/z*, 307.9 [M+H]⁺.

(E)-6-Fluoro-3-(4-trifluoromethyl-benzylidene)-1,3-dihydro-indol-2-one (3-7):



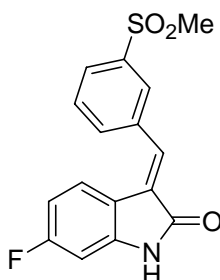
Pale yellow solid, yield 51.3%; melting point: 196.5 °C; ¹H NMR (300 MHz DMSO-d₆) δ 10.8 (br s, 1H), 7.87 (t, J = 9 Hz, 4H), 7.63 (s, 1H), 7.41 (t, J = 6.9 Hz, 1H), 6.63-6.70 (m, 2H); ¹³NMR (75 MHz, DMSO-d₆)* δ 168.5, 165.0, 161.7, 145.2, 145.1, 138.5, 133.2, 129.8, 128.2, 125.6, 125.6, 124.3, 124.2, 116.8, 107.8, 107.5, 98.4, 98.1; MS (APCI): *m/z* 308.0 [M+H]⁺.

(E)-6-Fluoro-3-(3-trifluoromethoxy-phenylidene)-1,3-dihydro-indol-2-one (3-8):



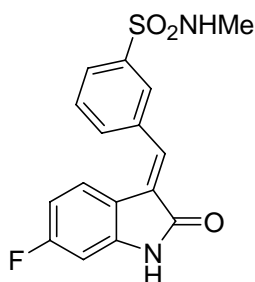
Pale yellow solid, yield 27.2%; melting point: 177.7 °C; ¹HNMR (300 MHz DMSO-d₆) δ 10.8 (s, 1H), 7.74-7.64 (m, 3H), 7.61 (s, 1H), 7.50 (d, J=8.4 Hz, 1H), 7.39 (q, J=8.4 Hz, 1H), 6.73-6.64 (m, 2H); ¹³CNMR (75 MHz, DMSO-d₆)* δ 168.6, 165.0, 161.7, 148.5, 145.2, 145.0, 136.6, 133.2, 130.9, 128.0, 127.9, 124.0, 123.9, 121.9, 121.7, 121.4, 116.9, 107.7, 107.4, 98.5, 98.1; MS (APCI): 324.5 *m/z* [M+H]⁺.

(E)-6-Fluoro-3-(3-methanesulfonyl-phenylidene)-1,3-dihydro-indol-2-one (3-9):



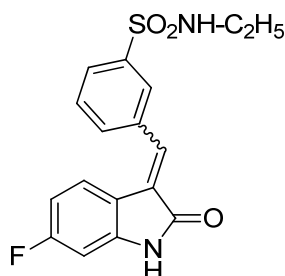
Pale yellow solid, yield 44.1%; melting point: 233.9 °C; ¹H NMR (300 MHz DMSO-d₆) δ 10.85 (s, 1H), 8.22 (s, 1H), 8.02 (t, J=6.3 Hz, 2H), 7.80 (t, J=7.8 Hz, 1H), 7.67 (s, 1H), 7.29 (t, J=8.4 Hz, 1H), 6.73-6.64 (m, 2H), 3.29 (s, 3H); ¹³CNMR (75 MHz, DMSO-d₆)* 168.5, 145.2, 145.1, 141.3, 135.5, 133.9, 133.1, 130.0, 128.1, 127.5, 127.3, 124.1, 123.9, 116.9, 116.8, 107.8, 98.5, 98.1, 43.3; MS (APCI): *m/z* 318.4 [M+H]⁺.

(E)-3-(6-Fluoro-2-oxo-1,2-dihydro-indol-3-ylidenemethyl)-N-methyl-benzenesulphonamide (3-10):



Yellow solid, Yield 22.3%; melting point: 201.4 °C; ¹H NMR (400 MHz, DMSO-d₆) δ 11.59 (s, 1H), 8.04-7.70 (m, 2H), 7.20-6.85 (m, 2H), 6.40 (d, J = 74.8 Hz, 1H), 4.24 (s, 2H), 4.06 (q, J = 7.0 Hz, 2H), 1.33 (dt, J = 7.0 Hz, 3H); ¹³C NMR (101 MHz, DMSO-d₆)* δ 168.5, 164.6, 162.1, 145.2, 145.0, 139.9, 135.3, 134.8, 133.4, 133.4, 132.9, 129.9, 129.0, 127.9, 127.4, 126.7, 124.0, 123.9, 116.9, 107.8, 107.7, 107.5, 107.5, 98.4, 98.2, 28.6; MS (ACPI): *m/z* 331.3 [M-H]⁻

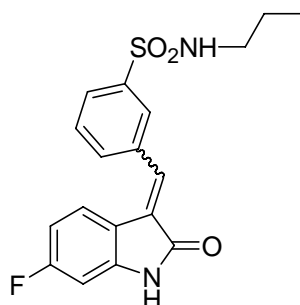
(E)-3-(6-Fluoro-2-oxo-1,2-dihydro-indol-3-ylidenemethyl)-N-ethyl-benzenesulfonamide (3-11):



Yellow solid, yield 2.90% (after 3 steps); melting point: 149.2 °C; ¹H NMR (400 MHz, DMSO-d₆), δ 10.85 (s, 1H), 8.04 (s, 1H), 7.88 (dd, J = 17.31, 7.80 Hz, 2H), 7.74 (t, J = 7.76 Hz, 1H), 7.70-7.66 (m, 1H), 7.64 (s, 1H), 7.35 (dd, J = 8.53, 5.55 Hz, 1H), 6.73 (dd, J = 9.12, 2.44 Hz, 1H), 6.65 (ddd, J = 9.71, 8.64, 2.48 Hz, 1H), 2.82 (dd, J = 6.62, 2.55 Hz, 2H), 0.98 (t, J = 7.22 Hz, 3H); ¹³C NMR (100 MHz, DMSO-d₆)*, δ 168.7, 164.7, 162.3, 145.2, 145.1, 141.2, 135.4, 133.6, 133.6, 133.0, 130.1, 128.1, 127.3, 126.6, 124.1, 124.0, 117.0, 117.0, 107.9, 107.6, 98.6, 98.4, 37.6, 14.8. MS (ESI): *m/z* 345.3 [M-H]⁻.

(E)-3-(6-Fluoro-2-oxo-1,2-dihydro-indol-3-ylidenemethyl)-N-propyl-benzenesulfonamide

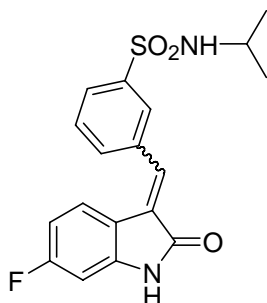
(3-12):



Yellow solid, yield 6.27% (after 3 steps), melting point: 183.7 °C; ¹H NMR (400 MHz, DMSO-d₆), 10.84 (s, 1H), 8.05 (s, 1H), 7.89 (dd, *J* = 18.45, 7.79 Hz, 2H), 7.77-7.63 (m, 3H), 7.35 (dd, *J* = 8.53, 5.55 Hz, 1H), 6.74-6.70 (m, 1H), 2.75 (dd, *J* = 12.99, 6.90 Hz, 2H), 1.43-1.33 (m, 2H), 0.79 (t, *J* = 7.39 Hz, 3H); ¹³C NMR (100 MHz, DMSO-d₆)*, δ 168.5, 145.2, 145.1, 141.2, 135.3, 133.5, 132.8, 129.9, 127.9, 127.2, 126.5, 124.0, 123.9, 116.9, 107.7, 107.4, 44.3, 22.4, 11.0; MS (ESI): *m/z* 359.3 [M-H]⁻; HRMS (ESI⁺) calcd C₁₈H₁₈FN₂O₃S, (M⁺) 361.1020, found 361.101..

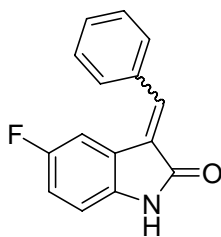
(E)-3-(6-Fluoro-2-oxo-1,2-dihydro-indol-3-ylidenemethyl)-N-isopropyl-

benzenesulfonamide (3-13):



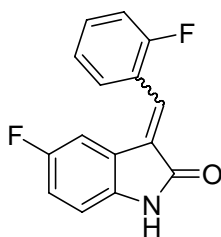
Yellow solid, yield 3.60% (after 3 steps), melting point: 156.1 °C; ¹H NMR (400 MHz, DMSO-d₆), δ 10.85 (s, 1H), 8.06 (s, 1H), 7.88 (dd, *J* = 6.1, 1.6 Hz, 2H), 7.72 (dd, *J* = 15.0, 7.3 Hz, 2H), 7.64 (s, 1H), 7.34 (dd, *J* = 8.5, 5.6 Hz, 1H), 6.73 (dd, *J* = 9.1, 2.3 Hz, 1H), 6.68-6.56 (m, 1H), 3.29 (dt, *J* = 12.9, 6.3 Hz, 1H), 0.95 (d, *J* = 6.5 Hz, 6H); ¹³C NMR (100 MHz, DMSO-d₆)*, δ 168.7, 164.696, 162.2, 145.2, 145.1, 142.5, 135.3, 133.7, 132.8, 130.0, 128.0, 127.2, 126.4, 124.0, 123.9, 117.0, 117.0, 107.8, 107.6, 98.6, 98.4, 45.4, 23.2. MS (ESI): *m/z* 359.3 [M-H]⁻.

(E)-3-Benzylidene-5-fluoro-1,3-dihydro-indol-2-one (4-1):



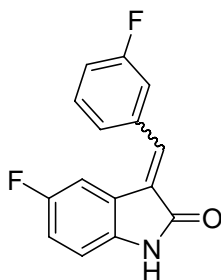
Orange solid, yield 87.4%, melting point: 199.5 °C; ¹H NMR (300 MHz DMSO-d₆) δ 10.64 (s, 1H), 7.79-7.61 (m, 3H), 7.52 (td, J = 8.2, 4.7 Hz, 3H), 7.18 (dd, J = 9.3, 2.1 Hz, 1H), 7.14-6.98 (m, 1H), 6.94-6.73 (m, 1H); ¹³C NMR (75 MHz, DMSO-d₆)* δ 168.9, 167.4, 159.0, 155.9, 139.6, 138.8, 137.9, 137.3, 134.3, 134.0, 132.4, 131.1, 130.4, 129.5, 129.2, 128.6, 127.8, 126.8, 122.2, 122.1, 116.9, 116.6, 111.3, 111.2, 109.8, 109.4; MS (APCI) *m/z* [M+H]⁺ 240.3.

(E)-5-Fluoro-3-(2-fluoro-benzylidene) -1,3-dihydro-indol-2-one (4-2):



Orange solid, yield 85.5%; melting point: 247.8 °C; ¹H NMR (300 MHz DMSO-d₆) δ 9.82 (s, 1H), 6.87 (t, J = 7.5 Hz, 1H), 6.80-6.66 (m, 2H), 6.51 (dd, J = 16.0, 8.3 Hz, 2H), 6.22 (dt, J = 9.2, 2.4 Hz, 1H), 6.13-5.90 (m, 2H); ¹³C NMR (75 MHz, DMSO-d₆)* δ 167.7, 160.9, 158.5, 157.6, 155.3, 139.1, 132.1, 132.0, 130.1, 129.2, 128.8, 124.5, 121.6, 121.4, 121.3, 121.2, 116.7, 116.4, 116.0, 115.7, 110.7, 110.6, 109.5, 109.2; MS (APCI) *m/z* [M+H]⁺ 258.3.

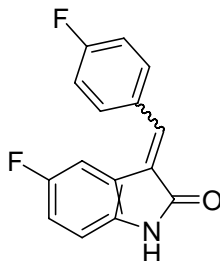
(E)-5-Fluoro-3-(3-fluoro-benzylidene) -1,3-dihydro-indol-2-one (4-3):



Orange solid, yield 33.4%; melting point: 196.9 °C; ¹H NMR (300 MHz, DMSO-d₆) δ 10.66

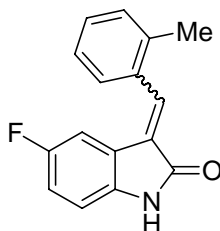
(s, 1H), 7.66 (s, 1H), 7.62-7.46 (m, 3H), 7.32 (s, 1H), 7.11 (d, $J = 8.3$ Hz, 2H), 6.86 (s, 1H); ^{13}C NMR (75 MHz, DMSO- d_6)* δ 168.9, 164.3, 161.1, 159.2, 156.1, 140.0, 137.0, 136.9, 136.3, 131.5, 131.4, 128.9, 125.6, 122.1, 122.0, 117.4, 117.3, 117.1, 117.1, 116.6, 116.3, 111.5, 111.4, 110.2, 109.8; MS (APCI) m/z $[\text{M}+\text{H}]^+$ 258.2.

(E)-5-Fluoro-3-(4-fluoro-benzylidene)-1,3-dihydro-indol-2-one (4-4):



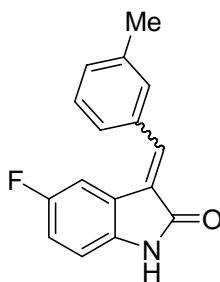
Orange solid, yield 53.6%, melting point: 226.6 °C; ^1H NMR (300 MHz DMSO- d_6), δ 10.64 (s, 1H), 7.76 (dd, $J = 8.1, 5.8$ Hz, 2H), 7.67 (s, 1H), 7.37 (t, $J = 8.7$ Hz, 2H), 7.18 (dd, $J = 9.2, 2.0$ Hz, 1H), 7.13-7.03 (m, 1H), 6.86 (dd, $J = 8.5, 4.6$ Hz, 1H); ^{13}C NMR (75 MHz, DMSO- d_6)* δ 168.5, 164.3, 161.0, 158.6, 155.5, 139.2, 136.3, 131.8, 131.7, 130.4, 130.4, 127.3, 121.7, 121.6, 116.6, 116.3, 116.1, 115.8, 110.9, 110.8, 109.4, 109.1; MS (APCI) m/z $[\text{M}+\text{H}]^+$ 258.3.

(E)-5-Fluoro-3-(2-methylbenzylidene)-1,3-dihydro-indol-2-one (4-5):



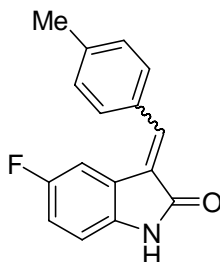
Orange solid, yield 50.5%; melting point: 201.3 °C; ^1H NMR (300 MHz DMSO- d_6) δ 10.65 (s, 1H), 7.76 (s, 1H), 7.53 (d, $J = 7.2$ Hz, 1H), 7.46-7.25 (m, 3H), 7.06 (dt, $J = 9.2, 2.3$ Hz, 1H), 6.85 (dd, $J = 8.5, 4.6$ Hz, 1H), 6.78-6.67 (m, 1H), 2.40-2.16 (m, 3H); ^{13}C NMR (75 MHz, DMSO- d_6) δ 168.3, 158.7, 155.6, 139.1, 136.9, 136.5, 133.4, 130.5, 129.8, 128.2, 128.1, 126.0, 122.1, 122.0, 116.5, 116.2, 110.9, 110.8, 109.4, 109.0, 19.4; MS (APCI) m/z $[\text{M}+\text{H}]^+$ 254.2.

(E)- 5-Fluoro-3-(3-methyl-benzylidene)-1,3-dihydro-indol-2-one (4-6),



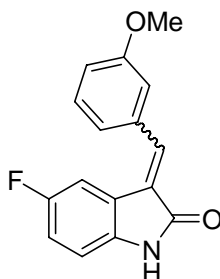
Orange solid, yield 38.7%, melting point: 229.0 °C; ¹H NMR (300 MHz DMSO-d₆) δ 10.63 (s, 1H), 7.67 (s, 1H), 7.54-7.39 (m, 3H), 7.32 (d, J = 7.3 Hz, 1H), 7.19 (dd, J = 9.4, 2.3 Hz, 1H), 7.09 (dt, J = 9.2, 2.4 Hz, 1H), 6.86 (dd, J = 8.5, 4.7 Hz, 1H), 2.37 (s, 3H); ¹³C NMR (75 mHz, DMSO-d₆)* δ 168.8, 158.9, 155.8, 139.5, 138.4, 137.8, 134.2, 130.9, 129.9, 129.0, 127.6, 126.4, 122.2, 122.1, 116.7, 116.4, 111.1, 111.0, 109.7, 109.3, 21.1; MS (APCI) *m/z* [M+H]⁺ 254.1.

(E)- 5-Fluoro-3-(4-methyl-benzylidene)-1,3-dihydro-indol-2-one (4-7):



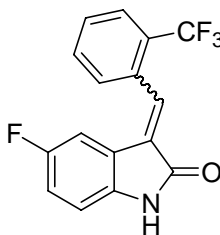
Orange solid, yield 63.2%, melting point: 232.2 °C; ¹H NMR (300 MHz DMSO-d₆) δ 10.62 (s, 1H), 7.66 (s, 1H), 7.58 (d, J = 7.8 Hz, 2H), 7.34 (d, J = 7.8 Hz, 2H), 7.25 (dd, J = 9.3, 2.0 Hz, 1H), 7.06 (dt, J = 9.2, 2.3 Hz, 1H), 6.85 (dd, J = 8.5, 4.7 Hz, 1H), 2.37 (s, 3H); ¹³C NMR (75 mHz, DMSO-d₆)* δ 168.7, 158.7, 155.6, 140.2, 139.1, 137.7, 131.1, 129.5, 129.4, 126.7, 122.0, 121.9, 116.4, 116.1, 110.8, 110.7, 109.4, 109.0, 21.1; MS (APCI) *m/z* [M+H]⁺ 254.2.

(E)- 5-Fluoro-3-(3-methoxy-benzylidene)-1,3-dihydro-indol-2-one (4-8):



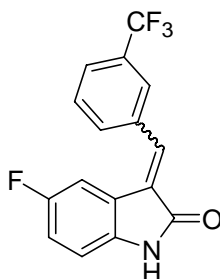
Orange solid, yield 61.7%; melting point: 177.4 °C; ¹H NMR (300 MHz DMSO-d₆), δ 10.64 (s, 1H), 7.68 (s, 1H), 7.47 (t, *J* = 7.85 Hz, 1H), 7.33-7.15 (m, 3H), 7.15-7.00 (m, 2H), 6.87 (dd, *J* = 8.4, 4.6 Hz, 1H), 3.80 (s, 3H); ¹³C NMR (75 MHz, DMSO-d₆)* δ 168.5, 159.4, 158.6, 155.5, 139.3, 137.3, 135.3, 130.0, 127.5, 121.3, 116.6, 116.3, 115.8, 114.3, 109.3, 55.2; MS (APCI) *m/z* [M+H]⁺ 270.1.

(E)- 5-Fluoro-3-(2-trifluoromethyl-benzylidene)-1,3-dihydro-indol-2-one (4-9):



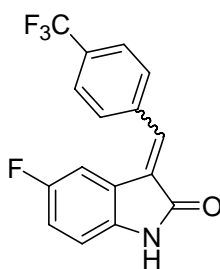
Orange solid, yield 42.6%; melting point: 184.1 °C; ¹H NMR (300 MHz DMSO-d₆) δ 10.74 (s, 1H), 7.92 (d, *J* = 7.3 Hz, 1H), 7.87-7.63 (m, 4H), 7.07 (t, *J* = 8.1 Hz, 1H), 6.94-6.75 (m, 1H), 6.43 (d, *J* = 7.9 Hz, 1H); ¹³C NMR (75 MHz, DMSO-d₆)* δ 167.7, 158.6, 155.5, 139.5, 133.0, 132.6, 130.1, 130.0, 127.2, 126.5, 126.5, 122.0, 121.4, 121.3, 117.2, 116.8, 111.2, 111.1, 109.7, 109.3 ; MS (APCI) *m/z* [M+H]⁺ 308.2.

(E)- 5-Fluoro-3-(3-trifluoromethyl-benzylidene)-1,3-dihydro-indol-2-one (4-10):



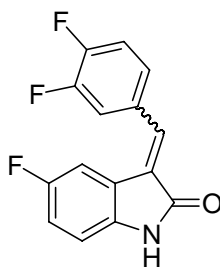
Orange solid, yield 7.1%, melting point: 234.2 °C; ¹H NMR (300 MHz DMSO-d₆) δ 10.7 (s, 1H), 8.00 (d, J=9.6Hz, 1H), 7.84-7.73 (m, 2H), 7.11-6.99 (m, 2H), 6.87 (q, J=4.5Hz, 1H); ¹³C NMR (75 MHz, DMSO-d₆)* δ 168.3, 158.7, 155.5, 139.6, 135.4, 135.2, 132.9, 130.0, 129.8, 129.4, 128.9, 126.2, 125.8, 125.7, 122.1, 121.4, 121.3, 117.1, 116.8, 111.1, 111.0, 109.4, 109.1; MS (APCI) *m/z* [m+1]⁺ 308.1.

(E)- 5-Fluoro-3-(2-trifluoromethyl-benzylidene)-1,3-dihydro-indol-2-one (4-11):



Orange solid, yield 3.3%, melting point: 203.4 °C; ¹H NMR (300 MHz DMSO-d₆) δ 10.70 (s, 1H), 7.88 (s, 4H), 7.72 (s, 1H), 7.09 (t, J = 9.0 Hz, 2H), 6.87 (dd, J = 8.0, 4.6 Hz, 1H); ¹³C NMR (75 MHz, DMSO-d₆)*: δ 168.2, 158.7, 155.6, 139.6, 138.3, 135.3, 129.9, 129.4, 129.0, 125.7, 125.7, 121.4, 121.2, 117.2, 116.9, 111.1, 111.0, 109.8, 109.5; MS (APCI) *m/z* [M+H]⁺ 308.1.

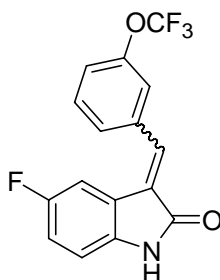
(E)- 3-(3,4-Difluoro-benzylidene)-5-fluoro-1,3-dihydro-indol-2-one (4-12):



Orange solid, yield: 36%; melting point: 190.2 °C; ¹H NMR (300 MHz, in DMSO-d₆): δ

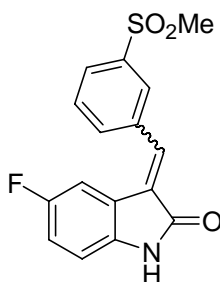
10.72 (s, 1H), 8.83 (q, J=8.7 Hz, 1H), 8.00 (s, 1H), 7.84 (s, 1H), 7.61-7.49 (m, 2H), 7.05 (td, J=9.0 Hz, 1H); ¹³C NMR (75 MHz, in DMSO-d₆)* δ 167.0, 159.4, 156.3, 137.1, 135.9, 131.4, 131.3, 131.3, 130.4, 127.1, 126.0, 125.9, 120.2, 119.9, 117.4, 117.2, 115.6, 115.3, 110.3, 110.2, 107.5, 107.2; MS (APCI): *m/z* 276.2 [M+H]⁺.

(E)-5-Fluoro-3-(3-trifluoromethoxy-benzylidene)-1,3-dihydro-indol-2-one (4-13):



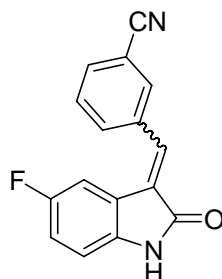
Orange solid, yield 68.7%; melting point: 191.0 °C; ¹H NMR (300 MHz DMSO-d₆) δ 10.7 (s, 1H), 7.75-7.66 (m, 4H), 7.52 (d, J=7.8 Hz, 1H), 7.15-7.07 (m, 2H), 6.88 (t, J=8.4, 1H); ¹³C NMR (75 MHz, DMSO-d₆)* δ 168.2, 167.0, 158.6, 155.5, 148.4, 148.1, 139.5, 137.3, 136.3, 136.3, 135.7, 135.3, 131.2, 131.0, 130.1, 128.7, 128.2, 128.0, 126.0, 125.9, 123.3, 122.8, 122.3, 121.7, 121.4, 121.3, 117.0, 116.7, 115.8, 115.5, 111.0, 110.9, 110.3, 110.2, 109.5, 109.2, 107.7; MS (APCI): *m/z* 324.3 [M+H]⁺.

(E)-5-Fluoro-3-(3-methanesulfonyl-benzylidene)-1,3-dihydro-indol-2-one (4-14):



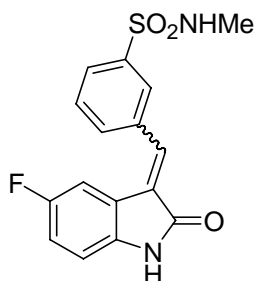
Orange solid, yield 30.0 %, melting point: 247.8 °C; ¹H NMR (300 MHz DMSO-d₆) δ 10.71 (s, 1H), 8.25 (s, 1H), 8.08-8.00 (m, 1H), 7.83 (t, J = 7.8 Hz, 1H), 7.76 (s, 1H), 7.13 (t, J = 8.7 Hz, 2H), 6.93-6.84 (m, 1H), 3.29 (s, 3H); ¹³C NMR (75 MHz, DMSO-d₆)* δ 168.2, 158.7, 155.6, 141.4, 139.6, 135.2, 134.1, 130.1, 129.0, 127.8, 127.4, 121.3, 121.2, 117.2, 116.9, 111.1, 111.0, 109.7, 109.3, 43.2; MS (APCI): *m/z* 318.2 [M+H]⁺.

(E) 3-(5-Fluoro-2-oxo-1,2-dihydro-indol-3-ylidenemethyl)-benzonitrile (4-15):



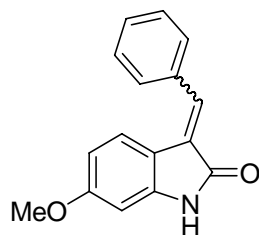
Orange solid, yield 56.8%, melting point: 190.5 °C; ¹H NMR (300 MHz DMSO-d₆) δ 10.7 (s, 1H), 8.85 (d, 1H), 8.43 (d, J=8.1 Hz, 1H), 7.87 (d, J=7.2 Hz, 2H), 7.69-7.58 (m, 2H), 7.07 (td, J=9.3 Hz, 1H), 6.81 (q, J=4.5 Hz, 1H); ¹³C NMR (75 MHz, DMSO-d₆)# δ 168.2, 166.9, 159.5, 156.4, 139.5, 137.4, 136.2, 135.5, 135.4, 134.8, 134.7, 134.6, 133.4, 133.2, 132.7, 130.1, 129.5, 129.1, 129.0, 128.5, 125.8, 125.6, 121.3, 121.2, 118.6, 118.3, 117.2, 116.8, 116.1, 115.8, 112.1, 111.3, 111.1, 111.0, 110.5, 110.4, 109.7, 109.3, 107.8, 107.5; MS (APCI): *m/z* 265.3 [M+1]⁺.

(E)-3-(5-Fluoro-2-oxo-1,2-dihydro-indol-3-ylidenemethyl)-N-methylbenzenesulphonamide (4-16):



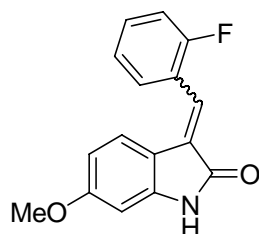
Orange solid, yield 15.6%; melting point: 224.7 °C; ¹H NMR (400 MHz, DMSO-d₆) δ 10.70 (s, 1H), 8.07 (s, 1H), 7.94 (d, J = 7.6 Hz, 1H), 7.88 (dd, J = 6.7 Hz, 1H), 7.79 (d, J = 7.7 Hz, 1H), 7.76 (d, J = 2.1 Hz, 1H), 7.61 (s, 1H), 7.16-7.03 (m, 2H), 6.88 (dd, J = 8.5 Hz, 1H), 2.48 (d, J = 9.5 Hz, 3H); ¹³C NMR (101 MHz, DMSO-d₆)# δ 168.2, 166.9, 158.3, 155.9, 139.9, 139.5, 139.5, 137.3, 136.4, 135.5, 135.0, 134.3, 133.1, 130.0, 129.7, 129.2, 128.8, 128.8, 128.1, 128.1, 127.9, 127.6, 126.7, 121.3, 121.3, 117.0, 116.8, 115.8, 115.6, 111.0, 111.0, 110.3, 110.2, 109.6, 109.3, 107.8, 107.6, 30.6, 28.6, 28.5; MS (ACPI): *m/z* 333.3 [M+H]⁺;

(E)-3-Benzylidene-6-methoxy-1,3-dihydro-indol-2-one (5-1):



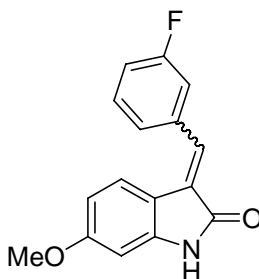
Bright yellow solid, yield 9.1%, melting point: 174.3 °C; ¹HNMR (300 MHz DMSO-d₆) δ 10.6 (br s, 1H), 7.67 (d, J=7.2 Hz, 2H), 7.52 (d, J= 6.9 Hz, 2H), 7.46-7.48 (m, 2H), 7.45 (s, 1H), 6.42 (d, J =6 Hz, 2H), 3.75 (s, 3H); ¹³CNMR (75 MHz, DMSO-d₆) δ 169.2, 161.1, 144.6, 134.7, 132.4, 129.2, 129.1, 128.6, 127.2, 123.5, 113.6, 106.5, 96.4, 55.2; MS (APCI): *m/z*, 270.0 [M+1]⁺. HRMS (APCI⁺) calcd C₁₆ H₁₄ NO₂, (M⁺) 252.1029, found 252.1019.

(E)- 3-(2-Fluoro-benzylidene)-6-methoxy-1,3-dihydro-indol-2-one (5-2):



Bright yellow solid, yield 27.8%, melting point: 192.5 °C; ¹HNMR (300 MHz DMSO-d₆) δ 10.6 (s, 1H), 7.74 (t, J=7.5 Hz, 1H), 7.47-7.54 (m, 1H), 7.32-7.36 (m, 2H), 7.34 (s, 1H), 7.19 (d, J = 9 Hz, 1H), 6.42 (m, 2H), 3.76 (s, 3H); ¹³CNMR (75 MHz, DMSO-d₆) δ 168.7, 161.4, 161.2, 144.8, 131.5, 130.3, 129.3, 124.6, 123.9, 122.5, 115.9, 113.4, 106.7, 96.4, 55.3; MS (APCI): *m/z*, 270.0 [M+1]⁺.

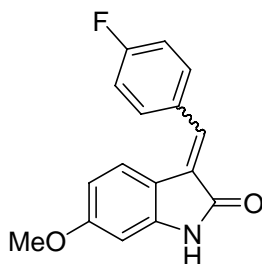
(E)- 3-(3-Fluoro-benzylidene)-6-methoxy-1,3-dihydro-indol-2-one (5-3):



Bright yellow solid, yield 25.2%, melting point: 181.6 °C; ¹HNMR (300 MHz DMSO-d₆) δ 10.6 (s, 1H, NH), 7.46-7.56 (m, 3H), 7.41 (s, 1H), 7.40 (d, J = 6Hz, 1H), 7.26-7.28 (m, 1H), 6.44(m, 2H), 3.76 (s, 3H); ¹³CNMR (75 MHz, DMSO-d₆) δ 137.2, 137.1, 130.7, 130.7, 128.1,

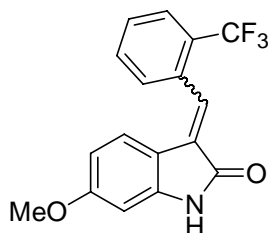
125.1, 123.7, 116.1, 115.8, 115.5, 113.3, 106.6, 96.5, 55.3; MS (APCI): m/z , 270.0 $[M+H]^+$.

(E)- 3-(4-Fluorobenzylidene)-6-methoxy-1,3-dihydro-indol-2-one (5-4):



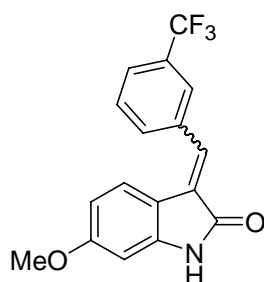
Bright yellow solid, yield: 19.26%, melting point: 204.1 °C; $^1\text{H NMR}$ (300 MHz, in DMSO- d_6) δ 10.6 (br s, 1H), 7.73 (dd, $J=14$ Hz, $J= 5.7$ Hz, 2H), 7.43 (d, $J=8.7$ Hz, 1H), 7.42 (s, 1H), 7.33 (t, $J = 8.7$ Hz, 2H), 6.41-6.44 (m, 2H), 3.75 (s, 3H); ^{13}NMR (75 MHz, DMSO- d_6) δ 169.2, 161.1, 144.7, 131.5, 131.4, 131.3, 131.1, 127.1, 123.5, 115.7, 113.5, 106.5, 96.4, 55.2; MS (APCI): m/z 270.0 $[M+H]^+$.

(E) 6-Methoxy-3-(2-trifluoromethyl-benzylidene)-1,3-dihydro-indol-2-one (5-5):



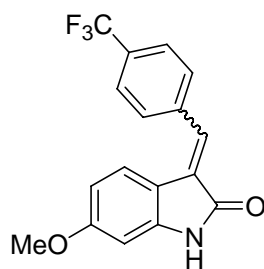
Bright yellow solid, yield 20.6%, melting point: 191.2 °C; $^1\text{HNMR}$ (300 MHz DMSO- d_6), δ 10.6 (br s, 1H), 7.85 (d, $J =7.8$ Hz, 1H), 7.70-7.75 (m, 2H), 7.64 (t, $J = 7.2$ Hz, 1H), 7.48 (s, 1H), 6.73 (d, $J = 8.7$, 1H), 6.45 (s, 1H), 6.30 (dd, $J = 8.4$ Hz, $J = 1.5$ Hz, 1H), 3.69 (s, 3H); ^{13}NMR (75 MHz, DMSO- d_6), δ 169.2, 161.9, 145.1, 133.7, 133.2, 130.6, 130.2, 129.9, 128.1, 127.6, 127.2, 126.7, 124.2, 122.5, 113.5, 107.2, 97.2, 55.7; MS (APCI): m/z 320.0 $[M+H]^+$.

(E)-6-Methoxy-3-(3-trifluoromethyl-benzylidene)-1,3-dihydro-indol-2-one (5-6):



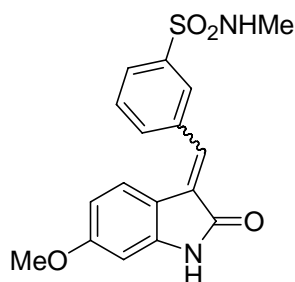
Bright yellow solid, yield 20.3%, melting point: 156.8 °C; ¹H NMR (300 MHz DMSO-d₆) δ 10.6 (br s, 1H), 7.97 (d, J = 7.2 Hz, 2H), 7.71-7.81 (m, 2H), 7.49 (s, 1H), 7.29 (d, J = 8.1 Hz), 6.39- 6.43 (m, 2H), 3.75 (s, 3H); ¹³C NMR (75 MHz, DMSO-d₆) δ 168.9, 161.4, 145, 135.9, 132.8, 130.3, 129.8, 129.6, 129.2, 128.6, 125.7, 125.6, 123.4, 113.2, 106.5, 96.6, 55.3; MS (APCI): *m/z*, 320.0 [M+H]⁺.

(E)-6-Methoxy-3-(4-trifluoromethyl-benzylidene)-1,3-dihydro-indol-2-one (5-7):



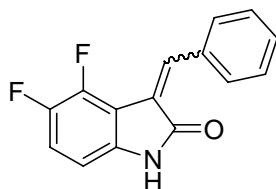
Bright yellow solid, yield 18.1%, melting point: 206.7 °C; ¹H NMR (300 MHz DMSO-d₆) δ 10.6 (br s, 1H), 7.86 (t, J = 9 Hz, 4H), 7.46 (s, 1H), 7.37 (d, J = 9 Hz, 1H), 6.41-6.44 (m, 2H), 3.75 (s, 3H); ¹³NMR (75 MHz, DMSO-d₆) δ 168.5, 165.0, 161.7, 145.2, 145.1, 138.5, 133.2, 129.8, 128.2, 125.6, 125.6, 124.3, 124.2, 116.8, 107.8, 107.5, 98.4, 98.1, 55.5; MS (APCI): *m/z* 320.0 [M+H]⁺.

(E)-3-(6-Methoxy-2-oxo-1,2-dihydro-indol-3-ylidenemethyl)-N-methyl-benzenesulphonamide (5-8):



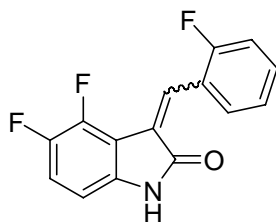
Bright yellow solid, yield 55.2%; melting point: 181.5 °C; ¹H NMR (400 MHz, DMSO-d₆) δ 10.62 (s, J = 9.8 Hz, 1H), 8.05 (s, 1H), 7.91 (d, J = 7.6 Hz, 1H), 7.83 (dd, J = 6.7 Hz, 1H), 7.73 (m, J = 9.8 Hz, 1H), 7.56 (d, J = 4.7 Hz, 1H), 7.48 (s, J = 11.6 Hz, 1H), 7.34 (t, J = 6.6 Hz, 1H), 6.46-6.38 (m, 2H), 3.78 (s, 3H), 2.46 (d, J = 4.4 Hz, 1H); ¹³C NMR (101 MHz, DMSO-d₆) , δ 168.9, 161.5, 145.0, 139.8, 135.8, 132.9, 130.3, 129.8, 128.6, 127.0, 126.6, 123.6, 113.2, 106.5, 96.7, 55.3, 28.6; MS (ACPI): *m/z* 343.3 [M-H]⁻

(Z)- 3-Benzylidene-4,5-difluoro-1,3-dihydro-indol-2-one (6-1):



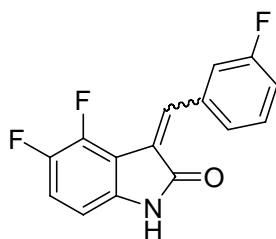
Bright yellow solid, yield 74.6%; melting point: 194.6 °C; ¹H NMR (300 MHz DMSO-d₆) δ 10.84 (s, 1H), 8.41-8.10 (m, 2H), 7.80 (s, 1H), 7.46 (d, J = 4.2 Hz, 3H), 7.25 (dd, J = 19.4, 8.5 Hz, 1H), 6.62 (dd, J = 8.1, 2.5 Hz, 1H); ¹³NMR (75 MHz, DMSO-d₆)* δ 168.4, 166.2, 147.4, 147.2, 147.0, 146.8, 144.1, 143.8, 143.7, 142.4, 142.2, 140.2, 140.1, 138.9, 137.9, 137.9, 134.9, 133.5, 132.1, 131.1, 130.1, 130.0, 129.8, 128.2, 127.9, 125.0, 124.3, 118.2, 117.9, 117.2, 117.0, 113.0, 112.8, 110.1, 109.9, 105.6, 105.2. MS (APCI): *m/z* 258.2 [M+H]⁺.

(Z)-4,5-Difluoro-3-(2-fluoro-benzylidene)-1,3-dihydro-indol-2-one (6-2):



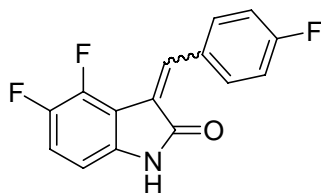
Yellow crystalline solid, yield 36.3%; melting point: 194.4 °C; ¹H NMR (300 MHz DMSO-d₆) δ 10.85 (s, 1H), 8.46 (t, J = 7.8 Hz, 1H), 7.91-7.74 (m, 1H), 7.51 (dd, J = 13.4, 6.3 Hz, 1H), 7.40-7.12 (m, 3H), 6.61 (dd, J = 8.4, 3.2 Hz, 1H); ¹³C NMR (75 MHz, DMSO-d₆)* δ 165.7, 162.0, 158.7, 147.2, 146.8, 144.1, 143.9, 143.6, 143.5, 138.2, 132.9, 132.7, 132.0, 126.7, 123.8, 123.8, 121.3, 121.1, 117.8, 117.5, 115.3, 115.0, 112.1, 105.3. MS (APCI): *m/z* 276.0 [M+H]⁺.

(Z)-4,5-Difluoro-3-(3-fluoro-benzylidene)-1,3-dihydro-indol-2-one (6-3):



Yellow crystalline solid, yield 52.3%; melting point: 214.2 °C; ¹H NMR (300 MHz DMSO-d₆) δ 10.90 (s, 1H), 8.38 (d, J = 11.13 Hz, 1H), 7.99-7.68 (m, 2H), 7.49 (dd, J = 14.60, 8.07 Hz, 1H), 7.39-7.19 (m, 2H), 6.79-6.48 (m, 1H); ¹³C NMR (75 MHz, DMSO-d₆)* δ 168.0, 166.0, 163.1, 159.9, 147.2, 143.8, 140.4, 138.1, 137.2, 135.5, 129.9, 129.7, 128.7, 126.1, 125.4, 118.5, 118.2, 117.9, 117.5, 117.3, 116.5, 116.1, 112.6, 109.7, 109.5, 105.6, 105.2; MS (APCI): *m/z* 276.0 [M+H]⁺.

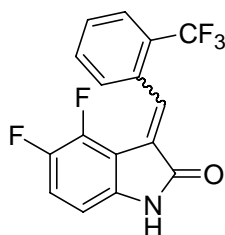
(Z)-4,5-Difluoro-3-(4-fluoro-benzylidene)-1,3-dihydro-indol-2-one (6-4):



Yellow crystalline solid, yield 88.6%; melting point: 235.6 °C; ¹H NMR (300 MHz DMSO-

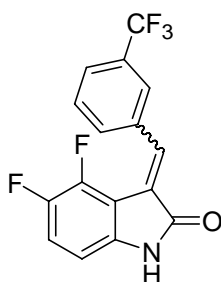
δ 10.84 (s, 1H), 8.44-8.26 (m, 2H), 7.75 (s, 1H), 7.33-7.13 (m, 3H), 6.59 (d, $J = 6.08$ Hz, 1H); ^{13}NMR (75 MHz, DMSO-d_6)* δ 168.231, 166.211, 165.036, 161.710, 146.905, 143.762, 140.955, 140.806, 137.816, 137.732, 134.922, 134.806, 132.577, 132.510, 132.466, 132.400, 131.351, 130.129, 130.092, 124.583, 117.077, 116.821, 115.322, 115.035, 114.746, 112.902, 112.748, 105.144; MS (APCI): m/z 276.0 $[\text{M}+\text{H}]^+$.

(*E/Z*)-4,5-Difluoro-3-(2-trifluoromethyl-benzylidene) -1,3-dihydro-indol-2-one (6-5):



Yellow crystalline solid, yield 54.1%; melting point: 235.8 °C; $^1\text{H NMR}$ (300 MHz DMSO-d_6) δ 10.90 (d, $J = 53.9$ Hz, 1H), 8.00-7.46 (m, 5H), 7.40-7.22 (m, 1H), 6.76-6.58 (m, 1H); ^{13}NMR (75 MHz, DMSO-d_6)* δ 167.4, 165.5, 147.1, 144.1, 140.3, 140.2, 138.7, 138.6, 136.0, 135.9, 134.0, 133.9, 132.0, 131.9, 131.8, 130.9, 130.8, 129.6, 129.4, 127.9, 127.3, 127.1, 126.8, 126.7, 126.4, 126.0, 125.9, 125.6, 125.5, 125.4, 125.4, 122.3, 119.1, 118.8, 118.4, 118.2, 111.6, 111.4, 109.2, 109.0, 106.0, 105.9, 105.7. MS (APCI): m/z 326.1 $[\text{M}+\text{H}]^+$.

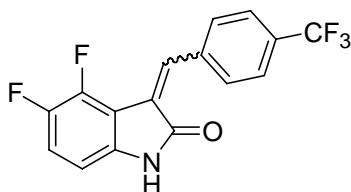
(*Z*)-4,5-Difluoro-3-(3-trifluoromethyl-benzylidene) -1,3-dihydro-indol-2-one (6-6):



Yellow crystalline solid, yield 51.7%; melting point: 215.5 °C; $^1\text{HNMR}$ (300 MHz DMSO-d_6) δ 10.9 (s, 1H), 8.75 (s, 1H), 8.32 (d, $J=7.2$ Hz, 1H), 7.83 (s, 1H), 7.76 (d, $J=7.2$ Hz, 1H), 7.65 (s, $J=7.2$ Hz, 1H), 7.28 (q, $J=8.4$ Hz, 1H), 6.63 (d, $J= 6.3$ Hz, 1H); $^{13}\text{CNMR}$ (75 MHz, DMSO-d_6)* δ 168.0, 166.1, 147.6, 147.4, 147.3, 147.0, 146.9, 144.2, 144.0, 143.9, 143.7, 140.5, 140.4, 140.1, 139.9, 138.3, 138.2, 136.7, 136.1, 135.8, 134.2, 133.8, 129.6, 129.2,

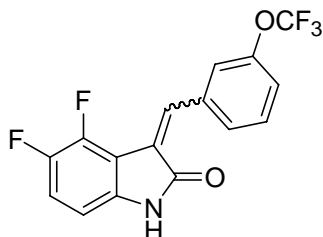
129.0, 128.9, 128.8, 128.5, 128.3, 128.0, 128.0, 127.0, 126.9, 126.6, 126.3, 126.1, 126.0, 122.4, 118.8, 118.5, 117.8, 117.6, 112.6, 112.4, 109.7, 109.5, 105.9, 105.9, 105.8, 105.4; MS (APCI): m/z 326.0 $[M+1]^+$

(Z)-4,5-Difluoro-3-(4-trifluoromethyl-benzylidene)-1,3-dihydro-indol-2-one (6-7):



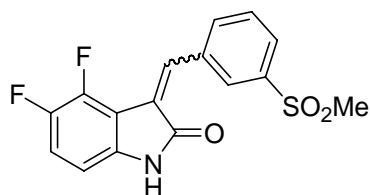
Yellow crystalline solid, yield 49.2%; melting point: 204.0 °C; ^1H NMR (300 MHz DMSO- d_6) δ 10.90 (s, 1H), 8.32 (d, $J = 7.93$ Hz, 2H), 7.92-7.73 (m, 3H), 6.78-6.52 (m, 1H), 7.38-7.23 (m, 1H); ^{13}C NMR (75 MHz, DMSO- d_6) δ 168.0, 166.0, 147.4, 147.0, 146.8, 144.3, 143.8, 143.7, 140.4, 140.4, 139.9, 139.7, 139.3, 138.4, 138.3, 137.2, 136.7, 132.1, 130.5, 130.4, 130.1, 129.7, 129.5, 129.1, 127.1, 126.4, 126.0, 125.9, 124.8, 124.8, 124.6, 124.6, 122.3, 118.8, 118.6, 118.0, 117.8, 112.5, 112.3, 109.7, 109.5, 105.8, 105.5, 105.5; MS (APCI): m/z 326.1 $[M+H]^+$.

(Z)-4,5-Difluoro-3-(3-trifluoromethoxy-benzylidene)-1,3-dihydro-indol-2-one (6-8):



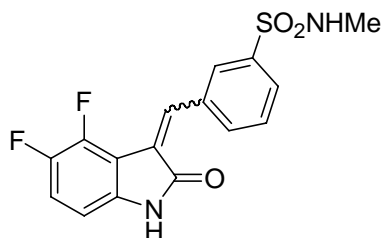
Yellow crystalline solid, yield 46.9%; melting point: 208.7 °C; ^1H NMR (300 MHz DMSO- d_6) δ 10.9 (s, 1H), 8.57 (s, 1H), 8.55 (d, $J=7.5$ Hz, 1H), 8.06 (d, $J=7.5$ Hz, 1H), 7.57 (t, $J=7.8$ Hz, $J=8.1$ Hz, 1H), 7.46 (d, $J=7.8$ Hz, 1H), 7.29-7.22 (m, 1H), 6.63-6.60 (m, 1H); ^{13}C NMR (75 MHz, DMSO- d_6) δ 167.8, 166.0, 147.9, 147.7, 147.4, 146.8, 144.1, 143.8, 143.7, 143.5, 140.3, 140.2, 139.9, 139.7, 138.1, 138.0, 137.2, 136.4, 135.3, 131.2, 129.9, 129.7, 128.8, 128.8, 126.4, 125.8, 123.4, 122.9, 122.0, 122.0, 121.8, 118.5, 118.3, 118.3, 117.6, 117.4, 112.5, 112.3, 109.4, 105.6, 105.2; MS (APCI): m/z 342.5 $[M+1]^+$.

(E/Z)-4,5-Difluoro-3-(3-methanesulfonylbenzylidene)-1,3-dihydro-indol-2-one (6-9):



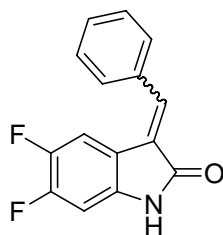
Yellow crystalline solid, yield 63.2%; melting point: 224.1 °C; ¹H NMR (300 MHz DMSO-d₆) δ 10.92 (d, *J* = 14.6 Hz, 1H), 8.78 (s, 1H), 8.47 (d, *J* = 7.8 Hz, 1H), 7.98 (d, *J* = 8.4 Hz, 1H), 7.93-7.80 (m, 1H), 7.72 (t, *J* = 7.8 Hz, 1H), 7.42-7.22 (m, 1H), 6.76-6.56 (m, 1H), 3.25 (d, *J* = 3.7 Hz, 3H); ¹³C NMR (75 MHz, DMSO-d₆)* δ 167.8, 165.9, 147.2, 146.8, 146.7, 144.1, 143.7, 143.5, 140.6, 140.3, 139.6, 139.5, 138.2, 138.2, 136.3, 136.2, 134.6, 134.6, 134.2, 129.8, 129.1, 128.9, 128.3, 127.5, 126.6, 117.8, 117.6, 112.4, 112.2, 109.6, 109.4, 105.3, 43.4, 43.3; MS (APCI): *m/z* 336.4 [M+H]⁺; Anal. Cal.cd for C₁₆H₁₁F₂NO₃S: C, 57.31; H 3.31; Found C, 57.32; H, 3.37.

(Z)-3-(4,5-Difluoro-2-oxo-1,2-dihydro-indol-3-ylidenemethyl)-N-methylbenzenesulphonamide (6-10):



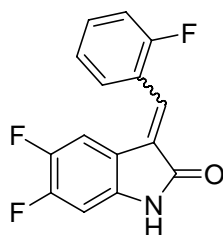
Yellow crystalline solid, yield 44.7%; melting point: 244.5 °C; ¹H NMR (400 MHz, DMSO-d₆) δ 10.89 (s, 1H), 8.62 (s, 1H), 8.35 (d, *J* = 7.7 Hz, 1H), 7.86 (dd, *J* = 22.8 Hz, 2H), 7.68 (t, *J* = 7.8 Hz, 1H), 7.49 (s, 1H), 7.38-7.18 (m, 1H), 6.64 (dd, *J* = 8.5 Hz, 1H), 2.45 (d, *J* = 20.7 Hz, 3H); ¹³C NMR (101 MHz, DMSO-d₆)* δ 168.0, 166.0, 147.1, 146.9, 146.5, 146.4, 144.6, 144.4, 144.2, 144.1, 140.4, 140.3, 140.1, 140.0, 139.3, 139.0, 138.3, 138.2, 136.8, 136.1, 135.3, 134.1, 133.5, 133.5, 129.5, 129.1, 128.9, 128.2, 127.5, 127.5, 127.4, 126.5, 126.1, 118.7, 118.5, 117.8, 117.6, 112.5, 112.4, 109.6, 109.5, 105.8, 105.7, 105.5, 105.4, 28.7, 28.5; MS (ACPI): *m/z* 351.2 [M+H]⁺;

(E)- 3-Benzylidene-5,6-difluoro-1,3-dihydro-indol-2-one (7-1);



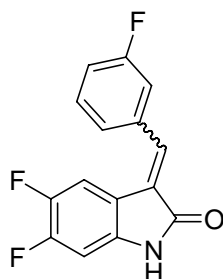
Chartreuse solid, yield 52.9%; melting point: 198.4 °C; ¹H NMR (300 MHz DMSO-d₆) δ 10.75 (s, 1H), 7.66 (d, *J* = 4.42 Hz, 3H), 7.60-7.41 (m, 3H), 7.37-7.28 (m, 1H), 6.94-6.83 (m, 1H); ¹³NMR (75 MHz, DMSO-d₆)* δ 168.6, 167.0, 152.1, 151.9, 148.8, 148.6, 146.1, 145.9, 142.9, 142.7, 140.0, 139.9, 138.4, 137.3, 137.0, 133.8, 133.6, 132.0, 130.7, 130.1, 129.2, 128.9, 128.2, 126.4, 125.4, 121.2, 121.1, 121.1, 116.8, 116.7, 116.7, 111.4, 111.1, 109.5, 109.2, 99.9, 99.6, 99.2, 98.9; MS (APCI): *m/z* 258.2 [M+H]⁺.

(E)- 5,6-Difluoro-3-(2-fluoro-benzylidene)-1,3-dihydro-indol-2-one (7-2):



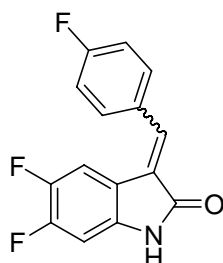
Chartreuse solid, Yield 50.2%, melting point: 230.2 °C; ¹H NMR (300 MHz DMSO-d₆) 10.90 (br, 1H), 7.75 (t, *J*=6.9 Hz, 1H), 7.59 (s, 2H), 7.43-7.38 (m, 2H), 7.10 (t, *J*=8.7 Hz, 1H), 6.92 (t, *J*=6.9 Hz, 1H); ¹³NMR (75 MHz, DMSO-d₆)* δ 168.1, 166.5, 161.2, 157.9, 152.4, 152.2, 149.1, 148.9, 146.3, 146.1, 143.1, 142.9, 140.2, 140.1, 137.9, 137.8, 132.4, 132.3, 132.0, 130.4, 128.6, 128.4, 127.6, 124.9, 124.9, 123.7, 123.7, 121.7, 121.5, 121.4, 121.2, 116.5, 116.5, 116.4, 116.4, 116.3, 116.0, 115.3, 115.0, 111.7, 111.5, 110.2, 109.9, 100.0, 99.7, 99.3, 99.0; MS (APCI): *m/z* 276.0 [M+H]⁺.

(E)-5,6-Difluoro-3-(3-fluorobenzylidene)-1,3-dihydro-indol-2-one (7-3):



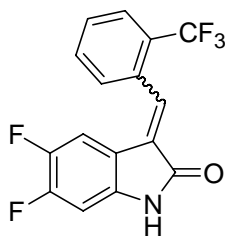
Chartreuse solid, Yield 21.8%; melting point: 189.4 °C; ¹H NMR (300 MHz DMSO-d₆) δ 10.78 (s, 1H), 7.77-7.41 (m, 4H), 7.42-7.16 (m, 1H), 7.07-6.72 (m, 1H); ¹³NMR (75 MHz, DMSO-d₆)* δ 168.4, 166.9, 163.8, 163.3, 160.6, 160.1, 152.3, 152.1, 149.0, 145.9, 143.0, 142.8, 140.3, 140.1, 137.5, 137.4, 136.6, 136.3, 136.2, 135.8, 135.7, 135.3, 131.1, 131.0, 130.2, 130.1, 128.7, 127.3, 126.6, 125.1, 120.8, 120.8, 120.7, 117.7, 117.6, 117.4, 116.9, 116.6, 116.5, 116.4, 116.4, 116.3, 116.1, 115.8, 111.6, 111.3, 109.7, 109.4, 100.0, 99.7, 99.3, 99.0; MS (APCI): *m/z* 276.0 [M+H]⁺.

(E)-5,6-Difluoro-3-(4-fluorobenzylidene)-1,3-dihydro-indol-2-one (7-4):



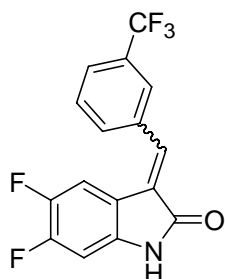
Chartreuse solid, yield 23.3%; melting point: 251.8 °C; ¹H NMR (300 MHz DMSO-d₆) δ 10.76 (s, 1H), 7.80-7.69 (m, 2H), 7.64 (s, 1H), 7.38 (d, *J* = 6.8 Hz, 3H), 6.99-6.78 (m, 1H); ¹³NMR (75 MHz, DMSO-d₆)* δ 144.0, 142.7, 140.6, 137.9, 130.6, 130.5, 128.0, 127.8, 125.8, 125.6, 123.2, 123.1, 120.9, 120.7, 118.4, 117.6, 116.6, 116.5, 114.2, 114.1, 113.0, 113.0, 112.9, 109.7, 102.0, 101.9, 101.9, 101.8, 101.6, 101.3, 101.0, 100.7, 97.7, 97.5, 88.4, 88.2 ; MS (APCI): *m/z* 276.0 [M+H]⁺.

(E)-5,6-Difluoro-3-(2-trifluoromethyl-benzylidene)-1,3-dihydro-indol-2-one (7-5)



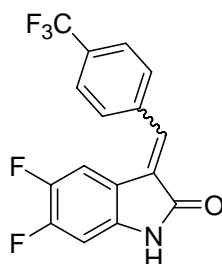
Yellow solid, Yield 55.4%; melting point: 176.5 °C; ¹H NMR (300 MHz DMSO-d₆) δ 10.87 (d, J = 1.0 Hz, 1H), 7.92 (d, J = 7.1 Hz, 1H), 7.86-7.59 (m, 4H), 7.07-6.76 (m, 1H), 6.62 (t, J = 8.9 Hz, 1H); ¹³C NMR (75 MHz, DMSO-d₆)* 167.8, 152.5, 152.3, 149.2, 149.0, 146.2, 143.0, 142.9, 140.4, 140.2, 133.1, 132.4, 132.1, 130.1, 130.0, 129.1, 127.2, 126.8, 126.6, 126.6, 126.5, 125.7, 122.0, 116.3, 116.2, 116.2, 116.1, 111.6, 111.3, 100.3, 100.0 ; MS (APCI): *m/z* 326.0 [M+H]⁺.

(E)- 5,6-Difluoro-3-(3-trifluoromethyl-benzylidene)-1,3-dihydro-indol-2-one (7-6):



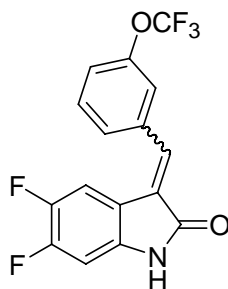
Chartreuse solid, yield 54.1%, melting point: 164.7 °C; ¹H NMR (300 MHz DMSO-d₆) δ 10.8(s, 1H); 8.02 (d, J=9.3 Hz, 2H), 7.80(d, J=7.2 Hz), 7.78 (d, J=7.2 Hz, 1H), 7.73 (s, 1H), 7.22 (t, J=9.0 Hz, 1H), 6.93 (q, J=7.2 Hz, 1H); ¹³C NMR (75 MHz, DMSO-d₆)* δ 168.2, 140.4, 140.2, 134.9, 132.8, 130.1, 129.8, 129.4, 127.7, 126.3, 126.2, 125.9, 125.7, 116.4, 116.3, 116.3, 111.4, 111.1, 100.1, 99.8; MS (APCI): *m/z*, 326.1 [M+1]⁺.

(E)-5,6-Difluoro-3-(4-(trifluoromethyl)benzylidene)-1,3-dihydro-indol-2-one (7-7):



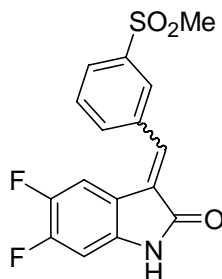
Chartreuse solid, yield 66.4%, melting point: 190.1 °C; ¹H NMR (300 MHz DMSO-d₆), δ 10.81 (s, 1H), 7.85 (s, 4H), 7.66 (s, 1H), 7.39-7.14 (m, 1H), 7.02-6.73 (m, 1H); ¹³CNMR (75 MHz, DMSO-d₆)* δ , 168.3, 166.7, 152.5, 152.3, 149.2, 149.0, 146.2, 146.0, 143.0, 142.8, 140.4, 140.3, 138.0, 137.9, 137.7, 137.3, 135.9, 134.8, 132.1, 129.9, 129.5, 129.5, 128.0, 127.7, 125.8, 125.8, 124.9, 124.9, 122.2, 122.2, 120.6, 120.5, 120.5, 116.3, 116.2, 116.2, 111.8, 111.5, 110.0, 109.7, 100.1, 99.8, 99.4, 99.105; MS (APCI): *m/z* 326.0 [M+H]⁺.

(E)-5,6-Difluoro-3-(3-(trifluoromethoxy)benzylidene)-1,3-dihydro-indol-2-one (7-8)



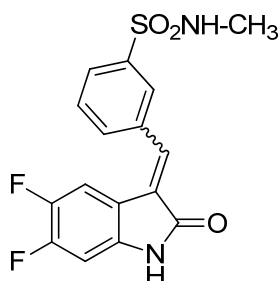
Chartreuse solid, yield 11.7%; melting point: 157.4 °C; ¹H NMR (300 MHz DMSO-d₆) δ 10.8 (s, 1H), 7.71-7.66 (m, 4H), 7.50 (d, J=7.5 Hz, 1H), 7.22 (q, J=11.4 Hz, J=10.5 Hz, 1H), 6.90 (q, J=10.5 Hz, 1H); ¹³CNMR (75 MHz, DMSO-d₆)* δ 168.2, 152.3, 152.1, 149.0, 148.8, 148.5, 146.0, 145.9, 142.9, 142.7, 140.3, 140.2, 136.1, 134.8, 131.1, 128.2, 127.7, 122.3, 121.7, 121.4, 118.3, 116.4, 116.3, 116.3, 116.2, 111.5, 111.2, 100.0, 99.7; MS (APCI): *m/z* 342.2 [M+1]⁺.

(E)-5,6-Difluoro-3-(3-methanesulfonylbenzylidene)-1,3-dihydro-indol-2-one (7-9):



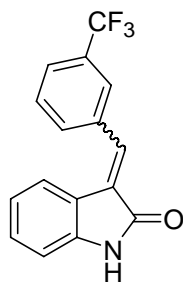
Chartreuse solid, yield 21.5%; melting point: 197.2 °C; ¹H NMR (300 MHz DMSO-d₆) δ ppm, δ 10.83 (s, 1H), 8.24 (s, 1H), 7.90-7.77 (m, 1H), 7.73 (s, 1H), 7.34-7.25 (m, 1H), 6.93(q, J=7.5 Hz, 1H), 3.29 (s, 3H) ¹³C NMR (75 MHz, DMSO-d₆)* δ 168.2, 166.8, 152.4, 152.2, 149.1, 148.9, 146.1, 145.9, 143.9, 142.9, 142.8, 141.4, 140.8, 140.4, 140.3, 137.8, 137.6, 136.0, 135.8, 135.1, 135.0, 134.7, 134.5, 134.0, 130.1, 129.8, 129.3, 128.3, 127.9, 127.8, 127.3, 120.5, 120.5, 116.3, 116.2, 116.2, 116.1, 111.7, 111.4, 109.9, 109.6, 100.1, 99.8, 99.4, 99.1, 43.5, 43.2; MS (APCI): *m/z* 336.5 [M+H]⁺.

(E)-3-(5,6-DiFluoro-2-oxo-1,2-dihydro-indol-3-ylidenemethyl)-N-ethyl-benzenesulfonamide (7-10):



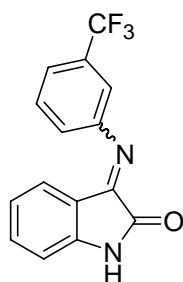
Chartreuse solid; yield 18.2%; melting point: 238.2°C; ¹H NMR (400 MHz, DMSO-d₆), δ 8.06 (s, 1H), 10.84 (s, 1H), 7.98-7.86 (m, 3H), 7.85-7.67 (m, 2H), 7.26 (dd, J = 10.82, 8.03 Hz, 1H), 6.93 (dd, J = 10.47, 6.93 Hz, 1H), 2.47 (d, J = 5.56 Hz, 2H); ¹³C NMR (100 MHz, DMSO-d₆)*, δ 168.2, 166.8, 139.9, 139.5, 136.2, 135.0, 135.0, 135.0, 134.8, 134.3, 133.1, 130.1, 129.7, 129.2, 128.0, 127.7, 127.7, 127.1, 126.7, 109.9, 100.1, 99.8, 99.3, 99.1, 28.5. MS (ESI): *m/z* 349.3 [M-H]⁻.

(E) 3-(3-Trifluoromethyl-benzylidene)-1,3-dihydro-indol-2-one (8-1):



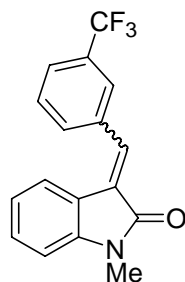
Yellow solid, yield 45.5%; melting point: 238.2°C; ¹H NMR (300 MHz DMSO-d₆) δ 10.67 (s, 1H), 8.02 (d, J=8.4 Hz, 2H), 7.83 (d, J=7.8 Hz, 1H), 7.76 (t, J=7.5 Hz, 1H), 7.68 (s, 1H), 7.33 (d, J=7.5 Hz, 1H), 7.25 (t, J=7.2 Hz, J=7.8 Hz, 1H), 6.90-6.81 (m, 1H); ¹³C NMR (75 MHz, DMSO-d₆) δ 168.2, 143.2, 135.6, 133.7, 132.9, 130.6, 129.9, 129.7, 129.3, 129.1, 125.8, 125.7, 122.1, 121.1, 120.4, 110.3; MS (APCI): *m/z* 290.4 [M+1]⁺.

(E/Z) 3-(3-Trifluoromethyl-phenylimino)-1,3-dihydro-indol-2-one (8-2):



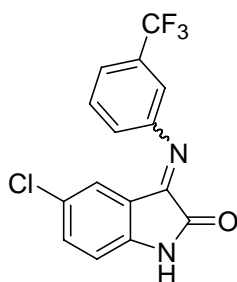
Orange solid, yield 82.3%; melting point: 144.4°C; ¹H NMR (300 MHz DMSO-d₆) δ 11.02 (d, J=39.0 Hz, 2H), 7.34-7.70 (m, 10H), 6.90 (t, J=8.4 Hz, 2H), 6.74 (t, J=7.8 Hz, 2H), 6.26 (d, J=7.8 Hz, 2H); ¹³C NMR (75 MHz, DMSO-d₆) δ 163.2, 158.5, 155.9, 154.1, 151.1, 149.9, 147.2, 146.1, 134.8, 134.6, 130.9, 130.6, 130.1, 129.4, 129.4, 125.7, 125.1, 123.1, 122.9, 122.3, 122.1, 121.8, 121.6, 121.3, 121.3, 121.0, 115.5, 115.5, 114.2, 114.2, 111.7, 110.9; MS (APCI): *m/z* 291.3 [M+H]⁺.

(E)- 1-Methyl-3-(3-trifluoromethyl-benzylidene)-1,3-dihydro-indol-2-one (8-3):



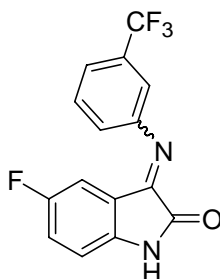
Yellow solid, yield 25.1%; melting point: 230.1°C; ¹H NMR (300 MHz DMSO-d₆) δ 8.01 (d, J=8.1 Hz, 2H), 7.85-7.76 (m, 3H), 7.34 (t, J=7.5 Hz, J=8.1 Hz, 2H), 7.07 (d, J=7.8 Hz, 1H), 6.90 (t, J=7.8 Hz, 1H), 3.21 (s, 3H); ¹³C NMR (75 MHz, DMSO-d₆)* δ 166.9, 144.3, 135.5, 134.3, 133.0, 130.6, 129.9, 129.7, 129.3, 128.1, 126.0, 126.0, 125.8, 125.8, 121.8, 121.7, 119.8, 109.1, 26.0; MS (APCI): *m/z* 304.2 [M+1]⁺.

(E/Z) 5-Chloro-3-(3-trifluoromethyl-phenylimino)-1,3-dihydro-indol-2-one (8-4):



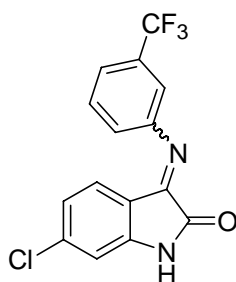
Orange solid, yield 84.8%; melting point: 181.5°C; ¹H NMR (300 MHz DMSO-d₆) δ 11.09 (d, J= 43.1Hz, 2H), 7.81-7.19 (m, 9H), 7.10-6.78 (m, 2H), 6.13 (d, J=2.0 Hz, 1H); ¹³C NMR (75 MHz, DMSO-d₆)* δ 162.9, 158.3, 155.1, 153.4, 150.6, 149.4, 146.0, 144.7, 134.0, 133.9, 131.0, 130.6, 130.2, 129.5, 129.3, 128.9, 126.4, 125.6, 125.3, 124.5, 123.0, 122.6, 122.6, 122.0, 121.7, 120.9, 120.9, 116.7, 115.6, 115.5, 114.3, 114.2, 113.3, 112.5; MS (APCI): *m/z* 325.3, 327.3 [M+H]⁺.

(E/Z)- 5-Fluoro-3-(3-trifluoromethyl-phenylimino)-1,3-dihydro-indol-2-one (8-5):



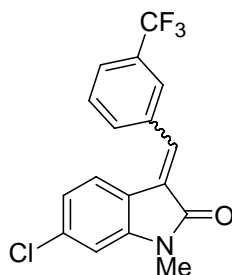
Orange solid, yield 52.5%; melting point: 157.3°C; ¹H NMR (300 MHz DMSO-d₆) δ 10.98 (d, J = 38.2 Hz, 2H), 7.73 (t, J=7.8 Hz, 1H), 7.64 (d, J = 7.7 Hz, 1H), 7.54 (t, J = 7.7 Hz, 1H), 7.47-7.24 (m, 8H), 6.95-6.90 (m, 2H), 5.89 (dd, J = 8.3, 2.2 Hz, 1H); ¹³C NMR (75 MHz, DMSO-d₆)* δ 163.2, 159.7, 159.4, 158.6, 158.3, 156.5, 155.5, 155.1, 153.9, 150.5, 149.4, 146.9, 143.6, 142.3, 131.1, 131.0, 130.6, 130.2, 129.8, 129.5, 129.4, 129.0, 125.9, 125.6, 124.6, 124.3, 122.9, 122.3, 122.2, 122.1, 121.6, 121.4, 121.1, 121.0, 120.9, 120.8, 120.7, 118.5, 118.4, 118.4, 115.9, 115.8, 115.5, 115.5, 114.3, 114.2, 113.5, 113.4, 112.9, 112.8, 112.1, 112.0, 111.8, 111.5, 111.1, 110.1, 109.8; MS (ESI): *m/z* 308.9 [M+H]⁺.

(E/Z) 6-Chloro-3-(3-trifluoromethyl-phenylimino)-1,3-dihydro-indol-2-one (8-6):



Orange solid, yield 34.2%; melting point: 192.4°C; ¹H NMR (300 MHz DMSO-d₆) δ 11.16 (br, 2H), 7.78-7.24 (m, 9H), 7.17-7.04 (m, 1H), 6.92 (dd, J = 6.9, 1.4 Hz, 2H), 6.83 (dd, J = 8.2, 1.6 Hz, 1H), 6.25 (d, J = 8.3 Hz, 1H); ¹³C NMR (75 MHz, DMSO-d₆)* δ 182.9, 163.2, 159.3, 158.4, 154.8, 153.1, 151.7, 150.7, 149.6, 148.6, 147.2, 142.2, 138.8, 138.7, 131.0, 130.9, 130.6, 130.2, 129.8, 129.4, 129.4, 128.9, 126.4, 126.1, 125.7, 124.5, 123.0, 122.6, 122.3, 122.2, 122.1, 121.7, 121.6, 120.8, 120.7, 119.9, 118.4, 116.7, 115.6, 115.5, 114.4, 114.3, 114.2, 112.1, 111.6, 110.9; MS (APCI): *m/z* 325.2, 327.2 [M+H]⁺.

(E)-6-Chloro-1-methyl-3-(3-trifluoromethyl-benzylidene)-1,3-dihydro-indol-2-one (8-7):



Orange solid, yield 16.6%; melting point: 120.8°C; ¹HNMR (300 MHz DMSO-d₆), δ 7.97 (d, J = 7.6 Hz, 2H), 7.88-7.68 (m, 3H), 7.30 (d, J = 8.2 Hz, 1H), 7.17 (s, 1H), 6.93 (d, J = 8.1 Hz, 1H), 3.19 (s, 3H); ¹³CNMR (75 MHz, DMSO-d₆)*, δ 167.0, 145.7, 143.4, 135.2, 135.1, 134.9, 134.4, 133.9, 132.9, 130.0, 129.3, 127.1, 126.3, 125.9, 125.9, 123.0, 122.3, 121.5, 121.4, 121.2, 118.6, 109.5, 26.2, 26.0. MS (APCI): *m/z* 338.4, 340.4 [M+1]⁺.

* More C atoms were detected in the ¹³C NMR data than the expected number. It is proposed that this may be due to isomerization during the scanning process which took place overnight, resulting in a mixture of isomers. The isomerization could be identified by comparing the proton spectrum which is done before carbon spectrum and the one which is done after the carbon spectrum. The presence of F atoms in the compound may have caused splitting of the peaks and contributed to the additional number of peaks in the spectrum.

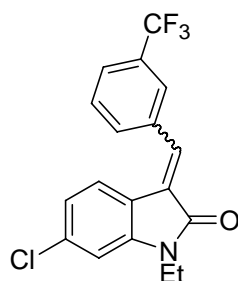
More C atoms were detected in the ¹³C NMR data than the expected number. It is proposed that this may be due to isomerization during the scanning process which took place overnight, resulting in a mixture of isomers. The isomerization could be identified by comparing the proton spectrum which is done before carbon spectrum and the one which is done after the carbon spectrum.

Appendix II Compounds that were not done by the candidate: Method and Charaterization

Syntheses of **8-8** and compound **8-9**

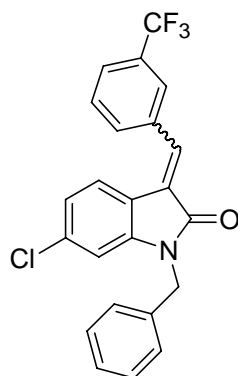
The mixture of **1-10** (0.7 mmol) and K_2CO_3 (1.4 mmol, 2eq) in 6 ml of acetonitrile was stirred at 80 °C for about 30 min, then to the reaction mixture was added bromoethane (1.4 mmol, 2eq) or benzyl bromide (1.4 mmol, 2eq) at rt. Then the mixture was stirred at 80 °C overnight before filtered to remove K_2CO_3 . The filtrate was concentrated under the reduce pressure and then purified by column chromatography with hexane-ethyl acetate (3:1) as eluting solvent to give the desired compounds.

(E)-6-Chloro-1-ethyl-3-(3-trifluoromethyl-benzylidene)-1,3-dihydro-indol-2-one, (8-8):



Yellow solid, yield: 35.0%, melting point: 121.3°C; 1H NMR (400 MHz DMSO- d_6) δ ppm δ 7.86 (s, 1H), 7.81 (s, 1H), 7.77 (d, $J=7.6$ Hz, 1H), 7.69 (d, $J=8$ Hz, 1H), 7.60 (t, $J=8$ Hz, $J=7.6$ Hz, 1H), 7.36 (d, $J=8.8$ Hz, 1H), 6.85-6.83 (m, 2H), 3.81 (q, 2H), 1.30 (t, $J=7.2$ Hz 3H); ^{13}C NMR (100 MHz, DMSO- d_6) δ ppm, δ 167.6, 144.8, 136.1, 135.6, 135.0, 132.3, 129.4, 127.9, 126.1, 126.1, 126.1, 126.0, 125.9, 125.9, 125.8, 125.8, 123.5, 121.6, 119.2, 109.1, 77.3, 77.0, 76.7, 34.9, 12.7; yield: 43.0%. MS (APCI): m/z 352.2, 354.2 $[M+H]^+$

(E/Z) 1-Benzyl-6-chloro-3-(3-trifluoromethyl-benzylidene)-1,3-dihydro-indol-2-one (8-9):

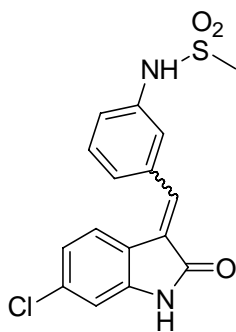


Yellow solid, yield: 43.0%, melting point: 109.4°C; ¹HNMR (400 MHz DMSO-d₆) δ ppm δ 8.55-8.50 (m, 2H), 7.89 (s, 1H), 7.79 (d, J=6.8, 2H), 7.69 (t, J=8 Hz, J=9.2 Hz, 1H), 7.63-7.45 (m, 3H), 7.38 (d, J=8 Hz, 1H), 7.36-7.29 (m, 11H), 7.02(dd, J=8.4 Hz, J=2.0Hz, 1H), 6.83 (dd, J=2Hz, J=8 Hz, 1H), 6.74-6.73 (m, 2H), 4.96 (s, 2H).; ¹³NMR (100 MHz, DMSO-d₆) δ ppm, δ 168.1, 165.8, 144.8, 142.8, 136.1, 135.7, 135.5, 135.4, 135.3, 135.2, 134.8, 134.1, 132.3, 131.5, 131.2, 130.6, 129.4, 128.9, 128.9, 128.8, 128.6, 128.6, 127.9, 127.8, 127.6, 127.2, 127.0, 126.9, 126.6, 126.2, 126.2, 125.9, 125.9, 125.3, 125.1, 123.4, 122.4, 122.1, 122.0, 120.2, 119.2, 109.6, 43.9, 43.7; yield: 43.0%.MS (APCI): *m/z* 416.3, 414.3 [M+H]⁺

Syntheses of **1-25**, **2-15**, **2-16**, **3-14**, **4-17**, **4-18**, **5-9**, **5-10**, **6-11**, **6-12**, **7-11** and **7-12**

The method of synthesizing following compound has been described in the section 2.5.3 using oxindoles and benzaldehydes. The method used in synthesizing 5,6 difluoro-oxindole has been described in section 2.5.6. The method used in synthesizing 3-Formyl-*N*-propyl-benzenesulfonamide or *N*-(3-Formyl-phenyl)-methanesulfonamide are described in section II-iv.

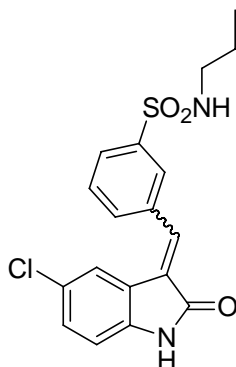
(*E*)-3*N*-[3-(6-Chloro-2-oxo-1,2-dihydro-indol-3-ylidenemethyl)-phenyl]methanesulfonamide (1-25):



Yellow solid, 26%, melting point 237.9 °C; ¹H NMR (400 MHz, DMSO-*d*₆) δ ppm 3.06 (s, 3H), 6.93-6.89 (m, 2H), 7.30 (d, *J* = 8.00 Hz, 1H), 7.40 (d, *J* = 7.66 Hz, 1H), 7.57-7.47 (m, 3H), 7.62 (s, 1H), 9.97 (s, 1H), 10.78 (s, 1H); ¹³C NMR (101 MHz, DMSO-*d*₆)* δ ppm 168.581, 144.326, 138.783, 136.083, 135.221, 134.332, 130.045, 126.880, 125.094, 124.174, 121.146, 120.997, 119.716, 119.576, 110.139; MS (ESI) *m/z* = 371.2 (M+Na)⁺, 347.1 (M-H)⁻

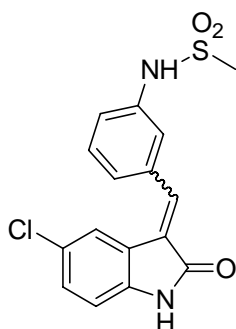
***E/Z* 3-(5-Chloro-2-oxo-1,2-dihydro-indol-3-ylidenemethyl)-*N*-propylbenzenesulfonamide**

(2-15):



Orange crystalline solid, yield 20%, melting point 169.1 °C, ¹H NMR (400 MHz, DMSO-d₆ δ ppm) 0.79 (dt, *J* = 7.41, 4.29 Hz, 3H), 1.39 (d sext., *J* = 7.34, 2.92 Hz, 2H), 2.77 (q, *J* = 6.76 Hz, 2H), 6.88 (dd, *J* = 25.46, 8.30 Hz, 1H), 7.33-7.24 (m, 1H), 7.69 (t, *J* = 7.82 Hz, 1H), 7.80-7.75 (m, 1H), 7.84 (d, *J* = 8.19 Hz, 1H), 7.92-7.88 (m, 1H), 8.06 (d, *J* = 5.10 Hz, 1H), 8.73 (s, 1H), 10.78 (s, 1H); ¹³C NMR (101 MHz, DMSO-d₆) δ ppm) 167.911, 141.954, 141.262, 140.828, 139.745, 136.716, 135.791, 135.040, 134.975, 134.321, 132.981, 130.113, 130.042, 129.594, 129.162, 128.231, 127.464, 127.364, 126.364, 126.300, 125.526, 125.095, 122.048, 121.878, 120.327, 111.679, 44.331, 44.301, 39.430, 22.419, 22.384, 11.060, 11.025; MS (ESI) *m/z* = 399.3 (M+Na)⁺, 375 (M-H)⁻

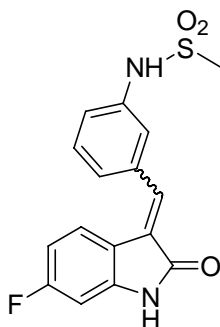
(*E*)-3*N*-[3-(5-Chloro-2-oxo-1,2-dihydro-indol-3-ylidenemethyl)-phenyl]methanesulfonamide (2-16):



Yellow solid, yield 26%, melting point 242.3 °C, ¹H NMR (400 MHz, DMSO-d₆ δ ppm) 3.06 (s, 3H), 6.86 (dd, *J* = 23.73, 8.31 Hz, 1H), 7.34-7.22 (m, 1H), 7.46-7.38 (m, 2H), 7.52 (dd, *J* = 10.38, 5.01 Hz, 1H),* 7.67 (s, 1H), 10.00 (s, 1H), 10.77 (s, 1H); ¹³C NMR (101 MHz,

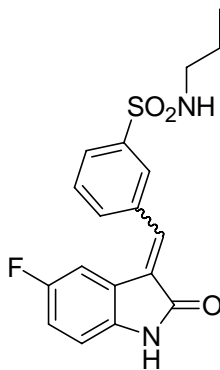
DMSO-d₆) δ ppm 168.228, 141.721, 138.843, 137.078, 135.094, 130.057, 129.844, 127.184, 125.118, 124.886, 122.259, 122.224, 121.079, 119.340, 111.504; MS (ESI) m/z = 371.2 (M+Na)⁺, 347.2 (M-H)⁻

(E)-3N-[3-(6-Fluoro-2-oxo-1,2-dihydro-indol-3-ylidenemethyl)-phenyl]-methanesulfonamide (3-14):



Pale green solid, yield 38%, melting point 231.3 °C, ¹H NMR (400 MHz, DMSO-d₆) δ ppm 3.05 (s, 3H), 6.72-6.64 (m, 2H), 7.49 (dd, J = 13.81, 5.92 Hz, 2H), 7.57 (dd, J = 7.29, 4.40 Hz, 2H), 9.97 (s, 1H), 10.79 (s, 1H); ¹³C NMR (101 MHz, DMSO-d₆) * δ ppm 168.847, 164.425, 161.978, 144.898, 144.775, 138.758, 135.279, 129.929, 126.886, 124.877, 120.872, 119.586, 117.095, 117.067, 107.633, 107.410, 98.262, 97.992. MS (ESI) m/z = 355.2 (M+23)⁺, 331.1 (M-1)⁻

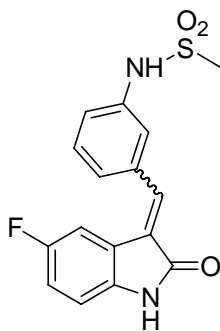
E/Z-3-(5-Fluoro-2-oxo-1,2-dihydro-indol-3-ylidenemethyl)-N-propylbenzenesulfonamide (4-17)



Yellow crystalline solid, yield 24%, melting point 163.4°C, ¹H NMR (400 MHz, DMSO-d₆) δ ppm 0.79 (dt, J = 7.41, 4.29 Hz, 3H), 1.39 (d sext., J = 7.34, 2.92 Hz, 2H), 2.77 (q, J = 6.76

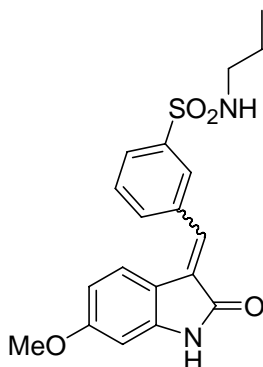
Hz, 2H), 6.88 (dd, $J = 25.46, 8.30$ Hz, 1H), 7.69 (t, $J = 7.82$ Hz, 1H), 7.77 (dd, $J = 9.59, 5.90$ Hz, 1H), 7.84 (d, $J = 8.19$ Hz, 1H), 7.92-7.88 (m, 2H), 8.06 (dd, $J = 5.10$ Hz, 1H), 8.58 (d, $J = 7.87$ Hz, 1H), 8.73 (s, 1H), 10.79 (s, 1H), 7.33-7.24 (m, 1H); ^{13}C NMR (101 MHz, DMSO- d_6) δ ppm) 167.911, 141.954, 141.262, 140.828, 139.745, 136.716, 135.791, 135.040, 134.975, 134.321, 132.981, 130.113, 130.042, 129.594, 129.162, 128.231, 127.464, 127.364, 126.364, 126.300, 125.526, 125.095, 122.048, 121.878, 120.327, 111.679, 44.331, 44.301, 39.430, 22.419, 22.384, 11.060, 11.025; MS (ESI) $m/z = 383$ (M+Na) $^+$, 358.9 (M-H) $^-$.

(E)-3N-[3-(5-Fluoro-2-oxo-1,2-dihydro-indol-3-ylidenemethyl)-phenyl]-methanesulfonamide (4-18):



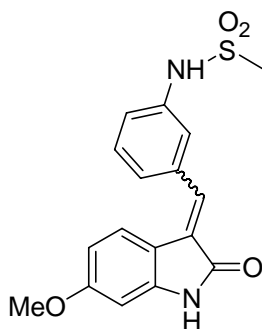
Dark yellow solid, yield 27%, melting point 231.3°C, ^1H NMR (400 MHz, DMSO- d_6 , δ ppm) 3.06 (s, 1H), 6.87 (dd, $J = 8.55, 4.62$ Hz, 1H), 7.10 (dt, $J = 9.14, 2.58$ Hz, 1H), 7.33-7.26 (m, 2H), 7.54-7.49 (m, 2H), 7.65 (s, 1H), 10.00 (s, 1H), 10.65 (s, 1H); ^{13}C NMR (101 MHz, DMSO- d_6)* δ ppm 168.452, 138.750, 136.743, 135.002, 129.980, 127.661, 127.632, 124.942, 121.464, 121.041, 119.394, 116.657, 116.423, 110.766, 110.046, 109.791*; MS (ESI) $m/z = 355.1$ (M+23) $^+$, 331.0 (M-1) $^-$

(E)-3-(6-Methoxy-2-oxo-1,2-dihydro-indol-3-ylidenemethyl)-N-propylbenzenesulfonamide (5-9):



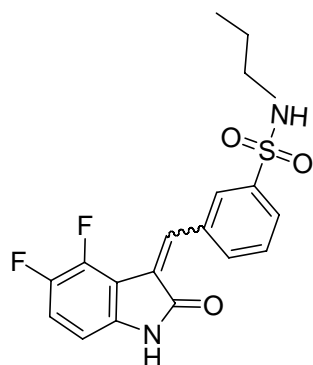
Yellow solid, yield 22%, melting point 191.5 °C, ¹H NMR (400 MHz, DMSO-d₆ δ ppm 0.79 (t, *J* = 7.39 Hz, 3H), 1.43-1.33 (m, 2H), 2.75 (dd, *J* = 12.37, 6.78 Hz, 2H), 3.76 (s, 3H), 6.39 (dd, *J* = 8.57, 2.41 Hz, 1H), 6.45 (d, *J* = 2.35 Hz, 1H), 7.32 (d, *J* = 8.56 Hz, 1H), 7.72 (t, *J* = 7.79 Hz, 2H), 7.86 (dd, *J* = 21.13, 7.78 Hz, 2H), 8.05 (s, 1H), 10.63 (s, 1H); ¹³C NMR (101 MHz, DMSO-d₆) δ ppm 168.963, 161.491, 145.056, 141.138, 135.752, 132.837, 130.469, 129.824, 128.571, 126.814, 126.426, 123.627, 113.207, 106.528, 96.687, 55.354, 44.338, 39.430, 22.406, 11.056; MS (ESI) *m/z* = 395.1 (M+Na)⁺, 371.4 (M-H)⁻

(E)-3N-[3-(6-Methoxy-2-oxo-1,2-dihydro-indol-3-ylidenemethyl)-phenyl]-methanesulfonamide (5-10):



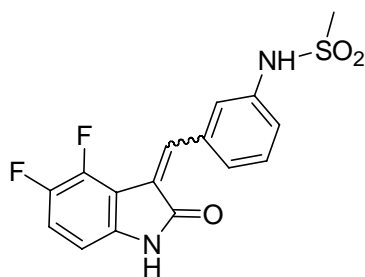
Dark yellow solid, yield 21%, melting point 206.4 °C, ¹H NMR (400 MHz, DMSO-d₆ δ ppm) 3.05 (s, 3H), 3.76 (s, 3H), 6.42 (dd, *J* = 6.94, 2.27 Hz, 2H), 7.27 (d, *J* = 8.02 Hz, 1H), 7.38 (d, *J* = 7.22 Hz, 2H), 7.54-7.42 (m, 3H), 9.94 (s, 1H), 10.57 (s, 1H) ¹³C NMR (101 MHz, DMSO-d₆) * δ ppm 169.199, 161.187, 144.729, 138.642, 135.743, 131.722, 129.747, 127.476, 124.834, 124.149, 120.452, 119.584, 113.405, 106.453, 96.437, 55.278 *;

(Z)-3-(4,5-Difluoro-2-oxo-1,2-dihydro-indol-3-ylidenemethyl)-N-propylbenzenesulfonamide (6-11):



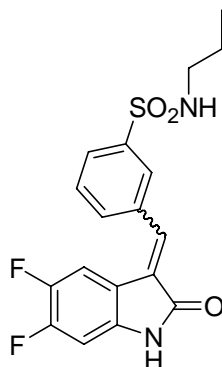
Orange crystalline solid, yield 32.3%, melting point 221.8 °C; ^1H NMR (400 MHz, *DMSO-d*₆) δ ppm 0.79 (dt, $J = 7.41, 4.29$ Hz, 3H), 1.39 (d sext., $J = 7.34, 2.92$ Hz, 2H), 2.77 (q, $J = 6.76$ Hz, 2H), 6.88 (dd, $J = 25.46, 8.30$ Hz, 1H), 7.69 (t, $J = 7.82$ Hz, 1H), 7.77 (dd, $J = 9.59, 5.90$ Hz, 1H), 7.84 (d, $J = 8.19$ Hz, 1H), 7.92-7.88 (m, 2H), 8.06 (d, $J = 5.10$ Hz, 1H), 8.58 (d, $J = 7.87$ Hz, 1H), 8.73 (s, 1H), 10.79 (s, 1H), 7.33-7.24 (m, 1H), ^{13}C NMR (101 MHz, *DMSO-d*₆) δ ppm 167.836, 165.920, 140.597, 140.251, 140.075, 139.968, 135.043, 134.000, 133.274, 129.226, 128.961, 128.751, 127.986, 127.240, 127.126, 44.287, 44.174, 22.408, 22.346, 11.054, 10.990; MS (ESI) $m/z = 401.1$ ($\text{M}+\text{Na}$)⁺, 377.0 ($\text{M}-\text{H}$)⁻

(Z)-3N-[3-(4,5-Difluoro-2-oxo-1,2-dihydro-indol-3-ylidene)methyl]-phenyl]-methanesulfonamide (6-12):



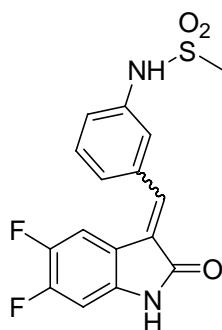
Dark yellow solid, yield 57%, melting point 250.4 °C; ^1H NMR (400 MHz, *DMSO-d*₆) δ ppm 3.09 (s, 3H), 6.64 (dd, $J = 8.49, 3.25$ Hz, 1H), 7.32-7.23 (m, 2H), 7.42 (t, $J = 7.92$ Hz, 1H), 7.79 (d, $J = 2.57$ Hz, 1H), 7.88 (d, $J = 7.87$ Hz, 1H), 8.05 (s, 1H), 9.87 (s, 1H), 10.85 (s, 1H), ^{13}C NMR (101 MHz, *DMSO-d*₆) * δ ppm 168.060, 165.920, 141.599, 141.490, 138.056, 137.872, 134.164, 128.959, 127.185, 125.456, 125.375, 122.184, 120.673, 117.293, 117.103, 112.653, 112.535, 105.223, 105.192, 105.159; MS (ESI) $m/z = 401.1$ ($\text{M}+\text{Na}$)⁺, 377.0 ($\text{M}-\text{H}$)⁻

(E/Z)-3-(5,6-Difluoro-2-oxo-1,2-dihydro-indol-3-ylidenemethyl)-N-propylbenzenesulfonamide (7-11) :



Orange crystalline solid, yield 18.5%, melting point 192.6 °C; ¹H NMR (400 MHz, DMSO-d₆) δ ppm δ 0.79 (dt, *J* = 7.40, 2.93 Hz, 1H), 1.39 (d sext., *J* = 7.28, 1.63 Hz, 2H), 2.76 (q, *J* = 7.46, 7.19 Hz, 1H), 6.90 (ddd, *J* = 27.38, 10.48, 6.84 Hz, 1H), 7.23 (dd, *J* = 10.80, 8.03 Hz, 1H), 7.73 (ddd, *J* = 23.51, 15.62, 7.81 Hz, 2H), 7.97-7.80 (m, 2H), 8.06 (s, 1H), 10.81 (s, 1H), 8.69-8.50 (m, 1H); ¹³C NMR (101 MHz, DMSO-d₆) δ ppm, δ 168.224, 166.811, 141.282, 140.821, 134.836, 134.232, 132.932, 130.106, 129.461, 129.179, 127.851, 127.482, 126.423, 111.511, 111.301, 109.903, 109.695, 100.091, 99.869, 99.349, 99.122, 44.299, 22.391, 11.058, 10.988. MS (ESI) *m/z* = 401.1 (M+Na)⁺, 377.0 (M-H)⁻

(E)-3N-[3-(5,6-Difluoro-2-oxo-1,2-dihydro-indol-3-ylidenemethyl)-phenyl]-methanesulfonamide (7-12):



Dark yellow solid, yield 21%, melting point 232.1°C; ¹H NMR (400 MHz, DMSO-d₆) δ ppm 3.07 (s, 3H), 6.91 (dd, *J* = 10.50, 6.93 Hz, 1H), 7.31 (d, *J* = 9.21 Hz, 1H), 7.40 (d, *J* = 7.68 Hz, 1H), 7.54-7.46 (m, 3H), 7.63 (s, 1H), 10.01 (s, 1H), 10.78 (s, 1H); ¹³C NMR (101 MHz, DMSO-d₆) * δ ppm 168.500, 140.042, 139.938, 138.754, 136.301, 136.273, 134.800, 130.056,

126.575, 125.095, 121.195, 119.371, 112.094, 111.885, 99.770, 99.546. MS (ESI) m/z = 401.1 (M+Na)⁺, 377.1 (M-H)⁻

Syntheses of 3-propylsulfamoyl-benzoic acid methyl ester and 3-methanesulfonylamino-benzoic acid methyl ester

The titled compounds serve as the starting material to synthesize 3-Formyl-*N*-propyl-benzenesulfonamide or *N*-(3-Formyl-phenyl)-methanesulfonamide which are described in section II.iv. The method of Wang *et. al*²²⁶ was followed with slight modifications. 0.5 g (2 mmol,) of 3 Chlorosulfonyl-benzoic acid methyl ester was dissolved in anhydrous dichloromethane (DCM, 30 mL) followed by addition of pyridine (0.344mL) and propanesulfonyl chloride (0.338 mL, mmol) in an ice bath. The reaction was left to stir for 17 hrs. Water (20 mL) and DCM (20 mL) were added to the reaction mixture and the layers separated. The aqueous layer was extracted with DCM (2×30 mL). The organic layer was then extracted with 1M HCL with (2 × 25 mL) to thoroughly remove excess pyridine. Subsequently, the organic layer was concentrated under vacuum to give the title compounds.

3-Propylsulfamoyl-benzoic acid methyl ester:

Brown solide, yield 95%, ¹H NMR (400 MHz, *ACN-d3*) δ ppm 0.82 (t, J = 7.40 Hz, 3H), 1.47-1.37 (m, 2H), 2.81 (dd, J = 13.28, 6.96 Hz, 2H), 3.92 (s, 3H), 5.68 (s, 1H), 7.69 (t, J = 7.83 Hz, 1H), 8.05-8.02 (m, 1H), 8.23-8.19 (m, 1H), 8.38 (t, J = 1.67 Hz, 1H)

Similaly, 3-Amino-benzoic acid methyl ester (0.5g) was dissolved in anhydrous dichloromethane (30 mL) followed by addition of pyridine (0.532mL) and methanesulfonyl chloride (0.509 mL, mmol) in an ice bath. The reaction was left to stir for 17 h. Water (20 mL) and DCM (20 mL) were added to the reaction mixture and the layers separated. The aqueous layer was extracted with DCM (2x30 mL). The organic layer was then extracted with 1N HCl (2 X 25mL) to thoroughly remove excess pyridine. Subsequently, the organic layer was concentrated under vacuum to obtain titled compound.

3-Methanesulfonylamino-benzoic acid methyl ester:

White solid, yield 85%, ¹H NMR (400 MHz, CDCl₃) ppm 3.04 (s, 3H), 3.94 (s, 3H), 6.95 (s, 1H), 7.45 (t, *J* = 8.13 Hz, 1H), 7.54-7.50 (m, 1H), 7.88-7.85 (m, 1H)

Syntheses of 3-formyl-*N*-propyl-benzenesulfonamide and *N*-(3-formyl-phenyl)-methanesulfonamide

The method of Billen *et al*²²⁷ was followed. 3-Propylsulfamoyl-benzoic acid methyl ester or 3-Methanesulfonylamino-benzoic acid methyl ester (2 mmol) was dissolved in 20mL of anhydrous THF to which Lithium aluminum hydride, LAH (1M in THF, 9 ml, 9 mmol) was added dropwise under nitrogen environment. The mixture was left to stir for 24h. The reaction mixture was then quenched with water (10mL) and EA (20mL). Few drops of 2M HCl were also added to remove traces of LAH and the mixture was then extracted 3 times with 20mL of EA. The organic phase was dried with anhydrous Na₂SO₄ and solvent was removed in vacuo. The resultant oil was reacted in the next step without further purification.

The synthesized 3-hydroxymethyl-*N*-propyl-benzenesulfonamide or *N*-(3-Hydroxymethyl-phenyl)-methanesulfonamide (1.08 mmol) was dissolved in dichloromethane (20 mL) followed by addition of pyridinium dichromate (3.5 eqv, 3.6 mmol). The reaction was stirred at room temperature for 18h under nitrogen environment. The brown crude mixture was then subjected to filtration through a plug of silica gel and subsequently washed with EA (250 mL). Solvent was removed under reduced pressure to give clear oil. Column chromatography using EA/Hex (2:3) was performed to further purify the product.

3-Formyl-*N*-propyl-benzenesulfonamide:

White crystalline solid. 78% yield, ¹H NMR (400 MHz, MeOH-*d*₄), δppm, δ0.86 (dt, *J* = 7.41, 1.86 Hz, 3H), 1.52-1.40 (m, 2H), 2.82 (td, *J* = 17.36, 7.05 Hz, 2H), 7.55 (t, *J* = 7.76 Hz, 1H), 7.81-7.69 (m, 1H), 7.98 (s, 1H), 8.13 (ddd, *J* = 7.86, 2.20, 1.19 Hz, 1H), 8.35 (t, *J* = 1.51 Hz, 1H), 10.07 (s, 1H)

***N*-(3-Formyl-phenyl)-methanesulfonamide:**

White crystalline solid, yield 86%, ¹H NMR (400 MHz, DMSO-d₆) ppm 7.51 (ddd, *J* = 8.00, 2.21, 1.22 Hz, 1H), 7.58 (t, *J* = 7.72 Hz, 1H), 7.66 (td, *J* = 7.47, 1.27 Hz, 1H), 7.72-7.70 (m, 1H), 10.09 (s, 1H), 9.98 (s, 1H), 3.05 (s, 3H).

* There is a hidden peak within the DMSO peak at 39.5ppm

Appendix III: Crystal data and structure refinement for 6-6

Empirical formula	C ₁₆ H ₈ F ₅ N O	
Formula weight	325.23	
Temperature	100(2) K	
Wavelength	0.71073 Å	
Crystal system	Triclinic	
Space group	P-1	
Unit cell dimensions	a = 6.908(5) Å	a = 82.396(15)°.
	b = 7.018(5) Å	b = 82.445(15)°.
	c = 13.699(10) Å	g = 84.923(15)°.
Volume	650.9(8) Å ³	
Z	2	
Density (calculated)	1.659 Mg/m ³	
Absorption coefficient	0.153 mm ⁻¹	
F(000)	328	
Crystal size	0.50 x 0.14 x 0.04 mm ³	
Theta range for data collection	2.94 to 27.49°.	
Index ranges	-8<=h<=8, -9<=k<=9, -17<=l<=17	
Reflections collected	8393	
Independent reflections	2975 [R(int) = 0.0577]	
Completeness to theta = 27.49°	99.8 %	
Absorption correction	Semi-empirical from equivalents	
Max. and min. transmission	0.9939 and 0.9273	
Refinement method	Full-matrix least-squares on F ²	
Data / restraints / parameters	2975 / 0 / 212	
Goodness-of-fit¹ on F²	1.060	
Final R indices [I>2sigma(I)]	R1 ² = 0.0628, wR2 ³ = 0.1373	
R indices (all data)	R1 = 0.0879, wR2 = 0.1475	
Largest diff. peak and hole	0.357 and -0.485 e.Å ⁻³	

$$^1\text{Goodness of fit} = \sqrt{\frac{\sum[w(F_O^2 - F_C^2)^2]}{n-p}},$$

$$^2R1 = \frac{\sum||F_O| - |F_C||}{\sum|F_O|},$$

$$^3wR2 = \sqrt{\frac{\sum[w(F_O^2 - F_C^2)^2]}{\sum[w(F_O^2)^2]}},$$

where F_O is observed electron densities, F_C is calculated electron densities, n is the number of data and p is the number of parameters refined.

Appendix IV : The second attempt of Western blot analysis of sirtuin inhibition by compounds 5-1 and 8-7

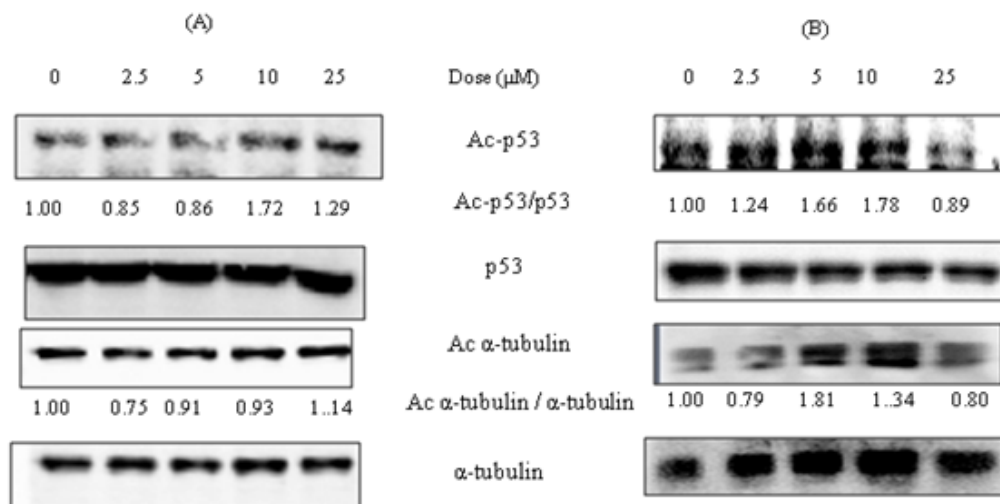


Figure IV-1 **5-1** induces hyper-acetylation of p53 and α -tubulin in (A) HepG2 and (B) HuH 7 cells after 12 h incubation. The ratios of acetylated p53/p53 and acetylated α -tubulin / α -tubulin were obtained as described in Figure 4-2. Loading controls were p53 and α -tubulin.

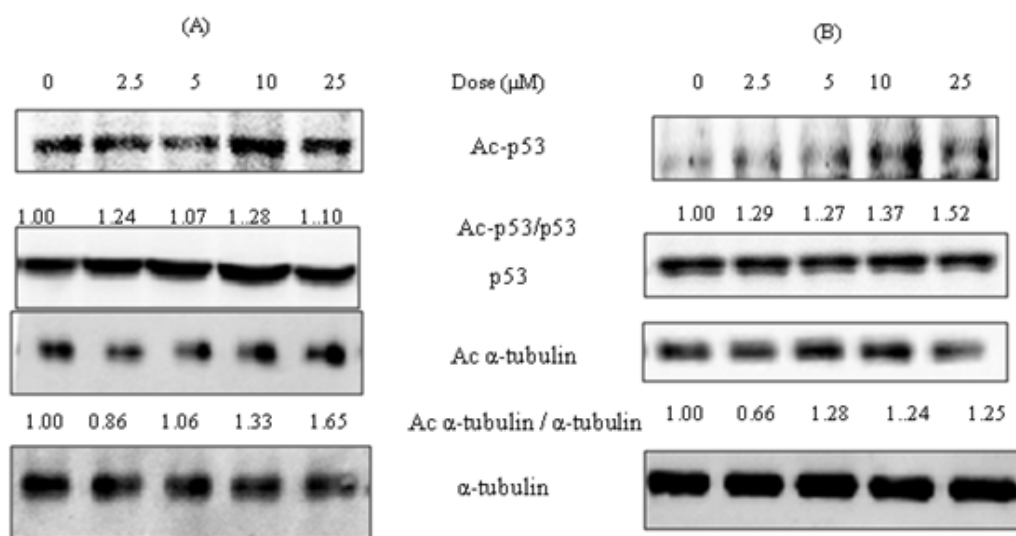


Figure IV-2 **8-7** induces hyper-acetylation of p53 and α -tubulin in (A) HepG2 and (B) HuH 7 cells after 12 h incubation. The ratios of acetylated p53/p53 and acetylated α -tubulin / α -tubulin were obtained as described in Figure 4-2. Loading controls were p53 and α -tubulin.

Appendix V: Determinations of drug likeness properties of the test compounds that are done by Drug Development Unit of NUS.

Determination of PAMPA permeability

The Parallel Artificial Membrane Permeability Assay (PAMPA) was used to determine The effective permeabilities (P_e) of 3-10, 3-12, and 7-6 were determined by PAMPA. Compound 47 and 1-23 was not determined due to the poor solubility.

Determinations were carried out on MultiScreen-IP PAMPA assay (donor) plates (MAIPNTR10) and MultiScreen Receiver Plates (MATRNPS50) from Millipore Corporation (USA) with 1% lecithin in dodecane (Sigma Aldrich, Singapore) as lipid barrier. 5 μ L of 1% lecithin in dodecane was dispensed into the wells of the donor plates. Aliquots (300 μ L) of test compound (5 μ M 1-18, 1.5 μ M 1-23, 10 μ M 3-10, 0.75 μ M 3-12 and 0.1 μ M 7-6 prepared in 0.1 \times PBS with 1% DMSO) were dispensed into the donor wells and equal volumes of the buffer solution (0.1 \times PBS with 1% DMSO) were added to the corresponding acceptor wells. The donor and acceptor plates were assembled and the unit was gently agitated on a mini shaker at room temperature (25 $^{\circ}$ C) for 6 hr or 16 hr. After this time, aliquots (250 μ L/well) from the donor and acceptor plates were transferred to separate glass inserts in HPLC vials. 35 μ L of the internal standard p-(dipropylsulfamoyl)benzoic (Sigma Aldrich, Singapore) (6.25 μ M in acetonitrile) was added to the sample which was then measured by LCMS (Shimadzu LC 20 series HPLC and AB Sciex Instruments 3200 Q TRAP LC/MS/MS). Measurements were based on the ratio of peak areas of the daughter ion and mother ion (M-H), normalized against the same ratio obtained for the internal standard. The mobile phase was Milli-Q water (0.1% formic acid) and acetonitrile (0.1% formic acid), run on gradient mode. The column was Phenomenex Luna column [3 μ , C₁₈(2), 100 A, 5 \times 4.6 mm] and injections were made at a volume of 2 μ L with flow rate of 0.6 mL/min. Calibration plots of test compounds were obtained under similar analytical conditions.

P_e of five standard compounds (warfarin, caffeine, quinidine, propranolol, verapamil, Sigma Aldrich Singapore) were determined under similar conditions. 500 μ M stock solutions were prepared and dispensed to the donor wells as described earlier. Quantification was by UV at λ_{\max} of 280 nm (verapamil, carbamazepine, warfarin, caffeine), 290 nm (propranolol) and 320 nm (quinidine). Calibration plots of reference compounds were determined under similar analytical conditions. Permeability of these standard compounds were reported to vary in the sequence verapamil (most permeable) > propranolol > carbamazepine > quinidine > caffeine > warfarin (least permeable).^{228,229}

P_e was obtained from Equation (1):

Equation(1):

$$p_e = -2.303 \times \frac{V_A V_D}{(V_A + V_D) \times A \times t} \times \log\left(1 - \frac{V_A + V_D}{V_D \times S \times \frac{C_A(t)}{C_D(0)}}\right)$$

where V_A and V_D = volumes of acceptor (cm^3) and donor (cm^3) wells respectively, A = area of the surface area of the membrane (0.24 cm^2), t = permeation time (s); S = fraction of sample remaining in the donor and acceptor wells after permeation time as determined from Equation (2). C_A and C_D in Equation (2) refer to the concentrations (μM) of compound in acceptor and donor wells respectively.

Equation(2):

$$S = \frac{V_a}{V_D} \times \frac{C_A(t)}{C_D(0)} + \frac{C_D(t)}{A(0)}$$

The Pe of each compound was obtained from at least 3 separate experiments using 2 different stock solutions. For each independent determination, triplicates (3 wells) were run for each compound.

Determination of cytotoxicities of test compounds

The cytotoxicities were determined on transforming growth factor-alpha mouse hepatocyte (TAMH) and mouse cardiomyocytes derived from AT-1 mouse atrial cardiomyocyte tumor cells (HL-1). TAMH (a gift from Prof Nelson Fausto, Department of Pathology, University of Washington) were cultured in DMEM-F12 (Dulbecco's Modified Eagle's Medium/ Nutrient Mixture F12) with ITS premix (5 mg insulin, 5 mg human transferrin, and 5 mg selenous acid), 100 nM dexamethasone, 10 mM nicotiamide, and 10 mg/L gentamicin. HL-1 (American Type Culture Collection, VA, USA) were cultured in Clay Comb Medium with 0.1 mM Norpinephrine, 2 mM L- Glutamine, 100 U/ml penicillin, 100 $\mu\text{g}/\text{ml}$ Streptomycin, and 10% v/v Fetal bovine serum.

Cytotoxicities of the compounds were determined by the CellTiter-Glo® Cell Viability Assay (Promega Corporation, Wisconsin, USA). An aliquot (200 μL , 6×10^4 cells/mL of TAMH, 7.5×10^4 cells/mL of HL-1) of medium was added to each well of a 96 well microtitre plate. After incubation for 24 h at 37 deg C, 5% CO_2 , media was removed from the well and replaced with fresh media (200 μL) containing a known concentration of test compound. The final concentration of DMSO in each well was maintained at 0.5 v/v. Incubation was continued for another 24 h at 37° C, 5% CO_2 , after which cell viability was determined with the Cell Titer-Glo® Cell Viability Assay Kit (Promega, Singapore) following manufacturer's instructions. The cell-reagent mixture was then transferred to a solid white flat-bottom 96-well plate (Greiner, Wemmel, Belgium) for the measurement of luminescence on a microplate reader (Tecan, Infinite 200). The viability of cells at a given concentration of test compound was determined from the equation (3):

$$\text{Percentage Cell Viability} = \frac{\langle lum_compound \rangle - \langle lum_blank \rangle}{\langle lum_vehcontrol \rangle - \langle lum_blank \rangle} \times 100\%$$

where lum_compound = luminescence of wells containing cells and test compound in media, lum_vehicle = luminescence of wells containing cells in media only and lum_blank = luminescence of wells containing media only.

Each concentration of test compound was evaluated at least 3 times on separate occasions, and two different stock solutions were used. The highest concentration of test compound used in the assay was 100 μ M. The IC₅₀ value (concentration that inhibited 50% of cell growth) was determined from the sigmoidal curve obtained by plotting percentage viability versus logarithmic concentration of test compound using GraphPad Prism 5 (San Diego, USA).

Determination of genotoxicities of test compounds

The Ames test kit as well as two strain of *Salmonella typhimurium* (TA98 and TA 100) were obtained from Molecular toxicology Inc. (Boone, North Carolina, USA) The *S. typhimurium* strains were grown from bacterial discs in nutrient broth at 37°C in a shaking incubator (~150 rpm) for about 10 hours. The absorbance of the cultures were measured at a wavelength of 660 nm on a UV spectrophotometer and those with absorbance values of 1.0- to 1.2 were deemed suitable for experiments. Histidine/biotin supplemented top agar was melted and aliquots of 2 mL were dispensed into culture tubes and kept at 45°C, 30-45 min. DMSO (100 μ L) or 2-aminoanthracene (19 μ M) was added to control culture tubes. Test compound (100 μ L in DMSO) was added to test control tubes to give final concentrations of 1 mM or 10 μ M. S9 mix (500 μ L, which comprise rat liver microsomes, phosphate-buffered solution, glucose-6-phosphate and NADP (Molecular Toxicology Inc, Boone, NC) was added to each tube, followed by 100 μ L of *S. typhimurium* strain (TA98 or TA100, Molecular Toxicology Inc, Boone, NC). The contents of each tube were quickly mixed, poured into a plate containing minimal glucose agar and swirled for even distribution. When the agar had hardened, the plates were incubated at 37 °C, 48h. The bacterial colonies were then counted. The absence of colonies would indicate the absence of mutagenicity. The experiments were done in duplicates.

Appendix VI: Purity data of the synthesized compounds

Compound Number	Mobile Phase A			Mobile Phase B		
	Composition ^a	RT (min) ^c	Area (%) ^d	Composition ^b	RT (min) ^c	Area (%) ^d
1-1	A1	5.5	98.9	B1	5.0	99.1
1-2	A1	6.8	99.1	B1	3.1	97.9
1-3	A1	8.0	99.9	B1	3.2	97.0
1-4	A1	7.5	97.1	B1	3.2	96.3
1-5	A1	12.5	99.9	B1	4.0	100.0
1-6	A1	8.0	96.0	B1	3.2	98.2
1-7	A1	3.2	95.7	B1	3.2	95.2
1-8	A1	4.1	100.0	B1	3.0	95.7
1-9	A1	7.2	96.3	B1	3.4	96.0
1-10	A2	6.9	100.0	B2	5.2	100.0
1-11	A1	11.2	100.0	B1	3.9	96.0
1-12	A2	5.5	98.1	B2	4.4	98.4
1-13	A2	6.2	98.4	B2	4.8	97.8
1-14	A2	7.7	100.0	B2	5.6	99.6
1-15	A2	7.7	100.0	B2	5.6	99.2
1-16	A2	3.3	100.0	B2	2.8	99.3
1-17	A2	2.8	99.4	B2	2.6	99.9
1-18	A3	3.2	97.5	B3	2.8	97.1
1-19	A3	4.0	98.2	B3	3.5	97.2
1-20	A3	18.3	98.3	B3	9.5	98.2
1-21	A3	4.4	97.8	B3	3.7	97.6
1-22	A3	5.3	96.7	B3	4.3	96.5
1-23	A3	6.5	98.5	B3	5.0	98.3
1-24	A3	6.2	87.1	B3	6.1	87.1
1-25	A3	4.6	96.7	B3	3.8	96.4
2-1	A1	7.1	96.3	B1	3.8	95.5
2-2	A1	6.9	95.1	B1	3.6	96.3
2-3	A1	7.3	94.8	B1	3.7	95.8
2-4	A1	7.7	98.4	B1	3.8	96.7
2-5	A1	6.3	95.1	B1	4.0	95.5
2-6	A1	9.5	95.1	B1	4.6	95.7
2-7	A1	7.1	96.3	B1	3.8	94.5
2-8	A1	7.6	95.4	B1	4.6	96.0
2-9	A2	6.1	100.0	B2	4.6	96.9
2-10	A2	5.3	98.3	B2	5.3	97.8
2-11	A2	3.6	97.8	B2	2.8	95.4
2-12	A2	2.8	81.7	B2	2.6	80.4
		3.09	18.3		2.7	17.1
2-13	A2	4.8	100.0	B2	4.0	97.7
2-14	A3	5.0	95.7	B3	3.5	95.6
2-15	A3	6.1	100.0	B3	4.8	98.9
2-16	A3	4.4	98.6	B3	4.3	98.6
3-1	A1	4.7	99.5	B1	2.8	100.0
3-2	A1	4.7	97.9	B1	2.7	100.0
3-3	A1	5.2	99.3	B1	2.8	100.0
3-4	A1	5.0	97.2	B1	2.8	94.8
3-5	A1	4.8	96.5	B1	2.9	94.3
3-6	A2	5.2	98.5	B2	4.2	96.0
3-7	A1	6.8	99.5	B1	3.3	100.0
3-8	A2	5.7	100.0	B2	4.5	99.4
3-9	A2	2.9	98.3	B2	2.7	97.0
3-10	A3	3.2	98.8	B3	2.8	97.6
3-11	A3	4.3	95.3	B3	3.7	96.2
3-12	A3	5.2	98.5	B3	4.2	98.3

Compound Number	Mobile Phase A			Mobile Phase B		
	Composition ^a	RT (min) ^c	Area (%) ^d	Composition ^b	RT (min) ^c	Area (%) ^d
3-13	A3	5.0	95.7	B3	4.1	95.3
3-14	A3	3.9	96.9	B3	3.3	96.4
4-1	A2	4.3	100.0	B2	3.7	100.0
4-2	A2	4.0	98.0	B2	3.5	98.3
4-3	A2	4.2	99.8	B2	3.6	99.8
4-4	A2	5.8	99.4	B2	3.6	99.8
4-5	A2	4.8	96.9	B2	4.1	96.8
4-6	A2	5.2	100.0	B2	4.3	98.6
4-7	A2	5.4	100.0	B2	4.5	98.3
4-8	A2	4.3	100.0	B2	3.7	100.0
4-9	A2	5.3	98.9	B2	3.6	99.5
4-10	A2	5.0	99.5	B2	4.1	100.0
4-11	A2	5.2	100.0	B2	4.2	100.0
4-12	A2	4.4	100.0	B2	3.7	98.2
4-13	A2	5.4	100.0	B2	4.3	99.4
4-14	A2	2.9	97.5	B2	2.7	96.2
4-15	A2	3.8	98.6	B2	3.4	98.5
4-16	A3	3.2	100.0	B3	2.7	100.0
4-17	A3	4.9	100.0	B3	4.1	99.5
4-18	A3	3.7	98.5	B3	3.2	98.2
5-1	A1	5.5	97.6	B1	2.7	100.0
5-2	A1	3.1	96.1	B1	2.6	95.2
5-3	A1	4.3	97.6	B1	2.7	100.0
5-4	A1	5.3	95.0	B1	2.7	100.0
5-5	A1	5.0	97.0	B1	2.6	100.0
5-6	A1	3.9	100.0	B1	3.0	100.0
5-7	A1	7.7	99.0	B1	3.0	100.0
5-8	A3	3.2	98.8	B3	2.7	98.5
5-9	A3	7.7	99.3	B3	5.5	99.1
5-10	A3	5.4	97.2	B3	4.1	97.2
6-1	A2	5.5	98.1	B2	4.4	98.0
6-2	A2	5.6	99.3	B2	4.4	99.6
6-3	A2	4.7	99.6	B2	4.5	99.6
6-4	A2	5.6	97.2	B2	4.5	96.8
6-5	A2	4.2	49.1	B2	3.6	49.0
		5.6	50.9		4.4	51.0
6-6	A2	6.7	99.2	B2	5.0	100.0
6-7	A2	6.1	100.0	B2	5.1	100.0
6-8	A2	7.5	100.0	B2	5.5	99.5
6-9		N.A.			N.A.	N.A.
6-10	A3	4.2	100.0	B3	3.2	99.4
6-11	A3	5.6	100.0	B3	4.5	100.0
6-12	A3	4.1	100.0	B3	3.5	100.0
7-1	A2	4.6	97.8	B2	2.9	97.1
7-2	A2	4.4	96.0	B2	3.7	95.4
7-3	A2	4.6	97.2	B2	3.7	97.0
7-4	A2	4.6	97.3	B2	3.8	97.7
7-5	A2	4.6	98.9	B2	3.9	99.1
7-6	A2	5.6	96.4	B2	4.4	96.0
7-7	A2	5.6	96.4	B2	4.4	96.0
7-8	A2	6.6	100.0	B2	5.4	97.5
7-9	A2	3.0	95.7	B2	2.7	95.9
7-10	A3	4.0	96.2	B3	3.5	96.5
7-11	A3	4.9	95.1	B3	4.1	95.0
7-12	A3	3.6	96.0	B3	3.2	95.9
8-1	A2	4.9	100.0	B2	4.1	99.1
8-2	A2	3.7	96.4	B2	3.2	97.9

Compound Number	Mobile Phase A			Mobile Phase B		
	Composition ^a	RT (min) ^c	Area (%) ^d	Composition ^b	RT (min) ^c	Area (%) ^d
8-3	A2	6.6	100.0	B2	5.4	99.7
8-4	A2	2.6	98.0	B2	2.6	100.0
8-5	A2	3.8	95.8	B2	3.3	97.3
8-6	A2	4.5	99.3	B2	3.7	98.0
8-7	A2	9.3	100.0	B2	7.1	97.1
8-8	A2	11.3	97.6	B2	8.2	95.2
8-9	A2	14.2	65.2	B2	9.9	65.3
		16.3	33.6		11.3	33.7

^a Composition of Mobile phase A: Methanol and Water

A1: 80% Methanol

A2: 25% Methanol + 50% acetonitrile

A3: 45% Acetonitrile+ 15% Methanol,

^b Composition of Mobile phase b: Acetonitrile and Water

B1: 80% Acetonitrile

B2: 75% Acetonitrile

B3: 60% Acetonitrile

^c Retention time of major peak in chromatogram. Chromatogram was run for at least 20 min for the detection of the major peak. Measurements were made at wavelength of 254 nm.